
Electronic Thesis and Dissertation Repository

4-22-2014 12:00 AM

The Electrochemistry of Hydrogen Peroxide on Uranium Dioxide and the Modelling of Used Nuclear Fuel Corrosion under Permanent Disposal Conditions

Linda Wu
The University of Western Ontario


Supervisor
David W. Shoesmith
The University of Western Ontario

Graduate Program in Chemistry

A thesis submitted in partial fulfillment of the requirements for the degree in Doctor of Philosophy

© Linda Wu 2014

Follow this and additional works at: <https://ir.lib.uwo.ca/etd>

 Part of the [Analytical Chemistry Commons](#), [Environmental Chemistry Commons](#), [Inorganic Chemistry Commons](#), [Materials Chemistry Commons](#), [Nuclear Commons](#), [Numerical Analysis and Scientific Computing Commons](#), [Other Computer Sciences Commons](#), [Physical Chemistry Commons](#), and the [Radiochemistry Commons](#)

Recommended Citation

Wu, Linda, "The Electrochemistry of Hydrogen Peroxide on Uranium Dioxide and the Modelling of Used Nuclear Fuel Corrosion under Permanent Disposal Conditions" (2014). *Electronic Thesis and Dissertation Repository*. 1970.

<https://ir.lib.uwo.ca/etd/1970>

This Dissertation/Thesis is brought to you for free and open access by Scholarship@Western. It has been accepted for inclusion in Electronic Thesis and Dissertation Repository by an authorized administrator of Scholarship@Western. For more information, please contact wlsadmin@uwo.ca.

**The Electrochemistry of Hydrogen Peroxide on Uranium Dioxide and the Modelling of
Used Nuclear Fuel Corrosion under Permanent Disposal Conditions**

(Thesis format: Integrated Article)

by

Linda Wu

Graduate Program
in
Chemistry

A thesis submitted in partial fulfillment
of the requirements for the degree of
Doctor of Philosophy

School of Graduate and Postdoctoral Studies
Western University
London, Ontario, Canada

© Linda Wu 2014

ABSTRACT

This thesis reports a series of investigations examining the corrosion process of used nuclear fuel under permanent disposal conditions. The motivation of the project is that the safety assessment of deep geological disposal of spent nuclear fuel requires a fundamental understanding of the processes controlling fuel corrosion which could lead to the release of radionuclides to the geosphere from a failed container.

One primary objective of this project was to develop a computational model in order to simulate fuel corrosion under the disposal conditions. The mathematical model was developed using COMSOL Multiphysics based on the finite element method. The chemical engineering module and the diluted species transportation module of the software are suitable for the simulations required. Literature research of the model development on the radiation-induced spent fuel corrosion revealed many key features required in modelling radiolytic corrosion (in particular for α -radiation). These features were incorporated into the model presented in the thesis along with the recently available kinetics data and mechanisms. Evaluation of different model setups and sensitivity tests of different parameters were performed. A series of simulations were designed and developed to determine the influence of redox conditions, with the emphasis on α -radiolysis and steel vessel corrosion products, on the corrosion rate of spent fuel.

The model presented in the thesis takes into account the α -radiolysis of water, the reaction of radiolytic H_2O_2 with UO_2 both directly and via galvanic coupling with noble metal particles, the reaction with H_2 via galvanic coupling, the Fenton reaction and other redox reactions involving H_2O_2 and H_2 . The calculated fuel corrosion rate is very sensitive to $[\text{Fe}^{2+}]_{\text{bulk}}$ produced by corrosion of the steel vessel. When the $[\text{Fe}^{2+}]_{\text{bulk}}$ is greater than $4.2 \mu\text{mol L}^{-1}$ even the radiolytically produced H_2 alone can suppress fuel corrosion without assistance from external H_2

for CANDU fuel with an age of 1000 years or larger. The ability of H₂ to suppress fuel corrosion is shown to be sensitive to fuel burnup (density of noble metal fission products) and a complete suppression of corrosion can be achieved at bulk H₂ concentrations in the order of 0.1 μmol L⁻¹. This approach is 1-dimensional and considers only the corrosion of a planar fuel surface. It will act as a preliminary step in the eventual development of 2-D and 3-D models involving the customized geometries necessary to account for the fractured nature of the spent fuel and the complex fuel bundle geometry.

A second objective of this project was to develop a more detailed understanding of the H₂O₂ decomposition process and its influence on UO₂ corrosion. Several variables (potential, pH, carbonate/bicarbonate, and fission products) can influence the reactivity of H₂O₂. Their influence on the surface composition and electrical conductivity of UO₂ will affect surface redox reaction rates and significantly alter the overall fuel corrosion rate. Electrochemical methods were used to separate a corrosion reaction into its two constituent half reactions allowing the determination of the rate dependence on potential for each half reaction. The primary electrochemical techniques used were cyclic voltammetry (CV) to examine a system in general, cathodic stripping voltammetry (CSV) to determine the consequences of a period of oxidation, corrosion potential (E_{CORR}) measurements to monitor redox conditions, linear polarization resistance (LPR) measurements to calculate corrosion rates, and electrochemical impedance spectroscopy (EIS) measurements to monitor changes in uranium oxide film properties. Since the changes in surface condition also have a significant impact on the H₂O₂ reactivity, the surface/solution analytical techniques were used to link the electrochemical/chemical processes to the compositional and structural changes observed on a UO₂ surface. These techniques included scanning electron microscopy (SEM) to analyze surface morphologies, X-ray photoelectron spectroscopy (XPS) to

determine the oxidation states of UO_2 surface, and inductively coupled plasma atomic emission spectroscopy (ICP-AES) to measure the dissolved U in solutions. In this thesis, the mechanisms of H_2O_2 decomposition on fuel surface and the consequent effect on UO_2 dissolution have been investigated under various conditions (pH, carbonate/bicarbonate).

At the lower pH values both the anodic oxidation and decomposition reactions are almost completely blocked by a thin surface layer of U^{VI} oxide. At higher pH this layer becomes more soluble and anodic oxidation occurs on the sublayer of $\text{U}^{\text{IV}}_{1-2x}\text{U}^{\text{V}}_{2x}\text{O}_{2+x}$, but is partially controlled by transport through a permeable, chemically dissolving U^{VI} oxide/hydroxide layer. At positive electrode potential, approximately 70% of the anodic current is consumed by H_2O_2 oxidation the remaining 30% going to produce soluble UO_2^{2+} . At higher pH values peroxide decomposition occurs on an unblocked $\text{U}^{\text{IV}}_{1-2x}\text{U}^{\text{V}}_{2x}\text{O}_{2+x}$ surface and the pH dependence of the reaction suggests HO_2^- is the electroactive form of peroxide.

The anodic behaviour of simulated nuclear fuel (SIMFUEL) in solutions containing H_2O_2 and $\text{HCO}_3^-/\text{CO}_3^{2-}$ has been studied electrochemically and using surface analytical techniques, in particular XPS. Two anodic reactions are possible, the oxidative dissolution of UO_2 and H_2O_2 oxidation. The rate of both reactions is controlled by the chemical release of U^{VI} surface species, and the rates can both be increased by the addition of $\text{HCO}_3^-/\text{CO}_3^{2-}$. Under anodic conditions the dominant reaction is H_2O_2 oxidation, although UO_2 dissolution may also be accelerated by the formation of a uranylperoxycarbonate complex. Similarly, under open circuit (corrosion) conditions both UO_2 corrosion and H_2O_2 decomposition are also controlled by the rate of release of U^{VI} surface species which blocks access of H_2O_2 to the underlying conductive $\text{U}^{\text{IV}}_{1-2x}\text{U}^{\text{V}}_{2x}\text{O}_{2+x}$ surface.

A series of electrochemical experiments has been conducted on SIMFUEL electrodes containing different dopants with the primary purpose of determining the relative importance of the UO_2 and ϵ -particle surfaces in the balance between UO_2 oxidation/dissolution and H_2O_2 decomposition. On the electrode containing both rare earth elements and noble metal particles, the anodic current is increased at high potentials, which is absent on the electrode containing only rare earth elements. The direct anodic oxidation of H_2O_2 occurs on ϵ -particles is interpreted at high potentials, making H_2O_2 oxidation the dominant reaction, the UO_2 surface being partially blocked by the presence of U^{VI} surface species.

Keywords: Uranium Dioxide, Corrosion, Nuclear Waste Disposal, Carbon Steel, Modelling Studies, COMSOL, Electrochemistry, SIMFUEL, Hydrogen Peroxide, Decomposition, Fission Products.

CO-AUTHORSHIP STATEMENT

Chapter 3 contains the contribution of Yannick Beauregard, who developed an early version of the corrosion model together with me.

Chapter 4 contains the contribution of Nazhen Liu, who performed the model calculations in Fig. 4.4 and Fig. 4.5.

Chapter 6 contains the contribution of Jon Goldik, who performed the X-ray photoelectron spectroscopy (XPS) measurements in Fig. 6.11 and Fig. 6.12.

This is dedicated to my grandfather

Bowen Zhu

朱伯穩

(1931 – 2013)

Acknowledgements

I would like to take the opportunity to thank the many people who have made this thesis possible.

First and foremost is my supervisor, Dr. David Shoesmith. Over the last 4½ years, Dave has always been there for me, giving guidance when I got lost, providing answers when I got puzzled, and supporting me when I got ideas. I truly appreciate his genuine concern about students, his endless passion towards work and life, his creativity and expertise in science and his great patience when I was even more stupid than today. Being lucky enough to have worked with Dave, I am grateful and I have learned what I need from this man and spent by far the most valuable years in my life.

I would also like to thank Dr. Peter Keech, Dr. Clara Wren and SSW (actually it's Dave again). Without these three there would be no MITACS project, no visit to NWMO, nor the new radiolytic corrosion project. I must also thank Chris Boyle, Dr. Fraser King, Kelly Liberda, Dr. Peter Maak, Dave Doyle and the entire APM team at NWMO who provided useful advice and help during my internship in Toronto. Also, Dr. Frank Garisto has provided numerous technical reports from NWMO and OPG which were found very helpful to this thesis.

Dr. Zack Qin has been a strong asset to my modelling work by providing thoughtful guidance and feedback. Dr. Jiju Joseph and the Wren group (Chemistry, UWO) were extremely helpful in providing radiation chemistry expertise for this thesis.

Surface Science Western and Biotron are acknowledged to be located walking distance from Chemistry Building and provide all the facilities that my research needed. I would like to thank

Dr. Mark Biesinger and Heather Bloomfield for their help with XPS and SEM, Dr. Charlie Wu for conducting ICP-AES analysis.

I would like to thank Jamie for helping me when I started in lab, reviewing thesis chapter when I am about to finish, and arranging my first-time-in-life sailing trips/ice-skating etc. All the members of Shoesmith/Wren groups are the best labmates/staff that you can ask for and I have really enjoyed the great atmosphere they create. I would also like to thank my friends and family for supporting and entertaining during my graduate study, especially my mom who is always listening and caring despite the 12-hour time difference. And to my grandparents, Bowen Zhu and Guozhen Xu, you have been great inspirations in my life and are truly missed.

Lastly, this research was funded under the Industrial Research Chair agreement between the Natural Science and Engineering Research Council (NSERC, Ottawa) and the Nuclear Waste Management Organization (NWMO, Toronto).

TABLE OF CONTENTS

ABSTRACT	ii
CO-AUTHORSHIP STATEMENT	vi
ACKNOWLEDGEMENTS	viii
TABLE OF CONTENTS	x
LIST OF TABLES	xvii
LIST OF FIGURES	xviii
SYMBOLS AND ACRONYMS	xxiv
Chapter 1: Introduction	1
1.1 Project motivation	1
1.2 Project overview	2
1.3 Thesis objectives	6
1.3.1 Strategy I: Modelling approach	7
1.3.2 Strategy II: Electrochemical approach	8
1.4 Background information	10
1.4.1 Water radiolysis	10
1.4.2 Spent fuel	12
1.4.2.1 General description	12
1.4.2.2 Composition	13
1.4.2.3 Electrical properties	15
1.4.2.4 Structural/solid state properties	17
1.4.2.5 Thermodynamic properties	19

1.4.2.6	Electrochemical properties	21
1.5	Reactions on UO ₂ surfaces	24
1.5.1	Redox reactions of H ₂ O ₂ on fuel surface	24
1.5.2	Factors influencing the rate of H ₂ O ₂ decomposition	29
1.5.2.1	pH	30
1.5.2.2	Carbonate/bicarbonate	30
1.5.2.3	Surface catalysis	31
1.5.3	The influence of carbonate/bicarbonate on fuel dissolution	34
1.5.4	The effect of steel corrosion products (Fe ²⁺ and H ₂) on fuel corrosion	37
1.5.4.1	Fe ²⁺	37
1.5.4.2	H ₂	38
1.5.5	Radiolytic corrosion model	40
1.6	Thesis outline	41
1.7	References	43
Chapter 2: Experimental techniques and details		57
2.1	Electrochemical experimental design	57
2.1.1	Electrochemical cell and equipment	57
2.1.2	Solutions	58
2.1.3	SIMFUEL working electrode	59
2.1.4	Cyclic voltammetry (CV) and cathodic stripping voltammetry (CSV)	62
2.1.5	Linear polarization resistance measurements	64
2.1.6	Electrochemical impedance spectroscopy (EIS)	66

2.2	X-ray photoelectron spectroscopy (XPS)	71
2.2.1	Basic principles of XPS	71
2.2.2	XPS experimental details	73
2.3	Scanning electron microscopy (SEM)	75
2.3.1	Basic principles of SEM	75
2.3.2	SEM experimental details	76
2.4	Inductively coupled plasma atomic emission spectroscopy (ICP-AES)	77
2.4.1	Basic principles of ICP-AES	77
2.4.2	ICP-AES experimental details	78
2.5	Instrument acknowledgements	78
2.6	References	79

Chapter 3: A model for the influence of steel corrosion products on nuclear fuel corrosion under permanent disposal conditions **81**

3.1	Introduction	81
3.2	Model description	81
3.2.1	Water radiolysis	83
3.2.2	UO ₂ oxidation by H ₂ O ₂	86
3.2.3	U ^V /U ^{VI} reduction by H ₂	87
3.2.4	Fenton reaction	90
3.2.5	H ₂ O ₂ decomposition	91
3.3	Model setup and results	92
3.3.1	The influence of the diffusion length	93
3.3.2	The effect of non-uniform dose rate distribution	95

3.3.3	The influence of Fe^{2+}	101
3.3.4	The influence of H_2	103
3.3.5	Influence of α -radiation dose rate	106
3.4	Summary and conclusions	107
3.5	References	108

Chapter 4: An improved model for the corrosion of used nuclear fuel inside a failed waste container under permanent disposal conditions **112**

4.1	Introduction	112
4.2	Model description	113
4.2.1	Water radiolysis	114
4.2.2	UO_2 oxidation by H_2O_2	121
4.2.3	$\text{U}^{\text{V}}/\text{U}^{\text{VI}}$ reduction by H_2	123
4.2.4	Reaction between H_2O_2 and H_2	125
4.2.5	Fenton reaction	126
4.2.6	H_2O_2 decomposition	127
4.3	Results and discussion	129
4.3.1	The effect of including a full α -radiolysis reaction set	130
4.3.2	Suppression of UO_2 corrosion by Fe^{2+}	133
4.3.3	Suppression of UO_2 corrosion by H_2	136
4.3.4	The influence of fuel burnup	141
4.4	Summary and conclusions	142
4.5	References	143

Chapter 5: An electrochemical study of H₂O₂ oxidation and decomposition on simulated nuclear fuel (SIMFUEL) 148

5.1	Introduction	148
5.2	Experimental	149
5.3	Results and discussion	150
5.3.1	Open-circuit potential in H ₂ O ₂ solution	150
5.3.2	Effect of pH on voltammetry	152
5.3.3	Effect of pH on H ₂ O ₂ oxidation	155
5.3.4	Dissolution experiments	164
5.3.5	Polarization resistance measurements	165
5.4	Summary and conclusions	168
5.5	References	170

Chapter 6: The anodic reactions on simulated nuclear fuel (SIMFUEL) in hydrogen peroxide solutions – effect of carbonate/bicarbonate 172

6.1	Introduction	172
6.2	Experimental	173
6.3	Results and discussion	174
6.3.1	Voltammetry	174
6.3.2	Dissolution experiments	182
6.3.3	Steady-state currents at various [CO ₃] _{tot}	184
6.3.4	XPS analysis	186
6.3.5	SEM imaging	191

6.3.6	Open circuit behaviour	192
6.3.7	CSV measurements	196
6.3.8	Polarization resistance measurements	199
6.4	Summary and conclusions	201
6.5	References	202

Chapter 7: The anodic reactions on simulated nuclear fuel (SIMFUEL) in hydrogen peroxide solutions – effect of fission products **204**

7.1	Introduction	204
7.2	Experimental	205
7.3	Results and discussion	207
7.3.1	Voltammetry	207
7.3.2	Potentiostatic measurements	208
7.3.3	Dissolution experiments	211
7.3.4	Steady-state currents at various $[\text{CO}_3]_{\text{tot}}$	214
7.3.5	EIS measurements	218
7.4	Summary and conclusions	223
7.5	References	224

Chapter 8: Summary and future work **227**

8.1	New contribution of this thesis	227
8.2	Project summary	228
8.3	Future work	231

LIST OF TABLES

Table 3.1. Default values of simulation parameters	92
Table 4.1. The primary yields (g-values) of α radiolysis species used in model calculations	116
Table 4.2. Full radiolysis reaction set and rate constants/equilibrium constants used in model calculations	118
Table 4.3. Default values of simulation parameters	129
Table 5.1. Distribution of charge between UO_2 oxidative dissolution and H_2O_2 oxidation	165
Table 6.1. Distribution of charge between UO_2 oxidative dissolution and H_2O_2 oxidation	184
Table 6.2. The fractions of U^{IV} , U^{V} , and U^{VI} in the surface of a SIMFUEL electrode before and after anodic oxidation in $0.1 \text{ mol L}^{-1} \text{ NaCl} + 0.02 \text{ mol L}^{-1} \text{ H}_2\text{O}_2$, $\text{pH} = 11.0$.	189
Table 7.1. The amount of the dissolved uranium in the anodic dissolution tests and the fraction of the total charge due to dissolution	212

LIST OF FIGURES

- Fig. 1.1. Illustration of the deep geological repository concept showing the container, emplacement room, and tunnel layout. Two emplacement plans are proposed, vertical boreholes and horizontal tunnels. 2
- Fig. 1.2. Solubility of uranium dioxide (UO_2) and schoepite ($\text{UO}_3 \cdot 2\text{H}_2\text{O}$) as a function of pH at 25°C . 3
- Fig. 1.3. Alpha, beta, and gamma radiation dose rates with respect to time for water in contact with a CANDU fuel bundle with a burn up of 220 MWh kgU^{-1} . 4
- Fig. 1.4. Illustration of possible electrochemical/chemical reactions within a failed copper/steel-dual-layer nuclear waste container. 5
- Fig. 1.5. Illustration of the procedure used to obtain corrosion currents (I_{CORR}), and hence corrosion rates, from electrochemically measured dissolution currents and corrosion potential (E_{CORR}) measurements. 9
- Fig. 1.6. Simplified schematic diagram showing the fuel dissolution driven by radiolytic oxidants. 12
- Fig. 1.7. Schematic illustrating the key changes induced by in-reactor fission and showing the three general categories of radionuclides. 14
- Fig. 1.8. A schematic diagram of the band structure for UO_2 , and its relationship to important energy scales (from electrochemical and spectroscopic data). 16
- Fig. 1.9. Fluorite crystal structure of stoichiometric UO_2 . (●) U atoms; (○) O atoms; (□) empty interstitial lattice sites. 18
- Fig. 1.10. Examples of stability diagrams for U systems. (A) Speciation of U in a hypothetical groundwater at 25°C . (B) Speciation of U^{VI} versus pH in NaCl solution at 25°C at a concentration of 0.001 mol L^{-1} . 19
- Fig. 1.11. Isosolubility lines for the U/ H_2O system as a function of pH and potential at 25°C . 20
- Fig. 1.12. Cyclic voltammogram recorded on a rotating UO_2 disc electrode at 10 mV s^{-1} and a rotation rate of 16.7 Hz using IR compensation in a $0.1 \text{ mol L}^{-1} \text{ NaClO}_4$ at pH 9.5. 22
- Fig. 1.13. Composition and corrosion behavior of UO_2 as a function of the UO_2 corrosion potential. 23
- Fig. 1.14. Steady-state corrosion potential (E_{CORR}) values measured as a function of H_2O_2 concentration in an unstirred $0.1 \text{ mol L}^{-1} \text{ NaClO}_4$ solution (pH=9.5). 27

Fig. 1.15. Schematic diagram showing the primary redox reactions involving H_2O_2 on a UO_2 surface.	29
Fig. 1.16. Solubility of the simulated fission product/actinide oxides in various solutions, including distilled water, $0.5 \text{ mol L}^{-1} \text{H}_2\text{O}_2$, $0.5 \text{ mol L}^{-1} \text{Na}_2\text{CO}_3$, and $0.5 \text{ mol L}^{-1} \text{Na}_2\text{CO}_3$ - $0.5 \text{ mol L}^{-1} \text{H}_2\text{O}_2$ solutions.	35
Fig. 1.17. The steady-state E_{CORR} recorded on a UO_2 electrode as a function of $[\text{H}_2\text{O}_2]$ in stirred $0.1 \text{ mol L}^{-1} \text{NaClO}_4$ (pH~9.5): (\circ) with, and (\bullet) without added $0.1 \text{ mol L}^{-1} \text{HCO}_3^-/\text{CO}_3^{2-}$.	36
Fig. 1.18. Illustration of a galvanic coupling between the UO_2 matrix and ϵ -particles.	39
Fig. 2.1. Diagram of the electrochemical cell setup.	58
Fig. 2.2 Schematic illustration of the experimental arrangement used to electroplate copper onto one face of SIMFUEL disk electrodes.	61
Fig. 2.3 Digital image of a SIMFUEL working electrode	62
Fig. 2.4. Potential-time profile for a cyclic voltammogram in which the potential is scanned from E_c to E_a , and then back to E_c .	63
Fig. 2.5. Potential-time profile for a typical cathodic stripping voltammogram when the potential is scanned from $E_{\text{App'd}}$ or E_{CORR} to E_c .	64
Fig. 2.6. Schematic of a linear polarization curve showing the linear potential used to measure the polarization resistance.	65
Fig. 2.7. Schematic showing the input AC voltage perturbation applied in an EIS measurement, and the resulting AC current response.	67
Fig. 2.8. (a) Bode and (b) Nyquist plots for a two time constant equivalent circuit. Intermediate phase angles are observed when both resistance and capacitance contribute to the overall impedance.	69
Fig. 2.9. Typical equivalent electrical circuit that can be used to fit a two time constant EIS spectrum.	70
Fig. 2.9. Schematic representation of the excitation of a core level electron, and subsequent photoelectron generation in XPS.	72
Fig. 2.10. Diagram for major components of a typical ICP-AES instrument.	78
Fig. 3.1. Reactions considered in the model.	83
Fig. 3.2. One-dimensional setup at the fuel/solution interface in the α -radiolysis model.	85
Fig. 3.3. H_2O_2 steady-state concentration profiles for various assumed diffusion lengths.	94
Fig. 3.4. Diffusive fluxes of UO_2^{2+} (equal to the UO_2 corrosion rate) as a function of various diffusion lengths.	95

Fig. 3.5. Fitting results for the α -dose rate profile.	97
Fig. 3.6. Illustration showing the two different dose rate distributions; uniform and exponential. The shaded areas indicate the total dose rate in each case.	98
Fig. 3.7. H_2O_2 steady-state concentration profiles for both uniform and exponential dose rate distributions.	100
Fig. 3.8. Diffusive fluxes of UO_2^{2+} calculated for the two dose rate distributions.	101
Fig. 3.9. $[\text{H}_2\text{O}_2]$ as a function of distance from fuel surface at various Fe^{2+} bulk concentrations.	102
Fig. 3.10. UO_2^{2+} flux (equal to the UO_2 corrosion rate) as a function of $[\text{Fe}^{2+}]$.	103
Fig. 3.11. UO_2^{2+} flux (equal to the UO_2 corrosion rate) as a function of $[\text{H}_2]_{\text{bulk}}$.	104
Fig. 3.12. Critical $[\text{H}_2]$ required to completely suppress fuel corrosion as a function of waste disposal time.	106
Fig. 4.1. Reactions included in the model for the α -radiolytic corrosion of spent nuclear fuel.	114
Fig. 4.2. The steady-state concentration profiles of α radiolysis species and dissolved UO_2^{2+} as a function of distance from the fuel surface; $[\text{H}_2]_{\text{bulk}} = [\text{Fe}^{2+}]_{\text{bulk}} = 0$. The solid lines are the model predictions using the full radiolysis reaction set, and the dashed lines are the estimated concentrations based on the radiolytic production of only H_2O_2 and H_2 .	131
Fig. 4.3. Steady-state $[\text{H}_2\text{O}_2]$ profiles calculated for various bulk $[\text{Fe}^{2+}]$; $[\text{H}_2]_{\text{bulk}} = 0.01 \mu\text{mol L}^{-1}$. The solid lines are the model predictions using the full radiolysis reaction set, and the dashed lines are the estimated concentrations based on only radiolytic production of H_2O_2 and H_2 .	134
Fig. 4.4. The calculated diffusive flux of UO_2^{2+} (equivalent to UO_2 corrosion rate) as a function of bulk Fe^{2+} concentration; $[\text{H}_2]_{\text{bulk}} = 0, 0.01$ and $0.1 \mu\text{mol L}^{-1}$.	135
Fig. 4.5. Steady-state $[\text{H}_2\text{O}_2]$ profiles calculated for various bulk H_2 concentrations; $[\text{Fe}^{2+}]_{\text{bulk}} = 0.01$ and $0.1 \mu\text{mol L}^{-1}$ as noted by arrows.	137
Fig. 4.6. The calculated diffusive flux of UO_2^{2+} (equivalent to UO_2 corrosion rate) as a function of bulk H_2 concentration; $[\text{Fe}^{2+}]_{\text{bulk}} = 0, 0.01$ and $0.1 \mu\text{mol L}^{-1}$.	139
Fig. 4.7. The calculated $[\text{H}_2]_{\text{crit}}$ required to completely suppress fuel corrosion as a function of time since emplacement in repository at different $[\text{Fe}^{2+}]_{\text{bulk}}$.	140
Fig. 4.8. The calculated diffusive flux of UO_2^{2+} (equivalent to UO_2 corrosion rate) as a function of ϵ -particle fraction for different bulk H_2 concentrations; $[\text{Fe}^{2+}]_{\text{bulk}} = 0.01 \mu\text{mol L}^{-1}$.	142

Fig. 5.1. Open-Circuit Potential (E_{OC}) as a function of pH recorded on a SIMFUEL electrode in solutions containing various $[H_2O_2]$ (0.004~0.02 mol L⁻¹). The dashed lines indicate the equilibrium potentials for the H_2O_2 reduction and oxidation half reactions calculated assuming a partial pressure for O_2 of 1 atmosphere. 151

Fig. 5.2. Voltammograms recorded on a SIMFUEL electrode at pH 9.5 and 12.6; $[NaCl] = 0.1$ mol L⁻¹; rotation rate = 16.7 Hz; scan rate = 10 mV.s⁻¹. 153

Fig. 5.3. Anodic current density recorded on a SIMFUEL electrode in a H_2O_2 solution at pH 9.5 and 12.6; $[NaCl] = 0.1$ mol L⁻¹; rotation rate = 25 Hz; scan rate = 10 mV s⁻¹. 155

Fig. 5.4. Anodic current densities recorded on a SIMFUEL electrode at various rotation rates; $[NaCl] = 0.1$ mol L⁻¹; $[H_2O_2] = 0$ (as background) or 0.02 mol L⁻¹; (a) pH = 9.5 and (b) pH = 12.6. 157

Fig. 5.5. Anodic current density recorded for various potential scan ranges. Each color indicates a scan from a different cathodic potential vertex as shown in the inset. Solid lines, 1st forward scan; dashed lines, 2nd forward scan; $[NaCl] = 0.1$ mol L⁻¹; $[H_2O_2] = 0.02$ mol L⁻¹; pH = 12.5. 158

Fig. 5.6. Current density at different potentials as a function of rotation rate; $[NaCl] = 0.1$ mol L⁻¹; $[H_2O_2] = 0.02$ mol L⁻¹; pH = 12.6. 159

Fig. 5.7. Anodic current densities recorded in solutions containing various $[H_2O_2]$ (the arrows indicate an increase from 0 to 0.02 mol L⁻¹) at various pH (a) 9.5, (b) 11.1 and (c) 12.5; rotation rate = 25 Hz; scan rate = 15 mV s⁻¹. 160

Fig. 5.8. Anodic current densities recorded at (a) 0.30 V and (b) 0.15 V as a function of $[H_2O_2]$ for various pH values. The dashed line indicates a first order dependence with respect to $[H_2O_2]$. 162

Fig. 5.9. Current density as a function of pH at 0.3 V in a solution containing $[H_2O_2] = 0.02$ mol L⁻¹. The dashed curves show the concentrations of the peroxide forms (H_2O_2 and HO_2^-) vs. pH. 164

Fig. 5.10. Polarization resistance, R_p , plotted as a function of rotation rate recorded on a SIMFUEL electrode; $[NaCl] = 0.1$ mol L⁻¹; $[H_2O_2] = 0.02$ mol L⁻¹; pH = 12.6. 166

Fig. 5.11. Reciprocal of polarization resistance, R_p^{-1} , as a function of $[H_2O_2]$ recorded on a SIMFUEL electrode at various pH values; $[NaCl] = 0.1$ mol L⁻¹; rotation rate = 25 Hz. 167

Fig. 5.12. Schematic illustration of the proposed mechanism for redox reactions involving H_2O_2 on fuel surface in an alkaline solution, and the H_2O_2 decomposition being catalyzed by the mixed U^{IV}/U^V states. 169

Fig. 6.1. CVs recorded on 1.5 at. % SIMFUEL in 0.1 mol L⁻¹ NaCl (dashed line), and 0.1 mol L⁻¹ NaCl + 0.1 mol L⁻¹ Na₂CO₃/NaHCO₃ (solid line), both solutions at pH 9.7. Rotation rate = 16.7 Hz; scan rate = 10 mV s⁻¹. 175

Fig. 6.2. Current densities recorded on 1.5 at.% SIMFUEL on the forward scan of CVs in 0.1 mol L⁻¹ NaCl containing different [H₂O₂] at pH 9.5 and 11.0; rotation rate = 25 Hz; scan rate = 15 mV s⁻¹; (a) and (c): [CO₃]_{tot} = 0; (b) and (d): [CO₃]_{tot} = 0.05 mol L⁻¹. 176

Fig. 6.3. Anodic current densities recorded on SIMFUEL as a function of [H₂O₂] in HCO₃⁻/CO₃²⁻-free/-containing solution. Data points were taken at E = 0.4 V in the CV scans (Fig. 6.63) and are corrected for the background current recorded in a solution without H₂O₂. 179

Fig. 6.4. Anodic currents recorded on 1.5 at.% SIMFUEL for various potential scan ranges as shown in the illustration of the scan procedure. Each color indicates two consecutive scans from a specific negative potential limit. Solid lines are the 1st forward scan and dashed lines are the 2nd forward scan. [NaCl] = 0.1 mol L⁻¹; [CO₃]_{tot} = 0.05 mol L⁻¹; [H₂O₂] = 0.02 mol L⁻¹; pH = 11.0; rotation rate = 25 Hz; scan rate = 15 mV s⁻¹. 181

Fig. 6.5. Tafel plots recorded on 1.5 at.% SIMFUEL in solutions containing different [CO₃]_{tot}. [NaCl] = 0.1 mol L⁻¹; [H₂O₂] = 0.02 mol L⁻¹; pH = 9.7; rotation rate = 16.7 Hz. 185

Fig. 6.6. Plots of the anodic current densities as a function of [CO₃]_{tot} at various applied potentials. 186

Fig. 6.7. Resolved U (4f_{5/2})/U (4f_{7/2}) regions of XPS spectra recorded on a 1.5 at.% SIMFUEL surface before and after anodic oxidation at E = 0.30 V for 0.5 hour in 0.1 mol L⁻¹ NaCl + 0.02 mol L⁻¹ H₂O₂ at pH 11.0 with or without HCO₃⁻/CO₃²⁻. The horizontal lines indicate the separation between specific satellite peaks and the U 4f_{5/2} peak. 188

Fig. 6.8. The valence band region of the XPS spectra recorded on a SIMFUEL surface before and after anodic oxidation at E = 0.30 V for 0.5 hour in 0.1 mol L⁻¹ NaCl + 0.02 mol L⁻¹ H₂O₂ (pH 11.0) with or without HCO₃⁻/CO₃²⁻. Dashed line: freshly polished specimen; red line: specimen after oxidation in HCO₃⁻/CO₃²⁻-free solution; blue line: specimen after oxidation in solution containing 0.05 mol L⁻¹ Na₂CO₃/NaHCO₃. 190

Fig. 6.9. SEM micrographs of SIMFUEL specimens before and after anodic oxidation at E = 0.30 V for 1.5 hours in 0.1 mol L⁻¹ NaCl + 0.02 mol L⁻¹ H₂O₂ at pH 11.0 with or without 0.05 mol L⁻¹ of HCO₃⁻/CO₃²⁻. 191

Fig. 6.10. E_{CORR} recorded on a 1.5 at.% SIMFUEL electrode as a function of [H₂O₂] in 0.1 mol L⁻¹ NaCl at pH = 9.5 with different [CO₃]_{tot}. 193

Fig. 6.11. The fraction of individual oxidation states present in the surface of a 1.5 at.% SIMFUEL electrode as a function of the H₂O₂ concentration in 0.1 mol L⁻¹ NaCl at pH 9.7. 195

Fig. 6.12. The fraction of individual oxidation states present in the surface of a 1.5 at.% SIMFUEL electrode as a function of the [H₂O₂] in 0.1 mol L⁻¹ NaCl + 0.1 mol L⁻¹ Na₂CO₃/NaHCO₃ at pH 9.7. 196

- Fig. 6.13. CSVs recorded on a SIMFUEL electrode after 30 min of E_{CORR} measurement in $0.02 \text{ mol L}^{-1} \text{ H}_2\text{O}_2$ and various $[\text{CO}_3]_{\text{tot}}$ at $\text{pH} = 9.5$. 197
- Fig. 6.14. The surface charge (proportional to the thickness of the corrosion product film) on a SIMFUEL surface as a function of $[\text{CO}_3]_{\text{tot}}$ in solutions containing different $[\text{H}_2\text{O}_2]$. 198
- Fig. 6.15. Reciprocal of polarization resistance, R_p^{-1} , as a function of $[\text{H}_2\text{O}_2]$ at $\text{pH} 9.5$ and 11.0 . $[\text{CO}_3]_{\text{tot}} = 0$ or 0.05 mol L^{-1} , rotation rate = 25 Hz . 200
- Fig. 6.16. Schematic illustration describing the H_2O_2 decomposition on UO_{2+x} surface and the effect of $\text{HCO}_3^-/\text{CO}_3^{2-}$. 201
- Fig. 7.1. An illustration of the possible coupling of the primary redox reactions involving H_2O_2 on fuel surface, with the emphasis on the H_2O_2 oxidation reaction being catalyzed by a UO_{2+x} surface or noble metal (ϵ) particles. 205
- Fig. 7.2. CV recorded on the RE and RE + ϵ electrodes in an Ar-purged 0.1 mol/L NaCl solution at $\text{pH} 9.5$. Scan rate = 5 mV/s , and the rotation rate = 0 Hz . IR compensated. 208
- Fig. 7.3. Steady-state currents recorded as a function of potential on the RE + ϵ and RE electrodes in $0.1 \text{ mol L}^{-1} \text{ NaCl} + 0.01 \text{ mol L}^{-1} \text{ HCO}_3^-/\text{CO}_3^{2-}$ solution at $\text{pH} 9.7$, $\omega = 16.7 \text{ Hz}$. 210
- Fig. 7.4. SEM micrographs of SIMFUEL specimens before and after oxidation at $E = 0.35 \text{ V}$ for 1 hour in $0.1 \text{ mol L}^{-1} \text{ NaCl} + 0.01 \text{ mol L}^{-1} \text{ HCO}_3^-/\text{CO}_3^{2-} + 0.02 \text{ mol L}^{-1} \text{ H}_2\text{O}_2$ solutions at $\text{pH} 9.7$ (1.5k magnification). 213
- Fig. 7.5. Oxidation current densities as a function of potential on SIMFUEL doped with (a) RE and (b) RE + ϵ in $0.1 \text{ mol L}^{-1} \text{ NaCl} + 0.02 \text{ mol L}^{-1} \text{ H}_2\text{O}_2$ solutions, $[\text{CO}_3]_{\text{tot}}$ varies from 0 to 0.2 mol L^{-1} . (c) is the difference in oxidation current densities between SIMFUEL doped with RE + ϵ and RE. All solutions are Ar-purged, $\text{pH} = 9.7$, $\omega = 16.7 \text{ Hz}$. 215
- Fig. 7.6. Bode plots for SIMFUEL (RE + ϵ) at different potentials; $[\text{H}_2\text{O}_2] = 0.02 \text{ mol L}^{-1}$; $[\text{CO}_3]_{\text{tot}} = 0.05 \text{ mol L}^{-1}$; $[\text{NaCl}] = 0.1 \text{ mol L}^{-1}$. 219
- Fig. 7.7. Equivalent circuit used for fitting EIS data for $E < 0.25 \text{ V}$ (circuit 1) and $E \geq 0.25 \text{ V}$ (circuit 2). 221

SYMBOLS AND ACRONYMS

at.%	Atomic percent
b	Radiation zone thickness
CPE	Constant phase element
CSV	Cathodic stripping voltammetry
CV	Cyclic voltammogram
D_i	Diffusion coefficient for species i
D_R	Radiation dose rate
E	Potential
E_{CORR}	Corrosion potential
EIS	Electrochemical impedance spectroscopy
$[\text{Fe}^{2+}]_{\text{bulk}}$	Bulk concentration of Fe^{2+}
f	Frequency
g_i	g -value for species i
$[\text{H}_2]_{\text{bulk}}$	Bulk concentration of H_2
$[\text{H}_2]_{\text{crit}}$	Critical $[\text{H}_2]$ that can completely suppress fuel corrosion
ICP-AES	Inductively coupled plasma atomic emission spectroscopy
j	Current density
k	Reaction rate constant
K_{eq}	Equilibrium constant
L	Diffusion boundary used in model calculation
LPR	Linear polarization resistance
MPM	Mixed Potential Model
NWMO	Nuclear Waste Management Organization
Q	Electric charge
R	Resistance

R_p	Polarization resistance
RE	Rare earth fission products
SCE	Saturated calomel electrode
SEM	Scanning electron microscopy
SIMFUEL	Simulated nuclear fuel
s_e	Noble metal particle coverage
t	Time
x	Distance from fuel surface
XPS	X-ray photoelectron spectroscopy
Z	Impedance
ϵ -particles	Noble metal fission product
ρ	Density
ω	Angular frequency

This page is intentionally left blank.

Chapter 1

INTRODUCTION

1.1 Project motivation

Canada's long-term plan for used nuclear fuel is the Adaptive Phased Management (APM) process recommended by Nuclear Waste Management Organization (NWMO) in 2005 and accepted by the Government of Canada in 2007 [1]. Used fuel will be safely and securely contained and isolated from the environment and people in a deep geological repository in a suitable rock formation using a multiple-barrier system as illustrated in Fig. 1.1. In the conceptual design, the repository would be located 500 meters underground in a stable crystalline [2] or sedimentary [3] rock formation. Spent nuclear fuel bundles discharged from CANDU (CANada Deuterium Uranium) reactors would be sealed in durable containers. The containers would be placed in excavated tunnels or boreholes and surrounded by compacted bentonite clay. When emplacement of waste containers is complete, and after a suitable monitoring period, the repository would be sealed.

While the prospects for the development of long-lived nuclear waste containers are very promising, their failure will eventually result in wet and potentially oxidizing conditions on the fuel surface leading to its degradation [4]. The safety assessment of deep geological disposal of spent nuclear fuel requires a fundamental understanding of the processes controlling fuel corrosion which could lead to the release of radionuclides to the geosphere from a failed container [5, 6].

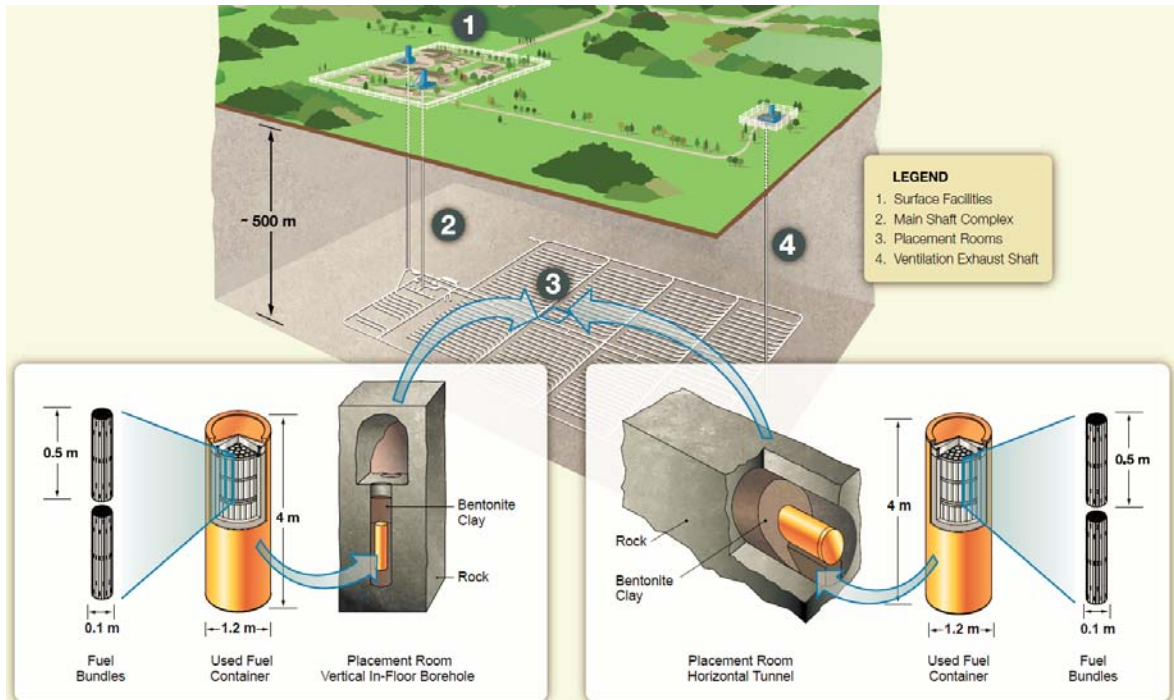


Fig. 1.1. Illustration of the deep geological repository concept showing the container, emplacement room, and tunnel layout. Two emplacement plans are proposed, vertical boreholes and horizontal tunnels. Image source: Ref [1].

1.2 Project overview

Since a large fraction ($> 95\%$) of radionuclides in spent fuel are located within the uranium dioxide (UO_2) grains, their release rate to the environment will be determined primarily by the UO_2 corrosion/dissolution rate. The UO_2 ceramic matrix is chemically inert and the rate of fuel dissolution is extremely slow in water under anoxic conditions [7, 8]. However, the solubility increases by orders of magnitude under oxidizing conditions when the fuel can dissolve as UO_2^{2+} [9, 10], Fig. 1.2. Therefore, the dissolution rate of spent fuel is very sensitive to the redox condition.

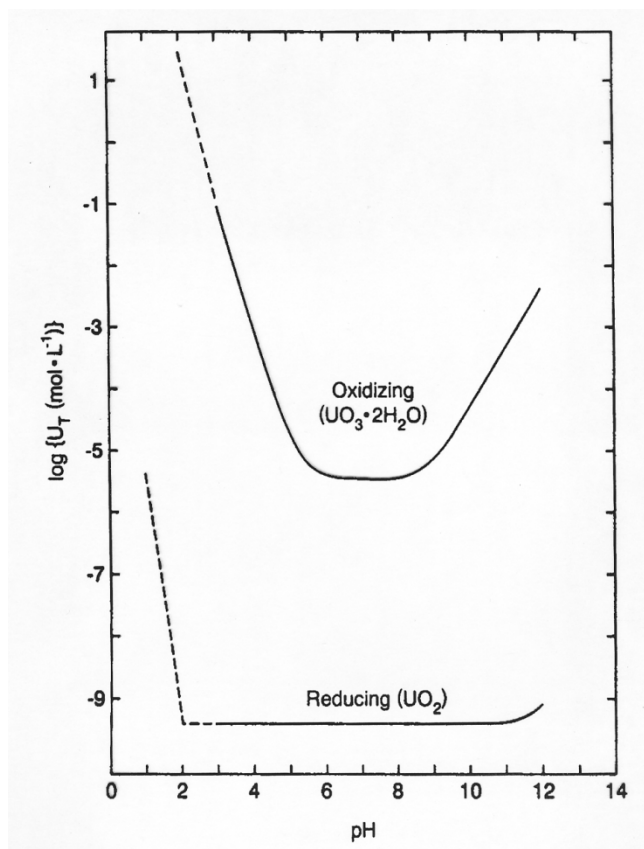


Fig. 1.2. Solubility of uranium dioxide (UO_2) and schoepite ($\text{UO}_3 \cdot 2\text{H}_2\text{O}$) as a function of pH at 25°C. Image source: Ref [8].

The concentration of dissolved oxidants in the repository is expected to be extremely low, since environmental oxidants will be consumed rapidly by container corrosion and mineral/biological oxidation processes. The only source of oxidants would be the radiolysis of water [5]. The radiation field (Fig. 1.3) associated with the fission products and actinides, particularly α -radiation, will remain high up to $\sim 10^5$ years making water radiolysis a source of oxidants [11]. The interaction of water and radiation can produce a number of reactive species, among which the molecular species (H_2O_2 , H_2 and O_2) are the predominant products [12, 13]. The molecular oxidant, H_2O_2 , has been shown to be the primary oxidant driving fuel corrosion [6, 14]. The molecular reductant, H_2 , is inert

compared to H_2O_2 , and has a higher diffusivity making its impact on the UO_2 surface relatively small. Therefore, the redox conditions at the fuel surface will be dominantly oxidizing [15].

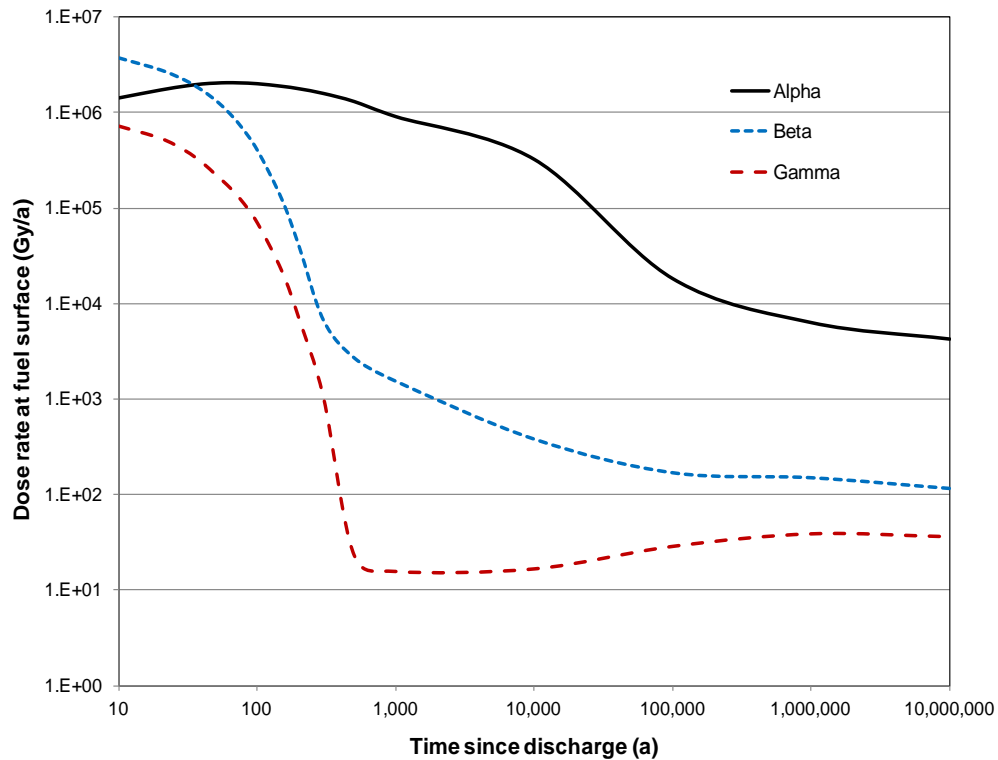


Fig. 1.3. Alpha, beta, and gamma radiation dose rates with respect to time for water in contact with a CANDU fuel bundle with a burn up of 220 MWh kgU^{-1} . Image source: Ref [11].

Different methodologies have been adopted to predict the long-term corrosion behaviour of spent fuel [6, 15, 16] and numerous influences on the dissolution rate have been identified, such as radiation strength (which varies with fuel type, burnup and age), pH, groundwater composition, and the fission product content within the fuel. There is also a possibility that reducing conditions can be restored within a failed container by the

anaerobic corrosion products of the steel container, i.e., H_2 and Fe^{2+} [17-19]. A Mixed Potential Model (MPM) has been developed to predict the fuel corrosion rates and how they may be influenced by possible processes inside a failed container, Fig. 1.4. The processes included in this model are diffusion, adsorption/desorption, precipitation/dissolution and the homogenous/interfacial redox reactions involved in corrosion of the spent fuel and the steel container [20].

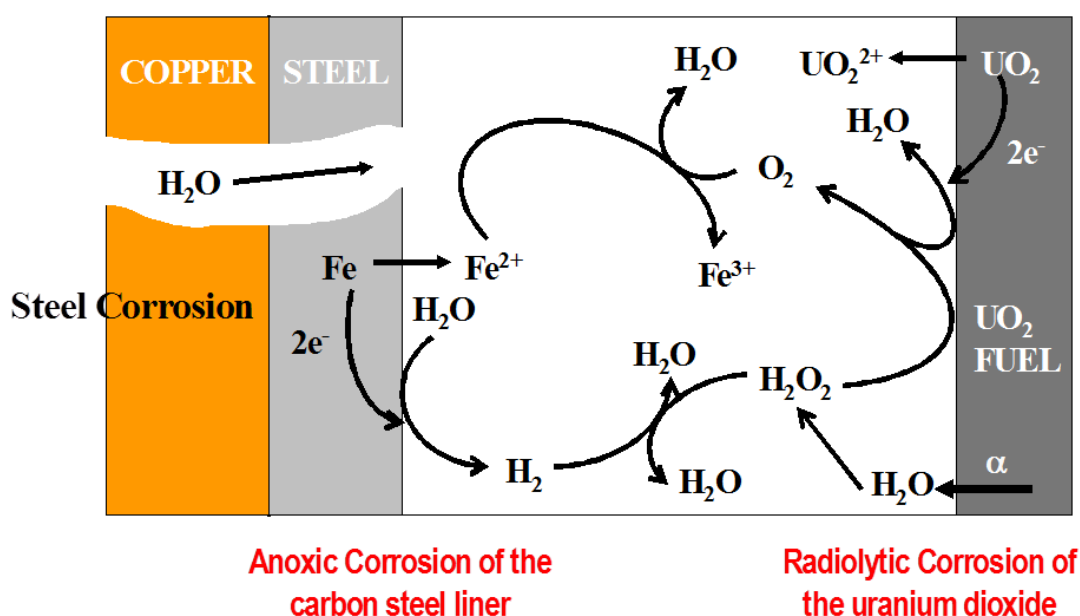


Fig. 1.4. Illustration of possible electrochemical/chemical reactions within a failed copper/steel-dual-layer nuclear waste container. Diagram adapted from Ref [20].

The development of source-term models to describe the processes involved in spent fuel dissolution has been the focus of considerable international effort [6, 21-23]. The recent development of radiolytic corrosion models has been reviewed [15], and a number of necessary improvements identified. Among these is a better understanding of the kinetics of reactions on fuel surfaces. In particular, there is a significant uncertainty in regards to

the balance between H_2O_2 reduction and its decomposition. Since H_2O_2 can not only act as a cathodic reagent for fuel corrosion, but also undergo surface-catalyzed decomposition to O_2 and H_2O , the balance between the two reactions will have a significant influence on the fuel corrosion rate [24-27]. A detailed study of this reaction will allow the predictions of fuel dissolution rate to be significantly improved.

1.3 Thesis objectives

One focus of this project is the development of a computational model to simulate fuel corrosion inside a failed container. A comprehensive model should consider the α -radiolysis of water, interactions between radiolysis products and the fuel surface, and the reactions involving the steel corrosion products. Since a wide range of kinetic data has become available during the past decade, improvement in the modelling of fuel corrosion is now possible using numerical simulations. Within such simulation it is important to evaluate the effects of radiolysis products, fuel burnup (fission product inclusions), container corrosion products, and the evolution of radiation fields as the fuel ages. In addition, due to the porous and fractured nature of spent fuel, local accumulations of radiolysis species are likely to occur and externally produced Fe^{2+} and H_2 may have limited access to reactive locations within fractures, porous grain boundaries and fuel bundles. Such geometric effects could influence on the overall radionuclide release rate, but are difficult to investigate in conventional experiments. Therefore, the eventual development of the model must account for such localized effects.

The other focus of this research project is to develop a more detailed understanding of the H_2O_2 decomposition process and its influence on UO_2 corrosion. Several variables

(potential, pH, carbonate/bicarbonate, and fission products) can influence the reactivity of H_2O_2 . Their influence on the surface composition and electrical conductivity of UO_2 will affect surface redox reaction rates and significantly alter the overall fuel corrosion rate.

Electrochemical methods can be used to separate a corrosion reaction into its two constituent half reactions allowing the determination of the rate dependence on potential for each half reaction. Since these changes in surface condition will also have a significant impact on the H_2O_2 reactivity, it is important to use surface/solution analytical techniques to link the electrochemical/chemical processes to the compositional and structural changes observed on a UO_2 surface. In this thesis, attempts have been made to clarify the mechanism of H_2O_2 decomposition on UO_2 and to determine the resulting effect on fuel corrosion.

1.3.1 Strategy I: Modelling approach

The recent review [15] of model development on radiation-induced spent fuel corrosion revealed many key features required in modelling radiolytic corrosion (in particular for α -radiation). The spatial distribution of radiolytic species is of particular importance since all the α -particle energy is deposited within a few tens of micrometers of the fuel/solution interface. Consequently, mass transport becomes important in coupling the homogeneous aqueous reactions and heterogeneous processes involved. This is especially important if the influence of container corrosion products, Fe^{2+} and H_2 , on the redox conditions at the fuel surface are to be quantitatively modelled.

The mathematical model can be numerically simulated using COMSOL Multiphysics based on the finite element method. The chemical engineering module and the diluted

species transportation module of COMSOL Multiphysics software are suitable for the simulations required. A series of simulations can be designed and developed to determine the influence of redox conditions, with the emphasis on α -radiolysis and steel corrosion products, on the corrosion rate of spent fuel. The first approach will be 1-dimensional and consider only the corrosion of a planar fuel surface. This will act as a preliminary step in the eventual development of 2-D and 3-D models involving the customized geometries necessary to account for the fractured nature of the spent fuel and the complex fuel bundle geometry.

1.3.2 Strategy II: Electrochemical approach

Corrosion is a process appropriately studied by electrochemical methods, which provide a means to monitor and control charge transfer processes on the surface of UO_2 .

Electrochemically, a corrosion reaction can be separated into two half reactions and the rate dependence on potential for each half reaction determined. In the present case the anodic is the oxidative dissolution of UO_2 while the cathodic reaction would be one of, or the sum of, the available oxidant reduction processes. Although no net current flows when the two half-reactions are coupled under natural corrosion conditions, one can apply a potential to separate fuel dissolution from the oxidant reduction reaction. The steady-state current resulting from the anodic or cathodic reaction(s) can then be measured as a function of applied potential. The expected corrosion potential under disposal condition can be measured under open-circuit conditions, and is determined by the kinetics of the surface redox reactions occurring.

The corrosion potential, E_{CORR} , is the potential difference existing across the solid-solution interface and is the potential at which the rate of anodic fuel dissolution is equal to the rate of oxidant reduction. For a UO_2 electrode the steady-state dissolution current can be shown to be logarithmically dependent on potential [28, 29]. These Tafel plots provide a substantial amount of information on the kinetics of an electrochemical reaction and can be used to determine corrosion rates as illustrated in Fig. 1.5. The UO_2 corrosion rate can be determined from an extrapolation of such Tafel plots to the E_{CORR} values measured in solutions simulating disposal conditions or containing various known concentrations of chemically added oxidants (e.g. O_2 , H_2O_2).

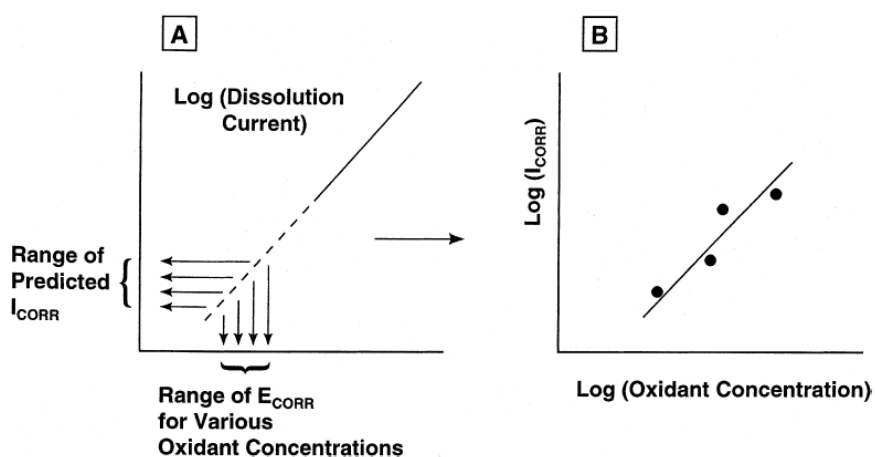


Fig. 1.5. Illustration of the procedure used to obtain corrosion currents (I_{CORR}), and hence corrosion rates, from electrochemically measured dissolution currents and corrosion potential (E_{CORR}) measurements: (A) Tafel relationship relating anodic dissolution currents to applied electrode potentials. The dashed section of the line indicates the extrapolation of measured currents to E_{CORR} to obtain values of I_{CORR} ; (B) I_{CORR} plotted logarithmically as a function of oxidant concentration. Image source: Ref [6].

The corrosion current is equal to the oxidative dissolution rate of UO_2 . Electrochemical experiments have been conducted to measure the corrosion current in various environments [28, 30, 31], and these values have been compared to those measured by chemical analyses in flow-through [32] and other dissolution experiments [33-35]. Considering the variability in the nature of the UO_2 specimens used by various investigators and other uncertain factors including the estimated surface areas of UO_2 powders, the agreement between the predicted and measured dissolution rates is acceptable. A more detailed comparison of the effect of oxygen, carbonate and radiation dose rates on dissolution rates has been published. [36].

1.4 Background information

1.4.1 Water radiolysis

The radiation fields associated with the fuel will produce a range of water radiolysis products that can alter the local redox conditions at the fuel surface leading to an increased dissolution rate. The production rate of radiolysis species depends on the strength of the radiation fields. Fig. 1.3 shows the alpha, beta, gamma dose rates calculated at the surface of a CANDU fuel bundle of average burn-up. The gamma and beta radiation fields decay markedly over the first 500 years, while the alpha radiation fields will remain significant for periods of $\sim 10^5$ years [11, 37]. It is reasonable to assume containment preventing contact of the fuel with groundwater will be maintained over the period when γ/β radiation fields are significant (a few hundred years), making α -radiolysis the only significant source of oxidants [38]. Alpha-radiation is a high linear energy transfer (LET) radiation which has a short penetration depth in matter [13]. A

typical energy of the alpha particles from fuel decay is 5 MeV, corresponding to a path length of $\sim 40 \mu\text{m}$ in water [39].

The α -radiolysis of an aqueous system yields a series of water decomposition products (H_2 , H_2O_2 , H^\bullet , OH^\bullet , HO_2^\bullet , e_{aq}^- , H^+ and OH^-) [12, 13]. In the presence of groundwater ions, the radical species $\text{CO}_3^{\bullet-}$ (in carbonate solutions) and Cl^\bullet (in chloride solutions) can also be produced. The rate of radiolytic production is determined by the dose rate, which represents the rate of energy deposition per unit of mass, and the g-value (the number of moles formed per joule of radiation energy absorbed) of a radiolysis species. Both oxidizing molecular and radical species (e.g. H_2O_2 , O_2 , OH^\bullet) and reducing species (e.g. H_2 , H^\bullet , e_{aq}^-) are formed during radiolysis. After formation, these radiolytic species undergo diffusion and a series of chemical reactions. The radiolytic radical species have high reactivity and thereby short lifetimes, leading to extensive recombination within a short distance to produce stable molecular/ionic species. As a consequence, the radical species have concentrations orders of magnitude lower than those of the stable molecular products. Therefore, the molecular species (H_2O_2 , H_2 , and O_2) are expected to be predominant near the fuel/water interface. The radiolytic oxidants are expected to have a much larger influence on redox conditions than their reducing counterparts, since the molecular reductant, H_2 , is inert at the anticipated temperature ($< 100 \text{ }^\circ\text{C}$) compared to the oxidant, H_2O_2 , and has a higher mobility and, hence, a relatively smaller impact at the UO_2 surface. The molecular oxidant, H_2O_2 , has been shown to be the primary driving force for fuel corrosion [14, 40], as illustrated in Fig. 1.6. The redox conditions at the fuel surface are dominantly oxidizing, at least during the early stages of disposal, when the fuel is in its reduced form (U^{IV}) [15].

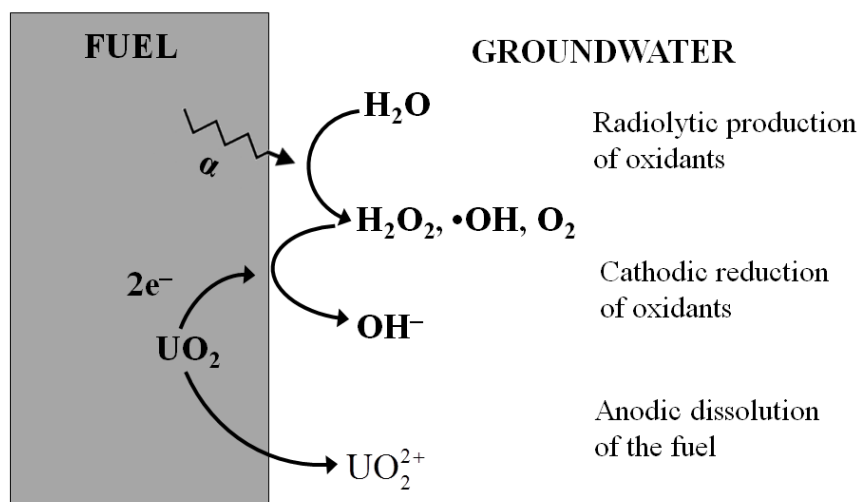


Fig. 1.6. Simplified schematic diagram showing the fuel dissolution driven by radiolytic oxidants. Image source: Ref [41].

1.4.2 Spent fuel

1.4.2.1 General description

The key characteristics of spent fuel for postclosure assessment are summarized in this section. CANDU fuel is a solid ceramic oxide (mainly UO_2) fabricated into pellets with a diameter of about 12 mm [38]. These pellets are sealed inside zirconium-tin (Zircaloy-4) tubes, ~ 0.5 m long, and arranged in a circular 10 cm array in fuel bundles. This fuel assembly (bundle) weighs 23.9 kg, of which 21.7 kg is UO_2 and 2.2 kg is Zircaloy [42]. As of June 2012, a total of approximately 2.35 million used CANDU fuel bundles (about 46,000 tonnes of heavy metal) were in storage at reactor sites [43].

The fuel surface area is an essential parameter in determining the dissolution rate. The minimum possible surface area is that of the intact fuel, $0.043 \text{ m}^2 \text{ kg}^{-1}$ [44]. During in-reactor irradiation, some pellet cracking will have occurred. Thus, the surface area of the

fuel depends on the fragment size. The geometric surface area of used fuel has been estimated to be about $0.2 \text{ m}^2 \text{ kg}^{-1}$, based on the size of fuel fragments from a CANDU bundle from a Bruce Power station [45]. If the fuel were to be completely broken into small particles of $\sim 0.6 \text{ mm}$ in dimension, the surface area would be $1 \text{ m}^2 \text{ kg}^{-1}$ [44]. The total surface area within a failed container can be calculated using the total mass of fuel bundles. The effective surface area is somewhat higher than the geometric area shown above, since the surface is rough. A typical value of the surface roughness factor is 3 [21].

1.4.2.2 Composition

The fuel is composed of sintered UO_2 pellets with a density of 10.96 g cm^{-3} , which is close to theoretical (97%), a nominal irradiated grain size of $10\text{--}50 \text{ }\mu\text{m}$, and an oxygen/uranium ratio of ~ 2.001 when unirradiated [5, 11]. Nuclide inventories in the fuel matrix generally increase with burnup. The average burnup based on data collected up to 2006 from all Ontario Power Generation reactors is $\sim 190 \text{ MWh kgU}^{-1}$ (initial U) [42], and the standard deviation is $\sim 42 \text{ MWh kgU}^{-1}$. A reference value of 220 MWh kgU^{-1} is used for repository studies. At this level of burnup, about 2% of the mass of unirradiated fuel will be converted to new nuclides, $\sim 98\%$ of the fuel remaining unchanged. These fission products differ widely in their compatibilities with the fluorite structure of UO_2 due to their physical/chemical properties and are grouped into three general categories.

(i) Some fission products have very limited solubility in the lattice (e.g; ^{85}Kr , ^4He , ^{39}Ar , ^{99}Tc , ^{129}I , ^{14}C , ^{135}Cs , ^{125}Sn , ^{79}Se) and are volatile at reactor operating temperatures, and migrate to the fuel/sheath gap during reactor operation.

(ii) Other fission products are less-volatile and migrate to grain boundaries, and reside in

either fission gas bubbles or separate into solid phases such as perovskites ((Ba, Sr) ZrO₃) and metallic alloy phases (ϵ -particles: Mo, Ru, Rh, Pd, Tc).

(iii) The majority of fission products and actinides/lanthanides (e.g; Pu, Am and Np) are retained within the UO₂ fuel matrix.

Among the new radionuclides, the ones of greatest environmental impact in a geologic repository will be those that have some combination of high radiotoxicity, geochemical mobility, and a long half-life. Examples are ⁹⁹Tc, ¹²⁹I, ⁷⁹Se, ¹³⁵Cs, ²³⁹Pu, ²³⁷Np, and ²³⁵U [10].

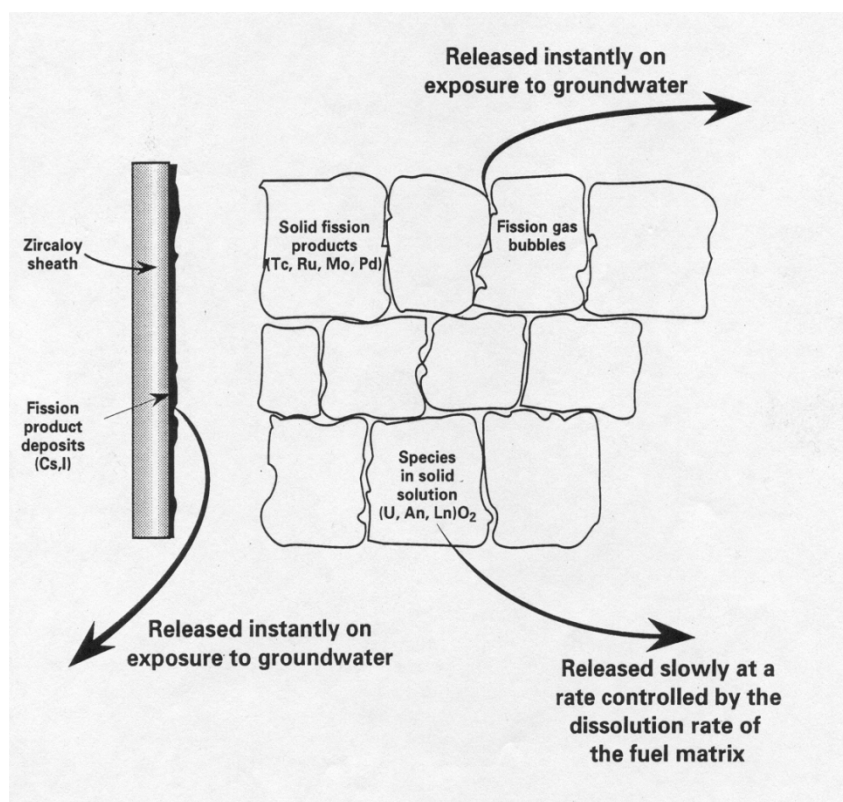


Fig. 1.7. Schematic illustrating the key changes induced by in-reactor fission and showing the three general categories of radionuclides [38].

As illustrated in Fig. 1.7, the radionuclide inventories located at the cladding gap and at grain boundaries and void spaces within the fuel are assumed to be released instantly as soon as groundwater contacts the fuel. Since more than 95% of the new nuclides are still located within the UO_2 grains, their release rate will be congruent with the dissolution rate of the UO_2 matrix. From a corrosion perspective, the fuel can be considered as a conductive (RE^{III} -doped) and chemically reactive matrix containing noble metal (ϵ) particles which could act as catalysts for redox reactions [17].

1.4.2.3 Electrical properties

A necessary requirement for electrochemical studies on UO_2 is the ability of the material to conduct electronic charge. In its stoichiometric form, UO_2 (in which the U atom has a $5f^2$ electronic configuration) can be considered as a Mott-Hubbard insulator [46-48], characterized by a partially filled cationic shell which has a sufficiently narrow bandwidth of the 5f level that the mobility of electrons is restricted by Coulomb interaction [49-51]. Electronic conductivity can still result by the activated process of a small polaron hopping mechanism [52, 53], in which the normally localized electrons can be transferred from one cation to the next by a series of thermally assisted jumps.

A schematic energy level diagram for UO_2 is given in Fig. 1.8 [54]. The narrow U 5f band, containing 2 electrons per uranium atom, falls in the gap between the filled valence band and the empty conduction band. The valence band consists of mainly O 2p characteristics with some contribution from U 6d and 5f orbitals, while the conduction band is a mixture of overlapping orbitals of U 7s, 6d and 5f. The occupied and unoccupied U 5f levels are known as the lower and upper Hubbard bands, respectively.

For stoichiometric UO_2 , electronic conductivity requires promotion of electrons from the occupied U 5f level to the conduction band, which has a high activation energy (1.1 eV) and, hence, a low probability at room temperature [53].

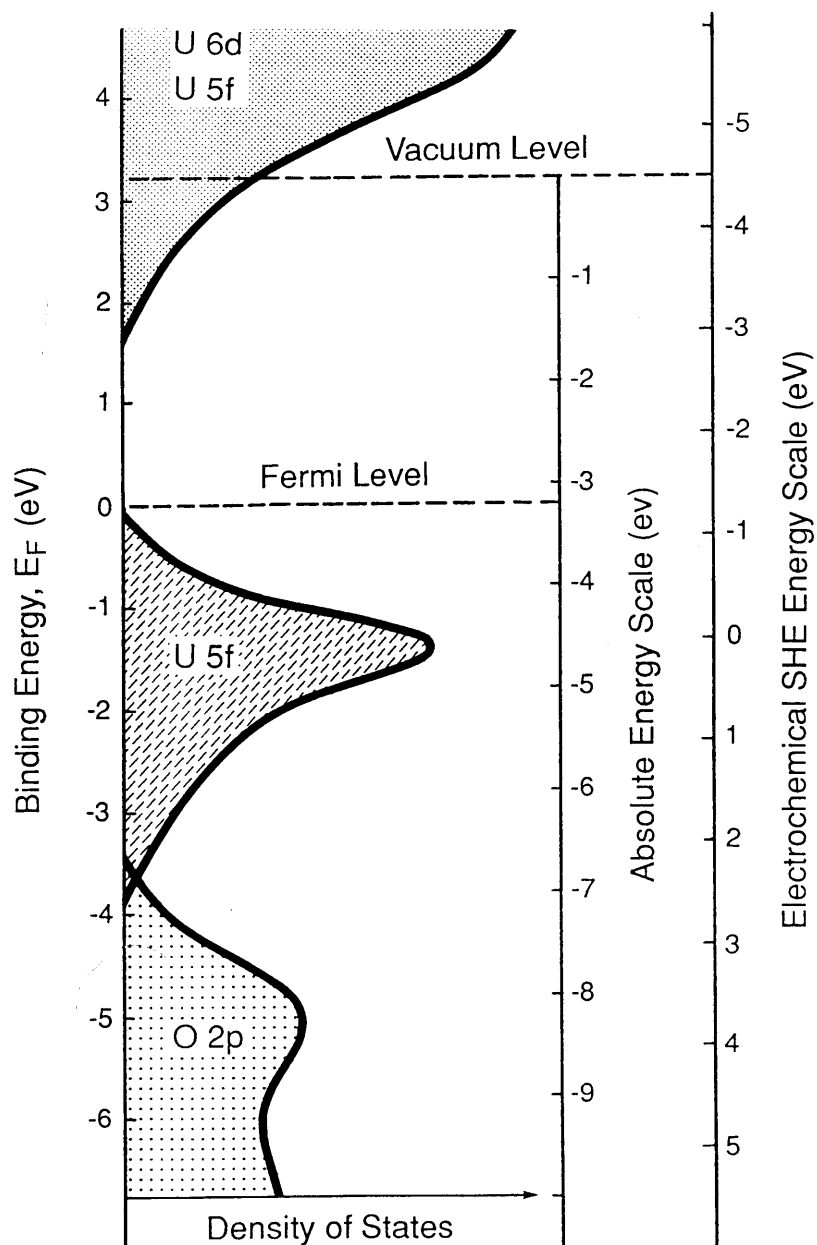


Fig. 1.8. A schematic diagram of the band structure for UO_2 , and its relationship to important energy scales (from electrochemical and spectroscopic data). Image source:

Ref [54].

However, stoichiometric UO_2 is rarely attained in practice, and the material is inevitably hyperstoichiometric to some extent, with an excess of O^{2-} ions at interstitial sites [54]. To maintain charge balance, a fraction of U^{IV} will be oxidized to $\text{U}^{\text{V}}/\text{U}^{\text{VI}}$ by the excess oxygen. This process creates holes in the occupied U 5f Hubbard band, which can migrate by the polaron hopping mechanism, with a low activation energy (~ 0.2 eV) [55-61]. In this regard, the hyperstoichiometric UO_{2+x} can be considered as a p-type semiconductor.

Substitution of lower valence cations (e.g., rare earth cations such as Y^{III}) for U^{IV} in the UO_2 lattice would also require an oxidation of U^{IV} to a higher state (U^{V}) creating mobile holes and, hence, increasing conductivity [62]. Thus, although the composition of simulated fuel pellets used in the project is expected to be very close to stoichiometric, the conductivity is enhanced by the rare earth dopants [63].

1.4.2.4 Structural/solid state properties

Uranium dioxide adopts the fluorite lattice structure, Fig. 1.9, like other actinide dioxides [64]. Each U atom is coordinated by eight neighbouring O atoms, while the O atoms are surrounded by a tetrahedron of four metal atoms. The unit cell parameter is $a = 5.470$ Å, with ionic radii of $r_{\text{U}^{4+}} = 0.97$ Å and $r_{\text{O}^{2-}} = 1.40$ Å [64]. Also present in the lattice are large, cubically coordinated interstitial sites, which can accommodate additional O^{2-} ions without causing a major distortion of the fluorite lattice. Oxidation involving the injection of these extra O^{2-} ions requires an appropriate numbers of U^{IV} to be oxidized to $\text{U}^{\text{V}}/\text{U}^{\text{VI}}$ [65].

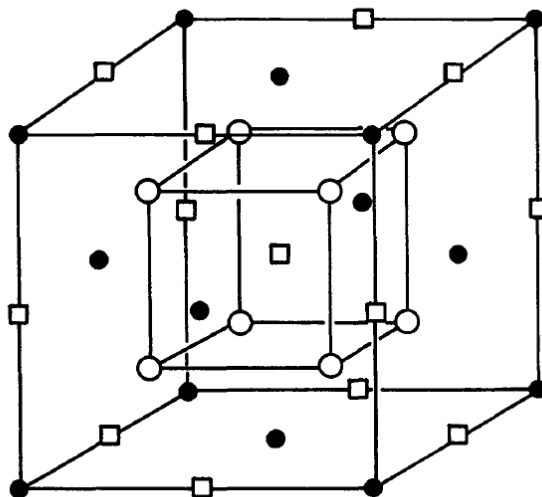


Fig. 1.9. Fluorite crystal structure of stoichiometric UO_2 . (●) U atoms; (○) O atoms; (□) empty interstitial lattice sites.

Based on neutron diffraction [65-67] and X-ray photoelectron spectroscopic data [68-71] for compositions from $\text{UO}_{2.13}$ to U_4O_9 ($\text{UO}_{2.25}$), the incorporation of additional O atoms into interstitial sites (Fig. 1.9) did not occur; rather O atoms were found in newly identified interstitial positions, termed O' and O'', displaced from the cubically coordinated sites by $\sim 1 \text{ \AA}$ in the (110) and (111) directions. These distortions had no apparent effect on the U sublattice. As UO_2 is further oxidized U_3O_7 ($\text{UO}_{2.33}$), the fluorite lattice became significantly distorted and an increase in density was observed [71, 72]. Beyond a limiting stoichiometry of $\text{UO}_{2.33}$, corresponding to a tetragonally distorted fluorite structure, further oxidation requires a major structural rearrangement, to a more open, layer-like phase, with lower density [73, 74]. The U^{VI} phases such as $\text{UO}_3 \cdot y\text{H}_2\text{O}$ and $\text{UO}_2(\text{OH})_2$ are electrical insulators, since they do not contain any 5f electrons. These oxidation stages are important in determining the kinetics of oxidative dissolution

(corrosion) of UO_2 .

1.4.2.5 Thermodynamic properties

A wide range of U phases and soluble U^{VI} species are thermodynamically possible in groundwater systems, as shown in Fig. 1.10(A), giving U a rich aqueous electrochemistry [7]. For the pH region 8-10, which is anticipated under disposal conditions, UO_2 in its reduced form (U^{IV}) would be highly insoluble. However, the solubility increases by many orders of magnitudes under oxidizing conditions, Fig. 1.11, and UO_2 dissolves by oxidation to uranyl (UO_2^{2+}) ions [10]. In the absence of complex species, the UO_2^{2+} is extensively hydrolyzed in aqueous solutions to form species such as $(\text{UO}_2)_x(\text{OH})_y^{2x-y}$ in the pH range of 3 to 6, Fig. 1.10(B).

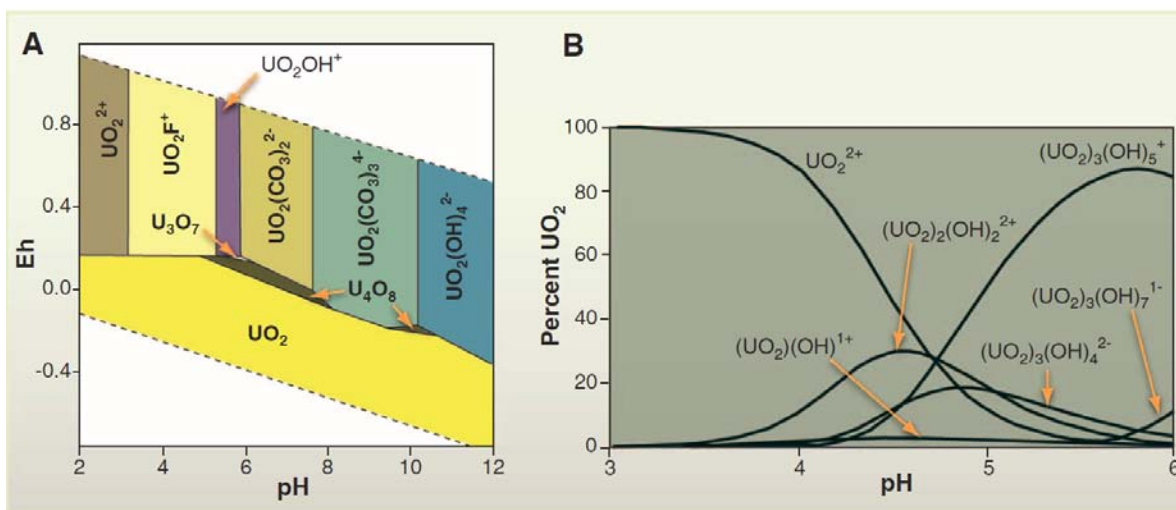


Fig. 1.10. Examples of stability diagrams for U systems. (A) Speciation of U in a hypothetical groundwater at 25°C. (B) Speciation of U^{VI} versus pH in NaCl solution at 25°C at a concentration of 0.001 mol L^{-1} . Source: Ref [74].

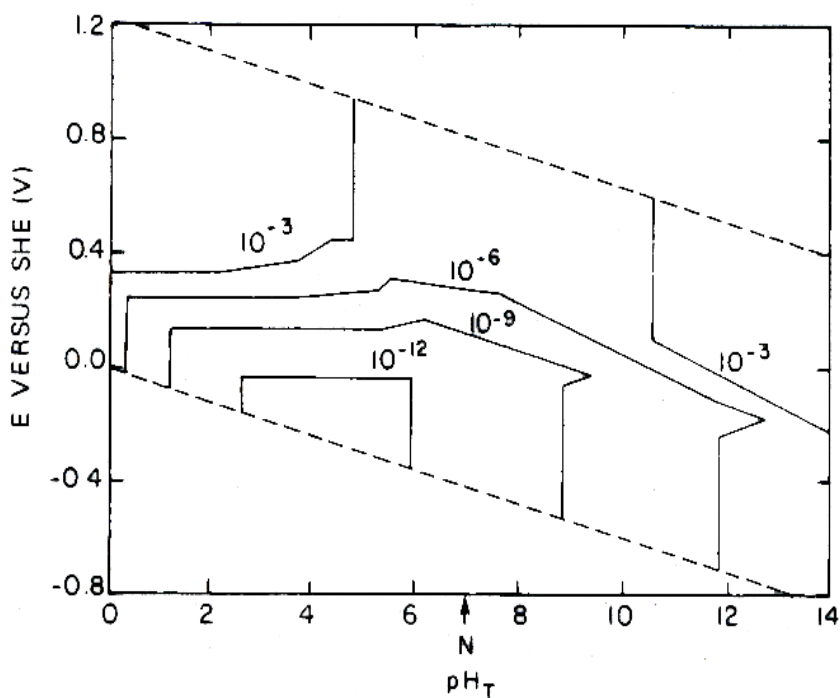


Fig. 1.11. Isosolubility lines for the U/H₂O system as a function of pH and potential at 25°C [75].

The dissolution rate of oxidized U^{VI} from a fuel surface can be significantly altered by complexation involving species present in ground waters, Fig. 1.10(A), by forming stable uranyl complexes. The uranyl ion concentration will be strongly influenced by complexing species, such as peroxide, carbonate, or nitrate, which greatly enhance solubility, or phosphate, silica, or vanadate, which reduce the solubility [76]. The extent of complexation will also be dependent on pH. For example, uranyl peroxide species, which are insoluble in acidic solutions are highly soluble under alkaline conditions, and uranyl carbonate complexes form only under moderately alkaline solutions [77].

The long-term fate of U released to the environment is dispersal or formation of

secondary uranyl minerals [10, 74, 78, 79], such as uranyl oxyhydrate minerals (e.g., schoepite). Many of these uranyl minerals can incorporate key radionuclides (e.g., isotopes of Sr, Cs, Pu, Np) thereby reducing their mobility [80, 81]. The thermodynamic database for such minerals is important in determining the long-term environmental impact of fuel dissolution [74, 82, 83]. Studtite, $[(\text{UO}_2)(\text{O}_2)(\text{H}_2\text{O})_2] \cdot 2\text{H}_2\text{O}$ or $\text{UO}_4 \cdot 4\text{H}_2\text{O}$, and metastudtite, $\text{UO}_4 \cdot 2\text{H}_2\text{O}$, are the only reported peroxide minerals and have been shown to form during spent fuel alteration by incorporation of the H_2O_2 created by alpha radiolysis [83-85]. Based on thermodynamic calculations, studtite has been shown to be the dominant alteration product in the presence of peroxide, even at extremely low concentrations ($\sim 10^{-14}$ mol L⁻¹) [83]. Studtite formation has been observed on the surface of spent fuel after short-term (1-2 years) contact with water [86, 87]. In leaching experiments using chemically added peroxide, studtite formation was observed to occur at high $[\text{H}_2\text{O}_2]$ [88-92] and can limit the subsequent rate of UO_2 reaction with H_2O_2 .

1.4.2.6 Electrochemical properties

In electrochemical experiments, the current as a function of potential is a primary measure of the changes on the UO_2 surface and how they influence the corrosion process and the composition of the corrosion product deposits. A cyclic voltammogram (CV) obtained on UO_2 is shown in Fig. 1.12. The various stages of oxidation and reduction seen within various potential ranges [6, 93] are numbered on the plot. On the forward scan, a shoulder (I) is observed in the potential range -0.8 to -0.4 V (vs. SCE), where the oxidation of bulk phase stoichiometric UO_2 is not thermodynamically possible. It has been proposed [6] that the oxidation occurs at non-stoichiometric locations, possibly within grain boundaries. Surface oxidation in this region appears reversible, as all anodic

charge consumed on the forward scan can be recovered on the negative scan. Peak II is attributed to the oxidation of the general UO_2 matrix involving the incorporation of O^{2-} ions at the interstitial sites in the fluorite lattice. While the exact composition of this thin layer is difficult to determine, a limiting stoichiometry of $\text{UO}_{2.33}$ appears to be obtained around -0.1 V. Further oxidation at higher potentials results in dissolution as UO_2^{2+} , which contributes to the rising current in region (III).

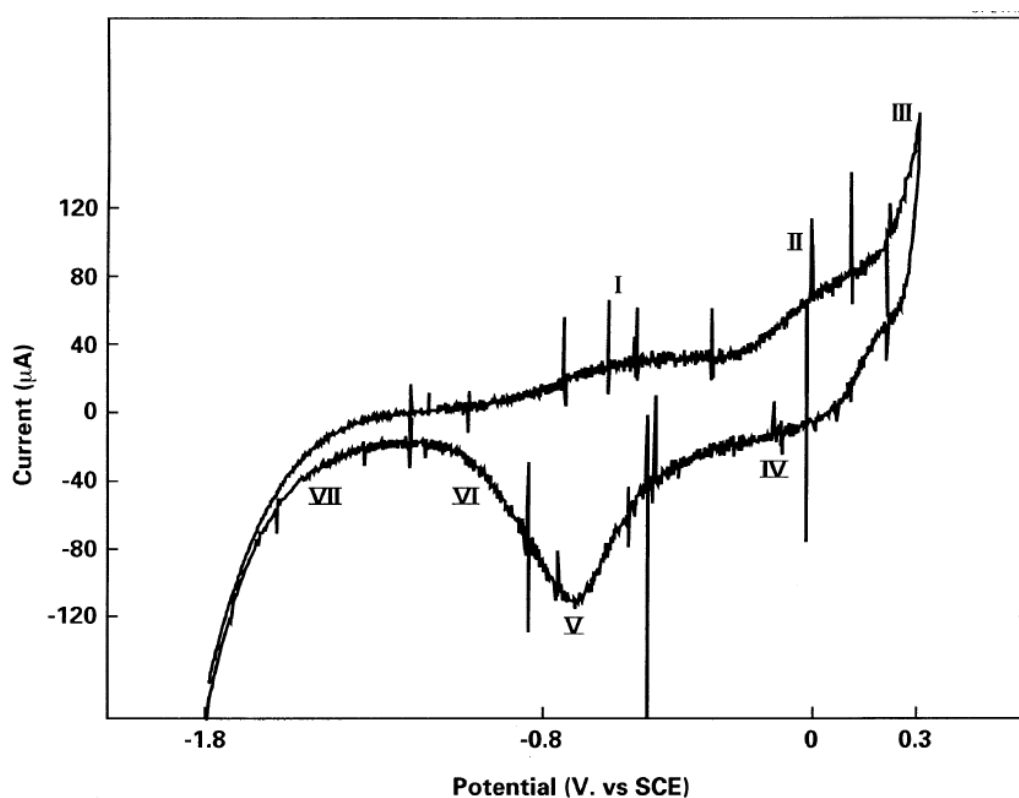


Fig. 1.12. Cyclic voltammogram recorded on a rotating UO_2 disc electrode at 10 mV s^{-1} and a rotation rate of 16.7 Hz using IR compensation in a $0.1 \text{ mol L}^{-1} \text{ NaClO}_4$ at pH 9.5. The Roman numerals indicate the various stages of oxidation or reduction described in the text. Source: Ref [6].

On the cathodic scan, a peak (IV) is sometimes observed at ~ -0.2 V. The small amount of charge associated with this peak suggests that it is due to the reduction of an adsorbed species (possibly UO_2^{2+}), although no definitive identification is available. Peak V is attributed to the reduction of oxidized layers, $\text{UO}_{2.33}$ and/or $\text{UO}_3 \cdot y\text{H}_2\text{O}$, formed on the anodic scan. On some UO_2 surfaces this peak appears as a doublet (V, VI). The size of this reduction peak depends on the amount of oxidation that takes place at the anodic scan, increasing as the potential limit is made more positive or the oxidation potential is held for longer times. The large current increase in region VII is due to the reduction of H_2O to H_2 .

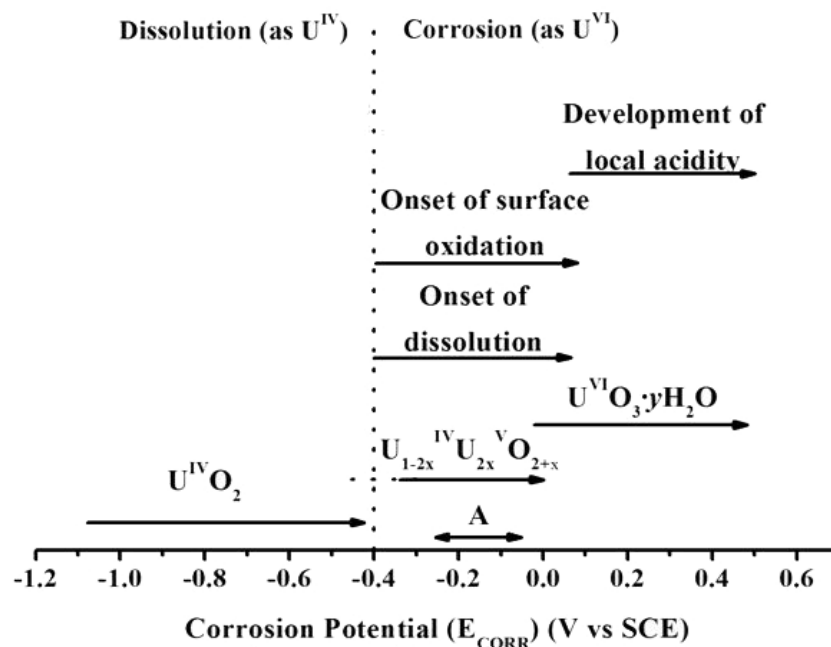


Fig. 1.13. Composition and corrosion behavior of UO_2 as a function of the UO_2 corrosion potential [6, 94].

Fig. 1.13 shows the composition of a UO_2 surface as a function of surface redox condition (expressed as a corrosion potential) in an aqueous environment. Also shown are the potential ranges for some important electrochemical processes on UO_2 , including surface oxidation and dissolution. The association between composition and potential shown in this figure has been determined by a combination of electrochemical and surface analytical experiments (voltammetry, photothermal deflection spectroscopy, photocurrent spectroscopy, and X-ray photoelectron spectroscopy) [6, 94]. The range of corrosion potentials predicted by the Mixed Potential Model (described in the subsequent section) is indicated by an arrow A. The vertical dashed line shown at -0.4 V (vs. SCE), represents the threshold for the onset of the transformation to a series of non-stoichiometric phases. For potentials greater than the threshold value fuel corrosion is expected to proceed at a rate controlled by the concentration of radiolytically produced oxidants. Below this threshold, radionuclides should only be released by the chemical dissolution of the U^{VI} matrix.

1.5 Reactions on UO_2 surfaces

1.5.1 Redox reactions of H_2O_2 on fuel surface

As discussed in Section 1.4.1, the radiolytically produced H_2O_2 is expected to be primary oxidant driving fuel corrosion [6, 15, 40]. The H_2O_2 can either be consumed on fuel surface, or diffuse away to be scavenged by reducing species present in the disposal environment (e.g., Fe^{2+} from canister corrosion). The coupling of H_2O_2 reduction and UO_2 oxidation serves as the primary pathway for UO_2 corrosion [95, 96].



Besides reaction (1.1), H_2O_2 can also undergo oxidation, reaction (1.3), to produce O_2 as an alternative oxidant although the UO_2 corrosion driven by O_2 is expected to be kinetically much slower ($1/200^{\text{th}}$) than that driven by H_2O_2 [6]. A coupling of reactions (1.1) and (1.3) will result in H_2O_2 decomposition to produce H_2O and O_2 , reaction (1.4).



Extensive study of H_2O_2 reduction, reaction (1.1), on UO_2 has been undertaken [25, 93, 95-97]. Goldik et al. studied the electrochemical kinetics and mechanism for H_2O_2 reduction on simulated fuel pellets (SIMFUEL) [95, 96, 98, 99], UO_2 specimens doped with non-radioactive fission products, including rare earths and noble-metal particles to mimic the effect of in-reactor irradiation [17]. They showed that the cathodic reduction of H_2O_2 is catalyzed by the ability of H_2O_2 to create its own $\text{U}^{\text{IV}}/\text{U}^{\text{V}}$ donor-acceptor sites



followed by the electrochemical regeneration of the U^{IV} sites,



The H_2O_2 reduction rate is independent of pH between pH 4 and 9, but suppressed at more alkaline values. The reduction of H_2O_2 is only weakly dependent on applied potential with a fractional reaction order with respect to H_2O_2 , consistent with partial control by the chemical reaction (1.5) [96]. At low overpotentials, H_2O_2 reduction proceeds significantly faster on the noble metal particles within the SIMFUEL than on

the UO_{2+x} lattice surface [98].

Early studies on H_2O_2 decomposition, reaction (1.4), have been reviewed [6, 24]. In a UO_2 dissolution experiment in H_2O_2 -containing solution, de Pablo et al. [26] measured both U release to solution and the H_2O_2 consumption rate. Since more H_2O_2 was consumed than U released it was calculated that H_2O_2 decomposition was also occurring although an inability to account for oxidized U retained on the surface as a corrosion product deposit made the measurement only qualitative. An accumulation of gas bubbles on UO_2 surfaces in the presence of H_2O_2 has been observed suggesting that a UO_2 surface can catalyze H_2O_2 decomposition [24, 100]. Christensen et al. [101] also claimed that H_2O_2 decomposition was occurring in borax buffer solutions ($\text{pH} = 8 \pm 0.2$) based on a discrepancy between the amount of dissolved U analyzed compared to the amount expected if all the H_2O_2 consumed had caused dissolution. Amme et al. [90] have observed in a dissolution experiment with added H_2O_2 that the uranium concentration in groundwater leachates were lower than that in pure water and attributed this to an unidentified scavenging mechanism causing the deactivation of H_2O_2 . This observation could be due to the H_2O_2 decomposition catalyzed by trace metal ions in groundwater [102].

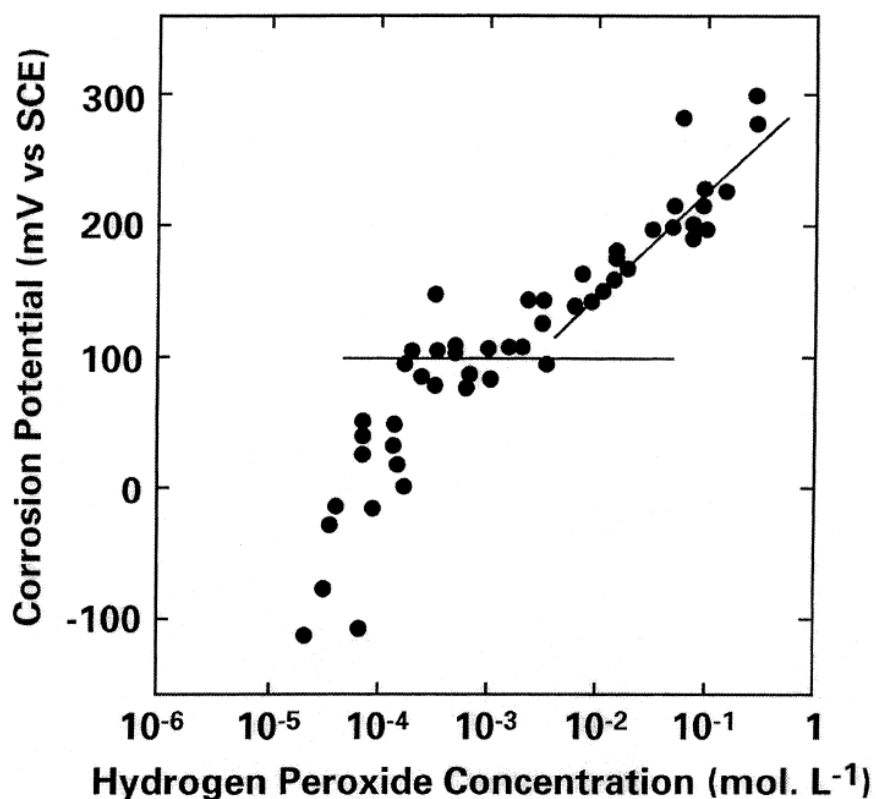


Fig. 1.14. Steady-state corrosion potential (E_{CORR}) values measured as a function of H_2O_2 concentration in an unstirred 0.1 mol L^{-1} NaClO_4 solution ($\text{pH}=9.5$) [30].

Attempts have been made to determine the mechanisms of surface redox reactions under open circuit (corrosion) conditions [6, 24, 30]. Fig. 1.14 shows that at low $[\text{H}_2\text{O}_2]$ ($< 10^{-4} \text{ mol.L}^{-1}$) the open circuit (or corrosion) potential, E_{CORR} , increased from $\sim -0.1 \text{ V}$ to $\sim 0.1 \text{ V}$ (vs. SCE) with increasing $[\text{H}_2\text{O}_2]$, and recent studies showed that the value of the steady-state E_{CORR} achieved was directly related to the extent of oxidation of the surface (determined by X-ray photoelectron spectroscopy (XPS)) [103].

Over the intermediate $[\text{H}_2\text{O}_2]$ range, 10^{-4} to $5 \times 10^{-3} \text{ mol.L}^{-1}$, E_{CORR} in Fig. 1.14 became independent of $[\text{H}_2\text{O}_2]$, a situation suggesting the dominant surface reaction could be H_2O_2 decomposition rather than H_2O_2 -driven UO_2 corrosion. In this concentration range,

E_{CORR} rose rapidly to the final steady-state value (~ 0.1 V) indicating that the oxidation step, $\text{U}^{\text{IV}}\text{O}_2$ to $\text{U}^{\text{IV}}_{1-2x}\text{U}^{\text{V}}_{2x}\text{O}_{2+x}$, was rapid. At potentials in this range both oxidative dissolution as $\text{U}^{\text{VI}}\text{O}_2^{2+}$ and H_2O_2 decomposition are possible. Based on the independence of E_{CORR} on $[\text{H}_2\text{O}_2]$, it was claimed that the corrosion of the surface and the decomposition of H_2O_2 on the $\text{U}^{\text{IV}}_{1-2x}\text{U}^{\text{V}}_{2x}\text{O}_{2+x}$ layer were both limited by the slow dissolution of U^{VI} species from a U^{VI} surface layer. XPS measurements confirmed the presence of U^{VI} on the electrode surface in this potential range.

For $[\text{H}_2\text{O}_2] \geq 5 \times 10^{-3} \text{ mol.L}^{-1}$, E_{CORR} increased approximately linearly with concentration and coverage of the electrode by U^{VI} species increased. Experiments in which the amount of dissolved U^{VI} was measured showed that, at these higher $[\text{H}_2\text{O}_2]$ dissolution was accelerated [25, 104] and the rate became first order with respect to $[\text{H}_2\text{O}_2]$. This increase in dissolution rate coupled to an apparently greater coverage by insulating and potentially blocking surface U^{VI} species was taken as an indication of enhanced dissolution at locally acidified sites on the electrode surface [24]. How these changes influenced the rate and extent of H_2O_2 decomposition was not investigated.

A more comprehensive study in the presence of the α -radiolysis of water [105], to produce the oxidant H_2O_2 , appeared to confirm this claim. The coupled reactions of H_2O_2 reduction and oxidation appeared to be buffered at $\text{pH} = 9.5$ and the slow rate of H_2O_2 decomposition was attributed to surface coverage by insulating U^{VI} species only slowly released by chemical dissolution as UO_2^{2+} in non-complexing solution. Since this U^{VI} species blocked the underlying conducting substrate surface the rate of H_2O_2 decomposition was limited by the rate of its release to solution. If this mechanism is

correct, then decomposition is inhibited by the extent of surface oxidation under open-circuit (corrosion) conditions.

1.5.2 Factors influencing the rate of H_2O_2 decomposition

As stated above, under corrosion conditions there are two competitive anodic reactions which can couple with the cathodic reduction of H_2O_2 : the oxidative dissolution of UO_2 (reaction (1.2)) and the simultaneous oxidation of H_2O_2 (reaction (1.3)), the latter leading to H_2O_2 decomposition (reaction (1.4)), as illustrated in Fig. 1.15. Therefore, the rates of fuel corrosion and H_2O_2 decomposition are determined by the balance between each anodic reaction. Since only a fraction of H_2O_2 is consumed in oxidizing UO_2 , this fraction is defined as the dissolution yield in some studies [27, 40], i.e., the ratio between the concentrations of dissolved U and total consumed H_2O_2 . It is essential to investigate the factors controlling the H_2O_2 decomposition and their effect on fuel dissolution rate.

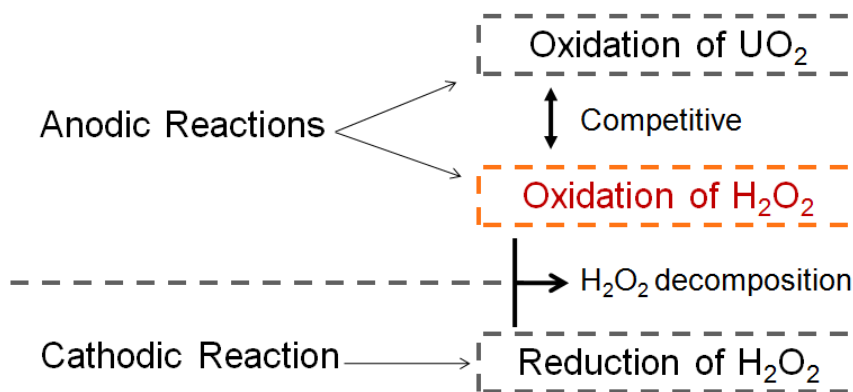


Fig. 1.15. Schematic diagram showing the primary redox reactions involving H_2O_2 on a UO_2 surface.

1.5.2.1 pH

The rate of H_2O_2 decomposition depends on the alkalinity of the solution, Haines and McCracken [106] reporting that the decomposition rate in a LiOH solution (pH 10.3) was 4-5 times that in neutral pH water. Navarro et al. [107] have also observed that H_2O_2 decomposed rapidly in aerated NaOH solutions with the maximum rate being attained in the pH range 11.5 to 11.7. Since this pH coincides with the first pK_a value of H_2O_2 , it was proposed that the presence of both H_2O_2 and the hydroperoxyl anion (HO_2^-) was necessary for uncatalyzed decomposition according to previously suggested mechanisms [108]. Spalek et al. [109] noted that the OH^- ion concentration exerted a significant effect on the decomposition rate in alkaline solutions and attributed this to the influence of OH^- ion on the activity of catalyzing species. Electrochemical studies [110, 111] showed that H_2O_2 oxidation could proceed at lower potentials in more alkaline solutions. While this was attributed to the involvement of protons in the H_2O_2 oxidation reaction the details of the mechanism were not elucidated.

1.5.2.2 Carbonate/bicarbonate

The carbonate-mediated decomposition of H_2O_2 has also been reported, the decomposition rate on Ag_2O , Pt, and Pd being shown to increase by a factor of 2 to 3 in K_2CO_3 compared to the rate measured in KOH solutions, while the opposite trend was observed on precipitated Ag [112]. Navarro et al. [107] also observed an enhanced decomposition in CO_2 /air-purged alkaline solutions which they attributed to the formation of an unstable intermediate, peroxy-carbonic acid (H_2CO_4). Csanyi and Galbacs [102], however, reported that the enhanced rate due to CO_2 disappeared in purified

solutions and suggested the catalytic effect observed [107] was due to the presence of trace transition metal carbonato complexes. This was supported by Lee et al. [113] who found the decomposition rate was 9 times faster in Na_2CO_3 than in NaOH solutions when trace levels of metals (<1 ppm wt.) were present. Richardson et al. [114] showed that HCO_3^- can activate H_2O_2 in the oxidation of sulfides via the formation of HCO_4^- , since the second order rate constants for sulfide oxidation by HCO_4^- were ~300-fold greater than those for H_2O_2 . Suess and Janik [115] and Wu et al. [116] reported that H_2O_2 decomposition was significantly accelerated in aqueous system by adding $\text{HCO}_3^-/\text{CO}_3^{2-}$ at high temperatures (50-90 °C), and attributed this to the formation of active CO_4^{2-} . Despite these endeavours whether or not $\text{HCO}_3^-/\text{CO}_3^{2-}$ promotes H_2O_2 decomposition under the disposal conditions remains unresolved.

1.5.2.3 Surface catalysis

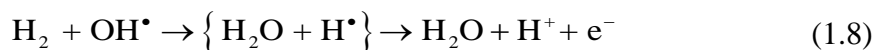
The H_2O_2 decomposition reaction can be accelerated by various catalytic sites on a spent fuel surface, i.e., (a) mixed $\text{U}^{\text{IV}}/\text{U}^{\text{V}}$ locations; and (b) noble metal fission products (ϵ -particles). That an oxidized $\text{U}^{\text{IV}}_{1-2x}\text{U}^{\text{V}}_{2x}\text{O}_{2+x}$ surface could support H_2O_2 decomposition is not unexpected since this reaction is known to be catalyzed on oxide surfaces especially those containing mixed oxidation states [30, 117]. The decomposition of H_2O_2 on the surfaces of various metal oxides (usually in particulate form) has been extensively studied [118, 119], and a variety of reaction pathways discussed. For oxides in which multiple oxidation states do not exist (TiO_2 , ZrO_2 , SiO_2 , Al_2O_3), it has been demonstrated that decomposition occurs on the oxide surface but the details of the mechanism remain unresolved. Recently the reaction on ZrO_2 was shown to involve the formation of OH^\bullet as intermediate species [120]. For decomposition on oxides within which redox

transformations are possible (iron oxides being the prime example) decomposition has been shown to involve coupling with redox transformations (e.g. $\text{Fe}^{\text{II}} \leftrightarrow \text{Fe}^{\text{III}}$) within the oxide [121, 122]. Decomposition then proceeds via reactions involving these two oxidation states and radical species such as OH^\bullet and HO_2^\bullet . This appears to be the case for H_2O_2 decomposition on UO_2 containing mixed oxidation states, e.g., $\text{U}^{\text{IV}}_{1-2x}\text{U}^{\text{V}}_{2x}\text{O}_{2+x}$.

Diaz-Arocas et al. [100] claimed that extensive decomposition of H_2O_2 occurred on a UO_2 surface and the accumulation of gas bubbles on the surface appeared to support this claim. Christensen et al. [101] reported that approximately half of the original concentration of $5 \times 10^{-2} \text{ mol L}^{-1}$ of H_2O_2 decomposed over 6 days on UO_2 at $\text{pH} = 8 \pm 0.2$. Shoesmith [6] and Sunder et al. [24] found that when carbonate was present, and dissolution unimpeded by deposits (U^{VI}), the increasing ratio of $\text{U}^{\text{IV}} + \text{U}^{\text{V}}$ over U^{VI} surface species appeared to sustain a higher decomposition rate up to H_2O_2 concentrations as high as 0.1 mol L^{-1} . Gimenez et al. [25] compared the dissolution rates of UO_2 in solutions containing different oxidants, H_2O_2 or ClO^- , at the same concentration and found that the dissolution rates in ClO^- were 2-3 times higher than those in H_2O_2 despite their similar redox potentials. This difference was thought to be a consequence of H_2O_2 decomposition on the UO_2 surface. A discrepancy between UO_2^{2+} release and H_2O_2 consumption was observed in dissolution experiments, only a portion of the H_2O_2 being involved in UO_2 corrosion [26, 40, 123, 124]. The exact fraction varied for different UO_2 specimens (e.g., unirradiated UO_2 , doped UO_2 and SIMFUEL) and could be influenced by the accumulation of surface corrosion deposits.

Based on a comparison between electrochemical experiments on a UO_2 surface subjected to α -radiation and radiolysis model calculation, Wren et al. [105] suggested a two-step

decomposition mechanism involving radiolytic H_2O_2 and H_2 . In the first step, the OH^\bullet radicals produced by the surface-catalyzed decomposition of H_2O_2 would react with H_2 produced by water radiolysis, resulting in the overall process, reaction (1.9).



with the e^- produced and consumed in the surface catalytic cycle, $\text{U}^{\text{IV}} \leftrightarrow \text{U}^{\text{V}}$. Since the rate of radiolytic production of H_2O_2 exceeds its rate of recombination with H_2 , E_{CORR} increased as H_2O_2 accumulated and surpassed equilibrium potential for the oxidation of H_2O_2 to O_2 , allowing H_2O_2 decomposition compete with UO_2 corrosion.

Besides the UO_2 surface, the noble metal (ϵ) particles can also catalyze H_2O_2 decomposition. These particles are metallic precipitates composed of fission products (Ru, Mo, Pd, and Rh) in the spent fuel [17, 125]. Their ability to catalyze aqueous redox reactions on fuel surface has been reported in previous studies [97, 98, 126-129], especially their ability to activate H_2 , by dissociation to produce H^\bullet , which leads to the reduction of U^{VI} species and H_2O_2 . From the electrochemical perspective, these particles act as anodes supporting H_2 oxidation and lead to $\text{U}^{\text{VI}}/\text{H}_2\text{O}_2$ reduction by galvanic coupling to the UO_2 matrix. However, in this study the focus is on the catalytic activity of ϵ -particles towards H_2O_2 . It is known that H_2O_2 decomposition can be accelerated in the presence of metallic catalysts [130]. The kinetics of this reaction on the noble metals Pd and Ru has been studied using chemical [112, 131] and electrochemical [132, 133] methods. The electrochemical reduction/oxidation of H_2O_2 has been studied on a series of

metallic sensors for H_2O_2 detection, such as Pd/Au [134, 135], Pd/Ir [136], and Pt [110, 137]. Although there exist a number of extensive studies on metallic catalysts, only a few studies have focused on H_2O_2 decomposition on spent nuclear fuel in which the noble-metal constituents are in the form of scattered ϵ -particles within the oxide. Goldik et al. [98] demonstrated electrochemically that H_2O_2 reduction was enhanced on SIMFUEL as the number/density of ϵ -particles was increased. Trummer et al. [97] observed that the H_2O_2 consumption on doped UO_2 pellets increased with Pd content in a $2 \text{ mmol L}^{-1} \text{ H}_2\text{O}_2$ solution under N_2 atmosphere, and the consumed H_2O_2 could not be balanced by the dissolved UO_2^{2+} suggesting catalytic H_2O_2 decomposition. In recent dissolution studies [27, 40, 124], a significant difference in the ratio between dissolved U and consumed H_2O_2 was found between pure UO_2 pellets and doped $\text{UO}_2/\text{SIMFUEL}$ pellets. The much lower dissolution yield measured on SIMFUEL (containing ϵ -particles) than that on pure UO_2 indicated a large fraction of the overall H_2O_2 consumption could be attributed to its decomposition.

1.5.3 The influence of carbonate/bicarbonate on fuel dissolution

For a Canadian deep geologic repository [138], the major groundwater species will be $\text{Ca}^{2+}/\text{Na}^+/\text{Cl}^-/\text{SO}_4^{2-}$ with a small amount of bicarbonate (10^{-4} to $10^{-3} \text{ mol.L}^{-1}$). The groundwater pH is expected to be in the range 6 to 10. The key groundwater species likely to accelerate fuel corrosion is $\text{HCO}_3^-/\text{CO}_3^{2-}$ which is a strong complexing agent for the $\text{U}^{\text{VI}}\text{O}_2^{2+}$ ion [8, 54, 139]. The influence of $\text{HCO}_3^-/\text{CO}_3^{2-}$ has been investigated in both chemical [140-143] and electrochemical dissolution experiments [24, 99, 144]. A carbonate concentration $\geq 10^{-3} \text{ mol.L}^{-1}$ was found to prevent the deposition of U^{VI} corrosion products on the UO_2 surface leading to a significant increase in the corrosion

rate. When a sufficient $\text{HCO}_3^{2-}/\text{CO}_3^{2-}$ concentration was present the formation of the underlying $\text{U}^{\text{IV}}_{1-2x}\text{U}^{\text{V}}_{2x}\text{O}_{2+x}$ film (Section 1.4.2.6 and 1.5.1), which forms prior to the onset of dissolution [6, 94], is also inhibited [140, 141].

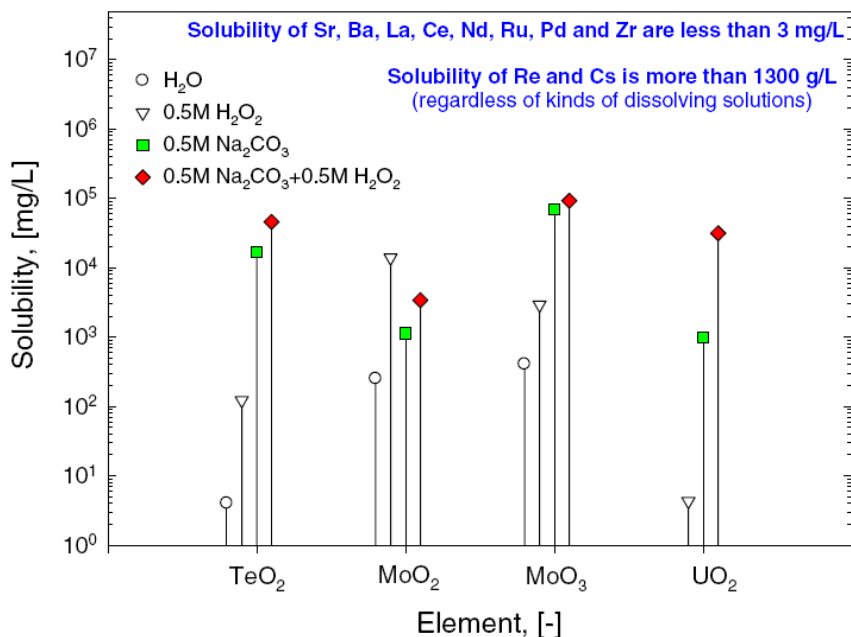


Fig. 1.16. Solubility of the simulated fission product/actinide oxides in various solutions, including distilled water, $0.5 \text{ mol L}^{-1} \text{H}_2\text{O}_2$, $0.5 \text{ mol L}^{-1} \text{Na}_2\text{CO}_3$, and $0.5 \text{ mol L}^{-1} \text{Na}_2\text{CO}_3-0.5 \text{ mol L}^{-1} \text{H}_2\text{O}_2$ solutions. Source: Ref [145].

As stated in Section 1.4.2.5, the solubility of UO_2 is strongly dependent on complexing ligands such as carbonate/bicarbonate and peroxide. Fig. 1.16 compares the solubility of UO_2 to that of other fission product oxides in a number of solutions [145]. Almost no UO_2 dissolved in distilled water, while significantly higher solubilities were obtained in solutions containing carbonate/bicarbonate. It has also been found that, in the presence of both H_2O_2 and $\text{HCO}_3^-/\text{CO}_3^{2-}$ at high concentrations, UO_2 corrosion is accelerated by the formation of a soluble peroxo-carbonato complex, $\text{UO}_2(\text{O}_2)_x(\text{CO}_3)_y^{2-2x-2y}$ [146, 147].

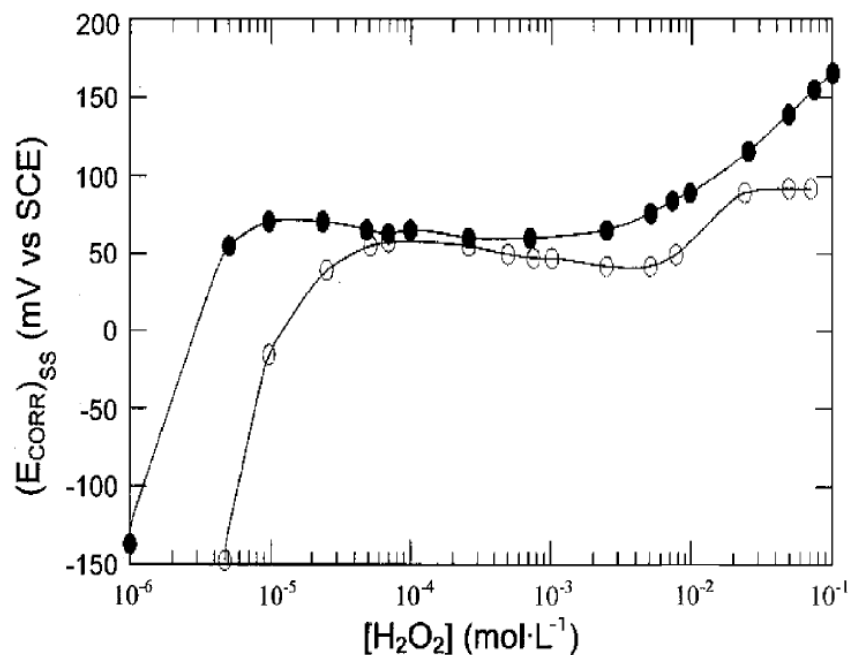


Fig. 1.17. The steady-state E_{CORR} recorded on a UO_2 electrode as a function of $[\text{H}_2\text{O}_2]$ in stirred 0.1 mol L^{-1} NaClO_4 ($\text{pH} \sim 9.5$): (○) with, and (●) without added 0.1 mol L^{-1} $\text{HCO}_3^-/\text{CO}_3^{2-}$. Source: Ref [24].

According to the electrochemical measurements of Goldik et al. [99], H_2O_2 reduction occurred at less cathodic potentials when carbonate/bicarbonate was present due to the absence of hydrated U^{VI} species on the electrode surface. At more cathodic potentials, the reduction was suppressed because of the blockage of active sites by carbonate ions.

Sunder et al. [24] investigated the corrosion behaviour of CANDU pellets in slightly alkaline ($\text{pH}=9.5$) solutions containing H_2O_2 and $\text{HCO}_3^-/\text{CO}_3^{2-}$, Fig. 1.17. The steady-state E_{CORR} appeared to remain independent of $[\text{H}_2\text{O}_2]$ up to nearly 0.1 mol L^{-1} . It was proposed that $\text{HCO}_3^-/\text{CO}_3^{2-}$ prevented the accumulation of U^{VI} corrosion products on the surface which remained less oxidized with E_{CORR} lower than in $\text{HCO}_3^-/\text{CO}_3^{2-}$ -free solution. That H_2O_2 decomposition was accelerated in the presence of carbonate was

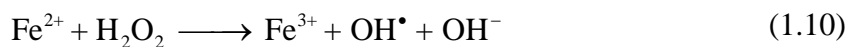
supported by the accumulation of gas bubbles on the fuel surface, a feature not seen in the absence of carbonate. It was proposed that H_2O_2 decomposition was accelerated on the exposed $\text{U}^{\text{IV}}/\text{U}^{\text{V}}$ sublayer.

1.5.4 The effect of steel corrosion products (Fe^{2+} and H_2) on fuel corrosion

The anaerobic corrosion of the repository barrier material (i.e., steel vessel) in groundwater leads to the formation of significant concentrations of redox scavengers, with $[\text{Fe}^{2+}]$ up to 10^{-6} - 10^{-4} mol L^{-1} and $[\text{H}_2]$ as high as 0.038 mol L^{-1} [18, 148].

1.5.4.1 Fe^{2+}

Iron redox cycling is expected to be one of the major mechanisms controlling the near-field conditions in a geologic repository for UO_2 spent nuclear fuel. The oxidation of Fe^{2+} by H_2O_2 occurs via a redox cycling reaction known as the Fenton mechanism [149-151]. In the simplified form, it is a two-step reaction involving the formation of a hydroxyl radical as an intermediate.



A range of experimental studies has been conducted to determine how Fe^{2+} would influence the fuel corrosion process. Electrochemical experiments with Pu-doped UO_2 electrodes [152] showed that, while the addition of Fe^{2+} at a concentration of 10^{-5} mol L^{-1} did not alter the corrosion potential (E_{CORR}), a $[\text{Fe}^{2+}]$ of 10^{-4} mol L^{-1} decreased the E_{CORR} by 0.140 V, indicating the consumption of alpha radiolytically produced oxidants by

Fe^{2+} . The corrosion product, studtite (Section 1.4.2.5 above), usually detected on UO_2 surfaces after exposure to H_2O_2 , was not found on the surfaces exposed to solutions with stoichiometric $\text{Fe(II)/H}_2\text{O}_2$ ratios [153]. Ollila and co-workers [154-156] conducted dissolution experiments on UO_2 doped with the α -emitter ^{233}U (to simulate the radiation dose rates expected after 3000 to 10000 years of disposal) in the presence of anaerobically corroding iron and found no evidence for irradiation-enhanced dissolution. Loida et al. [157] observed a significant decrease of radionuclide release (1-2 orders of magnitude) after the addition of iron powder to the solution being used in leaching experiments. These and similar experiments [21, 154, 155, 158, 159] indicate a significant reductive influence of steel corrosion products, both radiolytic oxidants and oxidized U^{VI} being reduced at the fuel surface. In the experiments with metallic iron, the suppression of UO_2 corrosion was a combined result of Fe^{2+} and H_2 gas.

1.5.4.2 H_2

Hydrogen has also been shown to suppress UO_2 corrosion on a range of UO_2 materials ranging from spent fuel itself to α -doped UO_2 and SIMFUELS [18, 148, 160, 161]. A key mechanism for the inhibition of corrosion by H_2 has been demonstrated to be the galvanic coupling of H_2 oxidation on ϵ -particles to UO_{2+x} reduction on the fuel surface [18, 127, 162, 163], with the oxidation/dissolution process appearing to be reversed at the U^{V} stage [127]. It should be noted that steel corrosion is not the only source of H_2 which can also be produced by water radiolysis [92].

Corrosion studies using irradiated spent fuel segments [143, 164-166] showed that dissolved H_2 (in the concentration range 1 to 42 mmol L^{-1}) inhibited fuel dissolution. Cera et al. [167] observed in a long-term fuel leaching experiment that even radiolytically

produced H_2 alone could inhibit fuel dissolution. The inhibiting effect of H_2 on UO_2 dissolution has been modelled by Eriksen and Jonsson [168] and Eriksen et al. [169]. Traboulsi et al. [92] recently performed a dissolution experiment on UO_2 in distilled water externally α -irradiated in either an open or closed atmosphere. The difference between these conditions was that the radiolytic H_2 would be evacuated with an open atmosphere but accumulated in the closed system. The authors reported that in the closed system the U concentration was suppressed by H_2 to about one third of that observed in the open atmosphere. In addition, the consumption of radiolytic H_2O_2 was almost completely suppressed when H_2 was allowed to accumulate.

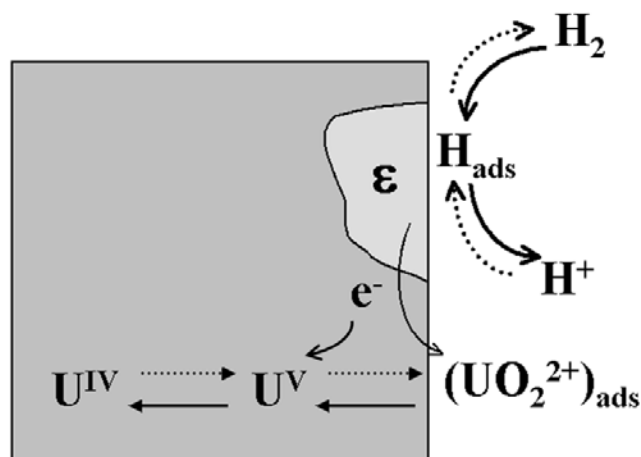


Fig. 1.18. Illustration of a galvanic coupling between the UO_2 matrix and ϵ -particles.

Image adapted from Ref [162].

In electrochemical experiments Broczkowski and co-workers observed a suppression of the corrosion potential by H_2 leading to a decrease in extent of surface oxidation on simulated fuel (SIMFUEL) [127, 162, 163]. The extent of this effect was found to depend on the number density of noble metal particles in the SIMFUEL pellets and the

concentration of dissolved H_2 . It was proposed that fuel oxidation/dissolution was suppressed by H_2 oxidation on the particles galvanically coupled to the fission-product-doped UO_2 matrix, as shown in Fig. 1.18. The kinetic parameters for reactions on UO_2 involving H_2 have been investigated [97, 128, 170, 171] to facilitate the modelling of fuel dissolution rates. The Swedish Nuclear Fuel and Waste Management Company (SKB) [160] have conducted a series of dissolution experiments with α -doped UO_2 , high burn-up spent fuel and MOX fuel and suggested the fractional alteration/dissolution rates for spent fuel to be in the order of 10^{-6} – 10^{-8} per year with a recommended value of 4×10^{-7} per year for $[\text{H}_2]$ above $10^{-3} \text{ mol L}^{-1}$ and Fe(II) concentrations typical for European repository concepts.

1.5.5 Radiolytic corrosion model

The development of radiolytic models (in particular for α -radiolysis) for spent fuel corrosion has recently been reviewed [15]. Poinssot et al. [22] modelled fuel corrosion assuming that the α -dose rate was uniform within a 45 μm thick water layer at the fuel surface, and that only half of the radiolytic oxidants reacted with the fuel, the remainder being consumed by other unidentified processes. A series of kinetic models, which included the influence of diffusive transport, were developed for both γ and α radiolytic processes by Christensen et al. [172] and Christensen [173], and a similar approach was adopted by Poulesquen and Jegou [39]. Since kinetic information for the reaction of radiolysis products with the fuel surface was unavailable, these models assumed that the heterogeneous reactions could be mimicked by an equivalent series of homogeneous reactions occurring within a thin layer of solution at the fuel surface. A mixed potential model based on electrochemical parameters for fuel corrosion was also developed [20,

174]. This model included an attempt to model both the corrosion of the fuel and the steel vessel as well as a range of additional homogeneous redox reactions and adsorption/desorption/precipitation processes. The model also included reactions occurring on noble metal particles but not the influence of H_2 . Jonsson et al. [175] developed a comprehensive model which integrated the available kinetic data and tried to account for the geometrical distribution of radiation dose rate and the effects of the oxidant scavengers Fe^{2+} and H_2 , fuel burn up, and ground water chemistry. The maximum rate of spent fuel dissolution under Swedish repository conditions was calculated and it was concluded that a H_2 pressure of 0.1 bar ($78 \mu\text{mol L}^{-1}$) would be sufficient to completely suppress the corrosion of 100-year old LWR fuel even if the influence of Fe^{2+} was neglected. When the expected $[Fe^{2+}]$ in a Swedish repository ($\sim 36 \mu\text{mol L}^{-1}$) was included, its effect and that of the radiolytically produced H_2 alone were calculated to be sufficient to effectively inhibit fuel corrosion. These studies have revealed many of the key features required in models for the radiolytic corrosion of spent fuel and the importance to account for the influence of container corrosion products, Fe^{2+} and H_2 , on the fuel corrosion rate.

1.6 Thesis outline

Chapter 2 briefly reviews the principles of the experimental techniques employed in this research.

In Chapter 3, a preliminary model is developed to determine the influence of steel corrosion products on α -radiolytic corrosion of spent nuclear fuel inside a failed waste container. This chapter evaluates different model setups and parameters, and provides a

basis for a more extensive model development.

In Chapter 4, an improved model is presented which includes a more comprehensive reaction set. The influence of the α -radiolysis products is evaluated using a full radiolytic reaction set. Corrosion of the fuel is modelled considering both the direct oxidation of UO_2 by H_2O_2 and the galvanically-coupled oxidation by H_2O_2 reduction on noble metal (ϵ) particles. Corrosion rate is found to be very sensitive to the corrosion products of steel container, Fe^{2+} and H_2 . The surface coverage of ϵ -particles also plays an important role in determining the dissolution rate. The critical H_2 concentrations required to completely suppress fuel corrosion are calculated.

Chapters 5-7 present the experimental results examining the influence of different variables on H_2O_2 decomposition using simulated spent fuel (SIMFUEL). The competition between H_2O_2 oxidation and UO_2 dissolution, reactions (1.2) and (1.3), and its effect on fuel corrosion rate have been studied.

In Chapter 5, the anodic oxidation and open circuit decomposition of H_2O_2 on UO_{2+x} surfaces have been investigated voltammetrically and using linear polarization resistance measurements in near neutral and alkaline solutions. The effect of the oxidized U^{VI} surface layer on H_2O_2 decomposition is discussed. The influence of the solution alkalinity on electrochemical oxidation of H_2O_2 is also studied.

In Chapter 6, the anodic behaviour of SIMFUEL in solutions containing both H_2O_2 and $\text{HCO}_3^-/\text{CO}_3^{2-}$ has been studied electrochemically and using surface/solution analytical techniques, in particular X-ray photoelectron spectroscopy (XPS) and inductively coupled plasma atomic emission spectroscopy (ICP-AES). Since the rates of the two

anodic reactions are both controlled by the chemical release of U^{VI} surface species and can be increased by the addition of HCO_3^-/CO_3^{2-} , this chapter focuses on the influence of HCO_3^-/CO_3^{2-} on the competition between H_2O_2 oxidation and UO_2 dissolution, and on the rate of H_2O_2 decomposition under open circuit conditions.

In Chapter 7, the effect of noble metal (ϵ) fission products on H_2O_2 decomposition has been studied electrochemically. The catalytic ability of UO_{2+x} and ϵ -particles towards the electrochemical oxidation of H_2O_2 has been investigated.

1.7 References

- [1] Nuclear Waste Management Organization (Toronto), Implementing Adaptive Phased Management 2014 to 2018, available at <http://www.nwmo.ca/>, last accessed in March 2014.
- [2] NWMO, Adaptive Phased Management - Used Fuel Repository Conceptual Design and Postclosure Safety Assessment in Crystalline Rock: Pre-Project Report, Report TR-2012-16, Nuclear Waste Management Organization, Toronto, ON, 2012.
- [3] NWMO, Adaptive Phased Management - Postclosure Safety Assessment of a Used Fuel Repository in Sedimentary Rock: Pre-Project Report, Report TR-2013-07, Nuclear Waste Management Organization, Toronto, ON, 2013.
- [4] F. Garisto, J. Avis, N. Calder, A. D'Adrea, P. Gierszewski, C. Kitson, T. Melnyk, K. Wei, and L. Wojciechowski, Third Case Study - Defective Container Scenario, Report 06219-REP-01200-10126-R00, Ontario Power Generation, Toronto, ON, 2004.
- [5] L.H. Johnson, and D.W. Shoesmith, Spent fuel, in "Radioactive Waste Forms for the Future", edited by W. Lutze, and R.C. Ewing, Elsevier, Amsterdam, 1988.
- [6] D.W. Shoesmith, Fuel corrosion waste process under waste disposal conditions, J. Nucl. Mater. 282 (2000) 1-31.
- [7] P.R. Tremaine, J.D. Chen, G.J. Wallace, and W.A. Boivin, Solubility of Uranium (IV) Oxide in Alkaline Aqueous Solutions to 300 °C, Journal of Solution Chemistry 10 (1981) 221-230.
- [8] I. Grenthe, J. Fuger, R.J. Konings, R.J. Lemire, A.B. Muller, C. Nguyen-Trung, and H. Wanner, Chemical Thermodynamics of Uranium, North Holland, Amsterdam, 1992.

- [9] D.W. Shoesmith, and S. Sunder, The prediction of nuclear fuel (UO₂) dissolution rates under waste disposal conditions, *J. Nucl. Mat.* 190 (1992) 20-35.
- [10] J. Bruno, and R.C. Ewing, Spent Nuclear Fuel, *Elements* 2 (2006) 343-349.
- [11] F. Garisto, Fourth Case Study: Features, Events and Processes, Report TR-2012-14, Nuclear Waste Management Organization, Toronto, ON, 2012.
- [12] G. Choppin, J.O. Liljenzin, and J. Rydberg, *Radiochemistry and nuclear chemistry*, Butterworth-Heinemann, Oxford, 2001.
- [13] J.W.T. Spinks, and R.J. Woods, *An Introduction to Radiation Chemistry*, The Third Edition, John Wiley and Sons Inc., New York, 1990.
- [14] E. Ekeröth, O. Roth, and M. Jonsson, The relative impact of radiolysis products in radiation induced oxidative dissolution of UO₂, *J. Nucl. Mater.* 355 (2006) 38-46.
- [15] T.E. Eriksen, D.W. Shoesmith, and M. Jonsson, Radiation induced dissolution of UO₂ based nuclear fuel – A critical review of predictive modelling approaches, *J. Nucl. Mater.* 420 (2012) 409–423.
- [16] SKB, Fuel and canister process report for the safety assessment SR-Site, Report TR-10-46, Swedish Nuclear Fuel and Waste Management Co (SKB), Stockholm, 2010.
- [17] D.W. Shoesmith, Used Fuel and Uranium Dioxide Dissolution Studies - A Review, Report NWMO TR-2007-03, Nuclear Waste Management Organization, Toronto, ON, 2007.
- [18] D.W. Shoesmith, The Role of Dissolved Hydrogen on the Corrosion/Dissolution of Spent Nuclear Fuel, Report NWMO TR-2008-19, Nuclear Waste Management Organization, Toronto, ON, 2008.
- [19] H. He, M.E. Broczkowski, K. O'Neil, D. Ofori, O. Semenikhin, and D.W. Shoesmith, Corrosion of Nuclear Fuel (UO₂) Inside a Failed Nuclear Waste Container, Report NWMO TR-2012-09, Toronto, ON, 2012.
- [20] D.W. Shoesmith, M. Kolar, and F. King, A mixed-potential model to predict fuel (uranium dioxide) corrosion within a failed nuclear waste container, *Corrosion* 59 (9) (2003) 802-816.
- [21] B. Grambow, A. Loida, A. Martínex-Esparza, P. Díaz-Arocas, J. de Pablo, J.-L. Paul, J.-P. Glatz, K. Lemmens, K. Ollila, and H. Christensen, Source Term for Performance Assessment of Spent Fuel as a Waste Form, Report EUR 19140 EN, European Commission, 2000.
- [22] C. Poinssot, C. Ferry, M. Kelm, B. Grambow, A. Martinez Esparza Valiente, L.H. Johnson, Z. Andriambololona, J. Bruno, C. Cachoir, J.-M. Cavedon, H. Christensen, C. Corbel, C. Jegou, K. Lemmens, A. Loida, P. Lovera, F. Miserque, J. de Pablo, A. Poulesquen, J. Quinones, V. Rondinella, K. Spahiu, and D.H. Wegen, Final report of the

European project spent fuel stability under repository conditions, Report CEA-R-6093, CEA, 2005.

[23] R.C. Ewing, and M.T. Peters, Source Term. In: OST&I Annual Report 2005, Report DOE/RW-0581, 2005, 5-51.

[24] S. Sunder, N.H. Miller, and D.W. Shoesmith, Corrosion of uranium dioxide in hydrogen peroxide solutions, *Corros. Sci.* 46 (2004) 1095-1111.

[25] J. Gimenez, E. Baraj, M.E. Torrero, I. Casas, and J. de Pablo, Effect of H_2O_2 , NaClO and Fe on the dissolution of unirradiated UO_2 in NaCl 5 mol kg^{-1} . Comparison with spent fuel dissolution experiments, *J. Nucl. Mater.* 238 (1996) 64-69.

[26] J. de Pablo, I. Casas, F. Clarens, F. El Aamrani, and M. Rovira, The effect of hydrogen peroxide concentration on the oxidative dissolution of unirradiated uranium dioxide, *Mat. Res. Soc. Symp. Proc.* 663 (2001) 409-426.

[27] R. Pehrman, M. Trummer, C.M. Lousada, and M. Jonsson, On the redox reactivity of doped UO_2 pellets – Influence of dopants on the H_2O_2 decomposition mechanism, *J. Nucl. Mater.* 430 (2012) 6-11.

[28] D.W. Shoesmith, S. Sunder, M.G. Bailey, and G.J. Wallace, The corrosion of nuclear fuel (UO_2) in oxygenated solutions, *Corros. Sci.* 29 (1989) 1115-1128.

[29] M.J. Nicol, and C.R.S. Needes, The anodic dissolution of uranium dioxide - I. In perchlorate solutions, *Electrochim. Acta* 20 (1975) 585-589.

[30] D.W. Shoesmith, and S. Sunder, An electrochemistry-based model for the dissolution of UO_2 , Report AECL-10488, Atomic Energy of Canada Ltd., Pinawa, Canada, 1991.

[31] S. Sunder, D.W. Shoesmith, and L.K. Strandlund, Anodic dissolution of UO_2 in slightly alkaline sodium perchlorate solutions, Report AECL-11440, COG-95-461, Atomic Energy of Canada Limited, 1996.

[32] J.C. Tait, and J.L. Luht, Dissolution rates of uranium from unirradiated UO_2 and uranium and radionuclides from used CANDU fuel using the single-pass flow-through apparatus, Report 06819-REP-01200-0006R00, Ontario Hydro, 1997.

[33] I. Casas, J. Giménez, J. de Pablo, and M.E. Torrero, in "Scientific Basis for Nuclear Waste Management XVI", edited by C.G. Interrante, and R.T. Pabalan, Materials Research Society, Pittsburgh, 1993, p. 67.

[34] S.A. Steward, and H.C. Weed, in "Scientific Basis for Nuclear Waste Management XVII", edited by A. Barkatt, and R.A. Van Konynenberg, Materials Research Society, Pittsburgh, 1994, p. 409.

[35] J. de Pablo, I. Casas, J. Giménez, M. Molera, and M.E. Torrero, in "Scientific Basis for Nuclear Waste Management XX", edited by W. Gray, and I. Triay, Materials Research Society, Pittsburgh, 1997, p. 535.

- [36] D.W. Shoesmith, S. Sunder, and J.C. Tait, Validation of an electrochemical model for the oxidative dissolution of used CANDU fuel, *J. Nucl. Mater.* 257 (1998) 89-98.
- [37] F. Garisto, D.H. Barber, E. Chen, A. Inglot, and C.A. Morrison, Alpha, Beta and Gamma Dose Rates in Water in Contact with Used CANDU Fuel, Report NWMO TR-2009-27, Nuclear Waste Management Organization, Toronto, ON, 2009.
- [38] J. McMurry, D.A. Dixon, J.D. Garroni, B.M. Ikeda, S. Stroes-Gascoyne, P. Baumgartner, and T.W. Melnyk, Evolution of a Canadian deep geologic repository: base scenario, Report 06819-REP-01200-10092-R00, Ontario Power Generation, Toronto, ON, 2003.
- [39] A. Poulesquen, and C. Jegou, Influence of Alpha radiolysis of water on UO₂ matrix alteration: chemical/transport model, *Nucl. Tech.* 160 (2007) 337-345.
- [40] C.M. Lousada, M. Trummer, and M. Jonsson, Reactivity of H₂O₂ towards different UO₂-based materials: The relative impact of radiolysis products revisited, *J. Nucl. Mater.* 434 (2013) 434-439.
- [41] D.W. Shoesmith, The Chemistry/Electrochemistry of Spent Nuclear Fuel as a Wasteform, in "Uranium: Cradle to Grave", edited by P. Burns, and G. Sigmon, Mineralogical Society of Canada, Short Course Series Vol 43, 337-368 (2013) and references therein.
- [42] J.C. Tait, H. Roman, and C.A. Morrison, Characteristics and radionuclide inventories of used fuel from OPG Nuclear Generating Stations. Volume 1 - Main report and Volume 2 - Radionuclide inventory data, Report 06819-REP-01200-10029-R00, Ontario Power Generation, Toronto, Canada, 2000.
- [43] M. Garamszeghy, Nuclear Fuel Waste Projections in Canada - 2012 Update, Report NWMO TR-2012-13, Nuclear Waste Management Organization, Toronto, Canada, 2012.
- [44] F. Garisto, M. Gobien, E. Kremer, and C. Medri, Fourth Case Study: Reference Data and Codes, Report NWMO-TR-2012-08, Nuclear Waste Management Organization, Toronto, ON, 2012.
- [45] L. Johnson, The dissolution of irradiated UO₂ fuel in groundwater, Report AECL-6837, Atomic Energy of Canada Limited, Pinawa, Canada, 1982.
- [46] P.W. Winter, The electronic transport properties of UO₂, *J. Nucl. Mater.* 161 (1989) 38-43.
- [47] P.A. Cox, Transition Metal Oxides: an introduction to their electronic structure and properties, Clarendon Press, Oxford, 1992.
- [48] G.J. Hyland, and J. Ralph, Electronic contributions to the high-temperature thermophysical properties of UO_{2+x}: a critical analysis, *High Temperatures-High Pressures* 15 (1983) 179-190.

- [49] Y. Baer, and J. Schoenes, Electronic Structure and Coulomb Correlation Energy in UO_2 Single Crystal, *Solid State Communications* 33 (1980) 885-888.
- [50] J. Schoenes, Recent Spectroscopic Studies of UO_2 , *Journal of the Chemical Society, Faraday Transactions 2*. 83 (1987) 1205-1213.
- [51] J. Schoenes, Electronic Transitions, Crystal Field Effects and Phonons in UO_2 , *Physics Reports* 63 (1980) 301-336.
- [52] J.M. Casado, J.H. Harding, and G.J. Hyland, Small-polaron hopping in Mott-insulating UO_2 , *Journal of Physics: Condensed Matter* 6 (1994) 4685-4698.
- [53] P. Ruello, K.D. Becker, K. Ullrich, L. Desgranges, C. Petot, and G. Petot-Ervas, Thermal variation of the optical absorption of UO_2 determination of the small polaron self-energy, *J. Nucl. Mater.* 328 (2004) 46-54.
- [54] D.W. Shoesmith, S. Sunder, and W.H. Hocking, *Electrochemistry of Novel Materials*, in ", edited by J. Lipkowski, and P.N. Ross, VCH publishers, New York, 1994.
- [55] A.J. Bosman, and H.J. Van Daal, Small-polaron versus Band Conduction in some Transition-metal Oxides, *Advances in Physics* 19 (1970) 1-112.
- [56] S. Aronson, J.E. Rulli, and B.E. Schaner, Electrical Properties of Nonstoichiometric Uranium Dioxide, *The Journal of Chemical Physics* 35 (1961) 1382-1388.
- [57] P. Nagles, M. Denayer, and J. Devreese, Electrical Properties of Single Crystals of Uranium Dioxide, *Solid State Communications* 1 (1963) 35-40.
- [58] P. Nagles, M. Denayer, and J. Devreese, Electronic Conduction in Single Crystals of Uranium Dioxide, *Journal of Applied Physics* 35 (1964) 1175-1180.
- [59] J.L. Bates, C.A. Hinman, and T. Kawada, Electrical Conductivity of Uranium Dioxide, *Journal of the American Ceramic Society* 50 (1967) 652-656.
- [60] J. Tateno, The dielectric properties at 9.1 GHz and nature of small polarons in nonstoichiometric uranium oxides, *Journal of Chemical Physics* 81 (1984) 6130-6135.
- [61] R.K. Willardson, J.W. Moody, and H.L. Goering, The Electrical Properties of Uranium Oxides, *Journal of Inorganic and Nuclear Chemistry* 6 (1958) 19-33.
- [62] N.J. Dudney, R.L. Coble, and H.L. Tuller, Electrical Conductivity of Pure and Yttria-Doped Uranium Dioxide, *Journal of the American Ceramic Society* 64 (1981) 627-631.
- [63] J.S. Betteridge, N.A.M. Scott, D.W. Shoesmith, L.E. Bahen, W.H. Hocking, and P.G. Lucuta, Effects of Hyperstoichiometry and Fission Products on the Electrochemical Reactivity of UO_2 Nuclear Fuel, Report AECL-11647, COG-96-331-I, Atomic Energy of Canada Limited, Pinawa, Canada, 1997.

- [64] D. Vollath, Gmelin Handbook of Inorganic Chemistry, The 8th Edition, Vol. C4, Chapter 3, Springer-Verlag, New York, 1984.
- [65] B.T.M. Willis, Crystallographic Studies of Anion-excess Uranium Oxides, Journal of the Chemical Society, Faraday Transactions 2 83 (1987) 1073-1081.
- [66] B.T.M. Willis, The Defect Structure of Hyper-stoichiometric Uranium Dioxide, Acta Crystallographica A34 (1978) 88-90.
- [67] B.T.M. Willis, Positions of the Oxygen Atoms in $\text{UO}_{2.13}$, Nature 197 (1963) 755-756.
- [68] G.C. Allen, P.A. Tempest, and J.W. Tyler, Coordination model for the defect structure of hyperstoichiometric UO_{2+x} and U_4O_9 , Nature 295 (1982) 48-49.
- [69] G.C. Allen, and P.A. Tempest, Linear Ordering of Oxygen Clusters in Hyperstoichiometric Uranium Dioxide, Journal of the Chemical Society, Dalton Transactions (1982) 2169-2173.
- [70] G.C. Allen, and P.A. Tempest, The Accommodation of Oxygen Clusters in Hyperstoichiometric Uranium Dioxide and Its Effects on Crystal Structure, Journal of the Chemical Society, Dalton Transactions (1983) 2673-2677.
- [71] G.C. Allen, and P.A. Tempest, Ordered defects in the oxides of uranium, Proceedings of the Royal Society of London A. 406 (1986) 325-344.
- [72] C.R.A. Catlow, Point defect and electronic properties of uranium dioxide, Proceedings of the Royal Society of London A. 353 (1977) 533-561.
- [73] D.K. Smith, B.E. Scheetz, C.A.F. Anderson, and K.L. Smith, Phase relations in the uranium-oxygen-water system and its significance on the stability of nuclear waste forms, Uranium 1 (1982) 79-110.
- [74] P.C. Burns, R.C. Ewing, and A. Navrotsky, Nuclear Fuel in a Reactor Accident, Science 335 (2012) 1184-1188.
- [75] J. Paquette, and R.J. Lemire, A description of the chemistry of aqueous solutions of uranium and plutonium to 200°C using potential pH diagrams, Nuclear Science and Engineering (1981) 79.
- [76] D. Gorman-Lewis, P.C. Burns, and J.B. Fein, Review of uranyl mineral solubility measurements, Journal of Chemical Thermodynamics 40 (2008) 335-352.
- [77] D.L. Clark, D.E. Hobart, and M.P. Neu, Actinide carbonate complexes and their importance in actinide environmental chemistry, Chemical Reviews 95 (1995) 25-48.
- [78] P.A. Finn, J.C. Hoh, S.F. Wolf, S.A. Slater, and J.K. Bates, The Release Of Uranium, Plutonium, Cesium, Strontium, Technetium And Iodine From Spent Fuel Under Unsaturated Conditions, Radiochim. Acta 74 (1996) 65-71.

- [79] R.J. Finch, E.C. Buck, P.A. Finn, and J.K. Bates, Oxidative Corrosion of Spent UO_2 fuel in vapor and dripping groundwater at 90°C , in: Scientific Basis for Nuclear Waste Management XXII, Materials Research Society, Boston, MA, 1998, Vol.556, pp. 431-438
- [80] P.C. Burns, R.C. Ewing, and M.L. Miller, Incorporation mechanisms of actinide elements into the structures of U^{6+} phases formed during the oxidation of spent nuclear fuel J. Nucl. Mater. 245 (1997) 1-9.
- [81] M. Douglas, S.B. Clark, J.I. Friese, B.W. Arey, E.C. Buck, and B.D. Hanson, Neptunium(V) partitioning to uranium(VI) oxide and peroxide solids, Environ. Sci. Technol. 39 (2005) 4117-4124.
- [82] T.Y. Shvareva, L. Mazeina, D. Gorman-Lewis, P. Burns, J.E.S. Szymanski, J.B. Fein, and A. Navrotsky, Thermodynamic characterization of boltwoodite and uranophane - Enthalpy of formation and aqueous solubility, Geochim. Cosmochim. Acta 75 (2011) 5269-5282.
- [83] K.-A.H. Kubatko, K.B. Helean, A. Navrotsky, and P.C. Burns, Stability of Peroxide-Containing Uranyl Minerals, Science 302 (2003) 1191-1193.
- [84] C.R. Armstrong, M. Nyman, T.Y. Shvareva, G.E. Sigmon, P.C. Burns, and A. Navrotsky, Uranyl peroxide enhanced nuclear fuel corrosion in seawater, Pro. Nat. Acad. Sci. 109 (2012) 1874-1877.
- [85] J. Abrefah, S. Marschmann, and E.D. Jenson, Examination of the surface coatings removed from K-East Basin fuel elements, Report PNNL-11806, Pacific Northwest National Laboratory, Richland, WA, 1998.
- [86] B.D. Hanson, B. McNamara, E.C. Buck, J.I. Friese, E. Jenson, K. Krupka, and B.W. Arey, Corrosion of commercial spent nuclear fuel. 1. Formation of studtite and metastudtite, Radiochim. Acta 93 (2005) 159-168.
- [87] B. McNamara, B.D. Hanson, and E. Buck, Mater. Res. Soc. Symp. Proc. 757 (2003) 401.
- [88] G. Sattonnay, C. Ardois, C. Corbel, J.F. Lucchini, M.F. Barthe, F. Garrido, and D. Gosset, Alpha-radiolysis effects on UO_2 alteration in water, J. Nucl. Mater. 288 (2001) 11-19.
- [89] M. Amme, B. Renker, B. Schmid, M.P. Feth, H. Bertagnolli, and W. Döbelin, Microspectrometric Identification of Corrosion Products formed on UO_2 Nuclear Fuel during Leaching Experiments, J. Nucl. Mater. 306 (2002) 202-212.
- [90] M. Amme, Contrary effects of the water radiolysis product H_2O_2 upon the dissolution of nuclear fuel in natural ground water and deionized water, Radiochim. Acta 90 (2002) 399-406.

- [91] C. Corbel, G. Sattonnay, S. Guilbert, F. Garrido, M.F. Barthe, and C. Jegou, Addition versus radiolytic production effects of hydrogen peroxide on aqueous corrosion of UO_2 , *J. Nuc. Mat.* 348 (2006) 1-17.
- [92] A. Traboulsi, J. Vandenborre, G. Blain, B. Humbert, J. Barbet, and M. Fattahi, Radiolytic Corrosion of Uranium Dioxide: Role of Molecular Species, *J. Phys. Chem. C* 118 (2013) 1071-1080.
- [93] B.G. Santos, J.J. Noël, and D.W. Shoesmith, The effect of pH on the anodic dissolution of SIMFUEL (UO_2), *J. of Electroanal. Chem.* 586 (2006) 1-11.
- [94] B.G. Santos, H.W. Nesbitt, J.J. Noël, and D.W. Shoesmith, X-ray photoelectron spectroscopy study of anodically oxidized SIMFUEL surfaces, *Electrochim. Acta* 49 (2004) 1863-1873.
- [95] J.S. Goldik, H.W. Nesbitt, J.J. Noël, and D.W. Shoesmith, Surface electrochemistry of UO_2 in dilute alkaline hydrogen peroxide solutions, *Electrochim. Acta* 49 (2004) 1699-1709.
- [96] J.S. Goldik, J.J. Noël, and D.W. Shoesmith, The electrochemical reduction of hydrogen peroxide on uranium dioxide electrodes in alkaline solution, *J. of Electroanal. Chem.* 582 (2005) 241-248.
- [97] M. Trummer, S. Nilsson, and M. Jonsson, On the effects of fission product noble metal inclusions on the kinetics of radiation induced dissolution of spent nuclear fuel, *J. Nucl. Mater.* 378 (2008) 55-59.
- [98] J.S. Goldik, J.J. Noël, and D.W. Shoesmith, The Effects of Simulated Fission Products in the Reduction of Hydrogen Peroxide on Simulated Nuclear Fuel Electrodes, *J. Electrochem. Soc.* 153 (2006) E151-E159.
- [99] J.S. Goldik, J.J. Noël, and D.W. Shoesmith, Surface electrochemistry of UO_2 in dilute alkaline hydrogen peroxide solutions: Part II. Effects of carbonate ions, *Electrochim. Acta* 51 (2006) 3278-3286.
- [100] P. Diaz-Arocas, J. Quinones, C. Maffiotte, J. Serrano, J. Garcia, and J.R. Almazan, Effect of secondary phase formation in the leaching of UO_2 under simulated radiolytic products, *Mater. Res. Soc. Symp. Proc.* 353 (1995) 641-646.
- [101] H. Christensen, R. Forsyth, R. Lundqvist, and L.O. Werme, Radiation Induced Dissolution of UO_2 , Report NS-90/85, Studsvik Energiteknik AB, Nyköping, Sweden, 1990.
- [102] L.J. Csanyi, and Z.M. Galbacs, Carbon dioxide-mediated decomposition of hydrogen peroxide in alkaline solutions, *J. Chem. Soc. Faraday Trans. 1.* 81 (1985) 113-116.

- [103] M. Razdan, Electrochemical and Surface Compositional Studies on UO_2 Corrosion Under Nuclear Waste Disposal Conditions, PhD Thesis, Western University, London, ON, 2013.
- [104] H. Christensen, and E. Bjergbakke, Radiation induced dissolution of UO_2 , in: J.K. Bates, and W.B. Seefeldt (Eds.) Scientific Basis for Nuclear Waste Management X, Material Research Society, Pittsburgh, 1987, pp. 115-122. (in: J.K. Bates, and W.B. Seefeldt (Eds.))
- [105] J.C. Wren, D.W. Shoesmith, and S. Sunder, Corrosion Behavior of Uranium Dioxide in Alpha Radiolytically Decomposed Water, *J. Electrochem. Soc.* 152 (2005) B470.
- [106] R.I. Haines, and D.R. McCracken, Decomposition of Hydrogen Peroxide under Coolant Chemistry Conditions, *Proceedings of the Water Chemistry of Nuclear Reactor Systems* 5 (1989) 309-310.
- [107] J.A. Navarro, M.A. de la Rosa, M. Roncel, and F. de la Rosa, Carbon dioxide-mediated decomposition of hydrogen peroxide in alkaline solutions, *J. Chem. Soc. Faraday Trans. 1.* 80 (1984) 249-253.
- [108] F.R. Duke, and T.W. Haas, The homogeneous base-catalyzed decomposition of hydrogen peroxide, *J. Phys. Chem.* 65 (1961) 304-306.
- [109] O. Spalek, J. Balej, and I. Paseka, Kinetics of the decomposition of hydrogen peroxide in alkaline solutions, *J. Chem. Soc. Faraday Trans. 1.* 78 (1982) 2349-2359.
- [110] Y. Zhang, and G.S. Wilson, Electrochemical oxidation of H_2O_2 on Pt and Pt + Ir electrodes in physiological buffer and its applicability to H_2O_2 -based biosensors, *J. Electroanal. Chem.* 345 (1993) 253-271.
- [111] J.O.M. Bockris, and L.F. Oldfield, The oxidation-reduction reactions of hydrogen peroxide at inert metal electrodes and mercury cathodes, *Trans. Faraday Soc.* 51 (1955) 249-259.
- [112] H.M. Cota, T. Katan, M. Chin, and F.J. Schoenweis, Decomposition of Dilute Hydrogen Peroxide in Alkaline Solutions, *Nature* 203 (1964) 1281.
- [113] H.H.B. Lee, A.-H. Park, and C. Oloman, Stability of hydrogen peroxide in sodium carbonate solutions, *TAPPI Journal* 83 (2000) August Issue.
- [114] D.E. Richardson, H. Yao, K.M. Frank, and D.A. Bennett, Equilibria, Kinetics, and Mechanism in the Bicarbonate Activation of Hydrogen Peroxide: Oxidation of Sulfides by Peroxymonocarbonate, *J. Am. Chem. Soc.* 122 (2000) 1729-1739.
- [115] H.U. Suess, and M. Janik, On the decomposition of hydrogen peroxide via the peroxocarbonic acid anion, *Technical Articles*, Technical Association of the Pulp and Paper Industry of Southern Africa/TAPPSA, http://www.tappsa.co.za/technical_articles.html, accessed (2009).

- [116] T. Wu, and J.D. Englehardt, A New Method for Removal of Hydrogen Peroxide Interference in the Analysis of Chemical Oxygen Demand, *Environ. Sci. Technol.* 46 (2012) 2291-2298.
- [117] F. Haber, and J. Weiss, The catalytic decomposition of hydrogen peroxide by iron salts, *Proc. R. Soc. London, Ser. A.* 147 (1934) 332-351.
- [118] A. Hiroki, and J.A. LaVerne, Decomposition of Hydrogen Peroxide at Water-Ceramic Oxide Interface, *J. Phys. Chem. B* 109 (2005) 3364-3370.
- [119] C.M. Lousada, A.J. Johansson, T. Brinck, and M. Jonsson, Mechanism of H₂O₂ Decomposition on Transition Metal Oxide Surfaces, *J. Phys. Chem. C* 116 (2012) 9533-9543.
- [120] C.M. Lousada, and M. Jonsson, Kinetics, Mechanism, and Activation Energy of H₂O₂ Decomposition on the Surface of ZrO₂, *J. Phys. Chem. C* 114 (2010) 11202-11208.
- [121] S.S. Lin, and M.D. Gurol, Catalytic decomposition of hydrogen peroxide on iron oxide: kinetics, mechanism and implications, *Environ. Sci. Technol.* 32 (1998) 1417-1423.
- [122] D. Fu, X. Zhang, P.G. Keech, D.W. Shoesmith, and J.C. Wren, An electrochemical study of H₂O₂ decomposition on single-phase γ -FeOOH films, *Electrochim. Acta* 55 (2010) 3787-3796.
- [123] M. Jonsson, E. Ekeröth, and O. Roth, Dissolution of UO₂ by one- and two-electron oxidants, *Mater. Res. Soc. Symp. Proc.* 807 (2004) 77.
- [124] S. Nilsson, and M. Jonsson, H₂O₂ and radiation induced dissolution of UO₂ and SIMFUEL pellets, *J. Nucl. Mater.* 410 (2011) 89-93.
- [125] H. Kleykamp, The chemical state of fission products in oxide fuels at different stages of the nuclear fuel cycle, *Nucl. Tech.* 80 (1988) 412-422.
- [126] H. Kleykamp, The chemical state of the fission products in oxide fuels, *J. Nucl. Mater.* 131 (1985) 221-246.
- [127] M.E. Broczkowski, P.G. Keech, J.J. Noël, and D.W. Shoesmith, Corrosion of Uranium Dioxide Containing Simulated Fission Products in Dilute Hydrogen Peroxide and Dissolved Hydrogen, *J. Electrochem. Soc.* 157 (2010) C275-C281.
- [128] S. Nilsson, and M. Jonsson, On the catalytic effects of Pd(s) on the reduction of UO₂²⁺ with H₂ in aqueous solution, *J. Nucl. Mater.* 374 (2008) 290-292.
- [129] D. Cui, J. Low, C.J. Sjustedt, and K. Spahiu, On Mo-Ru-Tc-Pd-Rh-Te alloy particles extracted from spent fuel and their leaching behavior under Ar and H₂ atmospheres, *Radiochim. Acta* 92 (2004) 551-555.
- [130] Gmelin Handbook of Inorganic Chemistry, Oxygen. Verlag Chemie, Weinheim. (1967) pp. 2353-2355

- [131] G. Bianchi, F. Mazza, and T. Mussini, Catalytic decomposition of acid hydrogen peroxide solutions on platinum, iridium, palladium and gold surfaces, *Electrochim. Acta* 7 (1962) 457-473.
- [132] E.L. Littauer, and K.C. Tsai, Catalytic Decomposition of Hydrogen Peroxide in Alkaline Solution, *J. Electrochem. Soc.* 126 (1979) 1924-1927.
- [133] N.A. Anastasijević, Z.M. Dimitrijević, and R.R. Adžić, Oxygen reduction on a ruthenium electrode in acid electrolytes, *Electrochim. Acta* 31 (1986) 1125-1130.
- [134] L. Gorton, A carbon electrode sputtered with palladium and gold for the amperometric detection of hydrogen peroxide, *Analytica Chimica Acta* 178 (1985) 247-253.
- [135] D.A. Johnston, M.F. Cardosi, and D.H. Vaughan, The Electrochemistry of Hydrogen Peroxide on Evaporated Gold/Palladium Composite Electrodes. Manufacture and Electrochemical Characterization, *Electroanalysis* 7 (1995) 520-526.
- [136] J.A. Cox, and R.K. Jaworski, Voltammetric reduction and determination of hydrogen peroxide at an electrode modified with a film containing palladium and iridium, *Anal. Chem.* 61 (1989) 2176-2178.
- [137] S.B. Hall, H. Kheyrandish, and A.L. Hart, Electrochemical oxidation of hydrogen peroxide at platinum electrodes - Part II effect of potential, *Electrochim. Acta* 43 (1998) 2015-2024.
- [138] J. McMurry, Reference Water Compositions for a Deep Geological Repository in the Canadian Shield, Report 06819-REP-01200-10135-R01, Ontario Power Generation, Toronto, ON, 2004.
- [139] I. Grenthe, D. Ferri, F. Salvatore, and G. Riccio, *J.Chem.Soc.Dalton Trans.* 11 (1984) 2439.
- [140] M. Hossain, E. Ekeröth, and M. Jonsson, Effects of HCO_3^- on the kinetics of UO_2 oxidation by H_2O_2 , *J. Nucl. Mater.* 358 (2006) 202-208.
- [141] J. de Pablo, I. Casas, J. Gimenez, V. Marti, and M.E. Torrero, Solid surface evolution model to predict uranium release from unirradiated UO_2 and nuclear spent fuel dissolution under oxidizing conditions, *J. Nucl. Mater.* 232 (1996) 138-145.
- [142] J. de Pablo, I. Casas, J. Gimenez, M. Molera, M. Rovira, L. Duro, and J. Bruno, The oxidative dissolution mechanism of uranium dioxide. I. The effect of temperature in hydrogen carbonate medium, *Geochim. Cosmochim. Acta* 63 (1999) 3097-3103.
- [143] S. Röllin, K. Spahiu, and U.B. Eklund, Determination of dissolution rates of spent fuel in carbonate solutions under different redox conditions with a flow-through experiment, *J. Nucl. Mater.* 297 (2001) 231-243.

- [144] P.G. Keech, J.S. Goldik, Z. Qin, and D.W. Shoesmith, The anodic dissolution of SIMFUEL (UO₂) in slightly alkaline sodium carbonate/bicarbonate solutions, *Electrochim. Acta* 56 (2011) 7923-7930.
- [145] E.H. Lee, J.K. Lim, D.Y. Chung, H.B. Yang, J.H. Yoo, and K.W. Kim, The oxidative-dissolution behaviors of fission products in a Na₂CO₃-H₂O₂ solution, *J. Radioanal. Nucl. Chem.* 281 (2009) 339-346.
- [146] S.M. Peper, L.F. Brodnax, S.E. Field, R.A. Zehnder, S.N. Valdez, and W.H. Runde, Kinetic Study of the Oxidative Dissolution of UO₂ in Aqueous Carbonate Media, *Ind. Eng. Chem. Res.* 43 (2004) 8188-8193.
- [147] G.S. Goff, L.F. Brodnax, M.R. Cisneros, S.M. Peper, S.E. Field, B.L. Scott, and W.H. Runde, First Identification and Thermodynamic Characterization of the Ternary U(VI) Species, UO₂(O₂)(CO₃)₂⁴⁻, in UO₂-H₂O₂-K₂CO₃ Solutions, *Inorg. Chem.* 47 (2008) 1984-1990.
- [148] M.E. Broczkowski, D. Zagidulin, and D.W. Shoesmith, The Role of Dissolved Hydrogen on the Corrosion/Dissolution of Spent Nuclear Fuel, in: "Nuclear Energy and the Environment", American Chemical Society Symposium, 2010, Vol.1046, Chapter 26, pp. 349-380
- [149] W.G. Barb, J.H. Boxendale, P. George, and K.R. Hargrove, Reactions of ferrous and ferric ions with hydrogen peroxide, Part II. The ferric ion reaction., *Trans. Faraday Soc.* 47 (1951) 591-616.
- [150] B. Voelker, and B. Sulzberger, Effects of fulvic acid on Fe(II) oxidation by hydrogen peroxide, *Environ. Sci. Technol.* 30 (1996) 1106.
- [151] R.G. Zepp, B.G. Faust, and J. Hoigne, Hydroxyl radical formation in aqueous reactions (pH 3-8) of iron(II) with hydrogen peroxide: The photo-Fenton reaction, *Environ. Sci. Technol.* 26 (1992) 313.
- [152] S. Stroes-Gascoyne, F. King, and J.S. Betteridge, The effects of alpha-radiolysis on UO₂ dissolution determined from preliminary electrochemical experiments with ²³⁸Pu-doped UO₂, Report 06819-REP-01300-10030-R00, Ontario Power Generation, Nuclear Waste Management Division, Toronto, Ontario, 20012.
- [153] M. Amme, W. Bors, C. Michel, K. Stettmaier, G. Rasmussen, and M. Betti, Effects of Fe(II) and Hydrogen Peroxide Interaction upon Dissolving UO₂ under Geologic Repository Conditions, *Environ. Sci. Technol.* 39 (2005) 221-229.
- [154] K. Ollila, Y. Albinsson, V.M. Oversby, and M. Cowper, Dissolution rates of unirradiated UO₂, UO₂ doped with ²³³U, and spent fuel under normal atmospheric conditions and under reducing conditions using an isotope dilution method, Report TR-03-13, Swedish Nuclear Fuel and Waste Management Co (SKB), Stockholm, Sweden, 2003.

- [155] K. Ollila, and V.M. Oversby, Dissolution of unirradiated UO_2 and UO_2 doped with ^{233}U under reducing conditions, Report TR-05-07, Swedish Nuclear Fuel and Waste Management Co (SKB), Stockholm, Sweden, 2005.
- [156] K. Ollila, Dissolution of Unirradiated UO_2 and UO_2 Doped with ^{233}U in 0.01 M NaCl under Anoxic and Reducing Conditions, Report POSIVA 2006-08, Posiva Oy, Olkiluoto, Finland, 2006.
- [157] A. Loida, B. Grambow, and H. Geckeis, Anoxic corrosion of various high burnup spent fuel samples, *J. Nucl. Mater.* 238 (1996) 11-22.
- [158] Y. Albinsson, A. Ödegaard-Jensen, V.M. Oversby, and L.O. Werme, Leaching of spent fuel under anaerobic and reducing conditions, in "Scientific basis for nuclear waste management XXVI", edited by R.J. Finch, and D.B. Bullen, Materials Research Society. (Materials Research Society Symposium Proceedings 757), Warrendale, PA, 2003, p. 407-413.
- [159] J. Quinones, J.A. Serrano, P. Diaz-Arocas, J.L. Rodriguez-Almazan, J. Cobos, J.A. Esteban, and M.-E. A., *Mat. Res. Soc. Symp. Proc.* 663 (2001) 435.
- [160] P. Carbol, J. Cobos-Sabate, J.-P. Glatz, C. Ronchi, V. Rondinella, D.H. Wegen, T. Wiss, A. Loida, V. Metz, B. Kienzler, K. Spahiu, B. Grambow, J. Quinones, and A. Martinez Esparza Valiente, The effect of dissolved hydrogen on the dissolution of ^{233}U -doped $\text{UO}_2(\text{s})$, high burn-up spent fuel and MOX fuel, Report TR-05-09, Swedish Nuclear Fuel and Waste Management Company, 2005.
- [161] M. Trummer, O. Roth, and M. Jonsson, H_2 inhibition of radiation induced dissolution of spent nuclear fuel, *J. Nuc. Mat.* 383 (2009) 226-230.
- [162] M.E. Broczkowski, J.J. Noël, and D.W. Shoesmith, The inhibiting effects of hydrogen on the corrosion of uranium dioxide under nuclear waste disposal conditions, *J. Nucl. Mater.* 346 (2005) 16-23.
- [163] M.E. Broczkowski, J.J. Noël, and D.W. Shoesmith, The influence of dissolved hydrogen on the surface composition of doped uranium dioxide under aqueous corrosion conditions, *J. of Electroanal. Chem.* 602 (2007) 8-16.
- [164] P. Carbol, P. Fors, S. Van Winckel, and K. Spahiu, Corrosion of irradiated MOX fuel in presence of dissolved H_2 , *J. Nucl. Mater.* 392 (2009) 45-54.
- [165] K. Spahiu, L.O. Werme, and U.B. Eklund, The influence of near field hydrogen on actinide solubilities and spent fuel leaching, *Radiochim. Acta* 88 (2000) 507-511.
- [166] K. Spahiu, D. Cui, and M. Lundström, The fate of radiolytic oxidants during spent fuel leaching in the presence of dissolved near field hydrogen, *Radiochim. Acta* 92 (2004) 625-629.
- [167] E. Cera, J. Bruno, L. Duro, and T.E. Eriksen, Experimental determination and chemical modelling of radiolytic processes at the spent fuel/water interface: Long contact

time experiments, Report TR-06-07, Swedish Nuclear Fuel and Waste Management Co (SKB), Stockholm, Sweden, 2006.

[168] T.E. Eriksen, and M. Jonsson, The effect of hydrogen on dissolution of spent fuel in $0.01 \text{ mol} \times \text{dm}^{-3} \text{ NaHCO}_3$ solution, Report TR-07-06, Swedish Nuclear Fuel and Waste Management Co (SKB), Stockholm, Sweden, 2007.

[169] T.E. Eriksen, M. Jonsson, and J. Merino, Modelling of time resolved and long contact time dissolution studies of spent nuclear fuel in 10 mM carbonate solution - a comparison between two different models and experimental data, *J. Nucl. Mater.* 375 (2008) 331-339.

[170] E. Ekeröth, M. Jonsson, T.E. Eriksen, K. Ljungqvist, S. Kovacs, and I. Puigdomenech, Reduction of UO_2^{2+} by H_2 , *J. Nucl. Mater.* 334 (2004) 35-39.

[171] S. Nilsson, and M. Jonsson, On the catalytic effects of $\text{UO}_2(\text{s})$ and $\text{Pd}(\text{s})$ on the reaction between H_2O_2 and H_2 in aqueous solution, *J. Nucl. Mater.* 372 (2008) 160-163.

[172] H. Christensen, S. Sunder, and D.W. Shoemith, Oxidation of nuclear fuel (UO_2) by the products of water radiolysis, development of a kinetic model, *J. Alloys Compd.* 213/214 (1994) 93-99.

[173] H. Christensen, Calculations Simulating Spent-Fuel Leaching Experiments, *Nucl. Tech.* 124 (1998) 165-174.

[174] F. King, and M. Kolar, The Mixed-Potential Model for UO_2 Dissolution, MPM Versions V1.3 and V1.4., Report No. 06819-REP-01200-10104-R00, Ontario Power Generation, 2003.

[175] M. Jonsson, F. Nielsen, O. Roth, E. Ekeröth, S. Nilsson, and M.M. Hossain, Radiation induced spent nuclear fuel dissolution under deep repository conditions, *Environmental Science & Technology* 41 (20) (2007) 7087-7093.

Chapter 2

EXPERIMENTAL TECHNIQUES AND DETAILS

In this chapter, the principles of the experimental techniques used in this project are briefly reviewed. Also included are the detailed descriptions of each type of experiment performed. For electrochemical experiments, however, more specific information on experimental parameters is provided in the individual experimental sections found in subsequent chapters.

2.1 Electrochemical experimental design

2.1.1 Electrochemical cell and equipment

All electrochemical measurements were performed in a standard three-electrode, three-compartment cell, as illustrated in Fig. 2.1. The cell contained one central chamber with two side arms separated from this main chamber by glass frits. A commercial saturated calomel reference electrode (SCE, Fisher Scientific) was placed in one side arm and connected to the central chamber of the cell by a Luggin capillary, the tip of which was located near the surface of working electrode. All potentials in this thesis were quoted on the SCE scale (+0.242 V vs. the standard hydrogen electrode). The counter electrode placed in the other side arm was a Pt sheet with a surface area of 6 cm² (99.9 % pure, Sigma-Aldrich), spot-welded to a Pt wire. A gas dispersion tube with a fritted end was inserted and used to de-aerate the solution. All experiments were conducted under an argon atmosphere at room temperature. The cell was placed in a grounded Faraday cage to minimize external noise. A Solartron model 1287 potentiostat was used to apply

potentials and record current responses. Corrware software (Scribner Associates) was used to control the potentiostat and analyze the data. An analytical rotator (Pine Instruments, model ASR) was employed when necessary to control the rotation rate of the working electrode.

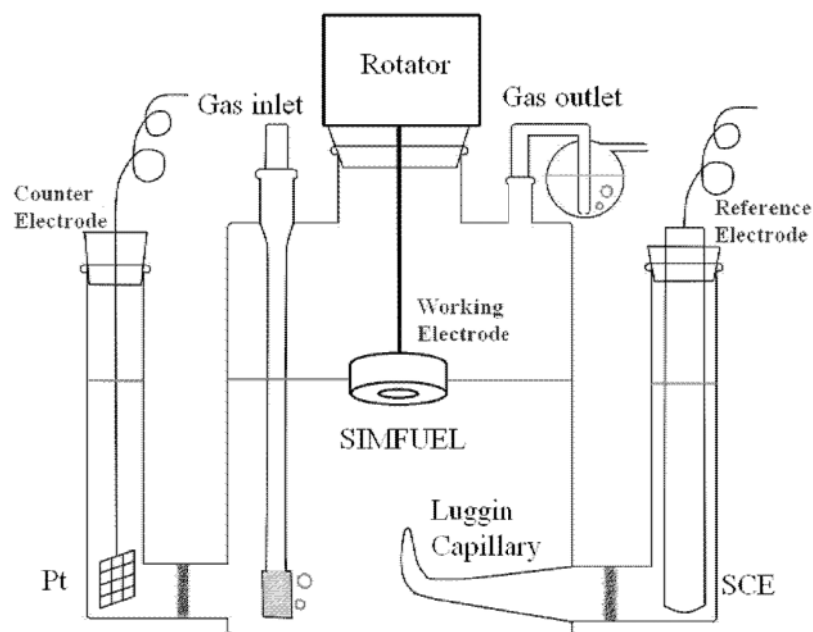


Fig. 2.1. Diagram of the electrochemical cell setup.

2.1.2 Solutions

All solutions were prepared using deionized water with a resistance of $18.2 \text{ M}\Omega \text{ cm}$ purified by a Millipore milli-Q-plus unit. The electrolyte was $0.1 \text{ mol L}^{-1} \text{ NaCl}$, and the solution pH was adjusted to the desired value, between 9.5 and 12.6, with NaOH (Caledon Chemical). An Orion model 250A+ pH meter and Orion 91-07 Triode pH/ATC probe were used to monitor the pH before and after electrochemical measurements. To prevent interfering cathodic reactions, such as oxygen reduction, all solutions were de-

aerated with argon (ultra-high purity, Praxair) for at least 30 minutes prior to experimentation, and purging was continued throughout each experiment.

2.1.3 SIMFUEL working electrode

The working electrodes were cut from simulated spent fuel pellets (SIMFUEL) fabricated by Atomic Energy of Canada Limited (Chalk River, Ontario). SIMFUEL is analogue of CANDU spent nuclear fuel made of natural UO_2 doped with nonradioactive fission products to replicate the chemical effects of in-reactor burnup [1]. SIMFUEL is useful for laboratory experiments, since it simulates key fuel properties without the associated radiation levels. Doping elements include up to 11 non-radioactive elements (Ba, Sr, Y, Ce, Nd, La, Zr, Mo, Pd, Rh, Ru), which can be divided into two groups (i) rare earth elements which dissolve in UO_2 matrix and significantly increase the conductivity; and (ii) noble metal particles which congregate in alloy precipitates, referred to as ϵ -particles. SIMFUEL has been extensively characterized by analytical techniques such as XRD, SEM, EDX, TEM, XPS, and ICP-AES [1-3]. The microstructure of SIMFUEL is virtually identical to that of typical CANDU fuel pellets, with grain sizes of the order 8-15 μm and a density greater than 95% of the theoretical value. Small, spherical (0.5-1.5 μm in diameter) noble metal particles are dispersed uniformly throughout the matrix with an average composition of 42-Ru/33-Mo/21-Pd/3-Rh. Perovskite (Ba, Sr) ZrO_3 phases ($\sim 0.1 \mu\text{m}$) are also present on grain boundaries, and the additives Y, Ce, Nd, La and Zr are dissolved in the UO_2 grains. The SIMFUEL used in this study replicates spent nuclear fuel with a 1.5 at.% or a 3 at.% burnup. To investigate the effects of different fission products, two types of SIMFUEL electrodes were used, one containing only rare earth elements and the other rare earth elements plus ϵ -particles.

As received, the SIMFUEL specimens are pellets ~ 20 mm long and 11.9 mm in diameter. To prevent cracking of this fragile ceramic material during cutting, the pellet was first mounted in a transparent epoxy (BUEHLER SAMPL-KWICK No.20-3562 powder and No. 20-3564 liquid), mixed in a ratio of 2:1 solid : liquid by volume, as a protection. Then the mounted pellet was cut into disks of 2-3 mm thickness, and the transparent epoxy was removed afterwards. A thin layer of copper was electroplated onto one side of each disk to facilitate electrical contact to an external measuring device. The Cu-plating procedure is illustrated in Fig. 2.2. The surface of the SIMFUEL disk was first polished with 600 grit paper and rinsed with deionized water, to generate a rough surface for good Cu adhesion. The disk was then secured into the end of a piece of rubber tubing and placed in a 0.1 mol L^{-1} CuSO_4 solution, with a piece of polished Cu metal as the counter electrode. Electronic grade mercury was poured into the tubing, and then a stainless steel wire was placed in the tubing, to facilitate electrical contact between the UO_2 sample and the power supply. A 10 mA current was applied for 20 minutes using a DC power supply (GPR-30H10D) to produce a thin and even distribution of copper on the SIMFUEL surface.

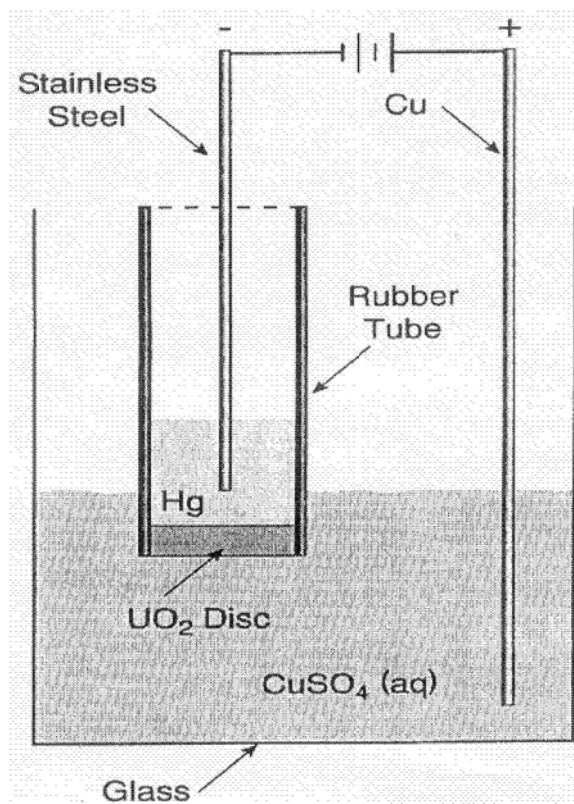


Fig. 2.2 Schematic illustration of the experimental arrangement used to electroplate copper onto one face of SIMFUEL disk electrodes.

A small round steel disk (~ 4 mm thick, 10 mm in diameter) was glued to the backside of each SIMFUEL disk with conducting silver epoxy (MG Chemicals 8331), and attached to a threaded steel shaft. Each electrode was then set in a sealing resin (Hysol EE 4183 and HD 3561) so that only one circular face of the electrode would be exposed to solution.

Fig. 2.3 shows a digital image of the electrode face that would be exposed to solution.

Prior to the start of each experiment, the electrode was polished with 600 grit, and then 1200 grit, SiC paper and rinsed with deaerated distilled deionized water.

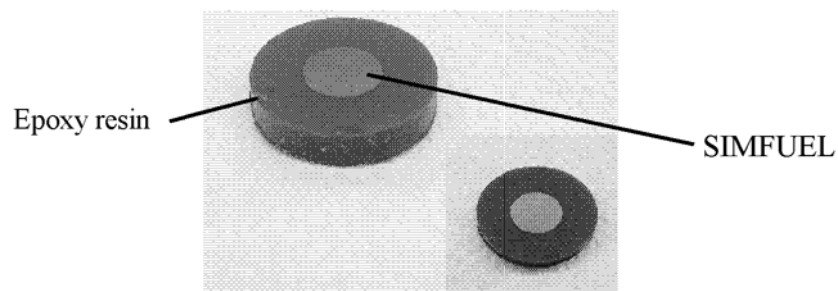


Fig. 2.3 Digital image of a SIMFUEL working electrode (photos courtesy of Dr. M. Razdan).

2.1.4 Cyclic voltammetry (CV) and cathodic stripping voltammetry (CSV)

Cyclic voltammograms allow the general electrochemical reactivity of a system to be examined. The potential profile for a typical CV experiment is shown in Fig. 2.4. The potential is scanned at a constant rate, from a negative limit (E_c) to a positive limit (E_a) in the forward scan, and then back to E_c in the reverse scan, and the current recorded and plotted as a function of potential. During CV scans, oxidative processes appear as positive currents, while reduction processes appear as negative currents.

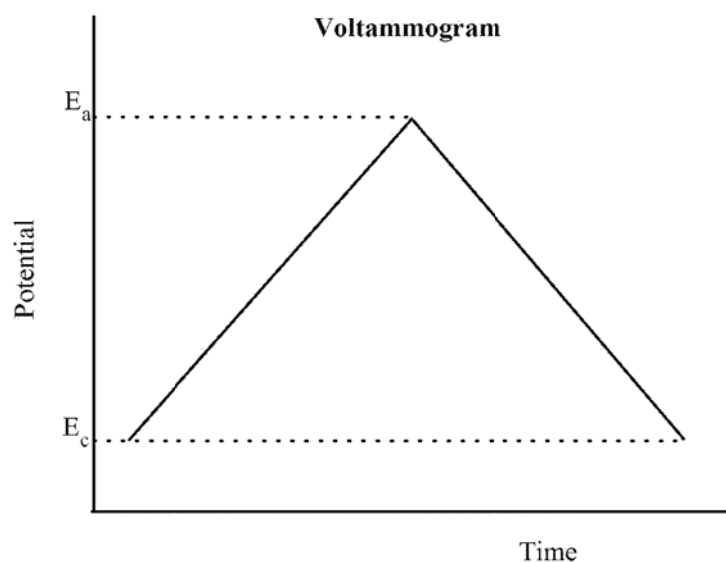


Fig. 2.4. Potential-time profile for a cyclic voltammogram in which the potential is scanned from E_c to E_a , and then back to E_c .

A cathodic stripping voltammogram (CSV) can be used to determine the consequences of a period of oxidation (at a known applied potential, $E_{App'd}$) or open circuit corrosion (which occurs at the corrosion potential, E_{CORR}), Fig. 2.5. By scanning the potential from $E_{App'd}$ or E_{CORR} back to the negative limit and recording the reduction current as a function of potential, the extent of oxidation can be determined, provided that it leads to reducible surface films or deposits. The features of the stripping currents can provide information on the nature and stability of the surface films formed.

The charge, Q , measured on the forward and reverse scans can be used to determine the extent of oxidation and reduction, respectively, using the equation

$$Q = mnF \quad (2.1)$$

where m is the number of moles of the starting material oxidized, n the number of electrons involved in an electrochemical reaction and F the Faraday constant. Q can be determined by integration of the measured current as a function of time. The charge obtained is indicative of the amount of reduction or oxidation that occurred within a specific potential interval.

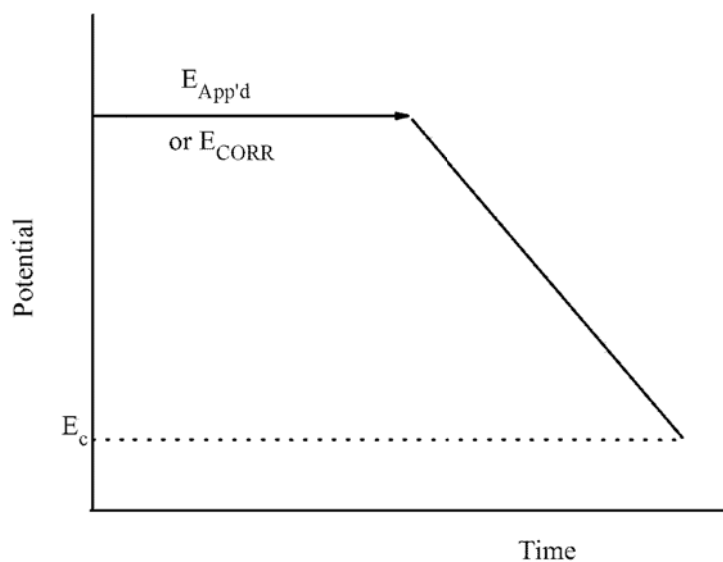


Fig. 2.5. Potential-time profile for a typical cathodic stripping voltammogram when the potential is scanned from $E_{App'd}$ or E_{CORR} to E_c .

2.1.5 Linear polarization resistance measurements

Linear polarization resistance is an electrochemical technique that can measure the instantaneous polarization resistance (R_p). A small potential perturbation in the range of ± 10 mV at a constant scan rate starts below and terminates above E_{CORR} . The slope of

the resulting linear current-potential relationship around E_{CORR} yields the R_p (in the absence of ohmic resistances such as the solution resistance), Fig. 2.6, which is inversely related to the uniform corrosion rate.

$$R_p = \left(\frac{\Delta E}{\Delta i} \right)_{\Delta E \rightarrow 0} \quad (2.2)$$

The current-potential relationship plotted in Fig. 2.6 is the sum of the currents from the two opposing (anodic and cathodic) reactions. For potentials close to E_{CORR} the exponential relationships can be linearized. A high R_p value implies a high corrosion resistance and vice versa.

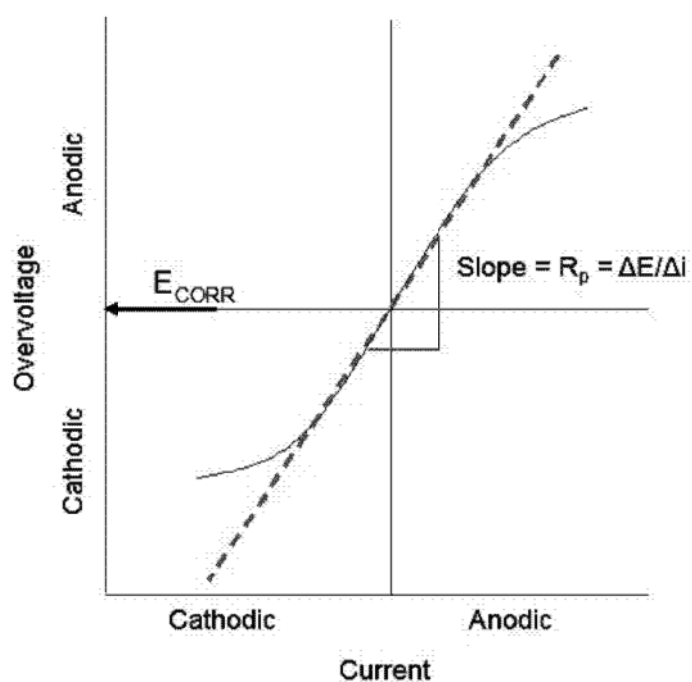


Fig. 2.6. Schematic of a linear polarization curve showing the linear potential used to measure the polarization resistance.

2.1.6 Electrochemical impedance spectroscopy (EIS)

The corrosion rate of UO_2 in aqueous system is determined by the properties of the surface oxide film, e.g., coverage, structure, composition, stability, porosity, thickness, conductivity, and chemistry within pores/pits. It is difficult to fully characterize these variables, especially when they evolve slowly with time as the corrosion product deposit develops. In addition, the UO_2 surface in its reduced state (U^{IV}) is sensitive to air (oxygen), thus an *in-situ* evaluation is favored. A useful method for the investigation in this project is electrochemical impedance spectroscopy (EIS). EIS is a transient technique which requires the system to be at steady-state to make meaningful measurements. It is used to probe the electrical properties of, or the charge-transfer processes occurring at, an interface or corrosion deposit by modelling such a system.

In this technique, a small sinusoidal input potential (± 10 mV), enough to perturb the electrochemical interface without driving the system far from its steady-state value, is applied and the resulting sinusoidal current measured. A wide range of frequencies (typically 10^6 to 10^{-3} Hz) are scanned in EIS measurements. The output signals allow the determination of the electrical properties of the system by assigning physical significance to circuit elements (i.e., resistors and capacitors) that are used to simulate the interface properties. Since numerous equivalent circuit models can be used to fit EIS data, a well defined physical understanding of the system is necessary prior to selecting a circuit.

One example is presented here to illustrate the method. The presence of the electrochemical double layer (due to charged species and water dipoles at the surface [4]) will result in a chargeable interface. The double layer exhibits a capacitance, due to the

charging and discharging of the surface and the resulting redistribution of ions in the solution in response to the sinusoidal input potential. During corrosion charge transfer between the sample surface and the solution creates a current leakage pathway across the double layer capacitor allowing electron or ion transfer to take place across the interface. This process would exhibit a resistance in parallel with the capacitor representing the double layer. A system with both resistive and capacitive attributes can be described as having a time constant (τ), which is the product of the measured resistance (R) and the capacitance (C).

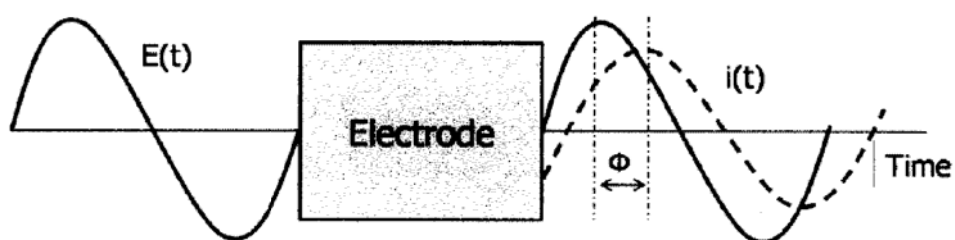


Fig. 2.7. Schematic showing the input AC voltage perturbation applied in an EIS measurement, and the resulting AC current response.

For this system, the current response to the applied sinusoidal potential generates a sinusoidal curve which may be shifted in phase, as shown in Fig. 2.7. The applied potential, $E(\omega)$, is related to the current response by the AC equivalent of Ohm's law expressed as a function of time,

$$E(\omega) = i(\omega) Z(\omega) \quad (2.3)$$

In this equation, ω is the angular frequency and Z is the impedance, a transfer function that relates the input perturbation to the output response of the system as a function of ω . Experimentally, the small amplitude input is an alternating potential given by

$$\Delta E = |\Delta E| \exp(j\omega t) \quad (2.4)$$

where, j is the imaginary unit (i.e., $j^2 = -1$) and t is time. The measured current response is given by

$$\Delta i = |\Delta i| \exp(j[\omega t + \phi]) \quad (2.5)$$

where ϕ is the phase difference between the potential input and the response. The input signal is applied for a series of frequencies, and at each frequency the fundamental response of the cell to the applied voltage is measured in terms of the impedance modulus, $|Z|$, and the phase angle, ϕ . The impedance includes both a real (in-phase) and an imaginary (out of phase) component.

$$Z(\omega) = \frac{\Delta E \exp(j\omega t)}{\Delta i \exp(j[\omega t + \phi])} = Z_{\text{real}} + jZ_{\text{imaginary}} \quad (2.6)$$

The phase angle expresses the relative contributions of capacitive and resistive elements in the circuit. For a pure resistance, $\phi = 0^\circ$, and for a pure capacitance, $\phi = -90^\circ$.

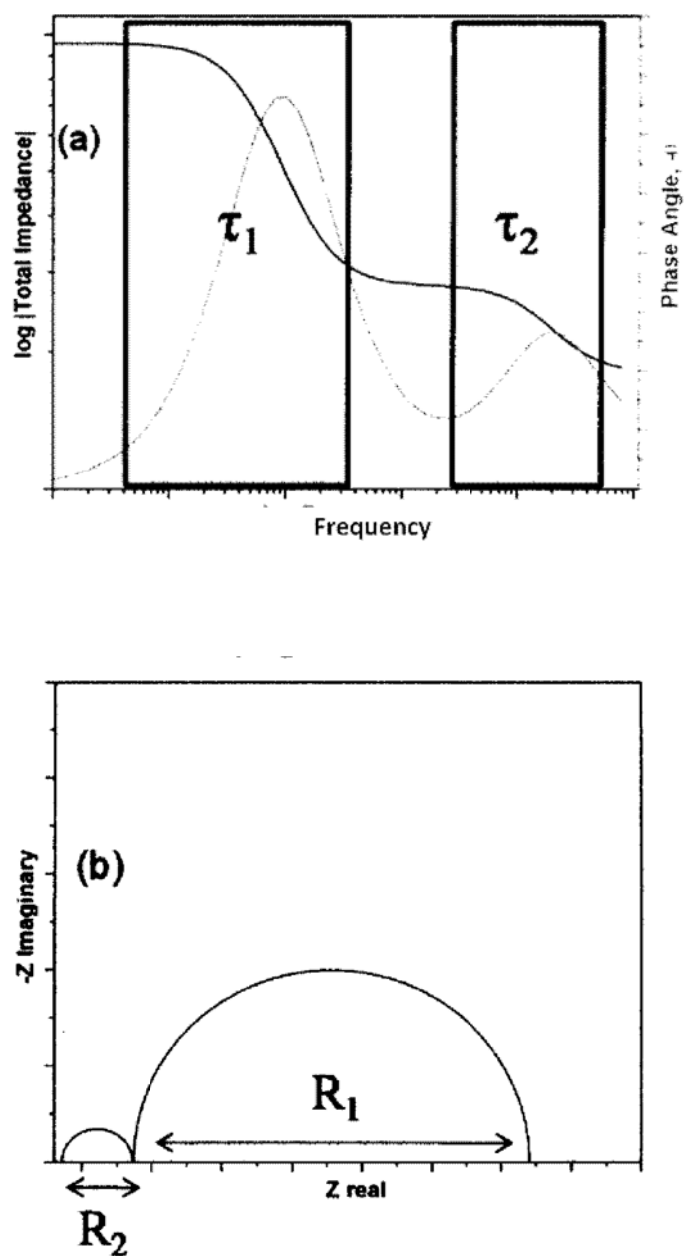


Fig. 2.8. (a) Bode and (b) Nyquist plots for a two time constant equivalent circuit.

Intermediate phase angles are observed when both resistance and capacitance contribute

to the overall impedance.

The corroding interface is complicated and, as such, its response to the input potential changes considerably with frequency, f ($\omega = 2\pi f$). In practice, the response of the system is monitored as a function of frequency and may be plotted as $\log|Z|$ and φ vs. $\log f$ Bode plots, as in Fig. 2.8(a). Individual circuit responses (time constants) are ideally shown as plateaus in the $\log|Z|$ vs. $\log f$ plot and as peaks in the φ vs. $\log f$ plot, although such a clear separation between each time constants is not often observed. EIS spectra can also be represented on a Nyquist plot, which is a plot of Z_{real} vs. $Z_{\text{imaginary}}$, Fig. 2.8(b). Qualitatively, while the Bode plots allow the impedance response over the whole frequency range to be observed, the Nyquist plot highlights the low frequency region, R1 in Fig. 2.8(b). The spectra are then modeled using an equivalent circuit, as shown in Fig. 2.9.



Fig. 2.9. Typical equivalent electrical circuit that can be used to fit a two time constant EIS spectrum.

Resistors are used to represent processes such as resistance to ionic migration within a surface film (R_{im}), and the resistance associated with charge passed at the oxide/solution interface (R_{ox}). The charge transfer resistance (R_{CT}), is inversely proportional to the rate of charge transfer at the sample/film interface. The sum of $R_{\text{im}} + R_{\text{ox}} + R_{\text{CT}}$ represents the

polarization resistance, R_p , which is ideally the same as the value determined by the LPR method. R_s is related to the conductivity of the solution and electrode etc. The capacitive response of a real electrode may not always be ideal. One common problem in corrosion is that the capacitance may not be independent of the input potential frequency. To accommodate this non-ideality, the capacitor is commonly replaced by a constant phase element (CPE) in the equivalent circuit in order to improve the quality of the fit, and hopefully to better understand the system by providing means to extract useful characteristic parameters [4, 5].

2.2 X-ray photoelectron spectroscopy (XPS)

2.2.1 Basic principles of XPS

X-ray photoelectron spectroscopy (XPS) is a surface sensitive technique, which can provide atomic and molecular information about the outer 3 to 10 nm of the surface of various materials [6, 7]. This technique was used in this project to obtain quantitative data on film composition and the chemical nature of several elements at SIMFUEL surfaces after electrochemical procedures. XPS is based on the phenomenon of photoionization (the photoelectric effect). The sample surface is irradiated with low energy X-rays and photoelectrons are ejected from core and valence levels of the atoms in the surface after direct energy transfer, Fig. 2.10.

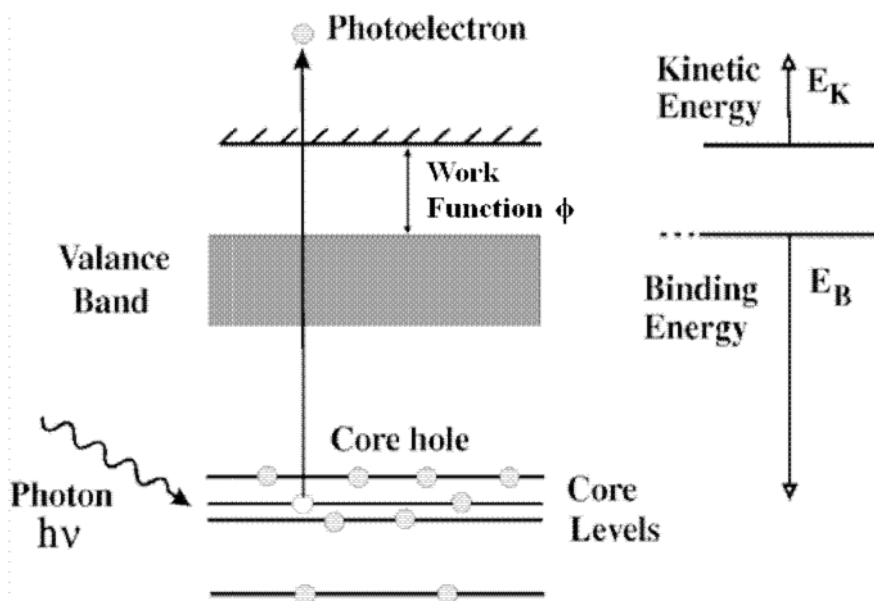


Fig. 2.10. Schematic representation of the excitation of a core level electron, and subsequent photoelectron generation in XPS. Image source: Ref [8].

The kinetic energy of the photoelectron (E_K) is the difference between the energy of the X-ray ($h\nu$) and the binding energy of the electron (E_B) plus the work function (ϕ).

$$E_K = h\nu - (E_B + \phi) \quad (2.7)$$

where the work function is the combination of the work function induced by the analyzer and the sample work function. Since electrons escaping from a sample have a low inelastic mean-free path, λ_m , XPS can be considered to be a surface sensitive technique, with most photoelectrons escaping from a depth of between 0.5 and 3.0 nm [9]. Due to collisions within the sample's atomic structure, those photoelectrons originating from

more than $\sim 3-10$ nm are unable to escape from the surface with sufficient energy to be detected.

A characteristic spectrum generated by XPS plots the measured photoelectron intensity as a function of E_B . For every element, there is a characteristic binding energy associated with each core atomic orbital; i.e. each element will give rise to a characteristic set of peaks in the photoelectron spectrum at kinetic energies determined by the photon energy and the respective binding energies. The intensity of the peaks is related to the concentration of that element within the analyzed region. Another valuable feature of XPS is its ability to distinguish between different oxidation states and chemical environments. The precise binding energy of an electron depends not only upon the energy level from which photoemission occurs, but also upon the oxidation state of the atom and the local environment. These subtle differences of energy levels appear as small shifts in the peak positions in the binding energy scale (chemical shifts). Distinct chemical states can be determined by obtaining high-resolution spectra and using peak fitting programs to deconvolute the spectra and give the percent composition of each state. In addition to the main peaks in photoelectron intensity, corresponding to the ground state after photoexcitation, there are a number of satellite peaks representing excited states. A satellite will be observed if more than one final state can be reached in the photoelectron process [10]. The position and shape of the satellite structure are used to confirm the change in oxidation state of the element by changes in the intensity, position and structure of the satellite peaks.

2.2.2 XPS experimental details

The spectrum collection was performed on a Kratos Axis NOVA spectrometer using a monochromatic Al K_{α} (1486.6 eV) source. The instrument work function was calibrated to give a binding energy of 83.96 eV for the Au $4f_{7/2}$ line for metallic gold and the spectrometer dispersion was adjusted to give a binding energy of 932.62 eV for the Cu $2p_{3/2}$ line of metallic copper. Survey scan analyses were carried out for the energy range 0-1100 eV, with an analysis area of $300 \times 700 \mu\text{m}^2$ and a pass energy of 160 eV. High resolution analyses were carried out with an analysis area of $300 \times 700 \mu\text{m}^2$ and a pass energy of 20 eV. Spectra have been charge-corrected to the main line of the C 1s spectrum (adventitious carbon) set to 285.0 eV. Spectra were analyzed using CasaXPS software (version 2.3.14).

High-resolution scans were performed for the U 4f region, covering the U $4f_{5/2}$ and U $4f_{7/2}$ peaks and their satellites, and for the U 5f valence band region. The U 4f spectra, including both the primary peaks (U $4f_{7/2}$ and U $4f_{5/2}$) and the satellite structures, were resolved into contributions from U^{IV}, U^V, and U^{VI}. The fractions of uranium oxidation states on the electrode surface were determined by the fitting results. The structure of the valence band region was used to check the validity of the fit. All high-resolution spectra were deconvoluted using a Shirley background correction [11]. Gaussian-Lorentzian peak shapes were used: 50% Lorentzian for the main $4f_{7/2}$ and $4f_{5/2}$ peaks and 30% Lorentzian for the satellite peaks.

The fitting procedures were based on reference spectra provided in the literature [10, 12-16]. The U 4f spectrum is characterized by two main peaks, U $4f_{7/2}$ and U $4f_{5/2}$, located at ~ 380 eV and ~ 391 eV. The spin-orbital interaction separates U $4f_{7/2}$ and U $4f_{5/2}$ peaks by around 10.9 eV. The area ratio of the U $4f_{5/2}$ to U $4f_{7/2}$ peaks is typically ~ 0.75 .

Previously reported binding energies for U^{IV} , U^V , and U^{VI} in the $U 4f_{7/2}$ peak of mixed-valent U-compounds vary with the chemical composition of the compounds examined [10]. For instance, the position of the U^{IV} peak varies in the literature between 379.5 eV [13] and 380.3 eV [16]. However, separations between the bands are relatively consistent in literature, i.e., 0.5-0.9 eV between U^{IV} and U^V and 0.8-1.1 eV between U^V and U^{VI} [10, 12-16]. The satellite peaks associated with the U^{IV} , U^V , and U^{VI} components of the $U 4f_{7/2}$ and the $U 4f_{5/2}$ peaks are also characteristic of the U4f spectrum. As the oxidation state of uranium increases, the intensity, position, and structure of these satellites change diagnostically. The distance between the main peak and the satellite peak is relatively consistent in literature: 6-7 eV for U^{IV} , 8-9 eV for U^V and 4 eV and 10 eV for U^{VI} [10, 12-16]. The position and shape of the satellite structure were also deconvoluted together with the main peaks.

The behaviour in the valence band region was used to check the validity of the fit. The valence band region is a narrow band around 1 eV, due to the two electrons present in the U 5f valence shell. As the surface becomes more oxidized, the intensity of the U 5f peak at ~ 1 eV diminishes in comparison to the peak at ~ 5.5 eV associated with U-O bonding [14, 17]. This provides evidence of surface oxidation since the removal of the valence electrons results in a decrease in peak intensity.

2.3 Scanning electron microscopy (SEM)

2.3.1 Basic principles of SEM

A Scanning Electron Microscope (SEM) uses electrons rather than light to form an image. It can be equipped with multiple detectors to investigate additional chemical

characteristics as well. SEM was primarily used in this project to investigate surface morphologies.

The resolution of microscopy techniques is limited by the wavelength of the employed light/particle. SEM can attain a high resolution, ~ 1 nm, by probing the surface with a beam of high energy electrons, in comparison with ~ 350 nm of optical microscopy (wavelength of blue light). The sample surface must be electrically conducting, otherwise the electron beam will charge up the surface. SEM must be carried out under a high vacuum ($\leq 10^{-6}$ Torr) to minimize interference from the molecules in air. High resolution images of surface topography, with excellent depth of field, are produced using a highly-focused, scanning (primary) electron beam. The electrons are generated by thermionic emission from a metal filament, and accelerated to 0.5-30 keV. The target surface then emits many low energy (< 50 eV) secondary electrons [18]. The intensity of these secondary electrons is mainly governed by the surface topography of the sample, and they can leave the surface if their energy is greater than the work function of 2-6 eV. An image of the sample surface can thus be constructed by measuring secondary electron intensity as a function of the position of the scanning primary electron beam. A system of electrical and magnetic field “optics” is used to focus the beam to a spot < 10 nm in diameter on the sample surface. The electron beam is scanned across the sample via magnetic scan coils. The current of electrons reflected from the surface is collected, amplified, and plotted as a two-dimensional micrograph image of the signal intensity.

2.3.2 SEM experimental details

SEM was used to image the electrode surfaces before and after electrochemical procedures. A Hitachi S-4500 (Hitachi, Japan) field emission SEM was used at an electron acceleration voltage of 15 kV. Micrographs were recorded at various magnifications (100 – 5000X).

2.4 Inductively coupled plasma atomic emission spectroscopy (ICP-AES)

2.4.1 Basic principles of ICP-AES

Inductively coupled plasma atomic emission spectroscopy (ICP-AES) is an analytical technique for the determination of trace element concentrations. In the measurement, a solution sample is introduced into an argon plasma and generates excited atoms and ions that emit photons at wavelengths that are characteristic for specific elements. The intensity of the signal is indicative of the concentration of the involved element according to a calibration curve created from solutions of known concentrations.

An illustration of the components within an ICP-AES instrument is shown in Fig. 2.11. The ICP torch is made of three concentric quartz tubes through which argon gas flows. A Tesla unit creates a brief discharge arc through the argon flow to initiate the ionization process. A radio frequency generator produces an intense electromagnetic field, causing the ions to flow in a circular path. A high temperature plasma is generated as a result of the inelastic collisions between the neutral argon atoms and the charged particles. An aqueous sample is then pumped into the plasma flame as an aerosol produced by a nebulizer. Various molecules in the sample break up into atoms which then lose electrons and recombine with electrons repeatedly in the plasma. Each element gives off photons of characteristic wavelengths. Within the optical chamber, the intensities of light

at all visible wavelengths can be measured simultaneously by photodetectors, allowing the instrument to quickly analyze multiple elements.

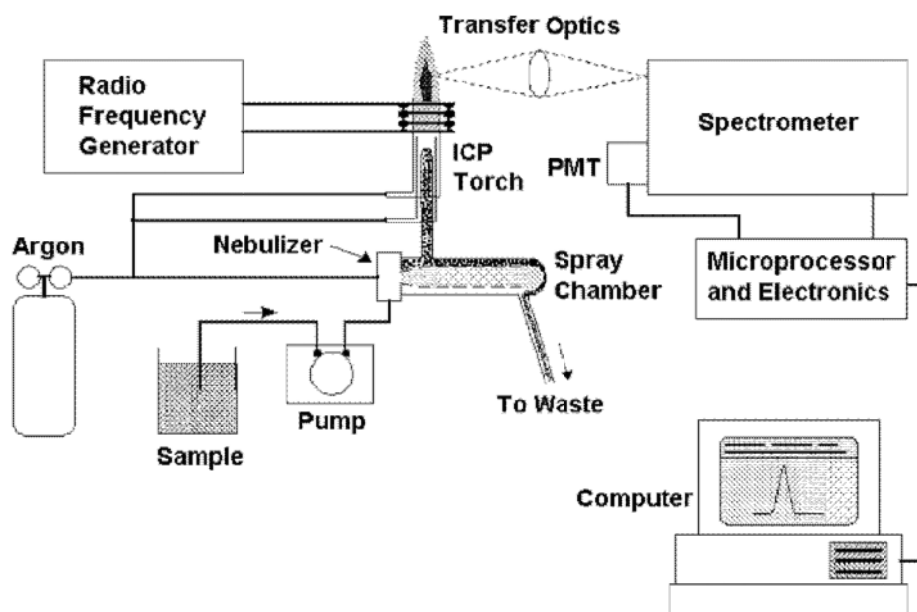


Fig. 2.11. Diagram for major components of a typical ICP-AES instrument. Source: Ref [19].

2.4.2 ICP-AES experimental details

In this project, the Perkin Elmer Optima 3300 Dual 24 View ICP-AES at the Biotron (Western University) was used. The uranium emission was monitored at a wavelength of 419 nm, which has few interfering emissions from other components. The lower detection limit of uranium was 0.01 mg/L. To avoid uranium precipitation, the samples were treated with nitric acid before injection. The calibration standards used in measurements ranged from 0.50 to 1.0 mg/L uranium and a 2% nitric acid solution was used as a blank sample.

2.5 Instrument acknowledgements

Surface Science Western supplied the Kratos Axis NOVA spectrometer used for XPS analyses and the Hitachi S-4500 field emission SEM. The author thanks Dr. Mark Biesinger for the help with XPS, Ms. Heather Bloomfield for the help with SEM, and Dr. Charlie Wu for conducting ICP-AES analysis in Biotron.

2.6 References

- [1] P.G. Lucuta, R.A. Verrall, H.-J. Matzke, and B.J.F. Palmer, Microstructural features of SIMFUEL - Simulated high-burnup UO₂-based nuclear fuel, *J. Nucl. Mater.* 178 (1991) 48-60.
- [2] S. Sunder, N.H. Miller, W.H. Hocking, and P.G. Lucuta, X-ray photoelectron spectra of SIMFUEL, *J. Alloys Compd.* 213/214 (1994) 503-505.
- [3] S. Sunder, D.W. Shoesmith, and N.H. Miller, Electrochemical Studies of Corrosion of SIMFUEL: Simulated Used UO₂ Fuel, *Mat. Res. Soc. Symp. Proc.* 294 (1993) 35-40.
- [4] A.J. Bard, and L.R. Faulkner, *Electrochemical Methods: Fundamentals and Applications*, 2nd ed., John Wiley & Sons, New York, NY, 2001.
- [5] W.H. Mulder, and J.H. Sluyters, Tafel current at fractal electrodes: Connection with admittance spectra, *J. Electroanal. Chem., Interfacial Electrochem.* 285 (1990) 103-115.
- [6] D. Briggs, and M.P. Seah, *Practical Surface Analysis by Auger and Photoelectron Spectroscopy*, John Wiley & Sons, Toronto, ON, 1983.
- [7] W.M. Riggs, and M.J. Parker, in "Methods of Surface Analysis", edited by A.W. Czanderna, Elsevier, New York, 1975, Chapter 4.
- [8] H.R. Verma, *Atomic and Nuclear Analytical Methods*, Springer, New York, 2007.
- [9] M.P. Seah, and W.A. Dench, Quantitative electron spectroscopy of surfaces: A standard data base for electron inelastic mean free paths in solids, *Surface and Interface Analysis* 1 (1979) 2.
- [10] M. Schindler, F.C. Hawthorne, M.S. Freund, and P.C. Burns, XPS spectra of uranyl minerals and synthetic uranyl compounds. I: The U 4f spectrum, *Geochim. Cosmochim. Acta* 73 (2009) 2471-2487.

- [11] D.A. Shirley, High-Resolution X-Ray Photoemission Spectrum of the Valence Bands of Gold, *Phys. Rev. B* 5 (1972) 4709.
- [12] B.G. Santos, H.W. Nesbitt, J.J. Noël, and D.W. Shoesmith, X-ray photoelectron spectroscopy study of anodically oxidized SIMFUEL surfaces, *Electrochim. Acta* 49 (2004) 1863-1873.
- [13] S. Van den Berghe, J.-P. Laval, B. Gaudreau, H. Terry, and M. Verwerft, XPS investigations on cesium uranates: mixed valency behaviour of uranium, *J. Nucl. Mater.* 277 (2000) 28-36.
- [14] E.S. Ilton, J.-F. Boily, and P.S. Bagus, Beam induced reduction of U(VI) during X-ray photoelectron spectroscopy: The utility of the U4f satellite structure for identifying uranium oxidation states in mixed valence uranium oxides, *Surface Science* 601 (2007) 908-916.
- [15] M. Razdan, Electrochemical and Surface Compositional Studies on UO₂ Corrosion Under Nuclear Waste Disposal Conditions, PhD Thesis, Western University, London, ON, 2013.
- [16] E.S. Ilton, A. Haiduc, C.L. Cahill, and A.R. Felmy, Mica Surfaces Stabilize Pentavalent Uranium, *Inorg. Chem.* 44 (2005) 2986-2988.
- [17] F. Mercier-Bion, R. Drot, J.J. Ehrhardt, J. Lambert, and E. Simoni, X-ray photoreduction of U(VI)-bearing compounds, *Surf. Interface Anal.* 43 (2011) 777-783.
- [18] P.E.J. Flewitt, and R.K. Wild, Physical Methods for Materials Characterisation, Chapter 6, IOP Publishing, Bristol, 1994.
- [19] C.B. Boss, and K.J. Fredeen, Concepts, Instrumentation, and Techniques in Inductively Coupled Plasma Optical Emission Spectroscopy, 2nd ed., Perkin-Elmer, 1997.

Chapter 3

A MODEL FOR THE INFLUENCE OF STEEL CORROSION PRODUCTS ON NUCLEAR FUEL CORROSION UNDER PERMANENT DISPOSAL CONDITIONS¹

3.1 Introduction

The development of source-term models to describe the processes involved in spent fuel dissolution has been the focus of considerable international effort [1-4]. In this chapter, a preliminary model is developed to examine the α -radiolytic corrosion of spent nuclear fuel inside a failed waste container. This model incorporates the key features revealed from literatures (Section 1.5.5) and the recently available kinetics data and mechanisms. The present chapter focuses on the evaluation of different model setups (e.g., radiation dose profile) and the sensitivity tests of different parameters (e.g., the thickness of diffusion layer). Calculations are performed to assess the influence of steel corrosion products on fuel corrosion rate.

3.2 Model description

As stated in Section 1.2, two corrosion fronts exist within the failed container: one on the fuel surface driven by radiolytic oxidants, and a second one on the steel vessel surface sustained by water reduction and producing the potential redox scavengers, Fe^{2+} and H_2 . The chemical properties of the fuel and the changes induced by in-reactor irradiation have been discussed in Section 1.4.2. From the corrosion perspective the fuel can be considered as a conductive and reactive matrix containing noble metal (ϵ) particles which

¹ A version of Chapter 3 has been published: L. Wu, Y. Beaugard, Z. Qin, S. Rohani, and D.W. Shoesmith, A model for the influence of steel corrosion products on nuclear fuel corrosion under permanent disposal conditions, *Corrosion Science* 61 (2012) 83-91.

could act as either cathodes or anodes depending on the prevailing solution redox conditions. A complex series of homogeneous solution and heterogeneous surface reactions will have a very significant influence on the redox conditions inside the failed container and, hence, on the fuel corrosion/radionuclide release process [5-7]. At its present stage of development the model is one dimensional and presumes the fuel surface is uniform. The rates of the various processes in the model are described by a series of one dimensional diffusion-reaction equations,

$$\frac{\partial c_i(x,t)}{\partial t} = D_i \frac{\partial^2 c_i(x,t)}{\partial x^2} + \sum_k R_k(i) \quad (3.1)$$

where $c_i(x,t)$ is the concentration of species i at point x and time t , D_i is the diffusion coefficient of species i , and $R_k(i)$ is the reaction rate of species i in reaction k . If i is a product in the reaction k , $R > 0$; on the other hand, if i is a reactant, $R < 0$. At steady state, Equation (3.1) reduces to

$$D_i \frac{\partial^2 c_i(x)}{\partial x^2} = -\sum_k R_k(i) \quad (3.2)$$

suggesting a balance between the diffusion and reaction processes at steady state.

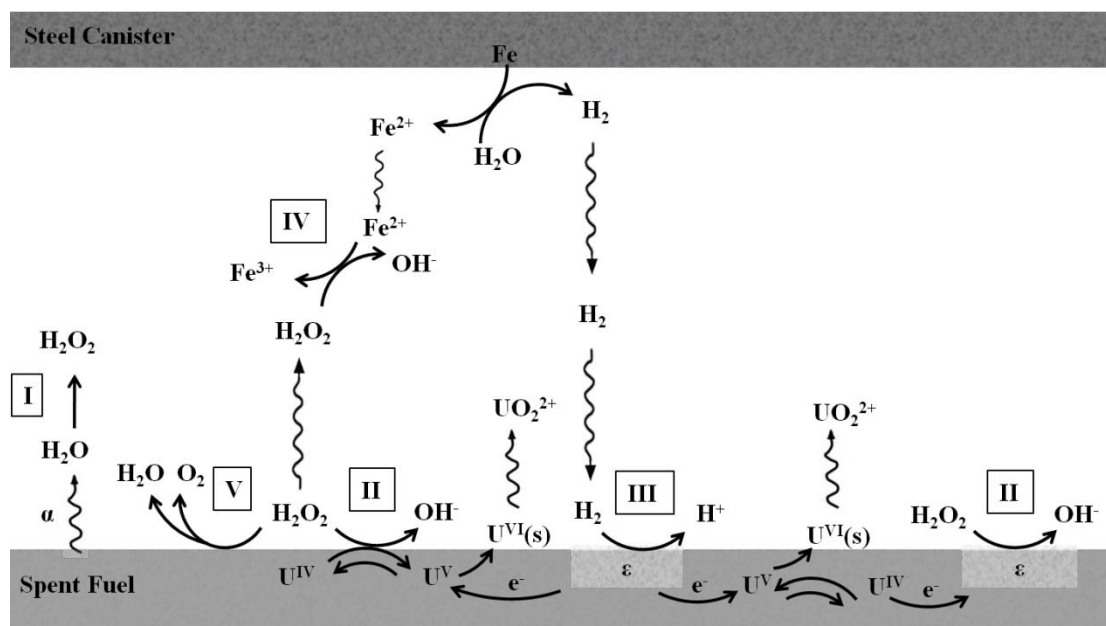
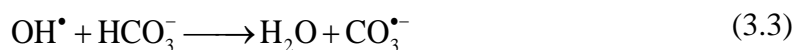


Fig. 3.1. Reactions considered in the model.

The main reactions involved in the fuel and steel corrosion processes are schematically illustrated in Fig. 3.1. The model includes: (I) the generation of H_2O_2 by water radiolysis; (II) the oxidative dissolution (corrosion) of UO_2 supported by H_2O_2 reduction on both the UO_2 surface and noble metal particles; (III) the reduction of oxidized U species ($\text{U}^{\text{V}}/\text{U}^{\text{VI}}$) catalyzed by H_2 oxidation on noble metal particles; (IV) the scavenging of H_2O_2 in homogeneous solution by reaction with Fe^{2+} ; (V) the decomposition of H_2O_2 to O_2 and H_2O assumed to require catalysis by the UO_2 and noble metal particle (not shown in Fig. 3) surfaces. Presently, the steel corrosion reaction is not explicitly modelled but assumed to generate constant concentrations of Fe^{2+} and H_2 . In practice these concentrations will be coupled by the overall stoichiometry of the steel corrosion process, but this is not presently incorporated into the model.

3.2.1 Water radiolysis

Among α -radiolysis products, only molecular oxidants are important since radical oxidants have short lifetimes and steady-state concentrations orders of magnitude lower than those of the molecular products as stated in Section 1.4.1. Here, the only radiolytic oxidant considered is H_2O_2 which has been shown to be the dominant one [8]. The influence of H_2 on α -radiolysis is considerable but relatively unimportant for UO_2 dissolution when compared to the noble metal catalysis effect [9] (described below). Additionally, the H_2 effect on radiolysis is effectively eliminated when $\sim 1 \text{ mmol L}^{-1}$ of carbonate is present in the exposure solution. This can be attributed to the ability of HCO_3^- to scavenge radiolytically-produced OH^\bullet radicals,



which prevents the reaction with H_2 to produce the reducing H^\bullet radical. Since $\text{CO}_3^{\bullet-}$ is a strong oxidant this facilitates oxidation while nullifying the H_2 effect. Since all groundwaters are likely to contain some carbonate, the influence of H_2 on α -radiolysis is therefore not included in this model. This approximation is verified in Chapter 4 which includes a more comprehensive radiolysis reaction set.

Fig. 3.2 shows the fuel/groundwater interface, with x indicating the distance from the fuel surface. Since the dose rate for α -emitters in the fuel decreases with distance from the fuel surface, H_2O_2 will be produced with decreasing concentration over a range determined by the energy of specific α -particles [10]. In the model radiolysis is considered to occur uniformly within a thin layer of solution on the fuel surface with a thickness, b , given by the average penetration distance of α -radiation in water. Beyond this layer no H_2O_2 is produced. This approximation is taken for simplification, and the

effect of non-uniform production of H_2O_2 is demonstrated to be marginal (Section 3.3.2 below). The diffusion layer is the distance over which species can diffuse to, or from, the fuel surface and beyond which uniform concentrations are presumed to prevail.

Configured in this manner the model can be used to simulate small or large separations between the site of radiolytic H_2O_2 production (the fuel surface) and the source of potential scavengers, Fe^{2+} and H_2 (the steel surface).

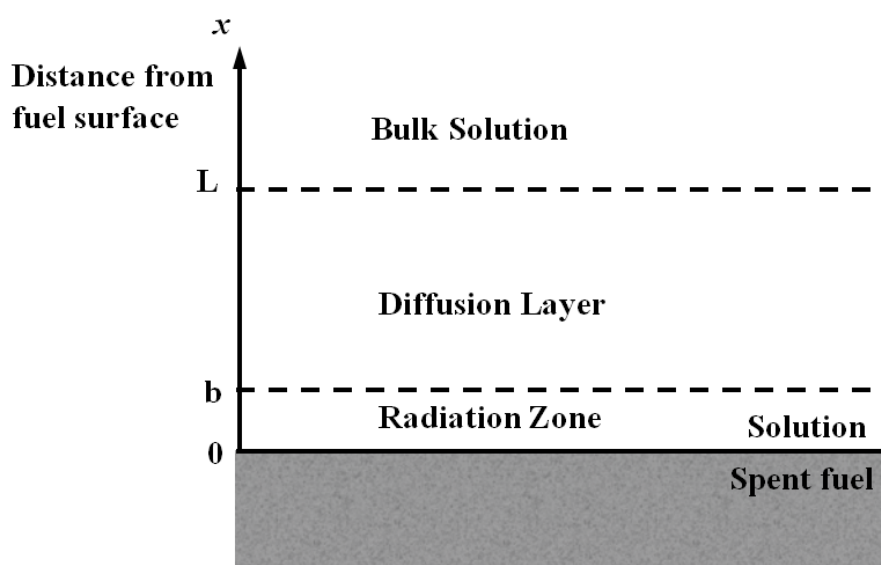


Fig. 3.2. One-dimensional setup at the fuel/solution interface in the α -radiolysis model.

The rate of H_2O_2 production is calculated using the expression,

$$R_{\text{H}_2\text{O}_2} = D_R \cdot g_{\text{H}_2\text{O}_2} \cdot \rho_{\text{H}_2\text{O}} \quad (0 \leq x \leq b) \quad (3.4)$$

where D_R is the dose rate representing the rate of the energy deposited per unit of mass, $g_{\text{H}_2\text{O}_2}$ is the radiolytic yield of H_2O_2 , which is the number of molecules produced per unit of radiation energy absorbed, and $\rho_{\text{H}_2\text{O}}$ is the density of water. The average alpha dose

rate at the fuel surface for a burnup of 220 MWh kgU⁻¹ at 1000 years is 9.03×10^5 Gy a⁻¹ [11] and $g_{\text{H}_2\text{O}_2}$ is 1.13 molecules per 100 eV [12].

3.2.2 UO₂ oxidation by H₂O₂

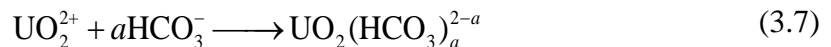
H₂O₂ can cause oxidation and dissolution (corrosion) of UO₂ via two reaction pathways [13, 14] as illustrated in Fig. 3.1: (i) it can react directly with the UO₂ surface,



or, (ii) it can be reduced on noble metal particles leading to oxidation and corrosion by galvanic coupling to the UO₂ matrix. Irrespective of the location of the cathodic reaction, it would be expected to be first order with respect to [H₂O₂] [8, 15]

$$R_{\text{II}} = k_{\text{II}} \cdot [\text{H}_2\text{O}_2] \quad (x = 0) \quad (3.6)$$

Oxidation would proceed through the creation of a U^V intermediate prior to formation of U^{VI} and dissolution as UO₂²⁺ [1, 16, 17]. In carbonate-free solution this can lead to the formation of surface corrosion products (UO₃·yH₂O or more complicated uranyl phases in groundwaters as stated in Section 1.4.2.5) which would significantly influence the fuel dissolution rate [15]. In this model it is assumed that the location of dissolution is unimpeded in this manner, a situation which would exist in the presence of sufficient carbonate to completely complex the dissolution product [5],



The experimental value for the rate constant, k_{II} , is 7.33×10^{-8} m s⁻¹ on pure UO₂ [15].

This value was measured on UO₂ powder and hence may not be the appropriate value for

spent fuel since the combination of noble metal particles and a rare earth-doped UO_2 matrix would be expected to accelerate the corrosion reaction via galvanic coupling. In the absence of a measured rate constant for this system a value of $7.33 \times 10^{-5} \text{ m s}^{-1}$ has been adopted. This value was used as an upper limit in simulations [18]. Some experimental evidence to justify such a high value will be presented below.

3.2.3 $\text{U}^{\text{V}}/\text{U}^{\text{VI}}$ reduction by H_2

A considerable effort has been expended on the study of the effect of H_2 on fuel corrosion since this reaction appears to have the potential to completely suppress corrosion and, hence, radionuclide release [19, 20]. Calculations indicate that dissolved H_2 concentrations as high as 0.038 mol L^{-1} [19] can be achieved as a consequence of steel corrosion in sealed repositories. The key requirement for H_2 to suppress fuel corrosion is that a mechanism to activate H_2 by dissociation to produce the H^\bullet radical species on the fuel surface be available. A range of studies have shown that this can be achieved by interaction of H_2 with both γ - and α -radiation and by catalysis on noble metal particles [19].

It has been experimentally demonstrated that the oxidation of the surface of simulated fuels (SIMFUELS which are both rare earth-doped and contain noble metal particles) can be suppressed in the presence of dissolved H_2 [5, 21-23]. The primary mechanism for this suppression is the galvanic coupling of H_2 oxidation on noble metal particles to UO_{2+x} reduction on the fuel surface [23]. While the details of this reaction remain unresolved, it is most likely that the oxidation/dissolution process is reversed at the U^{V} stage, as illustrated in Fig. 3.1 (detailed description in Section 1.5.4.2), and does not involve the

reduction of dissolved UO_2^{2+} species. However, it has been shown that dissolution can commence as soon as oxidation of the UO_2 surface (to $\text{U}^{\text{IV}}_{1-2x}\text{U}^{\text{V}}_{2x}\text{O}_{2+x}$) begins [1] and occurs as UO_2^{2+} . To accommodate this feature in the model, it is assumed that a $\text{U}^{\text{VI}}(\text{s})$ surface species is formed. At steady-state the surface coverage by this species will remain constant with the rate of release of U^{VI} to solution (as UO_2^{2+}) balanced by its rate of reformation by further oxidation of the $\text{U}^{\text{IV}}_{1-2x}\text{U}^{\text{V}}_{2x}\text{O}_{2+x}$ surface. Since it is assumed that the oxidation rate is rate determining, the surface coverage by $\text{U}^{\text{VI}}(\text{s})$ will approach zero. In the model the overall reaction can be expressed as



The rate expression derived by Trummer et al [24] for this reaction is,

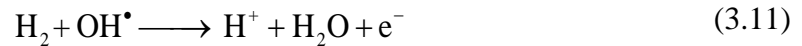
$$R_{\text{III}} = k_{\text{III}} \cdot s_{\varepsilon} \quad (x=0) \quad (3.9)$$

where s_{ε} is the coverage of noble metal particles on the fuel surface, and the first-order rate constant k_{III} was measured to be $4 \times 10^{-7} \text{ m s}^{-1}$ for pellets containing 1 at.% Pd.

The value for the rate constant was measured on a UO_2 pellet containing 1 at.% Pd to simulate the presence of noble metal particles [24]. Since the UO_2 powder from which the pellet was made was nuclear grade, it is likely that the composition was close to stoichiometric. By comparison to a rare earth-doped SIMFUEL, the matrix conductivity would be low, and the range of galvanic coupling limited. Recent measurements of the resistivities of 1.5 at.% SIMFUEL (rare earth-doped) and a simulated fuel containing noble metal particles and not rare earth-doped showed that their resistivities are very different (182 ohm cm compared to 15,400 ohm cm, respectively [25]). As a consequence,

the use of this rate constant could significantly underestimate the influence of galvanic coupling in its ability to suppress corrosion by catalyzing H₂ oxidation. It should be noted that the rate constants used for reactions (3.5) and (3.8) probably do not capture the correct balance between the ability of noble metal particles to catalyze reaction (3.5), which accelerates dissolution, and reaction (3.8) which suppresses it. This makes the use of the chosen value of k_{III} somewhat arbitrary.

Whether or not H₂ can react directly with the UO₂ surface remains unresolved. While Wren et al [12] claimed that a U^{IV}_{1-2x}U^V_{2x}O_{2+x} layer could catalyze the reaction between H₂O₂ and H₂, thereby limiting the oxidation rate,



Nilsson and Jonsson [26] could find no evidence for this reaction. More recent results on a rare earth-doped SIMFUEL containing no noble metal particles suggested this reaction did occur when the concentration ratio [H₂]/[H₂O₂] was large, but the evidence was not totally convincing [27]. Irrespective of these uncertainties, the direct scavenging of H₂O₂ in this manner is unlikely to be kinetically competitive with this reaction on noble metal particles which is rapid but still considered to have only a small effect on the corrosion rate [28]. At present H₂O₂ scavenging in this manner, either by reaction on noble metal particles or on the UO₂ surface is not explicitly included in the model although its effect is implicitly included in experimental observations on SIMFUEL.

It has also been claimed [29] that H_2 can reduce aqueous UO_2^{2+} to UO_2 via a homogeneous reaction:

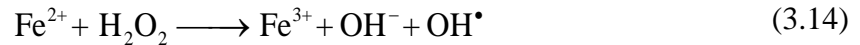


$$R_{III}^i = k_{III}' \cdot [H_2] \cdot [UO_2^{2+}] \quad (0 \leq x \leq L) \quad (3.13)$$

This reaction is also built into the model although the second-order rate constant k_{III}' is fairly low ($3.6 \times 10^{-9} \text{ L mol}^{-1} \text{ s}^{-1}$). However, if this reaction is catalyzed by ϵ -particles, the reaction rate will increase significantly [26]. Although there is no reliable data at the low $[H_2]$ considered in this model, this aqueous phase reduction of $[UO_2^{2+}]$ by H_2 is not expected to affect spent fuel dissolution, and only lowers the concentration of radionuclides in solution. Hence, this catalyzed reduction of UO_2^{2+} by H_2 is not included in the present model.

3.2.4 Fenton reaction

As stated in Section 1.5.4.1, ferrous ions produced from the anoxic corrosion of the steel canister will undergo a homogeneous reaction with H_2O_2 in the Fenton reaction,



The overall rate constant with respect to $[Fe^{2+}]$ is k_{IV} [30]. Reaction (3.14) is the rate determining step and produces OH^\bullet radicals that can then react with Fe^{2+} or other potential reductants, such as H_2 . In the limiting case that reaction (3.15) is the only pathway for OH^\bullet consumption, the H_2O_2 reduction rate is given by

$$R_{\text{IV}}(\text{H}_2\text{O}_2) = \frac{1}{2} R_{\text{IV}}(\text{Fe}^{2+}) = -\frac{1}{2} k_{\text{IV}}[\text{Fe}^{2+}][\text{H}_2\text{O}_2] \quad (0 \leq x \leq L) \quad (3.16)$$

In the other limiting case where all the OH^\bullet radicals formed in reaction (3.14) are scavenged by alternative reaction pathways, Fe^{2+} oxidation occurs only via reaction (3.14) and the overall reaction rate of H_2O_2 consumption can be expressed as

$$R_{\text{IV}}(\text{H}_2\text{O}_2) = R_{\text{IV}}(\text{Fe}^{2+}) = -k_{\text{IV}}[\text{Fe}^{2+}][\text{H}_2\text{O}_2] \quad (0 \leq x \leq L) \quad (3.17)$$

In this model, the Fenton reaction is taken to be unimpeded by other reactions and the rate equation (3.16) is adopted. The rate constant, k_{IV} , has been shown to be very sensitive to pH, temperature and salinity [30]. Considering the long-term disposal conditions (e.g., saline groundwater, neutral pH 8-10, 25 °C), a value of $1 \times 10^6 \text{ L mol}^{-1} \text{ s}^{-1}$ is assumed for k_{IV} in this model [31-33].

3.2.5 H_2O_2 decomposition

The oxidation of H_2O_2 can couple to its reduction resulting in an overall decomposition to H_2O and O_2 ,



A number of studies have observed this reaction on UO_2 [34-37] and the relevant literature review can be found in Section 1.5.1 and 1.5.2.3. An issue with most of these studies is that they were conducted at high $[\text{H}_2\text{O}_2]$ ($> 10^{-4} \text{ mol L}^{-1}$) in solutions containing no carbonate and, hence, complicated by the formation of corrosion product deposits on the fuel surface. When carbonate was present and dissolution unimpeded by deposits, the discrepancy between UO_2^{2+} release and H_2O_2 consumption suggested $\sim 20\%$

of the H_2O_2 was not involved in the corrosion reaction; i.e., only 80% caused fuel dissolution, based on a dissolution experiments using UO_2 powder [8, 38].

In none of these studies was a quantitative kinetic analysis performed. Additionally, decomposition would be expected to be promoted by the presence of noble metal particles, but this has not been studied quantitatively. Given these uncertainties, we have assumed in the model that 20% of the H_2O_2 is consumed by decomposition. Since reaction (3.18) would produce the additional oxidant, O_2 , which can also cause corrosion, some fraction of the decomposed H_2O_2 would still lead to fuel corrosion. However, the rate of reaction of O_2 with UO_2 is considerably slower than that of H_2O_2 [39] and this fraction is assumed in the model to be negligible. The adoption of a fraction of 20% can be considered conservative.

3.3 Model setup and results

The mathematical model outlined above is difficult to solve analytically, but numerical solutions can be developed using COMSOL Multiphysics, a commercial simulation package based on the finite element method. The model was simulated using the diluted species transportation module of COMSOL Multiphysics (version 4.2.0.150, COMSOL Inc.). The default values of the simulation parameters are listed in Table 3.1. A series of sensitivity analyses has been performed to examine the effects of diffusion length, $[\text{Fe}^{2+}]$, $[\text{H}_2]$, and α -radiation dose rate, in which the parameters, other than those examined, were maintained at the default values.

Table 3.1. Default values of simulation parameters

Parameter	Symbol	Value	Units
Diffusion layer thickness	L	1×10^{-3}	m
Radiation zone thickness [11]	b	1.3×10^{-5}	m
Average α dose rate [11]	D_R	9.03×10^5	Gy a ⁻¹
H ₂ O ₂ diffusivity [12]	$D_{H_2O_2}$	1×10^{-9}	m ² s ⁻¹
UO ₂ ²⁺ diffusivity [12]	D_{UO_2}	1×10^{-9}	m ² s ⁻¹
H ₂ diffusivity [12]	D_{H_2}	5.85×10^{-9}	m ² s ⁻¹
Fe ²⁺ diffusivity	D_{Fe}	1×10^{-9}	m ² s ⁻¹
H ₂ O ₂ bulk concentration	$C_{H_2O_2\text{bulk}}$	0	mol L ⁻¹
H ₂ bulk concentration	$C_{H_2\text{bulk}}$	1×10^{-6}	mol L ⁻¹
Fe ²⁺ bulk concentration [40]	$C_{Fe\text{-bulk}}$	1×10^{-6}	mol L ⁻¹
ϵ -particle coverage [9]	s_ϵ	0.01	-
H ₂ O ₂ surf. reaction rate const. [18]	k_{II}	7.33×10^{-5}	m s ⁻¹
H ₂ surf. reaction rate const. [24]	k_{III}	4×10^{-7}	m s ⁻¹
H ₂ /UO ₂ ²⁺ bulk reaction rate const. [29]	k_{III}'	3.6×10^{-9}	L mol ⁻¹ s ⁻¹
Fe ²⁺ bulk reaction rate const. [30]	k_{IV}	1×10^6	L mol ⁻¹ s ⁻¹
H ₂ O ₂ decomposition ratio [38]	ratio	0.2	-

3.3.1 The influence of the diffusion length

As discussed above the diffusion layer is the distance over which species diffuse to or from the UO₂ surface. In the present form of the model this length could be taken to crudely represent either the depth of an inert-walled pore in a corrosion product deposit

(μm), the distance from a flaw in the cladding (at which location the $[\text{H}_2]$ remains undisturbed) to the site of H_2O_2 production at a reactive surface location on the fuel (mm to cm), or the distance from the reactive fuel location to the site of H_2 production on the steel vessel wall (many cm).

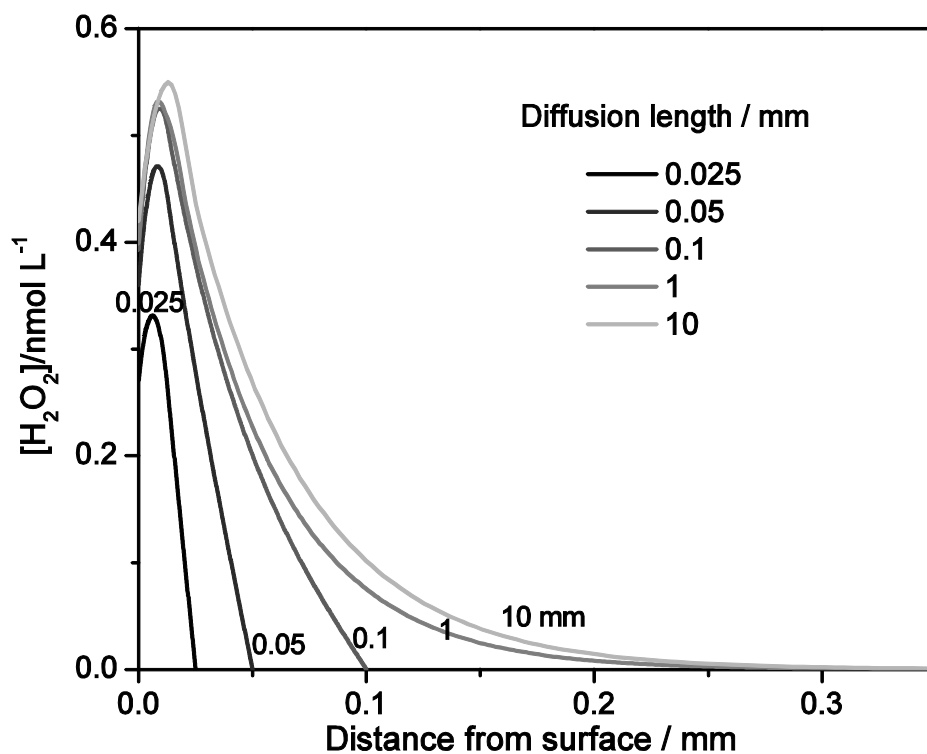


Fig. 3.3. H_2O_2 steady-state concentration profiles for various assumed diffusion lengths.

Fig. 3.3 shows the simulated H_2O_2 concentration profiles as a function of diffusion length.

The $[\text{H}_2\text{O}_2]$ exhibits a maximum near the radiation penetration depth ($0 < x < b$),

decreasing at locations closer to the surface due its consumption by fuel corrosion and

decreasing at larger distances along the diffusion path due to consumption in the Fenton

reaction. The concentration reaches zero at the assumed diffusion length; i.e., at the

boundary with the undisturbed bulk solution ($x = L$). Irrespective of the diffusion length, the great majority of the H_2O_2 is consumed within 0.2 to 0.3 mm of the corroding fuel surface.

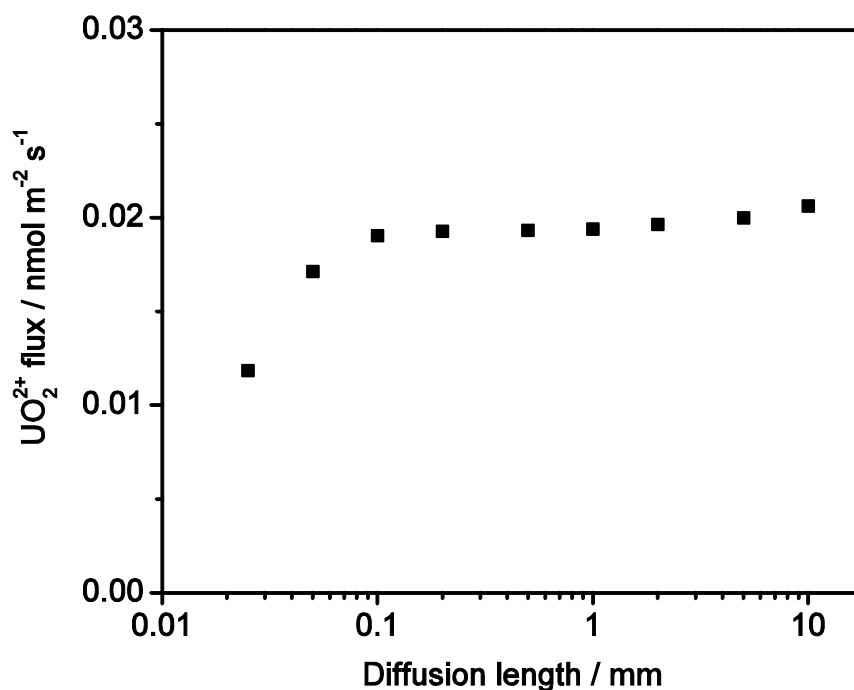


Fig. 3.4. Diffusive fluxes of UO_2^{2+} (equal to the UO_2 corrosion rate) as a function of various diffusion lengths.

The steady-state diffusive flux of UO_2^{2+} away from the UO_2 surface is equal to the fuel corrosion rate. As shown in Fig. 3.4, the flux (corrosion rate) only increases by a factor of ~ 2 as the diffusion length increases by three orders of magnitude, and is nearly independent of diffusion length for $L > 0.1$ mm. Thus, the effect of diffusion length on the fuel corrosion is marginal.

3.3.2 The effect of non-uniform dose rate distribution

In the present model, the dose rate is assumed to be uniformly distributed within a radiation zone near the fuel/water interface ($x \leq b$) and to be zero in the solution beyond this region ($x > b$). However, the dose rate will actually be non-uniformly distributed since the α -particles will lose energy along the penetration pathway. Therefore, the use of this simplified uniform distribution should be tested.

The dose rate distribution in water in contact with used fuels has been studied using different approaches. One approach is based on the thermal power of the fuel and the ratio between the specific stopping power values in water and in UO_2 [11, 41, 42]. Another approach takes the geometrical consideration of radiation emitters and energy deposition into account, and simulations have been performed on spherical [43] and planar [10] geometries for spent fuel. Despite the different approaches, good agreement is achieved between the two calculations [43]. Here, we compare the results using the uniform dose rate distribution with the non-uniform geometrical distribution obtained in reference [10].

Nielsen and Jonsson [10] calculated the dose rate by dividing the fuel matrix (α -radiation emitter) into thin layers at different depths from the surface using a planar geometry assumption. The maximum distance that α -particles can travel in UO_2 is $\sim 13 \mu\text{m}$; thus, only emitters located near the fuel surface contribute to solution radiolysis. The α -particles able to escape from the surface have a reduced energy after travelling through the fuel matrix. By integrating all contributions, the dose rate was obtained as a function of distance into the solution.

The calculated α -dose rate profile shows a sharp decrease with distance from the surface. Although this result is not specific for CANDU fuel, the authors conclude that fuels of different burnup and age will have the same profile of geometrical dose distribution which only differs in magnitude. It is found that their profile can be well fitted by an exponential function,

$$D(x) = A \left[\exp\left(-\frac{x}{B}\right) + C \right] \quad (x \leq \delta) \quad (3.19)$$

where A , the magnitude of the curve, depends on the burnup and age of the fuel, B , which determines the shape of the curve and remains the same between different fuels, and C is a constant that assures the dose rate reaches zero at the maximum penetration depth δ .

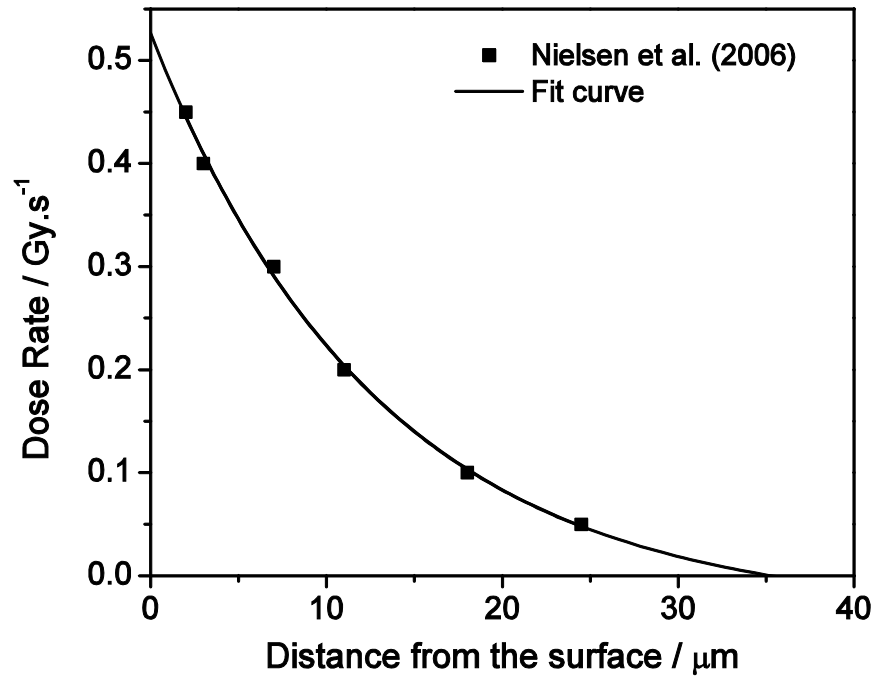


Fig. 3.5. Fitting results for the α -dose rate profile, using the data from reference [10].

The fitted curve for the dose rate distribution is plotted in Fig. 3.5, yielding the values $A = 0.563 \text{ Gy s}^{-1}$, $B = 12.97 \text{ }\mu\text{m}$ and $C = -0.0657$. The value of A needs to be adjusted to make the total dose rate consistent for both a uniform and an exponential distribution, i.e., a value for A that yields an area under the curve $D(x)$ equal to that under the line D_R is required, Fig. 3.6.

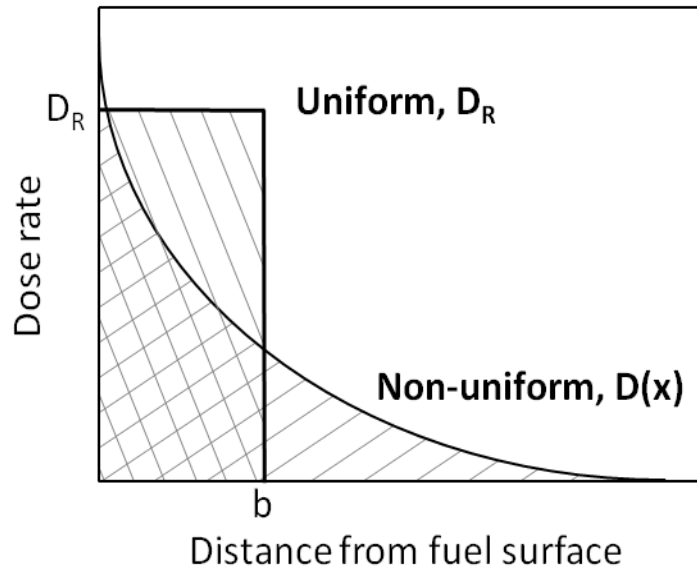


Fig. 3.6. Illustration showing the two different dose rate distributions; uniform and exponential. The shaded areas indicate the total dose rate in each case.

For the total dose rates from each distribution to be equal,

$$\int_{x=0}^{\delta} D(x)dx = D_R \cdot b \quad (3.20)$$

where the maximum penetration depth δ of α -particles in water is calculated to be 35.3 μm according to the fitting result. Using $D_R = 9.03 \times 10^5 \text{ Gy a}^{-1}$ and $b = 13 \mu\text{m}$ [11], the value of A is calculated to be $1.20 \times 10^6 \text{ Gy a}^{-1}$. Therefore the exponential distribution of dose rate can be expressed as a function of distance over the range $0 \leq x \leq 35.3 \mu\text{m}$,

$$D(x) = 1.20 \times 10^6 \times [\exp(-\frac{x}{12.97}) - 0.0657] (\text{Gy a}^{-1}) \quad (3.21)$$

As a comparison the uniform distribution within the range $0 \leq x \leq 13 \mu\text{m}$ is given by

$$D(x) = D_R = 9.03 \times 10^5 (\text{Gy a}^{-1}) \quad (3.22)$$

Fig. 3.7 shows a comparison of the steady-state $[\text{H}_2\text{O}_2]$ profiles calculated based on either the uniform or exponential dose distribution. The position of the peak shifts to higher values of x , except for $L = 0.025 \text{ mm}$, and the peak values for $[\text{H}_2\text{O}_2]$ appear lower when using an exponential distribution. These profiles reflect the balance between the various consumption pathways for H_2O_2 , including UO_2 oxidation, the Fenton reaction and mass transport.

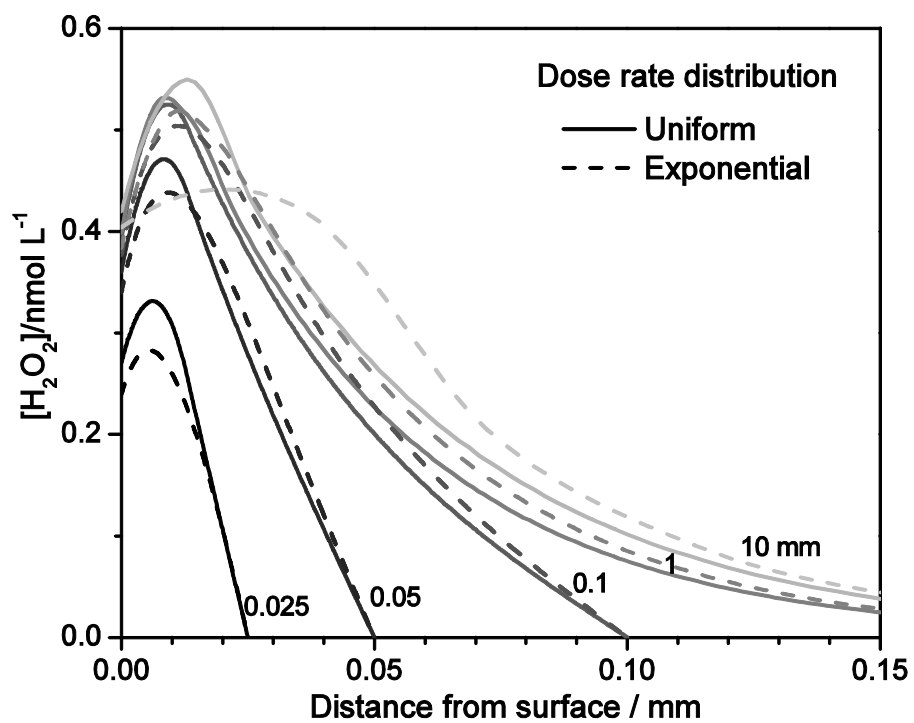


Fig. 3.7. H_2O_2 steady-state concentration profiles for both uniform and exponential dose rate distributions.

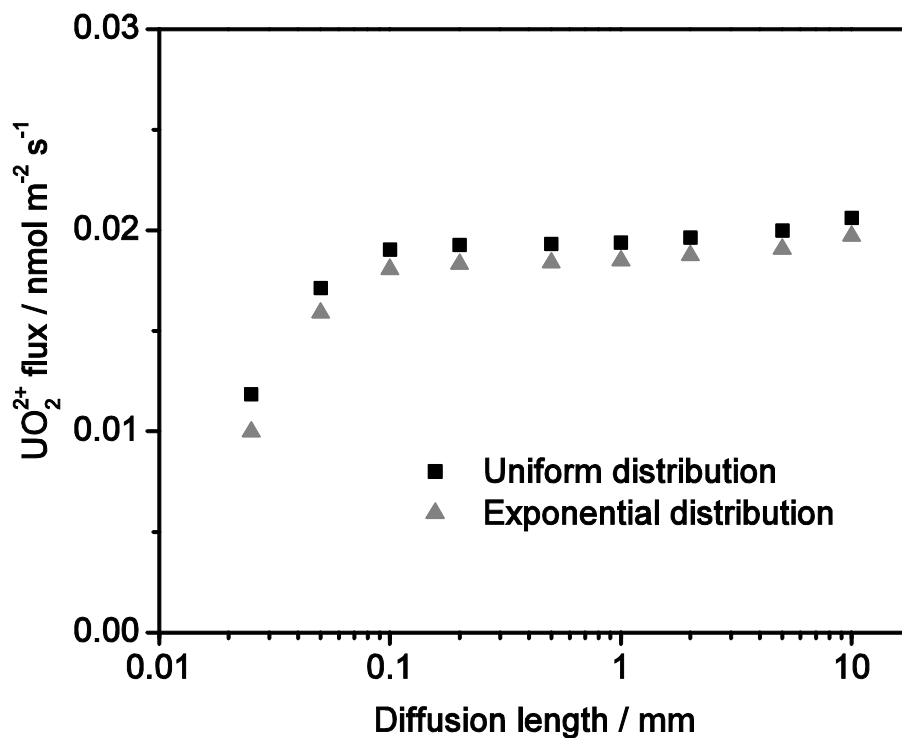


Fig. 3.8. Diffusive fluxes of UO_2^{2+} calculated for the two dose rate distributions. (\blacktriangle) exponential distribution; (\blacksquare) uniform distribution.

The influence of dose rate distributions on the UO_2^{2+} fluxes (corrosion rates) is shown in Fig. 3.8. The differences for the two distributions are marginal for varying diffusion lengths. Moreover, the results for a uniform distribution are slightly higher than those for an exponential distribution, suggesting that the former is a conservative approach. Based on this comparison the use of a simplified uniform distribution is justified.

3.3.3 The influence of Fe^{2+}

The Fenton reaction will consume H_2O_2 in solution and would be expected to suppress the corrosion rate. Fig. 3.9 shows the influence of $[\text{Fe}^{2+}]$ on the $[\text{H}_2\text{O}_2]$ distribution

profile for $[\text{Fe}^{2+}]_{\text{bulk}}$ up to $10^{-6} \text{ mol L}^{-1}$. For groundwaters with a pH in the expected range of 8 to 10, the solubility of Fe^{2+} will be in the range 10^{-4} to $10^{-6} \text{ mol L}^{-1}$ [44]. In the absence of Fe^{2+} , and beyond the range of influence of the corroding surface, there is a constant flux of H_2O_2 to the bulk of solution. As $[\text{Fe}^{2+}]_{\text{bulk}}$ is increased, H_2O_2 is scavenged by the Fenton reaction at locations progressively closer to the UO_2 surface. For $[\text{Fe}^{2+}]_{\text{bulk}} \geq 10^{-6} \text{ mol L}^{-1}$, the H_2O_2 is effectively totally consumed for distances from the fuel surface $> 0.2 \text{ mm}$.

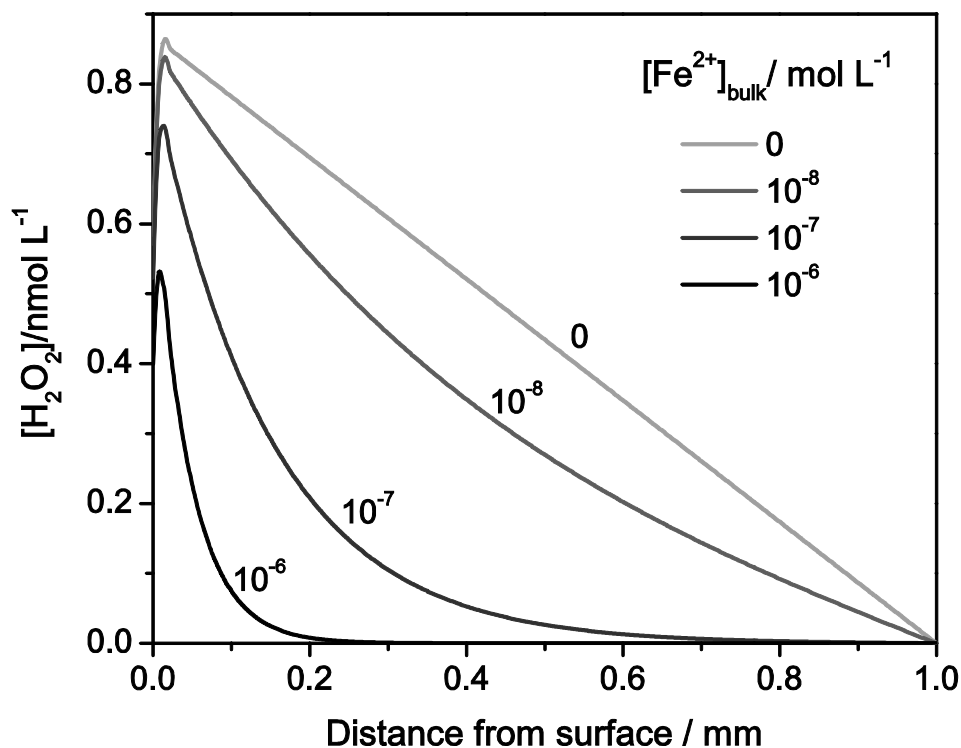


Fig. 3.9. $[\text{H}_2\text{O}_2]$ as a function of distance from fuel surface at various Fe^{2+} bulk concentrations.

At the fuel surface the influence of Fe^{2+} will be determined by the relative rates of the corrosion and Fenton reactions. As shown in Fig. 3.10, the Fenton reaction is able to influence the corrosion process, leading to a decrease in flux of UO_2^{2+} as the H_2O_2 is consumed and corrosion suppressed. However, this influence is relatively minor, the corrosion rate (flux of UO_2^{2+}) being reduced by only a factor of ~ 2 for an increase in $[\text{Fe}^{2+}]$ from 10^{-8} to 10^{-6} mol L^{-1} . Clearly, a $[\text{Fe}^{2+}]_{\text{bulk}}$ approaching the solubility limit would be required before any significant influence of the Fenton reaction on fuel corrosion would be observed.

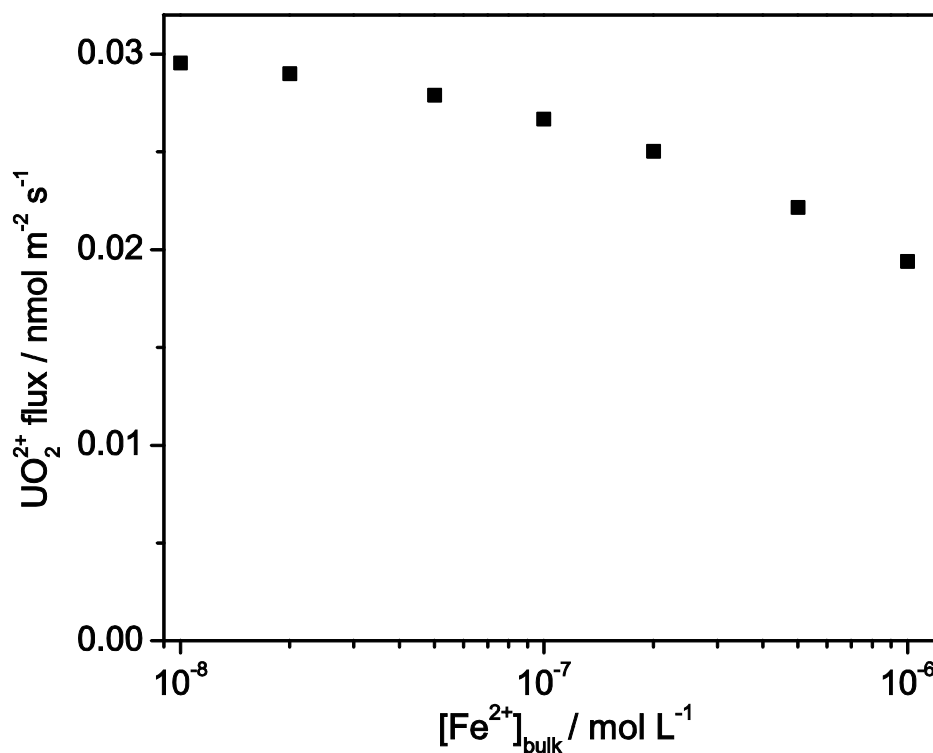


Fig. 3.10. UO_2^{2+} flux (equal to the UO_2 corrosion rate) as a function of $[\text{Fe}^{2+}]$.

3.3.4 The influence of H_2

Fig. 3.11 shows the UO_2^{2+} flux (corrosion rate) as a function of bulk $[\text{H}_2]$ over the range 0 to $> 10^{-5} \text{ mol L}^{-1}$. A linear relationship is obtained. Its extrapolation to zero fuel corrosion rate predicts the threshold $[\text{H}_2]$ at which the rate of UO_2 oxidation by H_2O_2 is balanced by the rate of its subsequent reduction by H_2 . This concentration can be considered the critical value, $[\text{H}_2]_{\text{crit}}$, at which fuel corrosion becomes completely suppressed. Based on this extrapolation, a value of $[\text{H}_2]_{\text{crit}} = 5.9 \times 10^{-6} \text{ mol L}^{-1}$ was obtained.

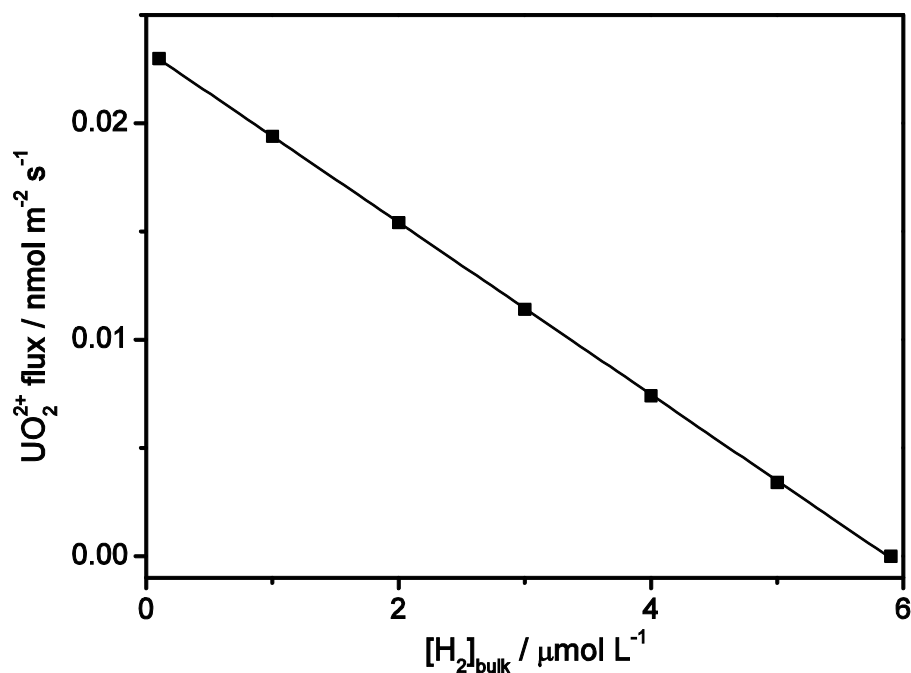


Fig. 3.11. UO_2^{2+} flux (equal to the UO_2 corrosion rate) as a function of $[\text{H}_2]_{\text{bulk}}$.

This value is considerably higher than those calculated by Trummer and Jonsson [9]. This is a direct consequence of adopting a large value for k_{II} , the rate constant for the reaction of H_2O_2 with the UO_2 surface, reaction (3.5). In the absence of a value for k_{II} measured

on noble metal-containing, rare earth-doped UO_2 (e.g., SIMFUEL) our value (Table 3.1) is somewhat arbitrarily chosen. Considering the magnitude and potential significance of this H_2 effect some justification confirming the magnitude is required. Two SIMFUEL experiments are considered here.

In the first experiment [21], the corrosion potential (E_{CORR}) of a 1.5 at.% SIMFUEL electrode was measured in 0.1 mol L^{-1} KCl ($\text{pH} = 9.5$; 60°C) as the overpressure of a 5% H_2/Ar purge gas was steadily increased. The E_{CORR} decreased as the overpressure was increased. The thermodynamic threshold for the onset of UO_2 oxidation is around -350 mV (vs. Ag/AgCl) and it has been verified experimentally by a combination of electrochemistry and X-ray photoelectron spectroscopy (XPS) [5, 17] that oxidation below this value is undetectable. Consequently, the $[\text{H}_2]$ required to suppress E_{CORR} to $\leq -350 \text{ mV}$ (vs. Ag/AgCl) can be considered as the critical value, $[\text{H}_2]_{\text{crit}}$, required to prevent corrosion when galvanic coupling is present and H_2 oxidation is sustained on noble metal particles [21]. Using the solubility of H_2 [45] and the fact that this solubility is proportional to the partial pressure of H_2 [46], $[\text{H}_2]_{\text{crit}}$ can be calculated to be $\sim 1.8 \times 10^{-5} \text{ mol L}^{-1}$, which is compatible with the calculated model value of $5.9 \times 10^{-6} \text{ mol L}^{-1}$.

In the second experiment [23] the ability of H_2 to prevent (or reverse) the oxidation of UO_2 was followed by measuring E_{CORR} on 1.5 at.% SIMFUEL when various concentrations of H_2O_2 were added to a 5% H_2/Ar -purged 0.1 mol L^{-1} KCl solution ($\text{pH} = 9.5$; 60°C). In these experiments a concentration of dissolved H_2 of $\sim 3 \times 10^{-5} \text{ mol L}^{-1}$ was able to suppress E_{CORR} to the thermodynamic limit for a $[\text{H}_2\text{O}_2]$ up to 10^{-10} to $10^{-9} \text{ mol L}^{-1}$. That oxidation of the UO_2 surface was prevented when this E_{CORR} value was established was demonstrated by XPS. Since the calculated $[\text{H}_2\text{O}_2]$ s for the model are

within the range of concentrations used in this experiment, $3 \times 10^{-5} \text{ mol L}^{-1}$ can be considered as a reasonable estimate of $[\text{H}_2]_{\text{crit}}$, which is compatible with the model value of $5.9 \times 10^{-6} \text{ mol L}^{-1}$. Based on the agreement between these experimental values and the model calculations, the adoption of the value of k_{II} (Table 3.1) seems reasonable.

3.3.5 Influence of α -radiation dose rate

Using the α -radiation dose rates for an aged CANDU fuel bundle with a burnup of 220 MWh kgU^{-1} [11], values of $[\text{H}_2]_{\text{crit}}$ for different waste disposal times can be calculated. Fig. 3.12 shows the H_2 required to completely suppress fuel corrosion as a function of disposal time. As expected this calculation demonstrates that the H_2 requirement (demand) decreases markedly with time as α -radiation fields decay.

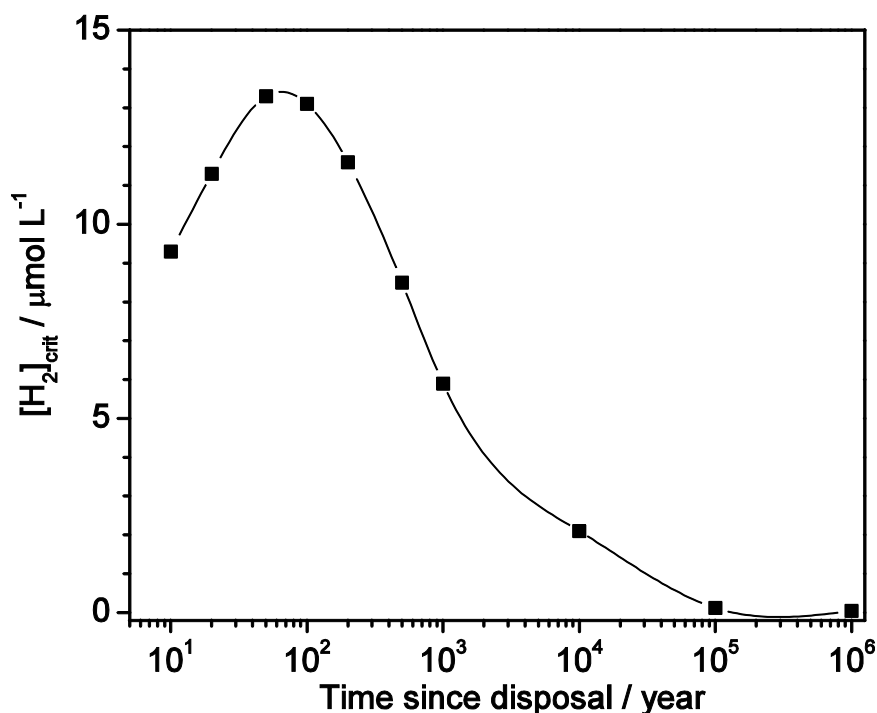


Fig. 3.12. Critical $[\text{H}_2]$ required to completely suppress fuel corrosion as a function of waste disposal time.

The increase in H₂ demand at short times is attributed to the in-growth of α -emitters as a consequence of the short term decay of γ/β - radiation fields emitted by the fuel but not considered here. This raises the question as to whether the H₂ demand would be substantially increased in the improbable event of the fuel being exposed to groundwater during the early period when γ/β fields are significant. This seems highly unlikely since H₂ is commonly added to nuclear reactor heat transport circuits to suppress the radiolysis of water. Additionally, studies on spent fuel corrosion when γ/β fields are substantial show a very clear suppression of fuel corrosion and radionuclide release in the presence of dissolved H₂ [19].

3.4 Summary and conclusions

A model has been developed to determine the influence of steel corrosion products on the α -radiolytic corrosion of spent fuel. The model takes into account the α -radiolysis of water, the reaction of radiolytic H₂O₂ with UO₂, the reaction with H₂ via galvanic coupling, and the Fenton reaction. The direct influence of H₂ on the production of H₂O₂ by α -radiolysis is not included.

The dominant redox control agent was found to be H₂. The ability of Fe²⁺ to scavenge H₂O₂ by the Fenton reaction has only a minor influence on the fuel corrosion process. Critical H₂ concentrations, the [H₂] required to completely suppress fuel corrosion, were calculated as a function of α -dose rate for various spent fuel ages. Even for the highest α -dose rates (anticipated after ~ 100 years of disposal) [H₂]_{crit} was $\leq 1.5 \times 10^{-5}$ mol L⁻¹.

In its present form the model should be considered preliminary, and containing some rate constants whose values should be considered somewhat arbitrary. A considerable

improvement in the available data base will be required before more justifiable predictions can be computed. Of particular importance is an improved quantitative kinetic understanding of the combined effects of RE^{III} doping and the number density of noble metal particles on H₂O₂ reduction and decomposition, H₂ oxidation, and the anodic reactivity of the UO₂ matrix. A more comprehensive model which addresses these issues is presented in Chapter 4.

3.5 References

- [1] D.W. Shoesmith, Fuel corrosion waste process under waste disposal conditions, *J. Nucl. Mater.* 282 (2000) 1-31.
- [2] B. Grambow, A. Loida, A. Martínex-Esparza, P. Díaz-Arocas, J. de Pablo, J.-L. Paul, J.-P. Glatz, K. Lemmens, K. Ollila, and H. Christensen, Source Term for Performance Assessment of Spent Fuel as a Waste Form, Report EUR 19140 EN, European Commission, 2000.
- [3] C. Poinssot, C. Ferry, M. Kelm, B. Grambow, A. Martinez Esparza Valiente, L.H. Johnson, Z. Andriambololona, J. Bruno, C. Cachoir, J.-M. Cavedon, H. Christensen, C. Corbel, C. Jegou, K. Lemmens, A. Loida, P. Lovera, F. Miserque, J. de Pablo, A. Poulesquen, J. Quinones, V. Rondinella, K. Spahiu, and D.H. Wegen, Final report of the European project spent fuel stability under repository conditions, Report CEA-R-6093, CEA, 2005.
- [4] R.C. Ewing, and M.T. Peters, Source Term. In: OST&I Annual Report 2005, Report DOE/RW-0581, 2005, 5-51.
- [5] D.W. Shoesmith, Used Fuel and Uranium Dioxide Dissolution Studies - A Review, Report NWMO TR-2007-03, Nuclear Waste Management Organization, Toronto, ON, 2007.
- [6] D.W. Shoesmith, The Role of Dissolved Hydrogen on the Corrosion/Dissolution of Spent Nuclear Fuel, Report NWMO TR-2008-19, Nuclear Waste Management Organization, Toronto, ON, 2008.
- [7] G.M. Kwong, Status of Corrosion Studies for Copper Used Fuel Containers Under Low Salinity Conditions, Report NWMO TR-2011-14, Nuclear Waste Management Organization, Toronto, ON, 2011.
- [8] E. Ekeröth, O. Roth, and M. Jonsson, The relative impact of radiolysis products in radiation induced oxidative dissolution of UO₂, *J. Nucl. Mater.* 355 (2006) 38-46.

- [9] M. Trummer, and M. Jonsson, Resolving the H₂ effect on radiation induced dissolution of UO₂-based spent nuclear fuel, *J. Nucl. Mater.* 396 (2010) 163-169.
- [10] F. Nielsen, and M. Jonsson, Geometrical α - and β -dose distributions and production rates of radiolysis products in water in contact with spent nuclear fuel, *J. Nucl. Mater.* 359 (2006) 1-7.
- [11] F. Garisto, D.H. Barber, E. Chen, A. Ingot, and C.A. Morrison, Alpha, Beta and Gamma Dose Rates in Water in Contact with Used CANDU Fuel, Report NWMO TR-2009-27, Nuclear Waste Management Organization, Toronto, ON, 2009.
- [12] J.C. Wren, D.W. Shoesmith, and S. Sunder, Corrosion Behavior of Uranium Dioxide in Alpha Radiolytically Decomposed Water, *J. Electrochem. Soc.* 152 (2005) B470.
- [13] J.S. Goldik, J.J. Noël, and D.W. Shoesmith, The electrochemical reduction of hydrogen peroxide on uranium dioxide electrodes in alkaline solution, *J. of Electroanal. Chem.* 582 (2005) 241-248.
- [14] J.S. Goldik, J.J. Noël, and D.W. Shoesmith, The Effects of Simulated Fission Products in the Reduction of Hydrogen Peroxide on Simulated Nuclear Fuel Electrodes, *J. Electrochem. Soc.* 153 (2006) E151-E159.
- [15] M. Hossain, E. Ekeröth, and M. Jonsson, Effects of HCO₃⁻ on the kinetics of UO₂ oxidation by H₂O₂, *J. Nucl. Mater.* 358 (2006) 202-208.
- [16] B.G. Santos, J.J. Noël, and D.W. Shoesmith, The effect of pH on the anodic dissolution of SIMFUEL (UO₂), *J. of Electroanal. Chem.* 586 (2006) 1-11.
- [17] B.G. Santos, H.W. Nesbitt, J.J. Noël, and D.W. Shoesmith, X-ray photoelectron spectroscopy study of anodically oxidized SIMFUEL surfaces, *Electrochim. Acta* 49 (2004) 1863-1873.
- [18] F. Nielsen, and M. Jonsson, Simulations of H₂O₂ concentration profiles in the water surrounding spent nuclear fuel taking mixed radiation fields and bulk reactions into account, *J. Nucl. Mater.* 374 (2008) 281-285.
- [19] M.E. Broczkowski, D. Zagidulin, and D.W. Shoesmith, The Role of Dissolved Hydrogen on the Corrosion/Dissolution of Spent Nuclear Fuel, in: "Nuclear Energy and the Environment", American Chemical Society Symposium, 2010, Vol.1046, Chapter 26, pp. 349-380
- [20] P. Carbol, J. Cobos-Sabate, J.-P. Glatz, C. Ronchi, V. Rondinella, D.H. Wegen, T. Wiss, A. Loida, V. Metz, B. Kienzler, K. Spahiu, B. Grambow, J. Quinones, and A. Martinez Esparza Valiente, The effect of dissolved hydrogen on the dissolution of ²³³U-doped UO₂(s), high burn-up spent fuel and MOX fuel, Report TR-05-09, Swedish Nuclear Fuel and Waste Management Company, 2005.
- [21] M.E. Broczkowski, J.J. Noël, and D.W. Shoesmith, The inhibiting effects of hydrogen on the corrosion of uranium dioxide under nuclear waste disposal conditions, *J. Nucl. Mater.* 346 (2005) 16-23.

- [22] M.E. Broczkowski, J.J. Noël, and D.W. Shoesmith, The influence of dissolved hydrogen on the surface composition of doped uranium dioxide under aqueous corrosion conditions, *J. of Electroanal. Chem.* 602 (2007) 8-16.
- [23] M.E. Broczkowski, P.G. Keech, J.J. Noël, and D.W. Shoesmith, Corrosion of Uranium Dioxide Containing Simulated Fission Products in Dilute Hydrogen Peroxide and Dissolved Hydrogen, *J. Electrochem. Soc.* 157 (2010) C275-C281.
- [24] M. Trummer, S. Nilsson, and M. Jonsson, On the effects of fission product noble metal inclusions on the kinetics of radiation induced dissolution of spent nuclear fuel, *J. Nucl. Mater.* 378 (2008) 55-59.
- [25] D. Ofori, M.E. Broczkowski, H. He, K. O'Neil, O. Semenikhin, and D.W. Shoesmith, The Influence of Various Factors on Fuel Corrosion under Nuclear Waste Disposal Conditions, Report TR-2011-20, Nuclear Waste Management Organization, 2011.
- [26] S. Nilsson, and M. Jonsson, On the catalytic effects of Pd(s) on the reduction of UO_2^{2+} with H_2 in aqueous solution, *J. Nucl. Mater.* 374 (2008) 290-292.
- [27] M.E. Broczkowski, P.G. Keech, J.J. Noël, and D.W. Shoesmith, The Role of Dissolved Hydrogen on Rare Earth-Doped Uranium Dioxide Corrosion in the Presence of Hydrogen Peroxide, *J. Electrochem. Soc.* 158 (2011) C439-C444.
- [28] S. Nilsson, and M. Jonsson, On the catalytic effects of $\text{UO}_2(\text{s})$ and Pd(s) on the reaction between H_2O_2 and H_2 in aqueous solution, *J. Nucl. Mater.* 372 (2008) 160-163.
- [29] E. Ekeröth, M. Jonsson, T.E. Eriksen, K. Ljungqvist, S. Kovacs, and I. Puigdomenech, Reduction of UO_2^{2+} by H_2 , *J. Nucl. Mater.* 334 (2004) 35-39.
- [30] F.J. Millero, and S. Sotolongo, The oxidation of Fe(II) with H_2O_2 in seawater, *Geochim. Cosmochim. Acta* 53 (1989) 1867-1873.
- [31] F. Garisto, T. Kempe, and P. Gierszewski, Technical Summary of the Safety Aspects of the Deep Geological Repository Concept for Used Nuclear Fuel, Report NWMO TR-2009-12, Nuclear Waste Management Organization, Toronto, ON, 2009.
- [32] D.G. Bennett, and R. Gens, Overview of European concepts for high-level waste and spent fuel disposal with special reference waste container corrosion, *J. Nucl. Mater.* 379 (2008) 1-8.
- [33] J. Kaija, K. Rasilainen, and R. Blomqvist, The use of selected safety indicators (concentrations, fluxes) in the assessment of radioactive waste disposal - Report 6, Report YST-114, Geological Survey of Finland - Nuclear Waste Disposal Research, 2003.
- [34] H. Christensen, R. Forsyth, R. Lundqvist, and L.O. Werme, Radiation Induced Dissolution of UO_2 , Report NS-90/85, Studsvik Energiteknik AB, Nyköping, Sweden, 1990.

- [35] P. Diaz-Arocas, J. Quinones, C. Maffiotte, J. Serrano, J. Garcia, and J.R. Almazan, Effect of secondary phase formation in the leaching of UO_2 under simulated radiolytic products, *Mater. Res. Soc. Symp. Proc.* 353 (1995) 641-646.
- [36] S. Sunder, N.H. Miller, and D.W. Shoesmith, Corrosion of uranium dioxide in hydrogen peroxide solutions, *Corros. Sci.* 46 (2004) 1095-1111.
- [37] J. de Pablo, I. Casas, F. Clarens, F. El Aamrani, and M. Rovira, The effect of hydrogen peroxide concentration on the oxidative dissolution of unirradiated uranium dioxide, *Mat. Res. Soc. Symp. Proc.* 663 (2001) 409-426.
- [38] M. Jonsson, E. Ekeröth, and O. Roth, Dissolution of UO_2 by one- and two-electron oxidants, *Mater. Res. Soc. Symp. Proc.* 807 (2004) 77.
- [39] T.E. Eriksen, D.W. Shoesmith, and M. Jonsson, Radiation induced dissolution of UO_2 based nuclear fuel – A critical review of predictive modelling approaches, *J. Nucl. Mater.* 420 (2012) 409–423.
- [40] C.F. Baes, and R.E. Mesmer, *The Hydrolysis of Cations*, Jon Wiley and Sons, New York, 1976.
- [41] S. Sunder, Calculation of radiation dose rates in a water layer in contact with used CANDU UO_2 fuel, *Nucl. Tech.* 122 (1998) 211-221.
- [42] F. Garisto, J. Avis, N. Calder, A. D'Adrea, P. Gierszewski, C. Kitson, T. Melnyk, K. Wei, and L. Wojciechowski, Third Case Study - Defective Container Scenario, Report 06219-REP-01200-10126-R00, Ontario Power Generation, Toronto, ON, 2004.
- [43] A. Poulesquen, C. Jégou, and S. Peugot, Determination of alpha dose rate profile at the UO_2 /water interface, in "Scientific Basis for Nuclear Waste Management XXIX.", edited by P. Van Iseghem, Material Research Society (*Mater. Res. Soc. Symp. Proc.* 932), Warrendale, PA, 2006, p. 505-512.
- [44] W. Xu, K. Daub, X. Zhang, J.J. Noël, D.W. Shoesmith, and J.C. Wren, Oxide formation and conversion on carbon steel in mildly basic solutions, *Electrochim. Acta* 54 (2009) 5727-5738.
- [45] R. Wiebe, V.L. Gaddy, and J. Conrad Heins, Solubility of Hydrogen in Water at 25°C from 25 to 1000 Atmospheres, *Industrial and Engineering Chemistry* 24 (1932) 823-825.
- [46] T.E. Crozier, and S. Yamamoto, Solubility of Hydrogen in Water, Seawater, and NaCl Solutions, *Journal of Chemical and Engineering Data* 19 (1974) 242-244.

Chapter 4

AN IMPROVED MODEL FOR THE CORROSION OF USED NUCLEAR FUEL INSIDE A FAILED WASTE CONTAINER UNDER PERMANENT DISPOSAL CONDITIONS¹

4.1 Introduction

In this chapter, an improved model for nuclear fuel corrosion inside a failed waste container has been developed based on the work presented in Chapter 3. The previous model contains many approximations and limitations and has been improved in a number of ways:

- (i) A complete set of α -radiolytic reactions has been included. Previously, the α -radiolysis process was simplified with H_2O_2 considered the only radiolysis product. Inclusion of a full reaction set allows this simplification to be evaluated;
- (ii) A less arbitrary approach to account for the decomposition of radiolytically-produced H_2O_2 has been adopted, since this process appears to be the major route for H_2O_2 consumption on a UO_2 surface [1, 2];
- (iii) An attempt to incorporate the influence of fuel burnup is included, since burnup will not only influence the dose rate but also affect the surface reactivity of the fuel [3];
- (iv) Instead of treating the oxidative dissolution (corrosion) of UO_2 as a general surface reaction, an attempt is made to take into account anodic dissolution supported by H_2O_2

¹ A version of Chapter 4 has been published: L. Wu, Z. Qin, and D.W. Shoesmith, An improved model for the corrosion of used nuclear fuel inside a failed waste container under permanent disposal conditions, Corrosion Science 84 (2014) 85-95.

reduction on both the UO_2 and noble metal particle surfaces, the latter being a product of the in-reactor fission process; and

(v) the reactions between H_2 and H_2O_2 and between H_2 and UO_2^{2+} catalyzed on noble metal particles have been added.

4.2 Model description

The reaction set used to describe the fuel corrosion process is modified compared to that used previously, as numbered and illustrated in Fig. 4.1. The current model includes: (1) a complete reaction set for the α -radiolysis of water including the generation of, and the interactions between, the radiolysis products; (2) the oxidative dissolution (corrosion) of UO_2 supported by H_2O_2 reduction on both the UO_2 surface (reaction 2a) and noble metal particles (reaction 2b); (3) the reduction of oxidized surface species ($\text{U}^{\text{V}}/\text{U}^{\text{VI}}$) by H_2 oxidation on noble metal particles (reaction 3a) and of dissolved UO_2^{2+} either by reaction with H_2 in solution (reaction 3b) or with H_2 catalyzed on the fuel surface (reaction 3c); (4) the reaction of H_2O_2 with H_2 catalyzed by noble metal particles; (5) the scavenging of H_2O_2 in homogeneous solution by reaction with Fe^{2+} ; and (6) the decomposition of H_2O_2 to O_2 and H_2O (not shown in Fig. 4.1). In the model the rates of these processes are described by a series of one dimensional diffusion-reaction equations as described in Chapter 3 (Section 3.2).

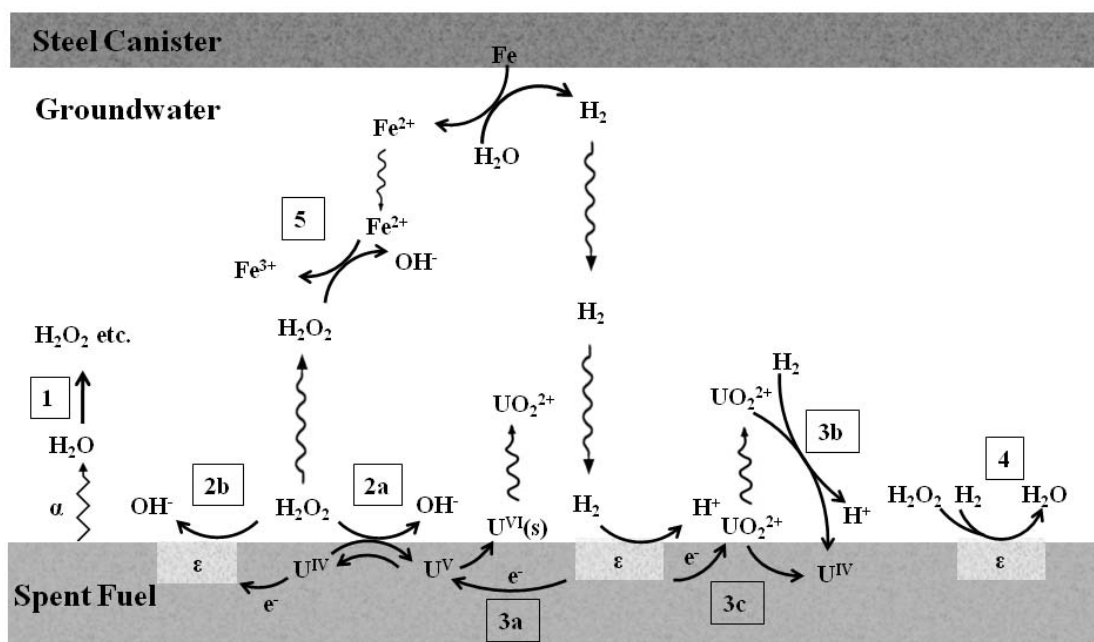


Fig. 4.1. Reactions included in the model for the α -radiolytic corrosion of spent nuclear fuel. This diagram is an improved version from Fig. 3.1 in Chapter 3.

4.2.1 Water radiolysis

The penetration depth of α -particles emitted by spent fuel into water is very short and a high concentration of radiolysis species is expected at the fuel/water interface. Due to the fractured nature of spent fuel, the accumulation of aqueous radiolysis species may occur locally within cracks, fission gas tunnels and porous grain boundaries. These features will be addressed in the future model development, and the present model focuses on the general corrosion of a uniform fuel surface.

A range of studies have calculated the dose rate profiles of α -radiation for different types of fuels using different approaches [4-7]. The α dose rate in water in contact with a spent

fuel bundle is determined by the source activity (which varies with different types of fuel, burnup and fuel age), the radiation energy and the distance from the source [8]. A typical energy of the alpha particles from fuel decay is 5 MeV, corresponding to a path length of $\sim 40 \mu\text{m}$ in water [9]. However, before reaching the fuel surface the alpha particles are attenuated by passage through the UO_2 matrix, and escape into the water with a reduced energy between 0 and 5 MeV. This was accounted for in the previous calculations [5, 6] by integrating all contributions as a function of the distance travelled within the fuel. The geometrical distribution of α dose rate in a water layer of $\sim 40 \mu\text{m}$ has been found to follow an exponential decay with distance from the fuel surface [5] as discussed in Section 3.3.2. According to the Bragg curve, which describes the extent of ionization along the radiation pathway [9], the radiolysis species are non-uniformly distributed along this pathway. Garisto et al. [4] adopted a different methodology [7, 10] using the thermal power of the fuel and the ratio between the specific stopping power values in water and in UO_2 . This led to an average energy of 2.5 MeV for the α particles emitted from the fuel surface, i.e., one half of the unattenuated energy assuming a uniform distribution of radionuclides and isotropic decay [4]. Based on this assumption, the authors calculated the range of α -radiation in water to be $13 \mu\text{m}$, corresponding to an energy of 2.5 MeV, and an average dose rate within this range. These different methodologies have been demonstrated to be in good agreement [6]. In Section 3.3.2 it is shown that, from the radiolytic corrosion perspective, it is reasonable to consider the α dose rate as uniformly distributed within this range. In this study, we adopted the values of α dose rate and range calculated by Garisto et al. [4] for the radionuclide inventories of CANDU used fuel.

The one-dimensional arrangement used to describe the fuel/groundwater interface remains the same as that described in Section 3.2.1 (Fig. 3.2). A thin layer of solution at the fuel/water interface with a thickness of 13 μm is designated the radiation zone. No radiolysis species are produced beyond this zone. The diffusion layer is the distance over which species can diffuse to, or from, the fuel surface and beyond which uniform concentrations are presumed to prevail. The bulk concentrations of H_2 and Fe^{2+} are assumed to depend on the corrosion behaviour of the steel vessel, and the concentrations of all radiolytic species and fuel corrosion products are assumed to be zero in the bulk solution. The thickness of the diffusion zone represents an arbitrary boundary beyond which the concentration of all species, irrespective of where they are produced, is assumed to become uniform. Clearly, this assumption is sensitive to the geometrical conditions within the failed container as discussed in Chapter 3. For a one-dimensional model, the previous calculations in Section 3.3.1 showed an insignificant dependence of the fuel corrosion rate on the chosen value of this thickness.

As stated in Section 1.4.1, the interaction of α -radiation with water yields a series of decomposition products (H_2 , H_2O_2 , H^\bullet , OH^\bullet , HO_2^\bullet , e_{aq}^- , H^+ and OH^-) [8, 11], among which the molecular species are dominant. Since H_2O_2 has been demonstrated to be the primary oxidant in the radiolytic corrosion of the fuel [12, 13], it was the only radiolysis product included in the previous model in Chapter 3.

Table 4.1. The primary yields (g-values) of α radiolysis species used in model calculations

Water decomposition species	g-value ($\mu\text{mol}/\text{J}$) [14]
-----------------------------	---

H ₂	0.1248
H ₂ O ₂	0.104
e _{aq} ⁻	0.0156
H [•]	0.0104
OH [•]	0.0364
HO ₂ [•]	0.0104
H ⁺	0.01872
OH ⁻	0.00312

In the present model, all the radiolysis species are included and their primary yields are expressed by g-values (the number of moles formed per joule of radiation energy absorbed), as listed in Table 4.1. The rate of radiolytic production for species i is calculated using the expression

$$R_i = D_R \cdot g_i \cdot \rho_{\text{H}_2\text{O}} \quad (0 \leq x \leq b) \quad (4.1)$$

where D_R is the dose rate representing the rate of energy deposited per unit of mass, g_i is the g-value of species i , and $\rho_{\text{H}_2\text{O}}$ is the density of water. Both oxidizing molecular and radical species (e.g. H₂O₂, O₂, OH[•]) and reducing species (e.g. H₂, H[•], e_{aq}⁻) are formed. After formation, these radiolytic species undergo diffusion and a series of chemical reactions (Table 4.2). All these species are used when calculating the consequences of aqueous radiolysis. However, in the simultaneous corrosion reactions only the molecular species (H₂O₂, O₂ and H₂) are considered, since the radical species, although reactive with the UO₂ surface, have low concentrations as a consequence of their short lifetimes.

Calculations for various radicals yield concentrations which are 2 to 5 orders of magnitude lower than those of the stable molecular products (Section 4.3.1 below). This approximation is consistent with other studies which also show the radical species produced by α -radiolysis have an insignificant impact on UO_2 corrosion compared to H_2O_2 [2, 12].

Table 4.2. Full radiolysis reaction set and rate constants/equilibrium constants used in model calculations [15, 16].

Reaction	Rate constant at 25°C (L mol ⁻¹ s ⁻¹ or s ⁻¹) ^a
$\text{H}_2\text{O} \xrightarrow{\alpha} \text{H}_2, \text{H}_2\text{O}_2, \text{e}_{\text{aq}}^-, \text{H}^\bullet, \text{OH}^\bullet, \text{HO}_2^\bullet, \text{H}^+, \text{OH}^-$	g-values in Table 4.1.
$\text{e}_{\text{aq}}^- + \text{e}_{\text{aq}}^- (+2\text{H}_2\text{O}) \rightarrow \text{H}_2 + 2\text{OH}^-$	7.26×10^9
$\text{e}_{\text{aq}}^- + \text{H}^\bullet (+\text{H}_2\text{O}) \rightarrow \text{H}_2 + \text{OH}^-$	2.76×10^{10}
$\text{e}_{\text{aq}}^- + \text{OH}^\bullet \rightarrow \text{OH}^-$	3.5×10^{10}
$\text{e}_{\text{aq}}^- + \text{H}_2\text{O}_2 \rightarrow \text{OH}^\bullet + \text{OH}^-$	1.4×10^{10}
$\text{e}_{\text{aq}}^- + \text{O}_2 \rightarrow \text{O}_2^-$	2.3×10^{10}
$\text{e}_{\text{aq}}^- + \text{HO}_2^\bullet \rightarrow \text{HO}_2^-$	1.3×10^{10}
$\text{e}_{\text{aq}}^- + \text{O}_2^- (+\text{H}_2\text{O}) \rightarrow \text{H}_2\text{O}_2 + 2\text{OH}^-$	1.3×10^{10}
$\text{H}^\bullet + \text{H}^\bullet \rightarrow \text{H}_2$	5.13×10^9
$\text{H}^\bullet + \text{OH}^\bullet \rightarrow \text{H}_2\text{O}$	1.1×10^{10}
$\text{H}^\bullet + \text{H}_2\text{O}_2 \rightarrow \text{OH}^\bullet + \text{H}_2\text{O}$	3.6×10^7

$\text{H}^\bullet + \text{O}_2 \rightarrow \text{HO}_2^\bullet$	1.3×10^{10}
$\text{H}^\bullet + \text{HO}_2^\bullet \rightarrow \text{H}_2\text{O}_2$	1.13×10^{10}
$\text{H}^\bullet + \text{O}_2^- \rightarrow \text{HO}_2^-$	1.13×10^{10}
$\text{H}^\bullet + \text{H}_2\text{O} \rightarrow \text{H}_2 + \text{OH}^\bullet$	4.58×10^{-5}
$\text{OH}^\bullet + \text{OH}^\bullet \rightarrow \text{H}_2\text{O}_2$	4.8×10^9
$\text{OH}^\bullet + \text{H}_2\text{O}_2 \rightarrow \text{HO}_2^\bullet + \text{H}_2\text{O}$	2.9×10^7
$\text{OH}^\bullet + \text{H}_2 \rightarrow \text{H}^\bullet + \text{H}_2\text{O}$	3.9×10^7
$\text{OH}^\bullet + \text{HO}_2^\bullet \rightarrow \text{O}_2 + \text{H}_2\text{O}$	8.8×10^9
$\text{OH}^\bullet + \text{O}_2^- \rightarrow \text{O}_2 + \text{OH}^-$	1.1×10^{10}
$\text{OH}^\bullet + \text{HO}_2^- \rightarrow \text{O}_2^- + \text{H}_2\text{O}$	8.1×10^9
$\text{H}_2\text{O}_2 \rightarrow 2\text{OH}^\bullet$	8.29×10^{-8}
$\text{HO}_2^\bullet + \text{HO}_2^\bullet \rightarrow \text{H}_2\text{O}_2 + \text{O}_2$	8.4×10^5
$\text{O}^- + \text{HO}_2^- \rightarrow \text{O}_2^- + \text{OH}^-$	7.8×10^8
$\text{O}^- + \text{O}_2 \rightarrow \text{O}_3^-$	3.7×10^9
$\text{O}^- + \text{H}_2 \rightarrow \text{H}^\bullet + \text{OH}^-$	1.3×10^8
$\text{O}_2^- + \text{HO}_2^\bullet (+\text{H}_2\text{O}) \rightarrow \text{H}_2\text{O}_2 + \text{O}_2 + \text{OH}^-$	1×10^8
$\text{O}_2^- + \text{O}_2^- (+2\text{H}_2\text{O}) \rightarrow \text{H}_2\text{O}_2 + \text{O}_2 + 2\text{OH}^-$	3×10^{-1}
$\text{O}_3^- \rightarrow \text{O}^- + \text{O}_2$	2.6×10^3
$\text{O}_3^- + \text{H}_2\text{O}_2 \rightarrow \text{O}_2 + \text{O}_2^- (+\text{H}_2\text{O})$	1.6×10^6

$\text{O}_3^- + \text{H}_2 \rightarrow \text{O}_2 + \text{H}^\bullet + \text{OH}^-$	2.5×10^5
$\text{O}_3^- + \text{HO}_2^- \rightarrow \text{O}_2 + \text{O}_2^- + \text{OH}^-$	8.9×10^5
Equilibrium reaction	K_{eq} at 25°C (mol L ⁻¹ or no unit) ^b
$\text{H}_2\text{O} \rightleftharpoons \text{H}^+ + \text{OH}^-$	$1.80 \times 10^{-16\text{c}}$
$\text{H}_2\text{O}_2 \rightleftharpoons \text{H}^+ + \text{HO}_2^-$	1.88×10^{-12}
$\text{H}_2\text{O}_2 + \text{OH}^- \rightleftharpoons \text{HO}_2^- + \text{H}_2\text{O}$	1.04×10^4
$\text{OH}^\bullet \rightleftharpoons \text{H}^+ + \text{O}^-$	1.88×10^{-12}
$\text{OH}^\bullet + \text{OH}^- \rightleftharpoons \text{O}^- + \text{H}_2\text{O}$	1.04×10^4
$\text{HO}_2^\bullet \rightleftharpoons \text{H}^+ + \text{O}_2^-$	1.54×10^{-5}
$\text{HO}_2^\bullet + \text{OH}^- \rightleftharpoons \text{O}_2^- + \text{H}_2\text{O}$	8.56×10^{10}
$\text{H}^\bullet \rightleftharpoons \text{H}^+ + \text{e}_{\text{aq}}^-$	2.78×10^{-10}
$\text{H}^\bullet + \text{OH}^- \rightleftharpoons \text{e}_{\text{aq}}^- + \text{H}_2\text{O}$	1.55×10^6

^a Unit for reaction rate constant: L mol⁻¹ s⁻¹ for second-order reactions; and s⁻¹ for first-order reactions. If water is provided in brackets, it is not counted when determining the reaction order.

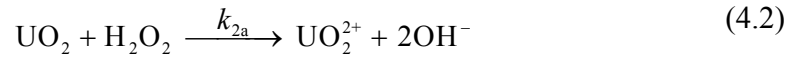
^b Unit for equilibrium constant: mol L⁻¹ for the reaction type A ↔ C + D; and no unit for A + B ↔ C + D.

^c The following definition of the equilibrium constant for the dissociation of water is used: $K_{\text{eq}}(\text{H}_2\text{O}) = [\text{H}^+][\text{OH}^-]/[\text{H}_2\text{O}]$, where $[\text{H}_2\text{O}]$ is 55.417 mol L⁻¹ at 25°C [15]. In the other equilibrium reactions involving H₂O, this value of $[\text{H}_2\text{O}]$ is also used.

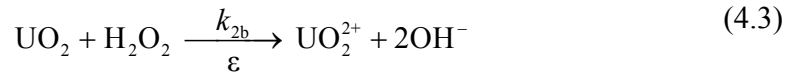
4.2.2 UO₂ oxidation by H₂O₂

Both the UO₂ surface and ϵ -particles can support the cathodic reduction of H₂O₂ to drive the anodic dissolution of UO₂ [17, 18]. Since the number density of ϵ -particles will vary with fuel burnup, the adoption of a single rate constant for the uniform cathodic reactivity of the fuel surface will not be able to account for the influence of an increasing number of ϵ -particles as burnup increases. The current model is improved by including two distinct reactions:

i) the direct reaction of UO₂ with H₂O₂, reaction (2a) in Fig. 4.1,



and; ii) the catalyzed oxidation of UO₂, reaction (2b) in Fig. 4.1, involving the galvanic coupling of H₂O₂ reduction on ϵ -particles to UO₂ oxidation:



In the previous model in Chapter 3, UO₂ oxidation/dissolution was assumed to proceed as a pseudo first order reaction, with the available UO₂ surface in excess compared to the oxidants, with an overall rate constant, k_2 ,



$$R_2 = k_2 \cdot [\text{H}_2\text{O}_2] \quad (x = 0) \quad (4.5)$$

In the absence of a measured rate constant for this reaction on actual spent fuel, a value of $7.33 \times 10^{-5} \text{ m s}^{-1}$ was adopted as an upper limit in the simulations of Nielsen et al. [19].

This limiting value was arbitrarily adopted in our previous model to avoid underestimating the experimentally demonstrated catalysis of corrosion by H_2O_2 reduction on ϵ -particles galvanically coupled to the UO_2 matrix. Some experimental evidence to support the adoption of this value was presented [20-22]. The use of this rate constant was considered conservative.

As stated above, the improved model separates this reaction into distinct reactions on UO_2 and ϵ -particles, reactions (2a) and (2b) in Fig. 4.1. Reaction (2a) is expressed as a first-order reaction with respect to $[\text{H}_2\text{O}_2]$

$$R_{2a} = k_{2a} \cdot [\text{H}_2\text{O}_2] \quad (x = 0) \quad (4.6)$$

The rate constant for the UO_2 oxidative dissolution adopted in the model, $k_{2a} = 1.0 \times 10^{-8} \text{ m s}^{-1}$, was measured on a pure UO_2 pellet fabricated by Westinghouse [1]. Recently, Nilsson et al. [23] and Pehrman et al. [1] have reported that only a small portion of the H_2O_2 consumed on a UO_2 surface resulted in UO_2 oxidation (see Section 4.2.6 below).

The catalytic reaction (2b) is also taken to be first-order with respect to H_2O_2 taking into account the surface fraction of ϵ -particles,

$$R_{2b} = k_{2b} \cdot s_\epsilon \cdot [\text{H}_2\text{O}_2] \quad (x = 0) \quad (4.7)$$

where s_ϵ is the fraction of fuel atoms that underwent fission to yield noble metal (ϵ) particles, e.g. 1.0 at.%. The experimental value for this catalytic rate constant k_{2b} is $6.92 \times 10^{-6} \text{ m s}^{-1}$ [24]. The total reaction rate is the sum of R_{2a} and R_{2b} :

$$R_{2_total} = R_{2a} + R_{2b} = k_{2a} \cdot [H_2O_2] + k_{2b} \cdot s_\epsilon \cdot [H_2O_2] \quad (x = 0) \quad (4.8)$$

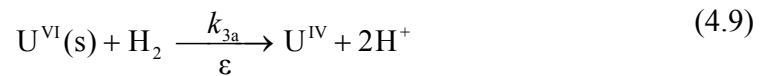
These reactions are taken to proceed unimpeded by the accumulation of corrosion product deposits, a situation that would prevail in the presence of a sufficient groundwater concentration of HCO_3^-/CO_3^{2-} , as in the previous model in Chapter 3.

The influence of the additional molecular oxidant, O_2 , was also considered. This oxidant can be formed directly by α -radiolysis or by H_2O_2 decomposition. However, sensitivity calculations show its inclusion has no significant effect on the fuel corrosion rate. This is not unexpected since the steady-state concentration of radiolytically-produced O_2 appears to be two orders of magnitude lower than that of H_2O_2 (see Section 4.3.1), and the rate constant for the reaction between O_2 and UO_2 is $1/200^{th}$ that of the reaction between H_2O_2 and UO_2 [13]. A similar conclusion was reached based on α -radiolysis simulations by Ekeroth et al. [12] and on experiments on UO_2 powder/pellets by Lousada et al. [2]. By contrast, on SIMFUEL the reaction with O_2 accounted for $\sim 30\%$ of the UO_2 corrosion since a significant amount of H_2O_2 was consumed by decomposition [2]. The consequences of H_2O_2 decomposition are discussed in Section 4.2.6.

4.2.3 U^V/U^{VI} reduction by H_2

Hydrogen has been shown to suppress UO_2 corrosion on a range of UO_2 materials ranging from spent fuel itself to α -doped UO_2 and SIMFUELS, which has been reviewed in Section 1.5.4.2. The main source of H_2 within a failed container is the anaerobic corrosion of the steel vessel, and dissolved H_2 concentrations as high as 0.038 mol L^{-1} are anticipated in sealed repositories [25]. There appear to be three possible pathways for reaction between U^V/U^{VI} and H_2 as numbered in Fig. 4.1.

Reaction (3a): A key mechanism for the inhibition of corrosion by H₂ has been demonstrated to be the galvanic coupling of H₂ oxidation on ε-particles to UO_{2+x} reduction on the fuel surface [20, 21, 26, 27], with the oxidation/dissolution process appearing to be reversed at the U^V stage [21]. As described in the previous model [22], the overall reaction can be expressed as involving a U^{VI} surface intermediate which can act as a precursor to dissolution, reaction (3a) in Fig. 4.1,

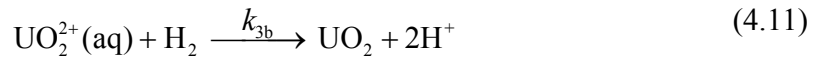


with a reaction rate R_{3a} , derived by Trummer et al. [28], to be

$$R_{3a} = k_{3a} \cdot s_\varepsilon \cdot [\text{H}_2] \quad (x = 0) \quad (4.10)$$

The measured rate constant (k_{3a}) was found to vary slightly with the amount of Pd present (added to simulate the presence of ε-particles) with values close to the diffusion controlled limit [28].

Reaction (3b): The reduction of dissolved UO₂²⁺ in the bulk of solution via a homogeneous reaction with H₂ [29], reaction (3b) in Fig. 4.1,

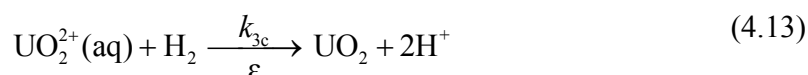


with the reaction rate determined by a second-order rate constant, k_{3b} ,

$$R_{3b} = k_{3b} \cdot [\text{H}_2] \cdot [\text{UO}_2^{2+}] \quad (0 \leq x \leq L) \quad (4.12)$$

This reaction is not expected to influence the release of radionuclides but only to lower the bulk concentration of UO_2^{2+} , assuming that the radionuclides (e.g. ^{99}Tc , ^{129}I , ^{79}Se , ^{135}Cs [30]) trapped within the fuel matrix are released irreversibly on UO_2 dissolution. The rate of this reaction is expected to be very low considering the low concentrations and the small rate constant, k_{3b} in Table 4.3.

Reaction (3c): Nilsson et al. [31] have claimed that the reaction (4.11) can also be catalyzed on the surface of ϵ -particles leading to a significant increase in its rate, based on experiments using Pd in aqueous UO_2^{2+} solution with a H_2 atmosphere. This surface catalytic reaction,



is shown as reaction (3c) in Fig. 4.1 and has a reaction rate given by

$$R_{3c} = k_{3c} \cdot s_\epsilon \cdot [\text{UO}_2^{2+}] \quad (x = 0) \quad (4.14)$$

Reaction (3c) is also not expected to change the release rate of radionuclides but only to lower the surface $[\text{UO}_2^{2+}]$. Sensitivity tests performed for this reaction show it has a marginal overall effect due to the low surface concentration of UO_2^{2+} . However, this reaction could have a larger impact in the presence of a high $[\text{UO}_2^{2+}]$ which could be the case when the behaviour in fuel fractures is considered.

4.2.4 Reaction between H_2O_2 and H_2

Catalysis of the reaction between H_2 and H_2O_2 has been demonstrated experimentally on Pd particles [32],



This reaction was found to be first order with respect to $[\text{H}_2\text{O}_2]$, but independent of H_2 pressure in the pressure range 1-40 bar [32]. Thus, the overall reaction rate can be expressed by

$$R_4 = k_4 \cdot s_\varepsilon \cdot [\text{H}_2\text{O}_2] \quad (0 \leq x \leq L) \quad (4.16)$$

where the reaction rate constant, k_4 , was measured to be $2.2 \times 10^{-5} \text{ m s}^{-1}$. This recombination reaction can reduce the surface concentrations of both H_2 and H_2O_2 . A sensitivity test has been performed and the surface $[\text{H}_2\text{O}_2]$ is shown to decrease marginally (7%) in the presence of this reaction compared to that in its absence.

4.2.5 Fenton reaction

Besides H_2 , the anaerobic corrosion of the steel vessel can produce Fe^{2+} ions that will react with H_2O_2 in the Fenton reaction and suppress radiolytic corrosion, which has been reviewed in Section 1.5.4.1.

As in the previous model in Chapter 3, the overall reaction is expressed as



which is a second order reaction [33] with a rate given by

$$R_5(\text{Fe}^{2+}) = 2R_5(\text{H}_2\text{O}_2) = -k_5[\text{Fe}^{2+}][\text{H}_2\text{O}_2] \quad (0 \leq x \leq L) \quad (4.18)$$

The rate of this reaction has been shown to be very sensitive to pH, temperature and salinity. Considering the long-term disposal conditions (e.g. pH 8-10, 25 °C, groundwater) [34-36], the value of k_5 has been assumed to be $1 \times 10^6 \text{ L mol}^{-1} \text{ s}^{-1}$ in this model [33]. Within the anticipated pH range, the solubility of Fe^{2+} is in the region of 10^{-6} to $10^{-4} \text{ mol L}^{-1}$, although the actual $[\text{Fe}^{2+}]$ could vary depending on the corrosion behaviour of the steel vessel [37].

4.2.6 H_2O_2 decomposition

The decomposition of H_2O_2 can form oxygen and water by the overall reaction,



It has been well established that this reaction follows first order kinetics, with an activation energy measured to be 42–65 kJ/mol over a wide range of temperatures [15, 38, 39]. However, the decomposition mechanism is not fully understood, the key question being whether or not the initiating step is H_2O_2 dissociation to form two hydroxyl radicals,



or the formation of some other intermediate that could occur on a metal/metal-oxide surface. Wren et al. [40] proposed a mechanism of H_2O_2 decomposition catalyzed by $\text{U}^{\text{IV}}/\text{U}^{\text{V}}$ surface species, but did not study the kinetics. Lousada and co-workers performed a series of experimental and density functional theory investigations [2, 41, 42] to show the formation of OH^\bullet will be a primary product during H_2O_2 decomposition on UO_2 and other transition metal oxide surfaces. Recently, Nilsson et al. [23] and

Pehrman et al. [1] studied the kinetics of the catalytic decomposition of H_2O_2 on different UO_2 pellets (pure UO_2 , doped UO_2 , and SIMFUEL) by monitoring the OH^\bullet production and concluded that the decomposition rate was virtually independent of matrix doping. They also measured the dissolution yield based on the ratio between the concentrations of dissolved U^{VI} and consumed H_2O_2 and attributed the difference between them to the catalytic decomposition of H_2O_2 . These results indicate that the surface-catalyzed decomposition of H_2O_2 is the major pathway for its consumption as opposed to H_2O_2 -promoted UO_2 dissolution. Interestingly, the dissolution yield for the pure UO_2 pellet (14%) was much higher than that for the SIMFUEL pellet (0.2%). Recent electrochemical results suggest this is most likely due to stabilization of the UO_2 lattice due to fission product doping [43].

The H_2O_2 decomposition rate is sensitive to many features including temperature, pH and the presence of solid/soluble catalysts [44-48]. The uncertainty about disposal conditions makes the choice of a rate constant arbitrary. Since H_2O_2 is the primary oxidant involved in fuel corrosion, and its decomposition by various reaction pathways would inevitably lead to a decrease in corrosion rate, a worst-scenario approach (estimating the highest corrosion rate) has been adopted when modelling the H_2O_2 decomposition. Therefore, $\text{Fe}^{\text{II/III}}$ catalyzed decomposition is not included in the model.

This model includes both the uncatalyzed homogeneous decomposition in solution and the catalyzed decomposition on the UO_2 surface. For the homogeneous decomposition, we adopted reaction (4.20) using a rate constant of $8.29 \times 10^{-8} \text{ s}^{-1}$ (k_{6a} in Table 4.3) [15]. For the surface-catalyzed decomposition, the rate constant, k_{6b} , was adopted from measurements on UO_2 pellets [1] using the relationship that 14% of H_2O_2 consumption

on the UO_2 surface (not including ϵ -particles) went to fuel dissolution and the remainder, 86%, to H_2O_2 decomposition. The reason for the low dissolution yield on SIMFUEL [23], as discussed above, was not clear. The possibility of decomposition catalyzed by ϵ -particles is under investigation and the preliminary results (Chapter 7) suggest this pathway is insignificant under corrosion conditions. Based on this study, decomposition of H_2O_2 catalyzed by ϵ -particles was not included in the present model.

4.3 Results and discussion

The mathematical model outlined above was numerically simulated using COMSOL Multiphysics based on the finite element method. The model was developed using the chemical engineering module and the diluted species transportation module of COMSOL Multiphysics (version 4.3.0.151, COMSOL Inc.). Calculations were performed to evaluate the effects of a full α -radiolysis reaction set, $[\text{Fe}^{2+}]_{\text{bulk}}$, $[\text{H}_2]_{\text{bulk}}$, the surface coverage by ϵ -particles and the age of the fuel. The default values of the simulation parameters are listed in Table 4.3. The parameters were maintained at the default values for all calculations unless otherwise stated.

Table 4.3. Default values of simulation parameters

Parameter	Symbol	Value	Unit
Diffusion layer thickness [22]	L	10^{-3}	m
Radiation zone thickness [4]	b	1.3×10^{-5}	m
Alpha radiation dose rate ^a [4]	D_R	9.03×10^5	Gy a ⁻¹
ϵ -particle coverage [49]	s_ϵ	0.01	–

UO ₂ pellet oxidation rate const. in H ₂ O ₂ [1]	k_{2a}	1.0×10^{-8}	m s^{-1}
H ₂ O ₂ /UO ₂ surf. reaction rate const. on ϵ [24]	k_{2b}	6.92×10^{-6}	m s^{-1}
H ₂ /U ^{VI} surf. reaction rate const. on ϵ [28]	k_{3a}	4×10^{-7}	m s^{-1}
H ₂ /UO ₂ ²⁺ bulk reaction rate const. [29]	k_{3b}	3.6×10^{-9}	$\text{L mol}^{-1} \text{s}^{-1}$
H ₂ /UO ₂ ²⁺ surf. reaction rate const. on ϵ [31]	k_{3c}	1.5×10^{-5}	m s^{-1}
H ₂ /H ₂ O ₂ surf. reaction rate const. on ϵ [32]	k_4	2.2×10^{-5}	m s^{-1}
Fe ²⁺ bulk reaction rate const. [33]	k_5	1×10^6	$\text{L mol}^{-1} \text{s}^{-1}$
H ₂ O ₂ homogeneous decomp. rate const. [15]	k_{6a}	8.29×10^{-8}	s^{-1}
H ₂ O ₂ surface-catalyzed decomp. rate const. ^b [1]	k_{6b}	6.14×10^{-8}	m s^{-1}

^a The unit Gy a^{-1} stands for the absorbed dose per annum. One gray (Gy) is the absorption of one joule of energy, in the form of ionizing radiation, per kilogram of matter. The value used in this model, $9.03 \times 10^5 \text{ Gy a}^{-1}$, is corresponding to CANDU fuel with a burnup of 220 MWh kgU^{-1} at 1000 years after discharge from reactor [4].

^b The rate constant of the surface catalyzed decomposition was calculated using the rate constant of the UO₂ oxidation and the dissolution yield (14%) measured on the Westinghouse UO₂ pellet [1]. The dissolution yield was based on the ratio between dissolved [U^{VI}] and consumed [H₂O₂] and the difference (86%) was attributed to catalytic decomposition of H₂O₂.

4.3.1 The effect of including a full α -radiolysis reaction set

The calculated results for the steady-state concentration profiles of radiolysis species and corrosion products are plotted in Fig. 4.2. The molecular species H₂O₂ and H₂ are predicted to have the highest concentrations, $\sim 10 \text{ nmol L}^{-1}$ near the fuel surface and

approaching zero along the diffusion pathway. The molecular product, O_2 , has a lower concentration of around 0.3 nmol L^{-1} including the contribution from H_2O_2 decomposition. Concentrations of the other radiolysis species (OH^\bullet , H^\bullet , O_2^- , HO_2^\bullet , e_{aq}^-) are 2-5 orders of magnitude lower than $[H_2O_2]$. Beyond the radiation zone ($x > 1.3 \times 10^{-2} \text{ mm}$), the $[OH^\bullet]$, $[H^\bullet]$ and especially $[e_{aq}^-]$ drop rapidly due to their high reactivity. The concentration of the corrosion product, UO_2^{2+} , exhibits a straight line if plotted linearly against distance, with a maximum of $\sim 1 \text{ nmol L}^{-1}$ at the fuel surface and decreasing to zero at the diffusion zone boundary ($x = L$). The slope of the line indicates a steady-state flux of UO_2^{2+} to the bulk solution, i.e., a constant UO_2 corrosion rate.

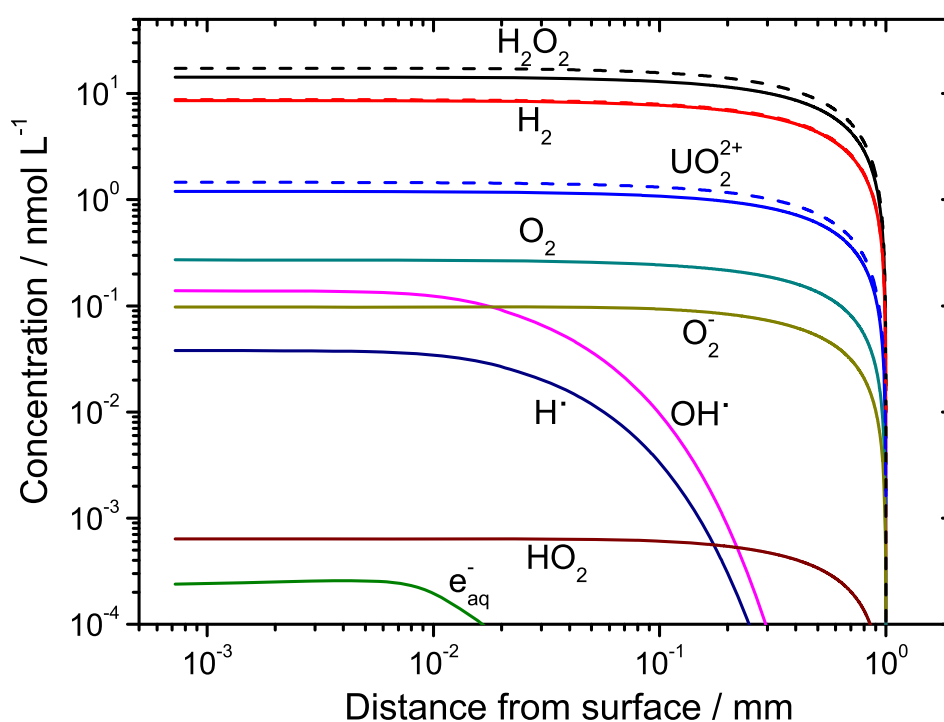


Fig. 4.2. The steady-state concentration profiles of α radiolysis species and dissolved UO_2^{2+} as a function of distance from the fuel surface; $[H_2]_{\text{bulk}} = [Fe^{2+}]_{\text{bulk}} = 0$. The solid

lines are the model predictions using the full radiolysis reaction set, and the dashed lines are the estimated concentrations based on the radiolytic production of only H_2O_2 and H_2 .

Fig. 4.2 also includes the concentration-distance profile (shown as dashed lines) calculated using only the radiolysis production of the molecular species (H_2O_2 , H_2). This simplified calculation uses a slightly larger g-value for H_2O_2 . In Table 4.1, the g-values used in the radiolysis reaction set are $0.104 \mu\text{mol J}^{-1}$ for H_2O_2 and $0.1248 \mu\text{mol J}^{-1}$ for H_2 . The simplified calculation makes a conservative assumption that all the other radicals are recombined to produce H_2O_2 ($2\text{OH}^\bullet \rightarrow \text{H}_2\text{O}_2$, $\text{H}^\bullet + \text{HO}_2^\bullet \rightarrow \text{H}_2\text{O}_2$) and the overall g-value of H_2O_2 is assumed to be $0.1248 \mu\text{mol J}^{-1}$ considering the mass balance during the radiolytic decomposition ($2\text{H}_2\text{O} \rightarrow \text{H}_2 + \text{H}_2\text{O}_2$). The comparison in Fig. 4.2 shows that the simplified calculation overestimates the $[\text{H}_2\text{O}_2]$ by $\sim 21\%$ and $[\text{H}_2]$ by $\sim 3\%$, leading to a faster corrosion rate which is indicated by an increase of $\sim 20\%$ in the $[\text{UO}_2^{2+}]$ profile. Although the plots in Fig. 4.2 assume no interference from the steel corrosion products, a similar trend is observed in the presence of external H_2 and Fe^{2+} , Fig. 4.3. The lower $[\text{H}_2\text{O}_2]$ calculated when using the full radiolysis reaction set is likely due to H_2O_2 consumption by reactions with reducing species such as H^\bullet , e_{aq}^- , and H_2 .

This simulation result is consistent with published literature. Corbel et al. [50] investigated the effect of α -radiolysis on UO_2 corrosion using a synchrotron alpha beam ($E_\alpha = 5\text{-}8 \text{ MeV}$). A linear dependence of the radiolytic $[\text{H}_2\text{O}_2]$ on absorbed radiation energy was observed, with a slope similar to the radiolytic yields of H_2O_2 . Pastina et al. [14] also measured H_2O_2 production in α -irradiated water ($E_\alpha = 5 \text{ MeV}$) saturated with Ar and found the observed production rate was slightly lower than the predicted rate based on a model which used only the radiolytic yield of H_2O_2 . It can be concluded that using

only the radiolytic production of H_2O_2 and H_2 to simulate α -radiolysis is an acceptable estimation and has the advantage of a much shorter calculation time. All the modelling calculations in this chapter, other than those presented in Fig. 4.2 and Fig. 4.3, still use the full radiolysis reaction set to account for the radiolysis effect. It is expected that the above simplification can be used for the more complicated calculations involved with 2-D and 3-D models.

4.3.2 Suppression of UO_2 corrosion by Fe^{2+}

Fig. 4.3 shows the influence of Fe^{2+} on the $[\text{H}_2\text{O}_2]$ profile in the $[\text{Fe}^{2+}]_{\text{bulk}}$ range of 0.01-1 $\mu\text{mol L}^{-1}$. In the absence of Fe^{2+} , H_2O_2 , at locations away from the UO_2 surface, is consumed only by its slow decomposition thus the maximum concentration is achieved. Beyond the radiation zone, the $[\text{H}_2\text{O}_2]$ decreases linearly along the diffusion pathway and reaches zero at the diffusion boundary indicating a constant H_2O_2 flux outwards to the bulk solution. For $[\text{Fe}^{2+}]_{\text{bulk}} \leq 0.01 \mu\text{mol L}^{-1}$, the consumption of $[\text{H}_2\text{O}_2]$ by the Fenton reaction is minor, the almost linear $[\text{H}_2\text{O}_2]$ profile approaching that calculated in the absence of Fe^{2+} . As the $[\text{Fe}^{2+}]_{\text{bulk}}$ increases to 0.1 $\mu\text{mol L}^{-1}$, the surface $[\text{H}_2\text{O}_2]$ rapidly decreases to one third of the maximum value. When approaching the solubility limit ($[\text{Fe}^{2+}]_{\text{bulk}} = 1 \mu\text{mol L}^{-1}$), the surface $[\text{H}_2\text{O}_2]$ is suppressed to only 10% of its maximum value, and beyond a distance from the fuel surface of 0.3mm the H_2O_2 is effectively completely consumed.

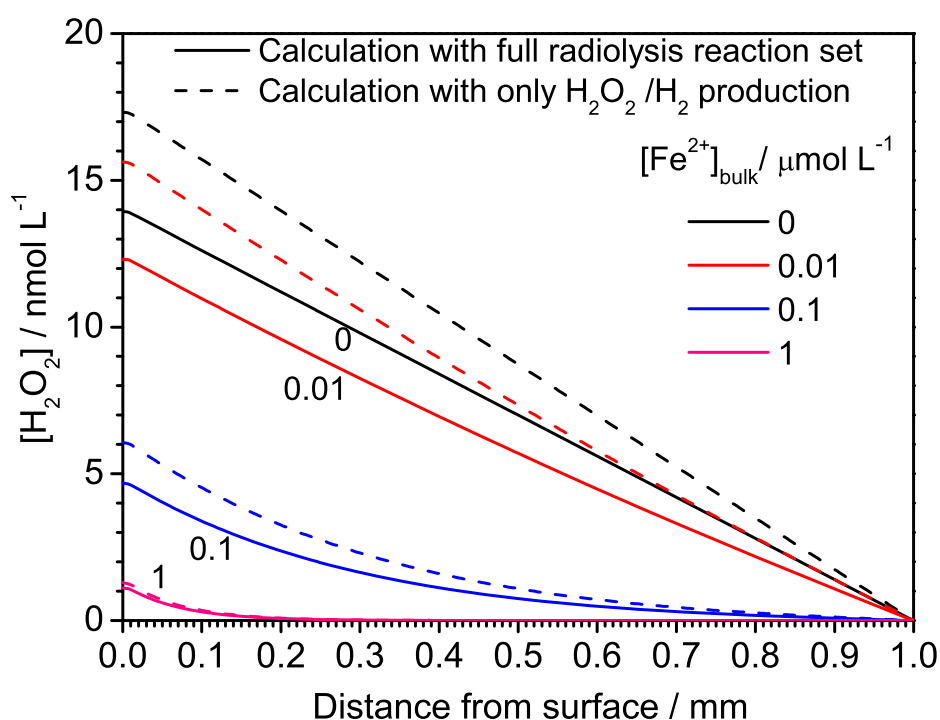


Fig. 4.3. Steady-state $[\text{H}_2\text{O}_2]$ profiles calculated for various bulk $[\text{Fe}^{2+}]$; $[\text{H}_2]_{\text{bulk}} = 0.01 \mu\text{mol L}^{-1}$. The solid lines are the model predictions using the full radiolysis reaction set, and the dashed lines are the estimated concentrations based on only radiolytic production of H_2O_2 and H_2 .

The decrease of $[\text{H}_2\text{O}_2]$ by reaction with Fe^{2+} can significantly reduce the fuel corrosion rate. This effect of Fe^{2+} also depends on the concentration of the other steel corrosion product, H_2 . Fig. 4.4 shows the fuel corrosion rate (expressed as a flux of dissolved UO_2^{2+} away from the fuel surface) as a function of $[\text{Fe}^{2+}]_{\text{bulk}}$ in the presence of different $[\text{H}_2]_{\text{bulk}}$. In general, The UO_2^{2+} flux decreases rapidly as $[\text{Fe}^{2+}]$ increases from 0.01 to 0.1 $\mu\text{mol L}^{-1}$. For the highest $[\text{H}_2]_{\text{bulk}}$ (0.1 $\mu\text{mol L}^{-1}$), fuel corrosion is completely suppressed for $[\text{Fe}^{2+}]_{\text{bulk}} > 0.07 \mu\text{mol L}^{-1}$, while for a lower $[\text{H}_2]_{\text{bulk}}$ (0.01 $\mu\text{mol L}^{-1}$), complete

suppression requires a bulk Fe^{2+} concentration of $1.5 \mu\text{mol L}^{-1}$. It is noticed that, when $[\text{Fe}^{2+}]$ is greater than $4.2 \mu\text{mol L}^{-1}$ even the radiolytically produced H_2 can completely suppress fuel corrosion without any external H_2 . This conclusion is in general agreement with the calculation of Jonsson et al. [51] considering the different fuel age (1000 vs. 100 years) and burnup (5-10 times lower for CANDU fuels compared to LWR fuels considered by Jonsson et al.).

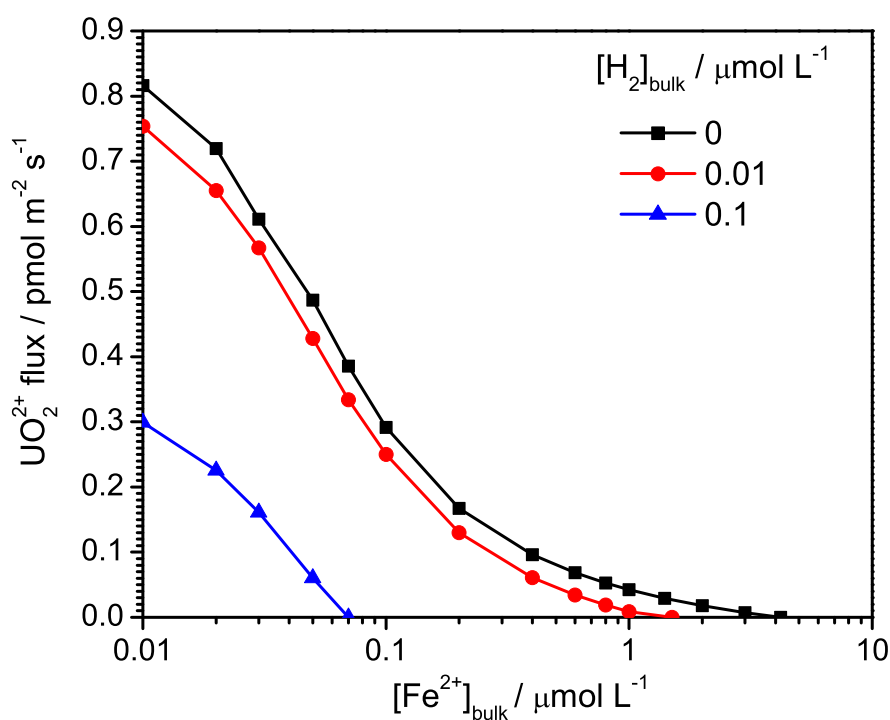


Fig. 4.4. The calculated diffusive flux of UO_2^{2+} (equivalent to UO_2 corrosion rate) as a function of bulk Fe^{2+} concentration; $[\text{H}_2]_{\text{bulk}} = 0, 0.01$ and $0.1 \mu\text{mol L}^{-1}$.

In the previous model in Chapter 3, calculations indicated that the corrosion rate was only reduced at an $[\text{Fe}^{2+}]$ of $1 \mu\text{mol L}^{-1}$ to $\sim 60\%$ of the value calculated ignoring any influence of Fe^{2+} . At the fuel surface the influence of Fe^{2+} is determined by the relative

rates of H_2O_2 consumption by corrosion and the Fenton reaction, and the much greater sensitivity of the corrosion rate to $[\text{Fe}^{2+}]$ is primarily due to the changes in the model for UO_2 corrosion (Section 4.2.2). In this revised model the rate constant for H_2O_2 -driven corrosion directly on the UO_2 surface (reaction (2a), Fig. 4.1) has been reduced by 3 orders of magnitude and the rate of reaction (2b) for corrosion catalyzed by H_2O_2 reduction on noble metal particles is greatly attenuated by the small percentage (1%) of particle coverage adopted. This significant reduction in overall fuel corrosion rate renders this rate much more sensitive to $[\text{Fe}^{2+}]$. Although relatively small by comparison, the incorporation of the full radiolysis reaction set also contributes to the enhanced effect.

4.3.3 Suppression of UO_2 corrosion by H_2

There are two possible mechanisms by which H_2 can suppress fuel corrosion: (i) it can suppress the radiolytic production of H_2O_2 by reactions in the radiolysis reaction set such as



a chain reaction which becomes efficient when the $[\text{H}_2]$ is sufficiently high compared to the $[\text{H}_2\text{O}_2]$; (ii) H_2 can act as a reductant by catalytic reaction on noble metal particles (reaction (3a) in Fig. 4.1), and possibly also reverse the corrosion reaction via reactions (3b) and (3c) in Fig. 4.1 as described in Section 2.3.

Experimental studies showed that the presence of small concentrations of H_2 had only a minor effect on H_2O_2 production by α -radiolysis [14] and that any H_2 effect is strongly

dependent on α dose rate and $[H_2]$ [49]. The calculations in Fig. 4.5 show the influence of H_2 , at concentrations of 0.01 to 1 $\mu\text{mol L}^{-1}$, on the $[H_2O_2]$ profiles at two different $[Fe^{2+}]_{\text{bulk}}$. In contrast to the effect of the Fenton reaction (Fig. 4.3) the $[H_2O_2]$ is suppressed by $< 30\%$ at these concentrations, consistent with the experimental expectations [14]. This demonstrates that the suppression of H_2O_2 production by H_2 is a relatively small contribution to the inhibiting effect of H_2 on fuel corrosion, consistent with the conclusions by Trummer et al. [49].

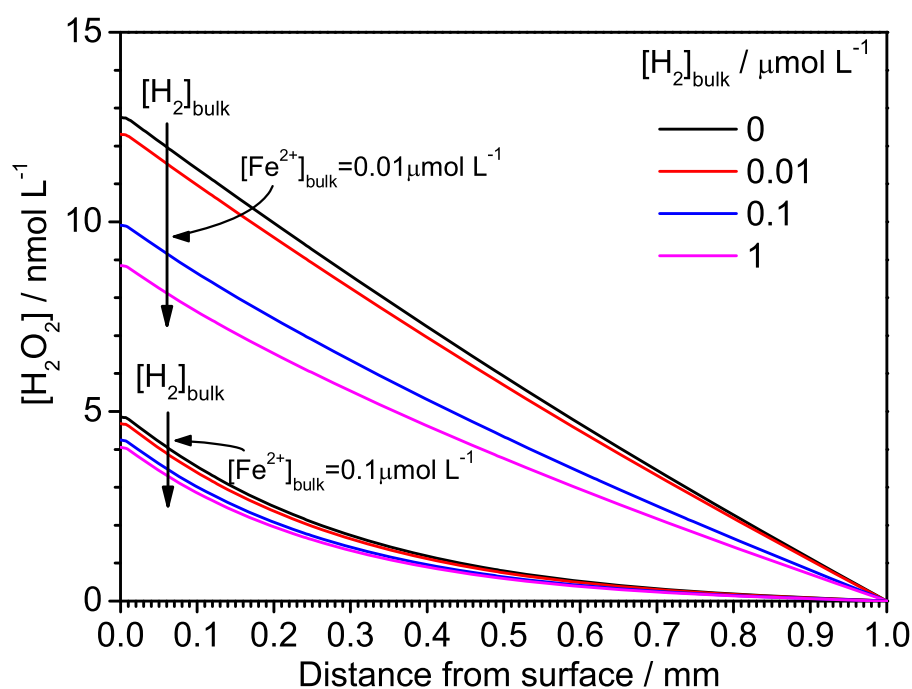


Fig. 4.5. Steady-state $[H_2O_2]$ profiles calculated for various bulk H_2 concentrations; $[Fe^{2+}]_{\text{bulk}} = 0.01$ and $0.1 \mu\text{mol L}^{-1}$ as noted by arrows.

Fig. 4.6 shows the UO_2^{2+} flux (corrosion rate) is significantly suppressed as the bulk $[H_2]$ increases, which is consistent with the calculations in the previous model [22]. A close-

to-linear decrease is obtained, and the UO_2 corrosion rate reaches zero for a specific $[\text{H}_2]_{\text{bulk}}$ (e.g. $0.202 \mu\text{mol L}^{-1}$ for $[\text{Fe}^{2+}]_{\text{bulk}} = 0$) indicating that the rate of UO_2 oxidation/dissolution by H_2O_2 is balanced by the rate of its reduction by H_2 . This concentration can be considered the critical H_2 concentration, $[\text{H}_2]_{\text{crit}}$, at which fuel corrosion is completely suppressed. The critical $[\text{H}_2]$ is about one order of magnitude less than that calculated previously [22]. This can be attributed partially to the new reaction scheme and rate constants adopted for UO_2 corrosion and also the use of a full reaction set for radiolysis. Trummer et al. [49] have also calculated the $[\text{H}_2]_{\text{crit}}$ required to prevent fuel corrosion for α -radiolysis in a closed system. For the same conditions ($D_{\text{R}} = 9.03 \times 10^5 \text{ Gy a}^{-1}$, $s_{\text{e}} = 1\%$, and $[\text{Fe}^{2+}] = 0$), they calculated $[\text{H}_2]_{\text{crit}}$ to be $0.0263 \mu\text{mol L}^{-1}$ comparing to our value of $0.202 \mu\text{mol L}^{-1}$. One reason for this difference could be that our model is for an open system which connects with the surrounding groundwater environment, whereas that of Trummer et al. is for a closed system.

A second source of H_2 is radiolytic production. However, the calculated steady-state concentration of radiolytic H_2 at the fuel surface appears to be too low ($< 0.01 \mu\text{mol L}^{-1}$, Fig. 4.2) to have a significant effect on UO_2 corrosion and its effect would be easily masked by the influence of external H_2 at a high $[\text{H}_2]_{\text{bulk}}$. A sensitivity test for the influence of radiolytic H_2 was performed for low $[\text{H}_2]_{\text{bulk}}$ (0 and $0.01 \mu\text{mol L}^{-1}$). Removal of the radiolytic H_2 from the calculations leads to an increase in fuel corrosion rate by $\sim 10\%$ for both $[\text{H}_2]_{\text{bulk}} = 0$ and $0.01 \mu\text{mol L}^{-1}$.

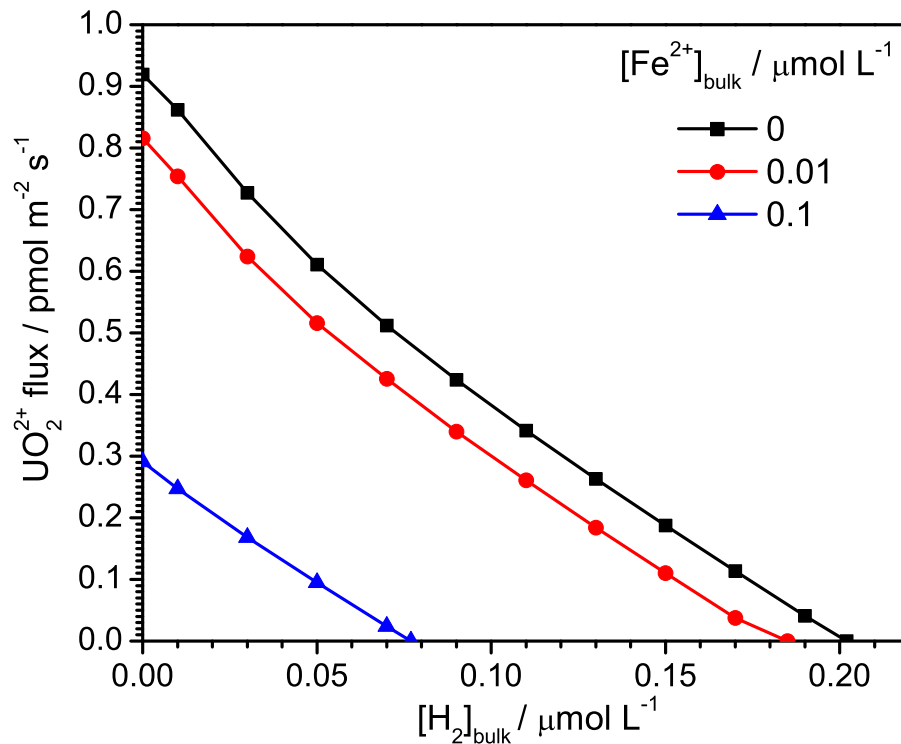


Fig. 4.6. The calculated diffusive flux of UO_2^{2+} (equivalent to UO_2 corrosion rate) as a function of bulk H_2 concentration; $[\text{Fe}^{2+}]_{\text{bulk}}=0, 0.01$ and $0.1 \mu\text{mol L}^{-1}$.

Since the α -radiation fields associated with the fuel decay as the fuel ages, the $[\text{H}_2]$ requirement for complete suppression of fuel corrosion ($[\text{H}_2]_{\text{crit}}$) has been calculated as a function of decay time for a CANDU fuel bundle with a burnup of 220 MWh kgU^{-1} , Fig. 4.7. As expected, the $[\text{H}_2]_{\text{crit}}$ decreases markedly with time since emplacement in the repository. The increase in the H_2 requirement over the first 50 years reflects the accumulation of α -emitters as a consequence of the short-term γ/β decay of radionuclides within the fuel.

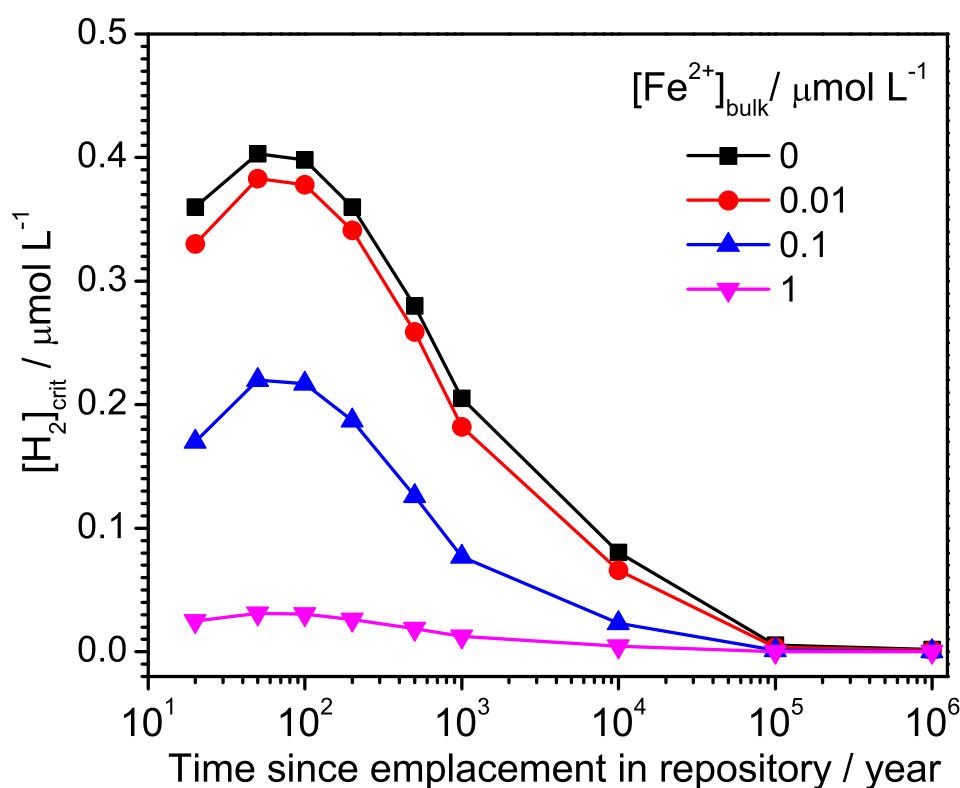


Fig. 4.7. The calculated $[H_2]_{crit}$ required to completely suppress fuel corrosion as a function of time since emplacement in repository at different $[Fe^{2+}]_{bulk}$.

Fig. 4.7 also shows the influence of $[Fe^{2+}]_{bulk}$ on $[H_2]_{crit}$. The influence of Fe^{2+} is marked, the $[H_2]$ requirement dropping by an order of magnitude as $[Fe^{2+}]_{bulk}$ increases from 0 to $1 \mu\text{mol L}^{-1}$. The trend is similar to that modelled by Jonsson et al. [51] as described in Section 1.5.5. The higher $[H_2]_{crit}$ calculated by Jonsson et al. reflects the much higher burnup (about 5–10 times) of Swedish LWR fuel compared to CANDU fuel. This decrease in required $[H_2]_{crit}$ is consistent with experimental studies showing there is a threshold α -activity (corresponding to fuel within the age range 3000–55000 years) below

which no measurable effect of alpha radiolysis on fuel dissolution could be observed [52-55].

4.3.4 The influence of fuel burnup

By separating the reactions catalyzed on ϵ -particles from those on the UO_2 surface (as described in Section 4.2.2) it is possible to attempt an estimate of the influence on corrosion of fuel burnup which determines the number density of ϵ -particles.

Fig. 4.8 shows the corrosion rate as a function of ϵ -particle surface fraction (s_ϵ) for various $[\text{H}_2]_{\text{bulk}}$. As expected the effect of the surface fraction of ϵ -particles is very dependent on the $[\text{H}_2]_{\text{bulk}}$. For a low $[\text{H}_2]$ ($0.1 \mu\text{mol L}^{-1}$), the rate first increases until s_ϵ reaches 2.5% and then decreases. This reflects the balance between the catalytic effect of the ϵ -particles on both oxidation and reduction reactions, reaction (2b) and (3a) in Fig. 4.1. The maximum rate is achieved at an intermediate ϵ -particle surface fraction. When $[\text{H}_2]_{\text{bulk}}$ increases, the reduction reaction (3a) begins to dominate over the oxidation reaction (2b) leading to a decrease in corrosion rate with increasing s_ϵ . At $[\text{H}_2]_{\text{bulk}} = 0.15 \mu\text{mol L}^{-1}$, an ϵ -particle fraction greater than 2.5% would result in complete suppression of fuel corrosion. As $[\text{H}_2]_{\text{bulk}}$ increases to $0.2 \mu\text{mol L}^{-1}$, an even lower ϵ -particle fraction (i.e., fuel burnup) is required for effective inhibition of corrosion. This observation is consistent with experimental observations that a higher fraction of Pd (as surrogate ϵ -particles) results in a lower UO_2 dissolution rate [24] and that an increase in size and number density of ϵ -particles suppresses the corrosion potential on a series of SIMFUELS [25, 27]. While the result for low $[\text{H}_2]_{\text{bulk}}$ is consistent with published observations that the highest fuel corrosion rates are achieved at intermediate burnups [56, 57], caution

should be exercised when making the comparison since the experiments were performed on spent fuel.

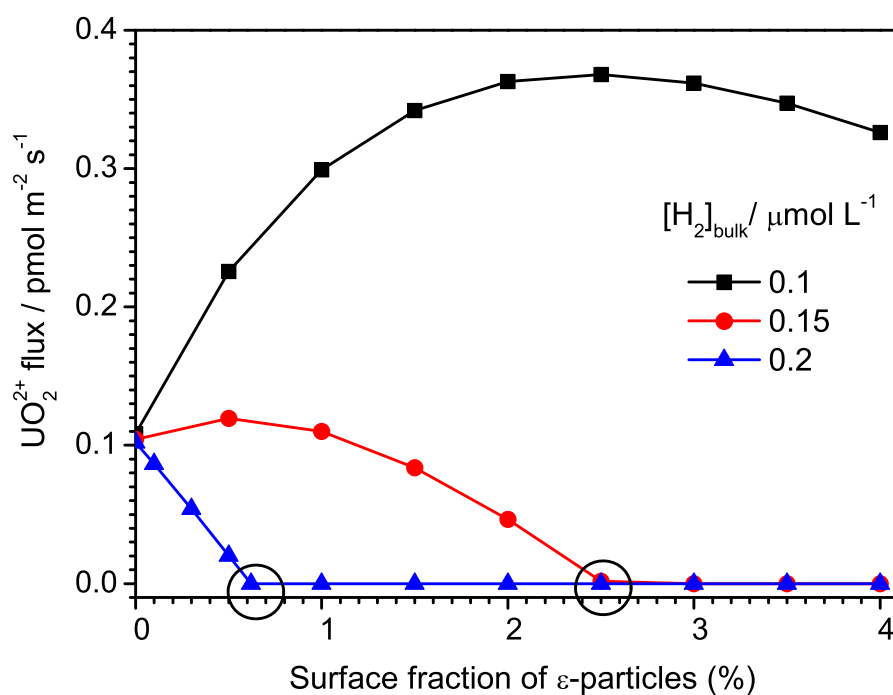


Fig. 4.8. The calculated diffusive flux of UO_2^{2+} (equivalent to UO_2 corrosion rate) as a function of ϵ -particle fraction for different bulk H_2 concentrations; $[Fe^{2+}]_{bulk} = 0.01\ \mu mol\ L^{-1}$.

4.4 Summary and conclusions

An improved model for nuclear fuel corrosion inside a failed waste container has been developed. A full α -radiolysis reaction set has been incorporated and the analysis shows that a simplified calculation which only accounts for the radiolytic production of H_2O_2/H_2 would provide a reasonable and conservative approximation, only overestimating H_2O_2 production and UO_2 corrosion rate by $\sim 20\%$. Instead of assuming a single general

reaction of H_2O_2 with the fuel surface, the direct reaction of UO_2 with H_2O_2 and the galvanically-coupled oxidation by H_2O_2 reduction on noble metal (ϵ) particles are both included. This allows the adoption of more experimentally justified rate constants and, by specifying the surface fraction of ϵ -particles, makes the model sensitive to fuel burnup. The surface-catalyzed decomposition of H_2O_2 appears to be the major pathway for H_2O_2 consumption on UO_2 and this effect has been included in this improved model.

The calculated fuel corrosion rate is very sensitive to $[\text{Fe}^{2+}]_{\text{bulk}}$ produced by corrosion of the steel vessel. When the $[\text{Fe}^{2+}]_{\text{bulk}}$ is greater than $4.2 \mu\text{mol L}^{-1}$ even the radiolytically produced H_2 alone can suppress fuel corrosion without assistance from external H_2 for CANDU fuel with an age of 1000 years or larger. The ability of H_2 to suppress fuel corrosion is shown to be sensitive to fuel burnup (number/density of ϵ -particles) and a complete suppression of corrosion can be achieved at bulk H_2 concentrations in the order of $0.1 \mu\text{mol L}^{-1}$. The small difference between the calculation results and previous experimental/modelling data is likely due to the different fuel types used in different studies and the uncertainties associated with different disposal conditions.

4.5 References

- [1] R. Pehrman, M. Trummer, C.M. Lousada, and M. Jonsson, On the redox reactivity of doped UO_2 pellets – Influence of dopants on the H_2O_2 decomposition mechanism, *J. Nucl. Mater.* 430 (2012) 6-11.
- [2] C.M. Lousada, M. Trummer, and M. Jonsson, Reactivity of H_2O_2 towards different UO_2 -based materials: The relative impact of radiolysis products revisited, *J. Nucl. Mater.* 434 (2013) 434-439.
- [3] D.W. Shoosmith, The Chemistry/Electrochemistry of Spent Nuclear Fuel as a Wasteform, in "Uranium: Cradle to Grave", edited by P. Burns, and G. Sigmon, Mineralogical Society of Canada, Short Course Series Vol 43, 337-368 (2013) and references therein.

- [4] F. Garisto, D.H. Barber, E. Chen, A. Ingot, and C.A. Morrison, Alpha, Beta and Gamma Dose Rates in Water in Contact with Used CANDU Fuel, Report NWMO TR-2009-27, Nuclear Waste Management Organization, Toronto, ON, 2009.
- [5] F. Nielsen, and M. Jonsson, Geometrical α - and β -dose distributions and production rates of radiolysis products in water in contact with spent nuclear fuel, *J. Nucl. Mater.* 359 (2006) 1-7.
- [6] A. Poulesquen, C. Jégou, and S. Peugeot, Determination of alpha dose rate profile at the UO_2 /water interface, in "Scientific Basis for Nuclear Waste Management XXIX.", edited by P. Van Iseghem, Material Research Society (Mater. Res. Soc. Symp. Proc. 932), Warrendale, PA, 2006, p. 505-512.
- [7] S. Sunder, Calculation of radiation dose rates in a water layer in contact with used CANDU UO_2 fuel, *Nucl. Tech.* 122 (1998) 211-221.
- [8] J.W.T. Spinks, and R.J. Woods, An Introduction to Radiation Chemistry, The Third Edition, John Wiley and Sons Inc., New York, 1990.
- [9] A. Poulesquen, and C. Jégou, Influence of Alpha radiolysis of water on UO_2 matrix alteration: chemical/transport model, *Nucl. Tech.* 160 (2007) 337-345.
- [10] F. Garisto, J. Avis, N. Calder, A. D'Adrea, P. Gierszewski, C. Kitson, T. Melnyk, K. Wei, and L. Wojciechowski, Third Case Study - Defective Container Scenario, Report 06219-REP-01200-10126-R00, Ontario Power Generation, Toronto, ON, 2004.
- [11] G. Choppin, J.O. Liljenzin, and J. Rydberg, Radiochemistry and nuclear chemistry, Butterworth-Heinemann, Oxford, 2001.
- [12] E. Ekeröth, O. Roth, and M. Jonsson, The relative impact of radiolysis products in radiation induced oxidative dissolution of UO_2 , *J. Nucl. Mater.* 355 (2006) 38-46.
- [13] D.W. Shoesmith, Fuel corrosion waste process under waste disposal conditions, *J. Nucl. Mater.* 282 (2000) 1-31.
- [14] B. Pastina, and J.A. LaVerne, Effect of Molecular Hydrogen on Hydrogen Peroxide in Water Radiolysis, *J. Phys. Chem. A* 105 (2001) 9316-9322.
- [15] A.J. Elliot, and D.M. Bartels, The Reaction Set, Rate Constants and g-Values for the Simulation of the Radiolysis of Light Water over the Range 20° to 350°C Based on Information Available in 2008, Report 153-127160-450-001, AECL, Mississauga, ON, 2009.
- [16] J. Joseph, B. Seonchoi, P. Yakabuskie, and J.C. Wren, A combined experimental and model analysis on the effect of pH and $\text{O}_2(\text{aq})$ on γ -radiolytically produced H_2 and H_2O_2 , *Radiation Physics and Chemistry* 77 (2008) 1009-1020.
- [17] J.S. Goldik, J.J. Noël, and D.W. Shoesmith, The electrochemical reduction of hydrogen peroxide on uranium dioxide electrodes in alkaline solution, *J. of Electroanal. Chem.* 582 (2005) 241-248.
- [18] J.S. Goldik, J.J. Noël, and D.W. Shoesmith, The Effects of Simulated Fission Products in the Reduction of Hydrogen Peroxide on Simulated Nuclear Fuel Electrodes, *J. Electrochem. Soc.* 153 (2006) E151-E159.

- [19] F. Nielsen, and M. Jonsson, Simulations of H₂O₂ concentration profiles in the water surrounding spent nuclear fuel taking mixed radiation fields and bulk reactions into account, *J. Nucl. Mater.* 374 (2008) 281-285.
- [20] M.E. Broczkowski, J.J. Noël, and D.W. Shoesmith, The inhibiting effects of hydrogen on the corrosion of uranium dioxide under nuclear waste disposal conditions, *J. Nucl. Mater.* 346 (2005) 16-23.
- [21] M.E. Broczkowski, P.G. Keech, J.J. Noël, and D.W. Shoesmith, Corrosion of Uranium Dioxide Containing Simulated Fission Products in Dilute Hydrogen Peroxide and Dissolved Hydrogen, *J. Electrochem. Soc.* 157 (2010) C275-C281.
- [22] L. Wu, Y. Beauregard, Z. Qin, S. Rohani, and D.W. Shoesmith, A model for the influence of steel corrosion products on nuclear fuel corrosion under permanent disposal conditions, *Corros. Sci.* 61 (2012) 83-91.
- [23] S. Nilsson, and M. Jonsson, H₂O₂ and radiation induced dissolution of UO₂ and SIMFUEL pellets, *J. Nucl. Mater.* 410 (2011) 89-93.
- [24] M. Trummer, O. Roth, and M. Jonsson, H₂ inhibition of radiation induced dissolution of spent nuclear fuel, *J. Nuc. Mat.* 383 (2009) 226-230.
- [25] M.E. Broczkowski, D. Zagidulin, and D.W. Shoesmith, The Role of Dissolved Hydrogen on the Corrosion/Dissolution of Spent Nuclear Fuel, in: "Nuclear Energy and the Environment", American Chemical Society Symposium, 2010, Vol.1046, Chapter 26, pp. 349-380
- [26] D.W. Shoesmith, The Role of Dissolved Hydrogen on the Corrosion/Dissolution of Spent Nuclear Fuel, Report NWMO TR-2008-19, Nuclear Waste Management Organization, Toronto, ON, 2008.
- [27] M.E. Broczkowski, J.J. Noël, and D.W. Shoesmith, The influence of dissolved hydrogen on the surface composition of doped uranium dioxide under aqueous corrosion conditions, *J. of Electroanal. Chem.* 602 (2007) 8-16.
- [28] M. Trummer, S. Nilsson, and M. Jonsson, On the effects of fission product noble metal inclusions on the kinetics of radiation induced dissolution of spent nuclear fuel, *J. Nucl. Mater.* 378 (2008) 55-59.
- [29] E. Ekeröth, M. Jonsson, T.E. Eriksen, K. Ljungqvist, S. Kovacs, and I. Puigdomenech, Reduction of UO₂²⁺ by H₂, *J. Nucl. Mater.* 334 (2004) 35-39.
- [30] J. Bruno, and R.C. Ewing, Spent Nuclear Fuel, *Elements* 2 (2006) 343-349.
- [31] S. Nilsson, and M. Jonsson, On the catalytic effects of Pd(s) on the reduction of UO₂²⁺ with H₂ in aqueous solution, *J. Nucl. Mater.* 374 (2008) 290-292.
- [32] S. Nilsson, and M. Jonsson, On the catalytic effects of UO₂(s) and Pd(s) on the reaction between H₂O₂ and H₂ in aqueous solution, *J. Nucl. Mater.* 372 (2008) 160-163.
- [33] F.J. Millero, and S. Sotolongo, The oxidation of Fe(II) with H₂O₂ in seawater, *Geochim. Cosmochim. Acta* 53 (1989) 1867-1873.

- [34] F. Garisto, T. Kempe, and P. Gierszewski, Technical Summary of the Safety Aspects of the Deep Geological Repository Concept for Used Nuclear Fuel, Report NWMO TR-2009-12, Nuclear Waste Management Organization, Toronto, ON, 2009.
- [35] D.G. Bennett, and R. Gens, Overview of European concepts for high-level waste and spent fuel disposal with special reference waste container corrosion, *J. Nucl. Mater.* 379 (2008) 1-8.
- [36] J. Kaija, K. Rasilainen, and R. Blomqvist, The use of selected safety indicators (concentrations, fluxes) in the assessment of radioactive waste disposal - Report 6, Report YST-114, Geological Survey of Finland - Nuclear Waste Disposal Research, 2003.
- [37] W. Xu, K. Daub, X. Zhang, J.J. Noël, D.W. Shoesmith, and J.C. Wren, Oxide formation and conversion on carbon steel in mildly basic solutions, *Electrochim. Acta* 54 (2009) 5727-5738.
- [38] C.C. Lin, F.R. Smith, N. Ichikawa, T. Baba, and M. Itow, Decomposition of Hydrogen Peroxide at Elevated Temperatures, *Inter. J. of Chem. Kinetics* 23 (1991) 971-987.
- [39] A. Hiroki, and J.A. LaVerne, Decomposition of Hydrogen Peroxide at Water-Ceramic Oxide Interface, *J. Phys. Chem. B* 109 (2005) 3364-3370.
- [40] J.C. Wren, D.W. Shoesmith, and S. Sunder, Corrosion Behavior of Uranium Dioxide in Alpha Radiolytically Decomposed Water, *J. Electrochem. Soc.* 152 (2005) B470.
- [41] C.M. Lousada, and M. Jonsson, Kinetics, Mechanism, and Activation Energy of H_2O_2 Decomposition on the Surface of ZrO_2 , *J. Phys. Chem. C* 114 (2010) 11202-11208.
- [42] C.M. Lousada, A.J. Johansson, T. Brinck, and M. Jonsson, Mechanism of H_2O_2 Decomposition on Transition Metal Oxide Surfaces, *J. Phys. Chem. C* 116 (2012) 9533-9543.
- [43] M. Razdan, and D.W. Shoesmith, Influence of Trivalent-Dopants on the Structural and Electrochemical Properties of Uranium Dioxide (UO_2), *J. Electrochem. Soc.* 161 (2014) H105-H113.
- [44] F.R. Duke, and T.W. Haas, The homogeneous base-catalyzed decomposition of hydrogen peroxide, *J. Phys. Chem.* 65 (1961) 304-306.
- [45] H.M. Cota, T. Katan, M. Chin, and F.J. Schoenweis, Decomposition of Dilute Hydrogen Peroxide in Alkaline Solutions, *Nature* 203 (1964) 1281.
- [46] C. Walling, R.E. Partch, and T. Weil, Kinetics of the Decomposition of Hydrogen Peroxide Catalyzed by Ferric Ethylenediaminetetraacetate Complex, *Pro. Nat. Acad. Sci.* 72 (1975) 140-142.
- [47] O. Spalek, J. Balej, and I. Paseka, Kinetics of the decomposition of hydrogen peroxide in alkaline solutions, *J. Chem. Soc. Faraday Trans. 1.* 78 (1982) 2349-2359.
- [48] J.F. Perez-Benito, Iron(III)-Hydrogen Peroxide Reaction: Kinetic Evidence of a Hydroxyl-Mediated Chain Mechanism, *J. Phys. Chem. A* 108 (2004) 4853-4858.
- [49] M. Trummer, and M. Jonsson, Resolving the H_2 effect on radiation induced dissolution of UO_2 -based spent nuclear fuel, *J. Nucl. Mater.* 396 (2010) 163-169.

- [50] C. Corbel, G. Sattonnay, S. Guilbert, F. Garrido, M.F. Barthe, and C. Jegou, Addition versus radiolytic production effects of hydrogen peroxide on aqueous corrosion of UO_2 , *J. Nuc. Mat.* 348 (2006) 1-17.
- [51] M. Jonsson, F. Nielsen, O. Roth, E. Ekeroth, S. Nilsson, and M.M. Hossain, Radiation induced spent nuclear fuel dissolution under deep repository conditions, *Environmental Science & Technology* 41 (20) (2007) 7087-7093.
- [52] V. Rondinella, J. Cobos, and T. Wiss, Leaching behaviour of low-activity alpha-doped UO_2 , in "Scientific Basis for Nuclear Waste Management XXVIII", edited by J.M. Hanchar, S. Stroes-Gascoyne, and L. Browning, Materials Research Society, Warrendale, PA, 2004, p. 167-173.
- [53] B. Muzeau, C. Jégou, F. Delaunay, V. Broudic, A. Brevet, H. Catalette, E. Simoni, and C. Corbel, Radiolytic oxidation of UO_2 pellets doped with alpha emitters ($^{238/239}\text{Pu}$), *J. Alloys Compd.* 467 (2009) 578-589.
- [54] C. Poinssot, C. Ferry, and A. Poulesquen, New perspectives for the spent nuclear fuel radionuclides release model in a deep geological repository, in "Scientific Basis for Nuclear Waste Management XXX", edited by D. Dunn, C. Poinssot, and B. Begg, Materials Research Society, Warrendale, PA, 2007, p. 111-116.
- [55] K. Ollila, and V.M. Oversby, Dissolution of unirradiated UO_2 and UO_2 doped with ^{233}U under reducing conditions, Report TR-05-07, Swedish Nuclear Fuel and Waste Management Co (SKB), Stockholm, Sweden, 2005.
- [56] E. Ekeroth, J. Low, H.-U. Zwicky, and K. Spahiu, Corrosion studies with high burnup LWR fuel in simulated groundwater, in "Scientific Basis for Nuclear Waste Management XXXII", edited by N.C. Hyatt, D.A. Pickett, and R.B. Rebak, Materials Research Society, Warrendale, PA, 2009, p. Q02-07.
- [57] C. Jegou, S. Peugot, V. Broudic, D. Roudil, X. Deschanel, and J.M. Bart, Identification of the mechanism limiting the alteration of clad spent fuel segments in aerated carbonated groundwater, *J. Nucl. Mater.* 326 (2004) 144-155.

Chapter 5

AN ELECTROCHEMICAL STUDY OF H₂O₂ OXIDATION AND DECOMPOSITION ON SIMULATED NUCLEAR FUEL (SIMFUEL)

5.1 Introduction

The experiments presented in this chapter describe a series of electrochemical and inductively coupled plasma atomic emission spectroscopy (ICP-AES) measurements performed to investigate the anodic oxidation and open circuit decomposition of H₂O₂ on UO_{2+x} surfaces as a function of pH (9.5-12.6).

Under corrosion conditions there are two competitive anodic reactions which can couple with the cathodic reduction of H₂O₂: the oxidative dissolution of UO₂ and the simultaneous oxidation of H₂O₂, the latter leading to H₂O₂ decomposition.



The rates of fuel corrosion and H₂O₂ decomposition are determined by the fraction of each anodic reaction. Consequently, the corrosion rate of fuel will be determined by the distribution of current between these two anodic reactions. Although the cathodic reduction of H₂O₂ on UO₂ has been extensively investigated [1-5], its anodic oxidation of has received minimal attention.

Early studies on H₂O₂ decomposition have been reviewed in Section 1.5.1. The corrosion potential of UO₂ in H₂O₂-containing solutions was found to be independent of [H₂O₂] over the range 10⁻⁴ to 10⁻² mol L⁻¹ (Fig. 1.14, Chapter 1), which was attributed to the

blockage of both decomposition and UO_2 dissolution by the presence of a U^{VI} layer on the electrode surface [6]. Consistent results were obtained in a more comprehensive study in the presence of the α -radiolysis of water to produce the oxidant H_2O_2 [7]. The rate of H_2O_2 decomposition appeared to be suppressed due to the surface coverage by insulating U^{VI} species that blocked the underlying conducting $\text{U}^{\text{IV}}/\text{U}^{\text{V}}$ surface. Consequently, the slow chemical dissolution of U^{VI} species as UO_2^{2+} would limit the H_2O_2 decomposition process in non-complexing solutions. If this mechanism is correct, then decomposition is inhibited by the extent of surface oxidation under open-circuit (corrosion) conditions. The rate of H_2O_2 decomposition was also shown to depend on the alkalinity of the solution (Section 1.5.2.1) although the details of the mechanism were not elucidated.

In the present chapter, a primary goal is to investigate the influence of the oxidized surface species (U^{VI}) on the electrochemical oxidation of H_2O_2 . A second goal is to determine the pH effect on the rate of H_2O_2 decomposition, and eventually on the dissolution rate of UO_2 .

5.2 Experimental

The electrochemical equipment setup and the SIMFUEL electrode preparation were described in Section 2.1. The SIMFUEL used in this study replicates spent nuclear fuel with a 1.5 at.% burnup. All experiments were Ar-purged (ultra-high purity, Praxair) and conducted at room temperature. Solutions were prepared using deionized water with a resistance of $18.2 \text{ M}\Omega \text{ cm}$ purified by Millipore milli-Q-plus units. The electrolyte was $0.1 \text{ mol L}^{-1} \text{ NaCl}$, and the solution pH was adjusted to a value between 9.5 and 12.6 with NaOH (Caledon Chemical). Hydrogen peroxide (3% w/v, LabChem) was added

immediately prior to experiments to obtain a concentration between 0 and 0.02 mol L⁻¹.

The solution pH was monitored before and after electrochemical measurements.

The working electrode was cathodically cleaned at an applied potential of -1.2 V for 1 min prior to each experiment to remove any air-formed oxides. Cyclic voltammetric and potentiodynamic experiments were conducted at a scan rate of 10 mV s⁻¹. The positive potential limit of the scan was 0.4 V and the negative limit was varied depending on the purpose of the experiment. In a dissolution experiment, the working electrode was kept at 0.3 V for 4 hours in a small electrochemical cell with a volume of 50 mL. Subsequently, the solution concentration of U was analyzed by inductively coupled plasma atomic emission spectroscopy (ICP-AES).

5.3 Results and discussion

5.3.1 Open-circuit potential in H₂O₂ solution

Within the pH range 9.5 to 12.5, the open circuit potential (E_{OC}) was independent of [H₂O₂] over the range 0.004 to 0.02 mol L⁻¹, Fig. 5.1, consistent with previous observations at pH = 9.5 [6]. Also shown in the figure are the calculated equilibrium potentials for the redox reactions:



and



which can couple to yield the overall decomposition, reaction (5.1).

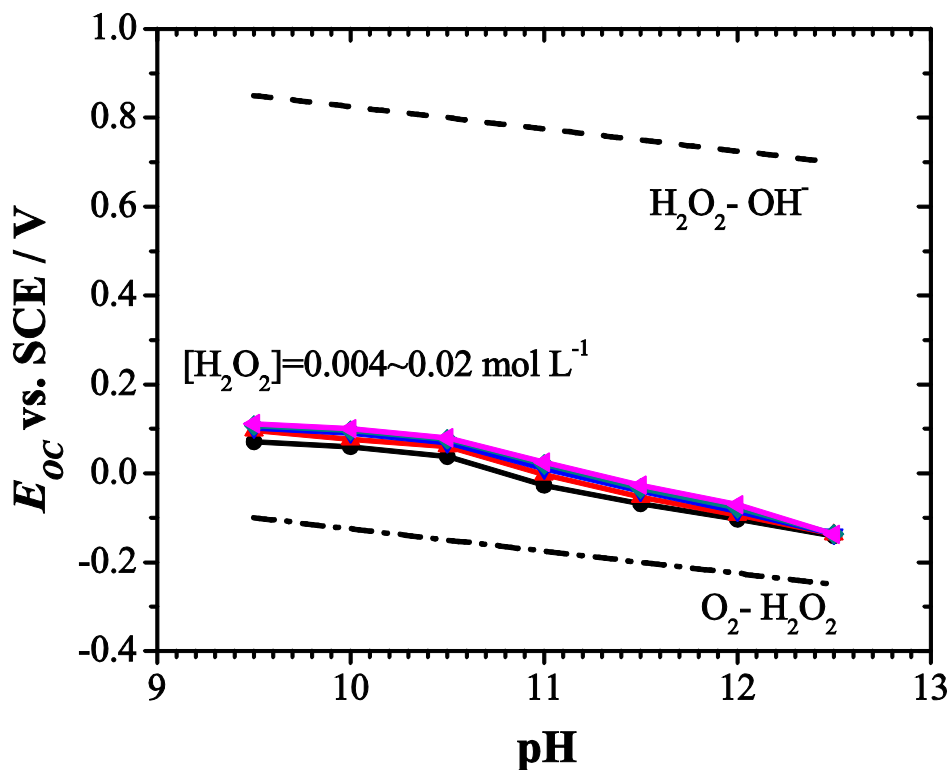


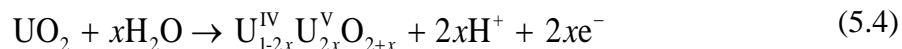
Fig. 5.1. Open-Circuit Potential (E_{OC}) as a function of pH recorded on a SIMFUEL electrode in solutions containing various $[H_2O_2]$ (0.004~0.02 mol L⁻¹). The dashed lines indicate the equilibrium potentials for the H_2O_2 reduction and oxidation half reactions calculated assuming a partial pressure for O_2 of 1 atmosphere.

As discussed previously [6, 7], this independence of E_{OC} on $[H_2O_2]$ could be interpreted one of two ways: (i) as the $[H_2O_2]$ was increased, the kinetics of both the anodic and cathodic reactions were equally affected, leading to a condition of redox buffering (i.e., an increase in decomposition rate without a change in E_{OC}); (ii) the overall decomposition reaction was independent of $[H_2O_2]$, as would be the case if the rate was controlled by the rate of release of the U^{VI} species from the surface to the solution.

Inspection of Fig. 5.1 shows two additional notable features: E_{OC} was closer to the equilibrium potential for the anodic half reaction (5.3) than the cathodic half reaction (5.2); and the dependence of E_{OC} on $[H_2O_2]$ changes between $pH = 10.5$ and 11.0 . The proximity of E_{OC} to $(E_e)_{anod}$ implied that for the decomposition reaction the anodic reaction was rapid and, hence, the potential-determining reaction, while the overall reaction was controlled by the kinetics of the cathodic half reaction. However, this presumption does not take into account that the decomposition reaction is effectively blocked by a U^{VI} surface layer. The change in slope between $pH = 10.5$ and 11.0 would then indicate a change in surface state leading to an acceleration of the H_2O_2 oxidation reaction.

5.3.2 Effect of pH on voltammetry

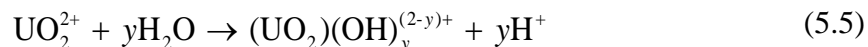
Fig. 5.2 shows cyclic voltammograms (CV) recorded at $pH 9.5$ and 12.5 in H_2O_2 -free solutions. The various stages of oxidation and reduction generally seen [5, 8] are numbered on the plot. Stage 1, which is associated with the anodic oxidation of non-stoichiometric surface locations, appeared to be insignificant on the stoichiometric SIMFUEL used in these experiments. The shallow shoulder in region 2 has been shown to be due to the anodic oxidation of the stoichiometric surface



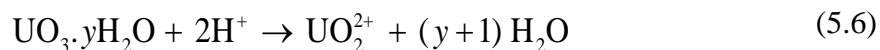
and was slightly more prominent at $pH = 12.5$ compared to 9.5 , indicating a thicker and/or more intensively oxidized layer was formed.

The most significant difference in anodic oxidation behaviour between the two pH s was

in region 3, for potentials ≥ 0.1 V. In near-neutral solutions, the surface was further oxidized to a passivating U^{VI} layer (commonly designated $UO_3 \cdot yH_2O$) and some soluble UO_2^{2+} . Hydrolysis of this dissolved uranyl ion then leads to local acidification



and local dissolution of the U^{VI} surface layer



This would account for the steep rise in current for $E > 0.3$ V (pH = 9.5 in Fig. 5.2), leading to extensive, but localized dissolution of the UO_2 surface.

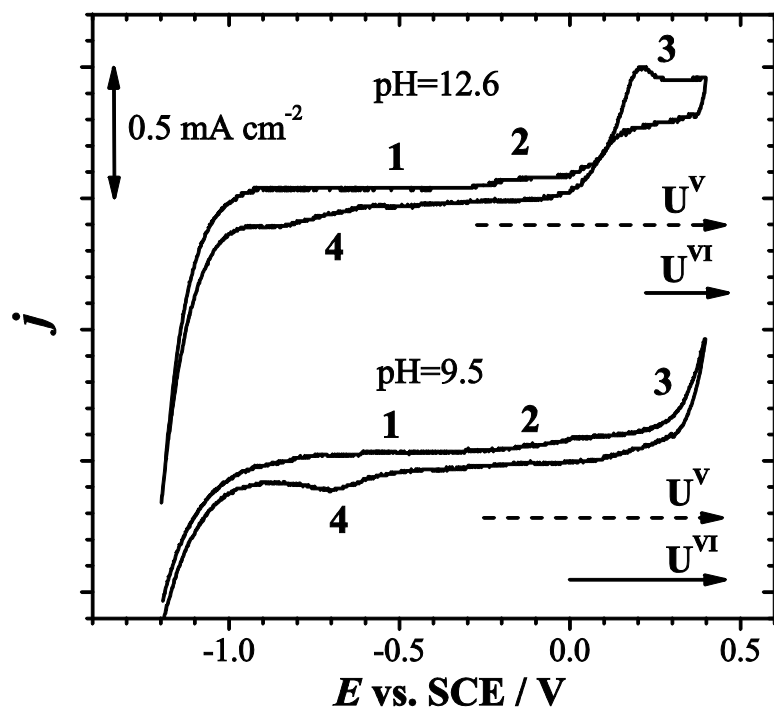


Fig. 5.2. Voltammograms recorded on a SIMFUEL electrode at pH 9.5 and 12.6; $[NaCl] = 0.1 \text{ mol L}^{-1}$; rotation rate = 16.7 Hz; scan rate = 10 mV s^{-1} .

By contrast, in alkaline solutions U^{VI} is over two orders of magnitude more soluble than in neutral solution [9] and passivation was avoided, the current rising rapidly (pH = 12.6 in Fig. 5.2) as extensive dissolution occurred for $E \geq 0.1$ V,



For potentials ≥ 0.2 V, the current plateau showed that anodic dissolution was controlled by a nonelectrochemical process, most likely the chemical dissolution of a U^{VI} surface layer as discussed elsewhere [5]. The constant current for potentials in the range 0.2 V to 0.4 V would then indicate that this surface U^{VI} layer increased in thickness with increasing potential. That this surface layer was not passivating was confirmed on the reverse scan, a substantial anodic current being observed until the potential fell below ~ 0.1 V. Additionally, a cathodic peak in region 4 for the reduction of oxidized surface layers was observed. The charge associated with this peak is approximately the same as that for the reduction of the oxidized layer formed at pH = 9.5, confirming that the majority of the charge on the anodic scan at pH = 12.6 went to the production of soluble UO_2^{2+} .

The chemical composition of the UO_2 surface at these two pH values has been determined previously by X-ray photoelectron spectroscopy (XPS) [5, 10] and the ranges over which the composition changes are indicated by the arrows in Fig. 5.2. While the onset of oxidation to produce U^V is similar at both pH values, the surface accumulation of U^{VI} at the higher pH is delayed by more extensive dissolution.

5.3.3 Effect of pH on H₂O₂ oxidation

Fig. 5.3 shows the anodic current recorded during anodic scans in solutions containing 0.02 mol L⁻¹ H₂O₂ at both pH values. The background currents recorded on the forward scan in the absence of H₂O₂ are also shown, as dashed lines, for comparison. The oxidation current at pH = 12.6 was considerably larger than that at pH = 9.5.

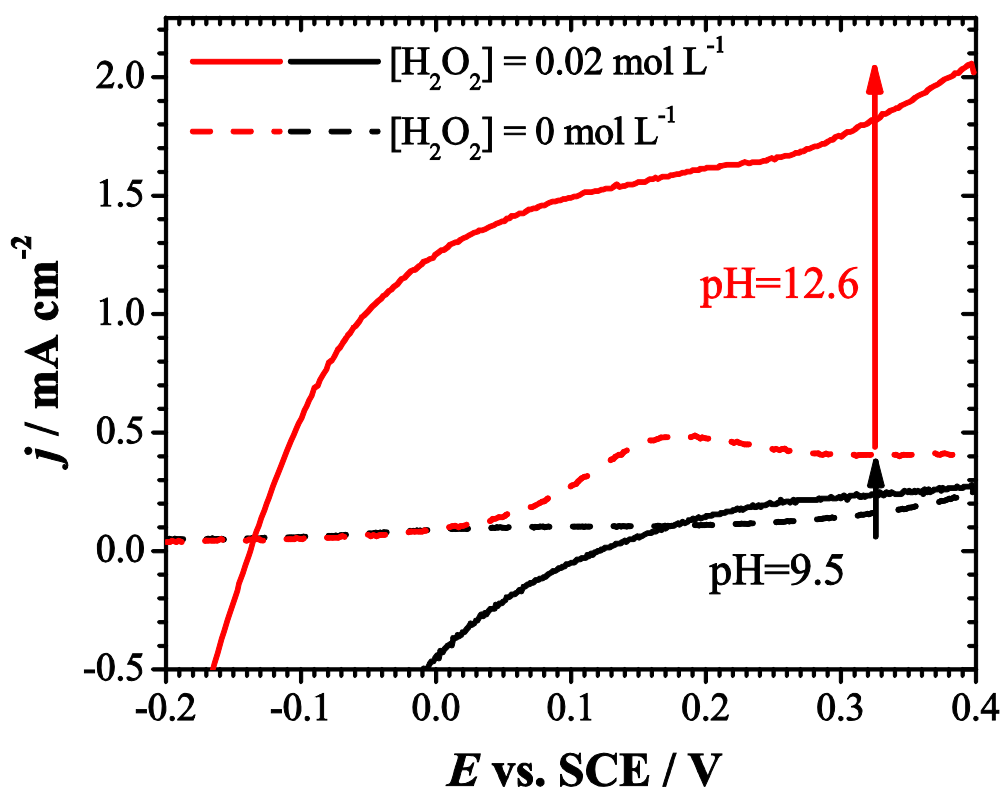


Fig. 5.3. Anodic current density recorded on a SIMFUEL electrode in a H₂O₂ solution at pH 9.5 and 12.6; [NaCl] = 0.1 mol L⁻¹; rotation rate = 25 Hz; scan rate = 10 mV s⁻¹.

At pH = 9.5, the anodic current was almost independent of electrode rotation rate consistent with expectations for a surface covered with a slowly dissolving insulating

layer of U^{VI} , Fig. 5.4(a). At pH = 12.6, while dependent on electrode rotation rate, the anodic current was only ~ 10% of the calculated diffusion limiting value, Fig. 5.4(b). That the current was suppressed by the anodic formation of an oxidized surface layer was confirmed by a series of dual scan experiments, in which the potential was scanned from various negative values to +0.4 V and then back to the original negative potential limit followed by a second scan between the same two potentials. This procedure was repeated for a sequence of increasingly negative initial potentials, as indicated in the inset to Fig. 5.5, although the currents recorded at potentials < -0.125 V are not shown for clarity. This figure shows that the anodic current on the second scan was suppressed until the negative limit of the potential was made sufficiently negative (< -0.6 V) to cathodically remove the film formed on the first scan. This observation is consistent with the CV in Fig. 5.2 which showed that the oxidized layer anodically formed in alkaline solutions was not cathodically reduced until the potential was in the range -0.7 V to -0.9 V.

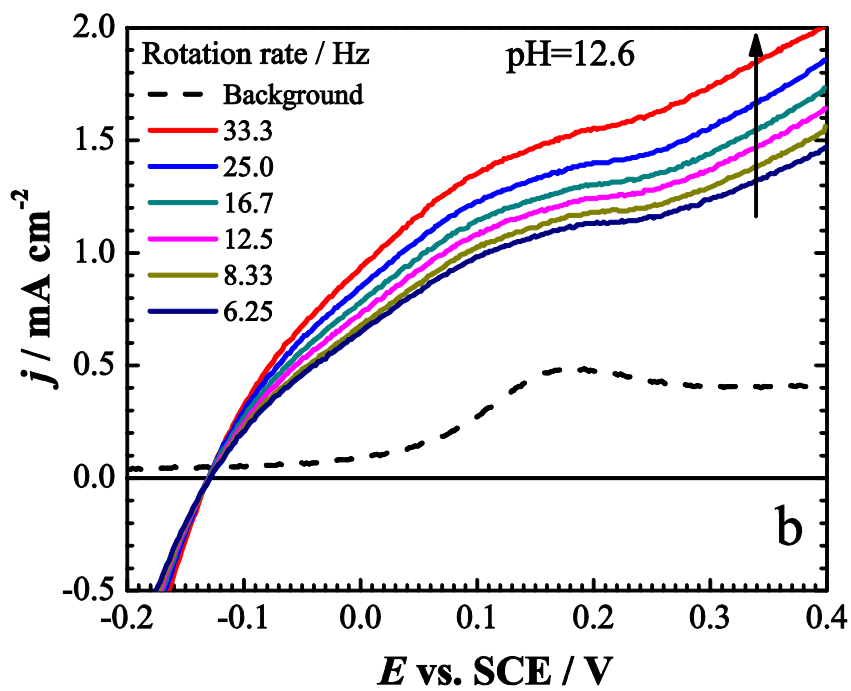
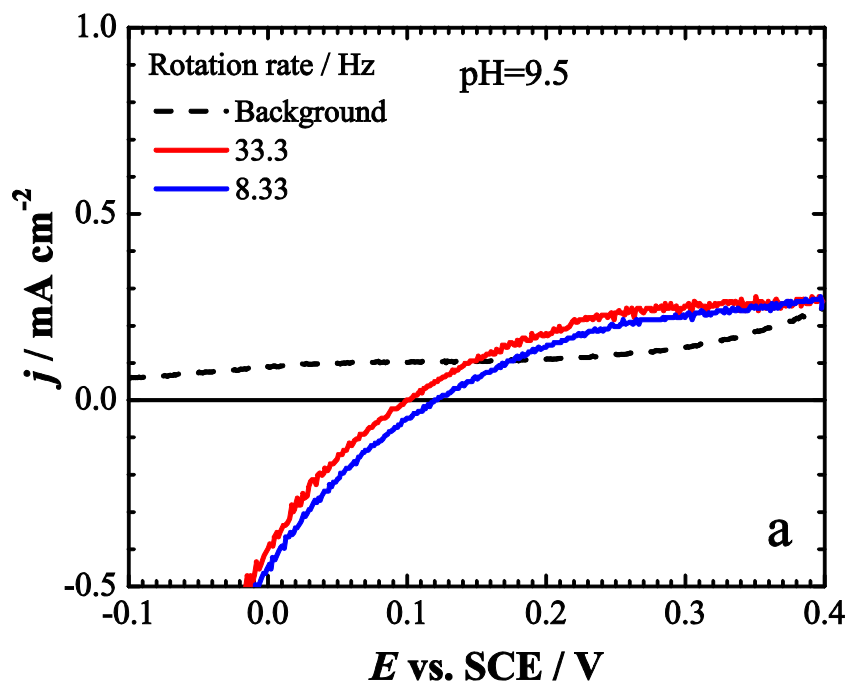


Fig. 5.4. Anodic current densities recorded on a SIMFUEL electrode at various rotation rates; $[\text{NaCl}] = 0.1 \text{ mol L}^{-1}$; $[\text{H}_2\text{O}_2] = 0$ (as background) or 0.02 mol L^{-1} ; (a) pH = 9.5 and (b) pH = 12.6.

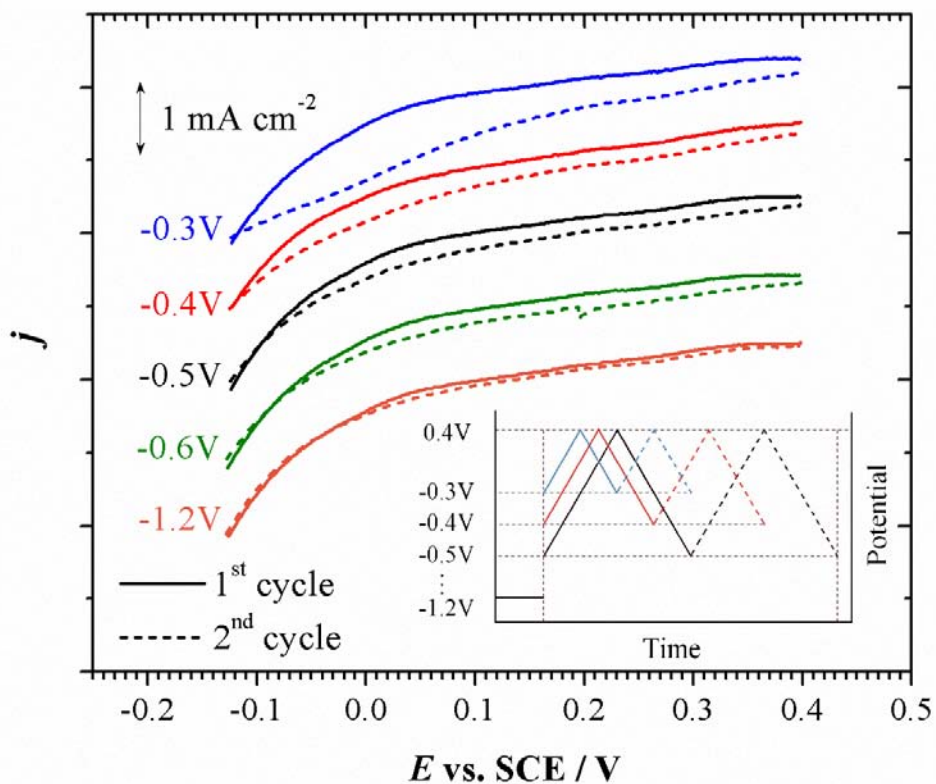


Fig. 5.5. Anodic current density recorded for various potential scan ranges. Each color indicates a scan from a different cathodic potential vertex as shown in the inset. Solid lines, 1st forward scan; dashed lines, 2nd forward scan; $[\text{NaCl}] = 0.1 \text{ mol L}^{-1}$; $[\text{H}_2\text{O}_2] = 0.02 \text{ mol L}^{-1}$; pH = 12.5.

The anodic current recorded at pH = 12.6 in Fig. 5.4(b) is plotted against the electrode rotation rate for a number of potentials in Fig. 5.6. The linear dependence demonstrates

that the current for H_2O_2 oxidation was not controlled by its transport in the bulk of solution but by diffusive transport across the non-protective but insulating U^{VI} surface layer formed anodically and whose thickness (the diffusion layer thickness) increased with potential.

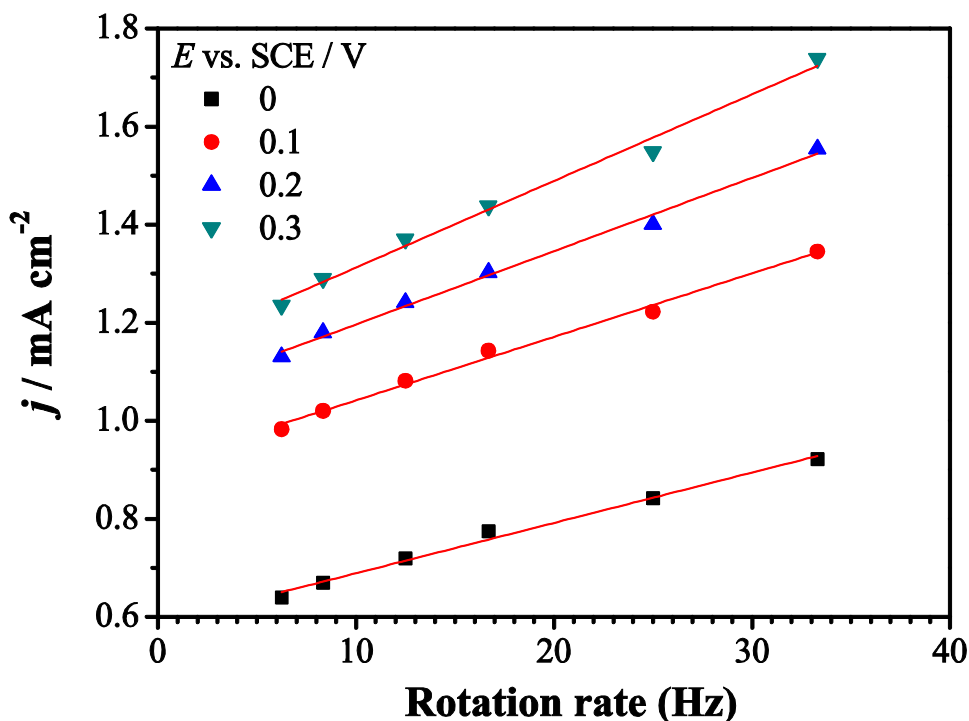
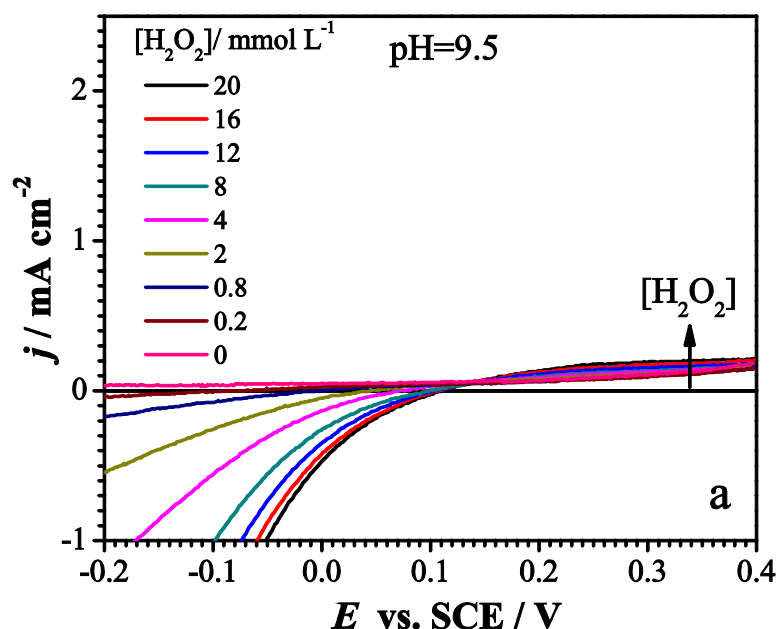


Fig. 5.6. Current density at different potentials as a function of rotation rate; $[\text{NaCl}] = 0.1 \text{ mol L}^{-1}$; $[\text{H}_2\text{O}_2] = 0.02 \text{ mol L}^{-1}$; $\text{pH} = 12.6$. Data are taken from the cyclic voltammetry measurements in Fig. 5.4(b).

A series of CV scans were recorded at various $[\text{H}_2\text{O}_2]$ and pH values, Fig. 5.7. At all pH values the cathodic reduction of H_2O_2 proceeded rapidly, the current increasing exponentially with a strong dependence on $[\text{H}_2\text{O}_2]$, over the potential range 0 to -0.2 V ; i.e., within region 2 in Fig. 5.2. In this potential region the surface composition would be

$U^{IV}_{1-2x}U^{V}_{2x}O_{2+x}$ with the U^V content decreasing as the potential became more negative. A detailed study of H_2O_2 reduction has been published elsewhere [3].

The oxidation currents were very dependent on the pH value. At pH = 9.5, the current increase when H_2O_2 was added was marginal. However, in more alkaline solutions the oxidation currents were considerably larger than the background current ($[H_2O_2] = 0$) confirming H_2O_2 oxidation was becoming more significant. At pH = 11.1 the anodic current plateau in the potential range 0.2 V to 0.4 V reflected the suppression of the H_2O_2 oxidation reaction by the U^{VI} surface layer. As the pH was increased further (e.g., to 12.5) the current became more dependent on $[H_2O_2]$. The possibility of a contribution to the current at very positive potentials from H_2O_2 oxidation on the noble metal particles present in SIMFUEL electrodes is discussed in Chapter 7.



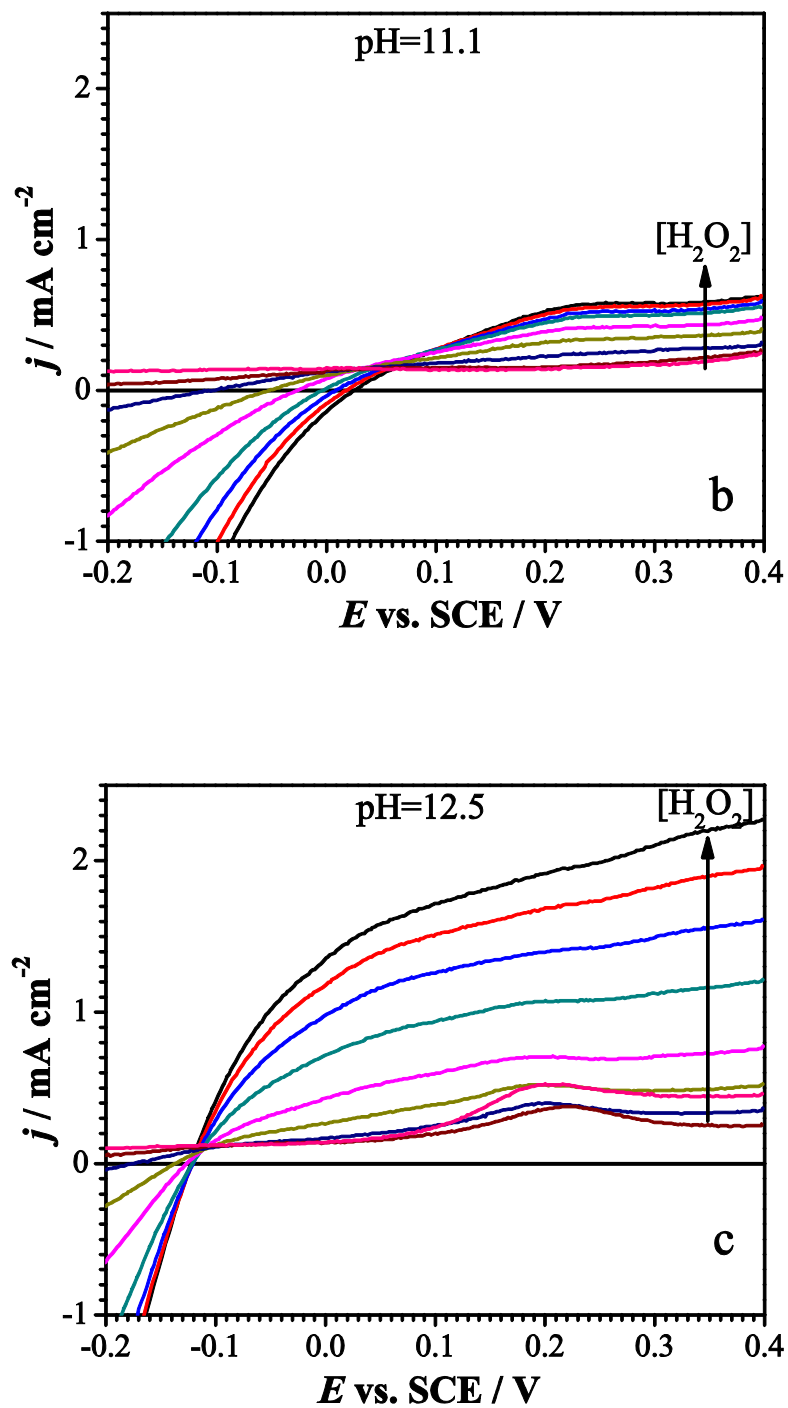
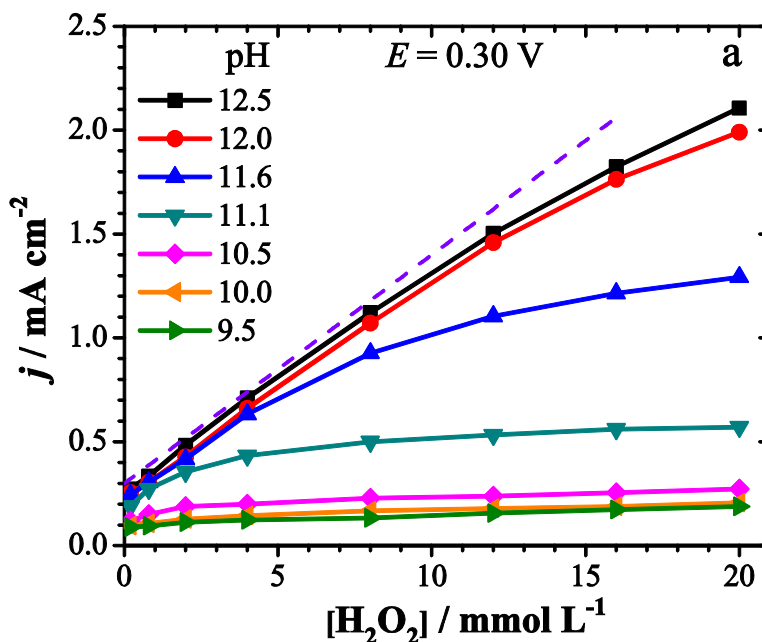


Fig. 5.7. Anodic current densities recorded in solutions containing various $[\text{H}_2\text{O}_2]$ (the arrows indicate an increase from 0 to 0.02 mol L^{-1}) at various pH (a) 9.5, (b) 11.1 and (c) 12.5; rotation rate = 25 Hz; scan rate = 15 mV s^{-1} .

Fig. 5.8 shows the anodic currents recorded at 0.15 V and 0.3 V, taken from the profiles in Fig. 5.7, for various pH values (9.5 to 12.5) as a function of $[\text{H}_2\text{O}_2]$. Identical behaviour was observed over the potential range 0.15 V to 0.3 V. At the lower end of the pH scale the current was independent of $[\text{H}_2\text{O}_2]$ except for a marginal dependence at the lowest concentrations. As the pH was increased above 10.5 the current increased markedly and became increasingly dependent on $[\text{H}_2\text{O}_2]$. At $\text{pH} \geq 11.6$ the current approached a first order dependence on $[\text{H}_2\text{O}_2]$ providing the concentration was not too high. A first order dependence on $[\text{H}_2\text{O}_2]$ coupled to the linear dependence of anodic current on electrode rotation rate (Fig. 5.6) is consistent with H_2O_2 oxidation being partially controlled by transport through a permeable U^{VI} surface layer whose thickness increases with potential.



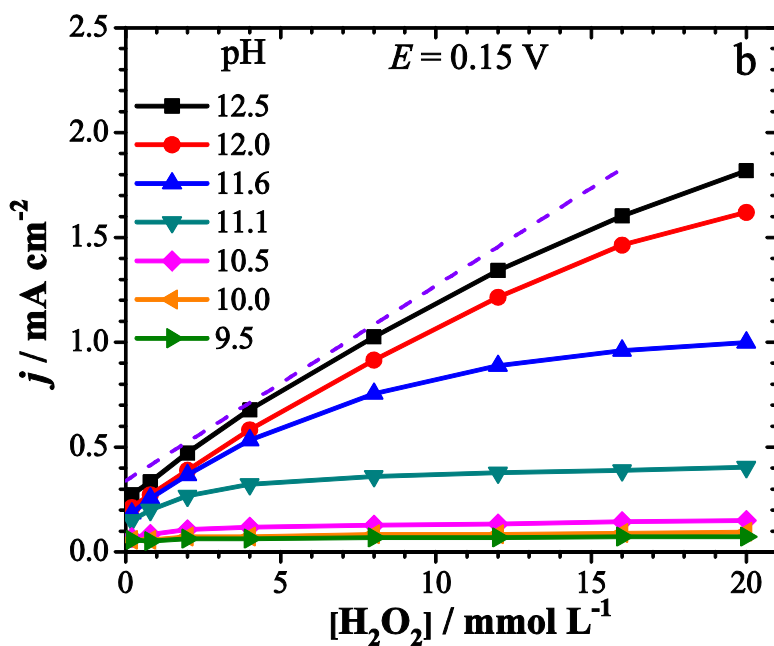


Fig. 5.8. Anodic current densities recorded at (a) 0.30 V and (b) 0.15 V as a function of $[\text{H}_2\text{O}_2]$ for various pH values. The dashed line indicates a first order dependence with respect to $[\text{H}_2\text{O}_2]$.

The overall increase in current with pH can be attributed to one, or both, of two features. Fig. 5.9 shows the anodic current at 0.3 V ($[\text{H}_2\text{O}_2] = 0.02 \text{ mol L}^{-1}$) plotted as a function of pH and compared to the concentrations of H_2O_2 and HO_2^- calculated using the accepted pK_a value of 11.6 [11] for the dissociation reaction



The similarity between the anodic current and the concentration of HO_2^- indicates the latter was the electroactive form of peroxide as previously observed for Pt [12, 13].

Alternatively, since the solubility of U^{VI} increases by $> 10^2$ over the pH range 9.5 to 12.5

[9], it is possible that the U^{VI} surface layer became thinner and the H_2O_2 oxidation less inhibited as the pH increased. Whether or not this is the predominant mechanism is not clear and further experimental evidence is required to separate the importance of these two possibilities.

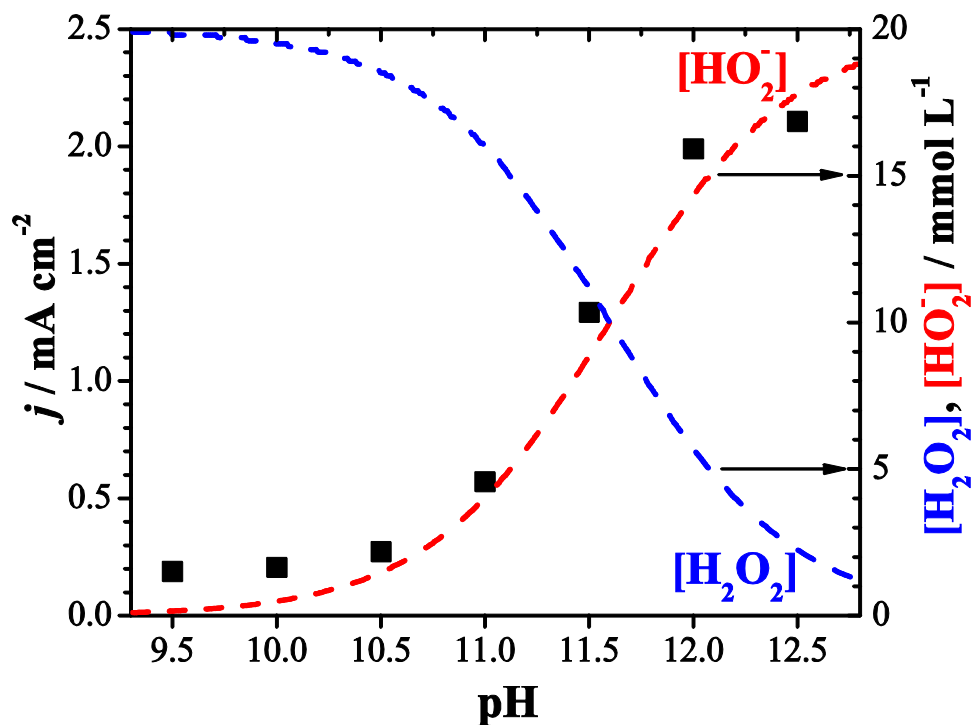


Fig. 5.9. Current density as a function of pH at 0.3 V in a solution containing $[H_2O_2] = 0.02 \text{ mol L}^{-1}$. The dashed curves show the concentrations of the peroxide forms (H_2O_2 and HO_2^-) vs. pH.

5.3.4 Dissolution experiments

Since the anodic current is comprised of two contributions (the dissolution of UO_2 and the oxidation of H_2O_2), an attempt to separate them was made by analyzing the U^{VI}

content of the solution after anodic oxidation at 0.3 V for 4h. The analyzed amount of dissolved UO_2^{2+} was converted to the charge required for oxidative dissolution of UO_2 as UO_2^{2+} . The total anodic charge was obtained by integration of the measured anodic current. The difference between these two charges can be attributed to H_2O_2 oxidation. Over this period of anodic oxidation the charge that retained on the electrode surface (in the form of oxidized U^{VI} solid) would have been negligible compared to the total charge. As noted in Table 5.1 the fraction of the current going to H_2O_2 oxidation was 71.5%. Inspection of the CV scans in Fig. 5.7(b) shows that (for the same conditions as those in the dissolution experiment: $\text{pH} = 11$, $E = 0.3$ V and $[\text{H}_2\text{O}_2] = 0.02$ mol L^{-1}) the ratio of the anodic currents in H_2O_2 -free and H_2O_2 -containing solutions is $\sim 30\%$, i.e., about 70% of total current appears to support the oxidation of H_2O_2 . The similarity in the charge and current density ratios confirm that the predominant anodic reaction at very positive potentials is H_2O_2 oxidation.

Table 5.1. Distribution of charge between UO_2 oxidative dissolution and H_2O_2 oxidation^a

	Charge (C)	Fraction in total anodic charge
Total anodic charge	0.09780	100%
Charge due to UO_2 dissolution	0.02792	28.5%
Charge due to H_2O_2 oxidation	0.06988	71.5%

^a SIMFUEL electrode potentiostatically oxidized at 0.3 V for 4 h in a solution of $[\text{NaCl}] = 0.1$ mol L^{-1} , $[\text{H}_2\text{O}_2] = 0.02$ mol L^{-1} , $\text{pH} = 11.0$. No rotation was applied.

5.3.5 Polarization resistance measurements

Using the plots in Fig. 5.4 and Fig. 5.7 it is possible to estimate the polarization resistance (R_p) by measuring the slope of the current–potential plots over the range $E_{OC} \pm 10$ mV.

At pH = 9.5, R_p was small since, at a positive E_{OC} of ~ 0.1 V, the surface was blocked by the insulating U^{VI} layer. At pH = 12.6, however, when the surface was not so readily blocked by such a layer, R_p decreased with electrode rotation, Fig. 5.10, while the value of E_{OC} did not change, Fig. 5.4(b). This combination of features indicated that the enhanced transport of H_2O_2 to the electrode surface promoted both the anodic and cathodic half reactions coupled at open circuit, indicating that the dominant reaction occurring was H_2O_2 decomposition; i.e., the coupling of reactions (5.2) and (5.3). When this is the case the term R_p^{-1} can be considered proportional to the H_2O_2 decomposition rate.

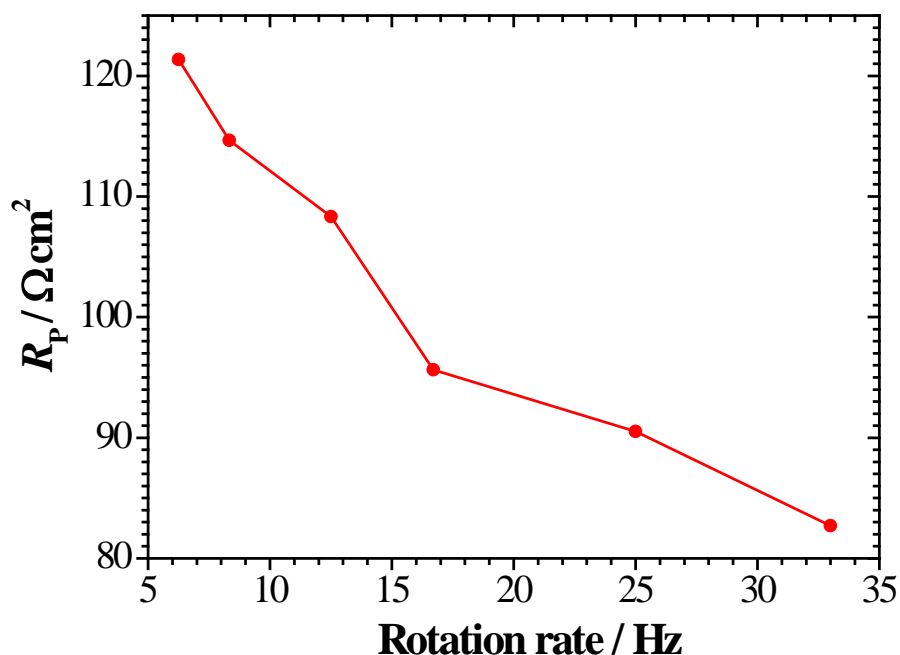


Fig. 5.10. Polarization resistance, R_p , plotted as a function of rotation rate recorded on a SIMFUEL electrode; $[\text{NaCl}] = 0.1 \text{ mol L}^{-1}$; $[\text{H}_2\text{O}_2] = 0.02 \text{ mol L}^{-1}$; pH = 12.6.

Values of R_p^{-1} measured as a function of $[\text{H}_2\text{O}_2]$ for a range of pH values are shown in Fig. 5.11. For $\text{pH} \leq 10.5$, R_p^{-1} was very low and only marginally dependent on $[\text{H}_2\text{O}_2]$. As the pH increased to ≥ 11.1 the value of R_p^{-1} increased markedly, and as observed for the anodic currents at applied potentials (Fig. 5.8) achieved a first order dependence for $[\text{H}_2\text{O}_2] < 5 \text{ mmol L}^{-1}$. As shown in Fig. 5.1, E_{OC} varied from $\sim 0.1 \text{ V}$ at $\text{pH} = 9.5$ when the electrode surface was expected to be covered by a U^{VI} surface layer (Fig. 5.2) to $\sim -0.1 \text{ V}$ at $\text{pH} = 12.5$ when the surface composition will be relatively free of U^{VI} (Fig. 5.2) exposing the underlying $\text{U}^{\text{IV}}_{1-2x}\text{U}^{\text{V}}_{2x}\text{O}_{2+x}$ layer.

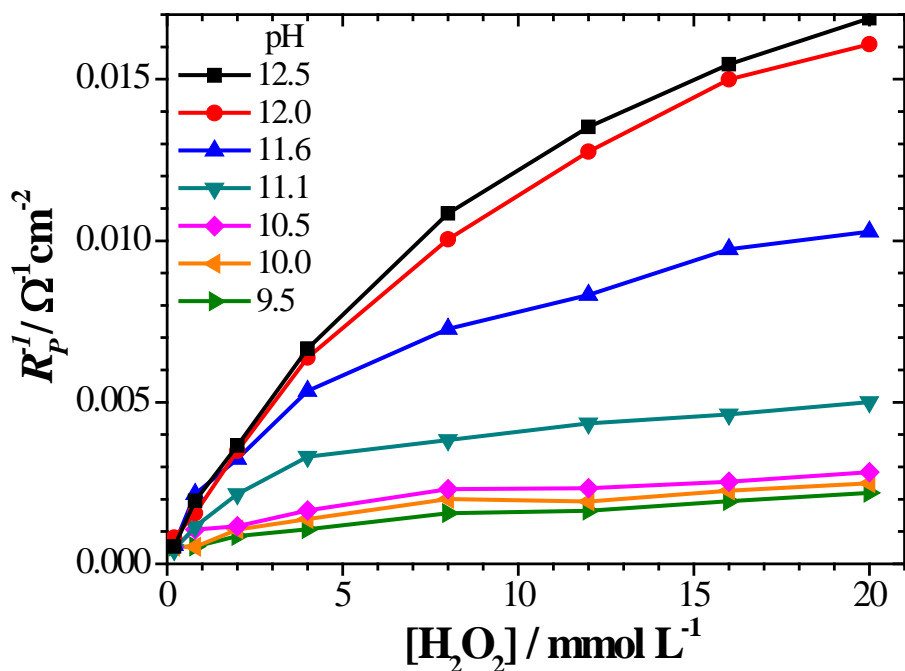


Fig. 5.11. Reciprocal of polarization resistance, R_p^{-1} , as a function of $[\text{H}_2\text{O}_2]$ recorded on a SIMFUEL electrode at various pH values; $[\text{NaCl}] = 0.1 \text{ mol L}^{-1}$; rotation rate = 25 Hz.

The decomposition of H_2O_2 on the surfaces of various metal oxides (usually in particulate form) has been extensively studied [14, 15], and a variety of reaction pathways discussed in Section 1.5.2.3. For decomposition on oxides within which redox transformations are possible (iron oxides being the prime example) decomposition has been shown to involve coupling with redox transformations (e.g. $\text{Fe}^{\text{II}} \leftrightarrow \text{Fe}^{\text{III}}$) within the oxide [16, 17].

Decomposition then proceeds via reactions involving these two oxidation states and radical species such as OH^\bullet and HO_2^\bullet .

At high pH, this mechanism appears to have been the case for H_2O_2 decomposition on $\text{U}^{\text{IV}}_{1-2x}\text{U}^{\text{V}}_{2x}\text{O}_{2+x}$. Surfaces with this composition have been shown to support reversible redox reactions [18] and would, therefore be expected to support H_2O_2 decomposition catalyzed by the oxidation/reduction of $\text{U}^{\text{IV}}/\text{U}^{\text{V}}$ sites, a process which involves the incorporation and release of O^{II} interstitial species [5, 10, 18]. In the present study, the proximity of E_{OC} to the equilibrium potential for the anodic reaction, Fig. 5.1, and its closer approach to this value at higher pH when the catalytic $\text{U}^{\text{IV}}_{1-2x}\text{U}^{\text{V}}_{2x}\text{O}_{2+x}$ surface is exposed, suggests the cathodic reaction is rate determining and the pH dependence is determined, at least partially, by the increase in concentration of the HO_2^- which is the electroactive species.

5.4 Summary and conclusions

The electrochemical oxidation and open circuit decomposition of H_2O_2 have been studied as a function of pH (9.5 to 12.6) and $[\text{H}_2\text{O}_2]$ (10^{-4} to 10^{-2} mol L^{-1}).

(i) At pH = 9.5 the anodic oxidation is slow and appears to be blocked by the presence of an insulating U^{VI} surface layer. As the pH is increased to > 10.5 the anodic oxidation is

accelerated but controlled partially by transport through a thin but chemically dissolving U^{VI} oxide/hydroxide surface layer.

(ii) At positive electrode potentials, $\sim 70\%$ of the anodic current goes to H_2O_2 oxidation and the remainder to UO_2 dissolution as $U^{VI}O_2(OH)_x^{(2-x)+}$ in solution of relatively high $[H_2O_2]$ (0.02 mol L^{-1}).

(iii) At open circuit the H_2O_2 decomposition reaction rate appears to be controlled by the cathodic half reaction. At low pH (≤ 10.5) it is blocked by the presence of U^{VI} surface states, but at higher pH appears to proceed rapidly on a $U^{IV}_{1-2x}U^V_{2x}O_{2+x}$ surface as illustrated in Fig. 5.12. The pH dependence of the rate suggests that HO_2^- is the electroactive form of peroxide.

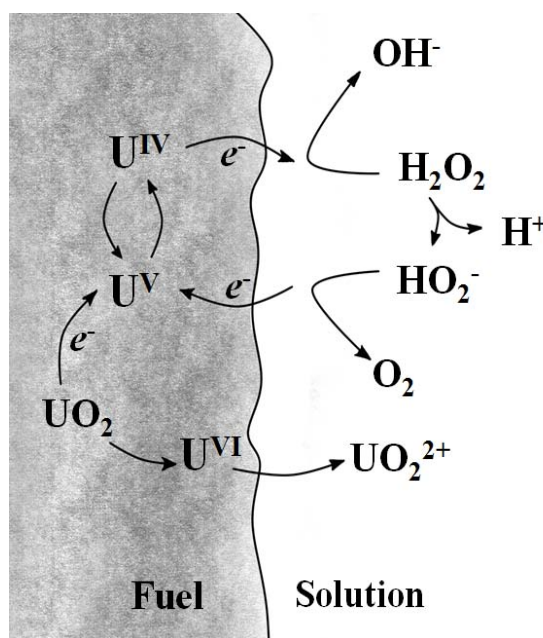


Fig. 5.12. Schematic illustration of the proposed mechanism for redox reactions involving H_2O_2 on fuel surface in an alkaline solution, and the H_2O_2 decomposition being catalyzed by the mixed U^{IV}/U^V states.

(iv) The independence of E_{OC} on a range of $[H_2O_2]$ in alkaline solutions (Fig. 5.1) could be attributed to the decomposition of H_2O_2 .

5.5 References

- [1] J.S. Goldik, H.W. Nesbitt, J.J. Noël, and D.W. Shoesmith, Surface electrochemistry of UO_2 in dilute alkaline hydrogen peroxide solutions, *Electrochim. Acta* 49 (2004) 1699-1709.
- [2] J. Gimenez, E. Baraj, M.E. Torrero, I. Casas, and J. de Pablo, Effect of H_2O_2 , $NaClO$ and Fe on the dissolution of unirradiated UO_2 in $NaCl$ 5 mol kg^{-1} . Comparison with spent fuel dissolution experiments, *J. Nucl. Mater.* 238 (1996) 64-69.
- [3] J.S. Goldik, J.J. Noël, and D.W. Shoesmith, The electrochemical reduction of hydrogen peroxide on uranium dioxide electrodes in alkaline solution, *J. of Electroanal. Chem.* 582 (2005) 241-248.
- [4] M. Trummer, S. Nilsson, and M. Jonsson, On the effects of fission product noble metal inclusions on the kinetics of radiation induced dissolution of spent nuclear fuel, *J. Nucl. Mater.* 378 (2008) 55-59.
- [5] B.G. Santos, J.J. Noël, and D.W. Shoesmith, The effect of pH on the anodic dissolution of SIMFUEL (UO_2), *J. of Electroanal. Chem.* 586 (2006) 1-11.
- [6] S. Sunder, N.H. Miller, and D.W. Shoesmith, Corrosion of uranium dioxide in hydrogen peroxide solutions, *Corros. Sci.* 46 (2004) 1095-1111.
- [7] J.C. Wren, D.W. Shoesmith, and S. Sunder, Corrosion Behavior of Uranium Dioxide in Alpha Radiolytically Decomposed Water, *J. Electrochem. Soc.* 152 (2005) B470.
- [8] D.W. Shoesmith, Fuel corrosion waste process under waste disposal conditions, *J. Nucl. Mater.* 282 (2000) 1-31.
- [9] I. Grenthe, J. Fuger, R.J. Konings, R.J. Lemire, A.B. Muller, C. Nguyen-Trung, and H. Wanner, *Chemical Thermodynamics of Uranium*, North Holland, Amsterdam, 1992.
- [10] B.G. Santos, H.W. Nesbitt, J.J. Noël, and D.W. Shoesmith, X-ray photoelectron spectroscopy study of anodically oxidized SIMFUEL surfaces, *Electrochim. Acta* 49 (2004) 1863-1873.
- [11] C.A. Bunton, and H.J. Foroudian, A quantitative treatment of micellar effects upon dephosphorylation by hydroperoxide anion, *Langmuir* 9 (1993) 2832-2835.

- [12] Y. Zhang, and G.S. Wilson, Electrochemical oxidation of H_2O_2 on Pt and Pt + Ir electrodes in physiological buffer and its applicability to H_2O_2 -based biosensors, *J. Electroanal. Chem.* 345 (1993) 253-271.
- [13] A. Hickling, and W.H. Wilson, The anodic decomposition of hydrogen peroxide, *J. Electrochem. Soc.* 98 (1951) 425-433.
- [14] A. Hiroki, and J.A. LaVerne, Decomposition of Hydrogen Peroxide at Water-Ceramic Oxide Interface, *J. Phys. Chem. B* 109 (2005) 3364-3370.
- [15] C.M. Lousada, A.J. Johansson, T. Brinck, and M. Jonsson, Mechanism of H_2O_2 Decomposition on Transition Metal Oxide Surfaces, *J. Phys. Chem. C* 116 (2012) 9533-9543.
- [16] S.S. Lin, and M.D. Gurol, Catalytic decomposition of hydrogen peroxide on iron oxide: kinetics, mechanism and implications, *Environ. Sci. Technol.* 32 (1998) 1417-1423.
- [17] D. Fu, X. Zhang, P.G. Keech, D.W. Shoesmith, and J.C. Wren, An electrochemical study of H_2O_2 decomposition on single-phase $\gamma\text{-FeOOH}$ films, *Electrochim. Acta* 55 (2010) 3787-3796.
- [18] H. He, Z. Ding, and D.W. Shoesmith, The determination of electrochemical reactivity and sustainability on individual hyper-stoichiometric UO_{2+x} grains by Raman microspectroscopy and scanning electrochemical microscopy, *Electrochem. Comm.* 11 (2009) 1724-1727.

Chapter 6

THE ANODIC REACTIONS ON SIMULATED NUCLEAR FUEL (SIMFUEL) IN HYDROGEN PEROXIDE SOLUTIONS – EFFECT OF CARBONATE/BICARBONATE

6.1 Introduction

In this chapter, the anodic behaviour of simulated nuclear fuel (SIMFUEL) in solutions containing H_2O_2 and $\text{HCO}_3^-/\text{CO}_3^{2-}$ has been studied electrochemically and using surface/solution analytical techniques, in particular X-ray photoelectron spectroscopy (XPS) and inductively coupled plasma atomic emission spectroscopy (ICP-AES).

For a Canadian deep geologic repository, $\text{HCO}_3^-/\text{CO}_3^{2-}$ is a key groundwater species that has a significant impact on fuel corrosion [1]. Previous studies on the influence of $\text{HCO}_3^-/\text{CO}_3^{2-}$ on UO_2 dissolution have been reviewed in Section 1.5.3. Bicarbonate/carbonate is a strong complexing agent for the $\text{U}^{\text{VI}}\text{O}_2^{2+}$ ion thus will significantly increase the solubility of fuel matrix [2-4]. The deposition of U^{VI} corrosion products on the UO_2 surface was found to be eliminated when a sufficient $\text{HCO}_3^{2-}/\text{CO}_3^{2-}$ concentration was present [5, 6].

As previously mentioned, two anodic reactions are possible, the oxidative dissolution of UO_2 and H_2O_2 oxidation. Results discussed in Chapter 5 suggested that the dominant reaction is H_2O_2 oxidation in alkaline solutions, and its rate is controlled partially by transport through a thin and slowly-dissolving U^{VI} oxide/hydroxide surface layer in non-complexing condition. The addition of $\text{HCO}_3^{2-}/\text{CO}_3^{2-}$ is expected to accelerate the release

of U^{VI} surface species, which will unblock the underlying conductive $U^{IV}_{1-2x}U^V_{2x}O_{2+x}$ surface. Presently, the balance between these two anodic reactions in the presence of HCO_3^{2-}/CO_3^{2-} is not known. The carbonate-mediated decomposition of H_2O_2 has also been reported and reviewed in Section 1.5.2.2. However, whether or not HCO_3^-/CO_3^{2-} promotes H_2O_2 decomposition under the disposal conditions remains unresolved.

In this chapter, a primary goal is to examine the influence of HCO_3^-/CO_3^{2-} on the UO_2 surface status and the H_2O_2 decomposition process. A second goal is to determine the competition between H_2O_2 decomposition and UO_2 oxidation in the presence of HCO_3^-/CO_3^{2-} .

6.2 Experimental

The electrochemical equipment setup and the SIMFUEL electrode preparation were described in Section 2.1. The SIMFUEL used in this study replicates spent nuclear fuel with a 1.5 at.% burnup. All experiments were conducted in Ar-purged solutions (ultra-high purity, Praxair) at room temperature. The solutions were prepared using deionized water (18.2 M Ω cm) purified using a Millipore milli-Q-plus unit. The base electrolyte was 0.1 mol L⁻¹ NaCl. The total carbonate concentration ($[CO_3]_{tot}$) was adjusted with Na_2CO_3 and $NaHCO_3$ (Caledon Chemical) ranging from 10^{-4} to 2×10^{-1} mol L⁻¹, and the solution pH was adjusted, when required, using 0.1 mol L⁻¹ NaOH (Caledon Chemical). Hydrogen peroxide (3% w/v, LabChem Inc.) was added immediately prior to an experiment to a specific concentration in the range from 2×10^{-4} to 2×10^{-2} mol L⁻¹. The solution pH was monitored before and after electrochemical measurements.

The working electrode was cathodically cleaned at an applied potential of -1.2 V vs. SCE for 2 min prior to an experiment in order to remove any air-formed oxides. Cyclic voltammetric (CV) experiments were performed starting from -0.4 V (unless indicated otherwise) and scanning to $+0.4$ V at a scan rate of 15 mV s^{-1} . The use of this scan rate minimized the consumption of H_2O_2 . Polarization curves were recorded at a sequence of individual potentials in the range 0.1 to 0.4 V with 10 min being allowed at each potential to ensure steady-state was achieved. In corrosion experiments, E_{CORR} was recorded for 30 min at various $[\text{CO}_3]_{\text{tot}}$ and $[\text{H}_2\text{O}_2]$. The electrode was then quickly transferred to a H_2O_2 -free solution to avoid interference from H_2O_2 reduction while recording a cathodic stripping voltammogram (CSV). In dissolution experiments, the working electrode was potentiostated at 0.3 V for 4 hours in a small electrochemical cell with a volume of 50 mL. Subsequently, the solution concentration of U was analyzed by inductively coupled plasma atomic emission spectroscopy (ICP-AES). Scanning electron microscopy (SEM) and X-ray photoelectron spectroscopy (XPS) were used to analyse electrode surfaces before and after anodic oxidation at 0.2/0.30 V. A detailed description of each experimental technique can be found in Chapter 2.

6.3 Results and discussion

6.3.1 Voltammetry

Goldik et al. [7] studied the voltammetric behaviour of H_2O_2 -free solutions with and without $\text{HCO}_3^-/\text{CO}_3^{2-}$, Fig. 6.1. The shallow anodic current in the potential range I was attributed to the anodic oxidation of the UO_2 matrix surface to $\text{U}^{\text{IV}}_{1-2x}\text{U}^{\text{V}}_{2x}\text{O}_{2+x}$ and the current increase at more positive potentials (II in Fig. 6.1) to the oxidation of this layer to

a $U^{VI}O_3$ layer accompanied by dissolution as $U^{VI}O_2^{2+}$. On the reverse scan this combined layer is reduced in the potential region C_1 . When HCO_3^-/CO_3^{2-} is present oxidative dissolution in region II is clearly accelerated (as $U^{VI}O_2(CO_3)_y^{(2-2y)+}$) and the smaller (almost negligible) reduction peak in the potential range -0.7 V to -0.9 V confirms that the formation of the U^{VI} layer is reduced.

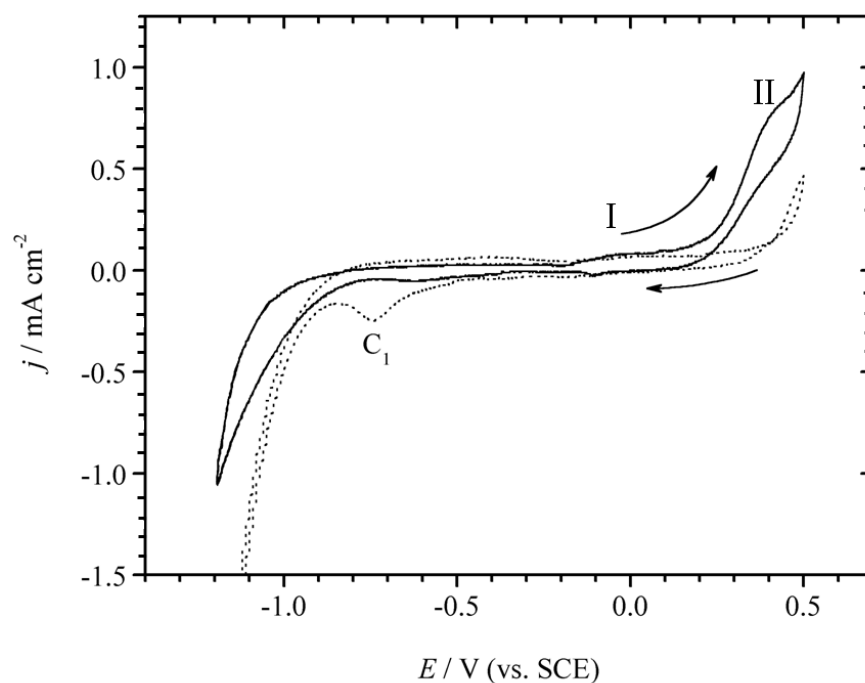
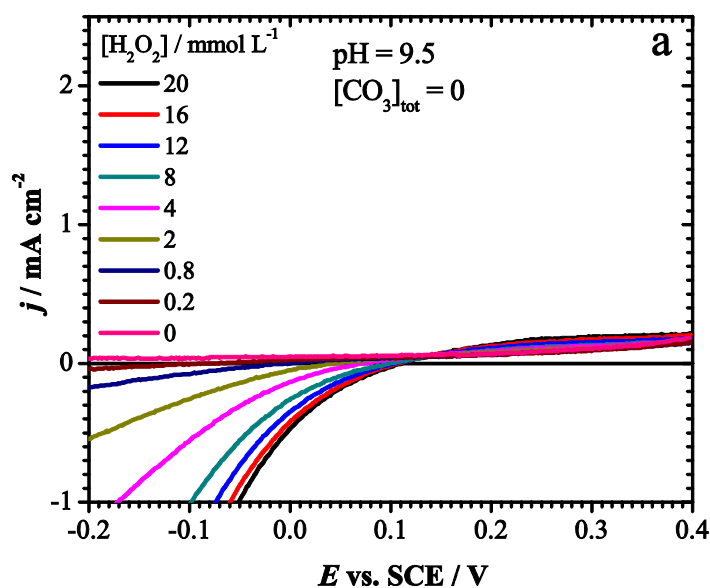
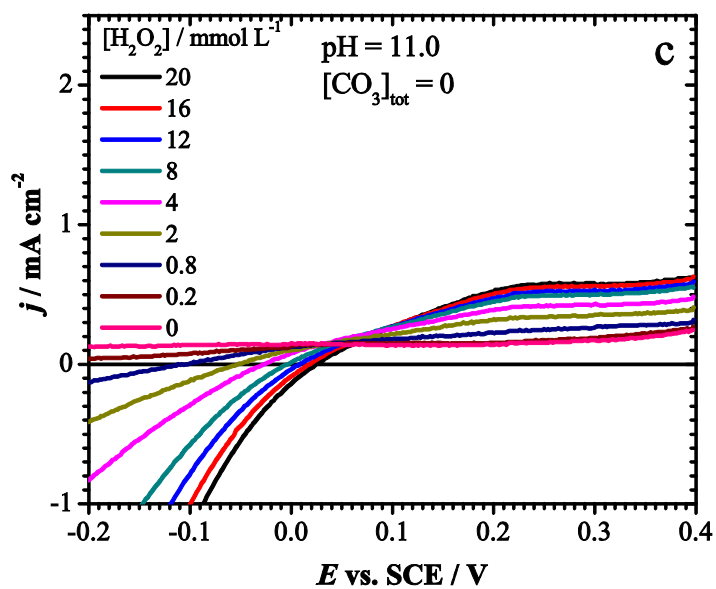
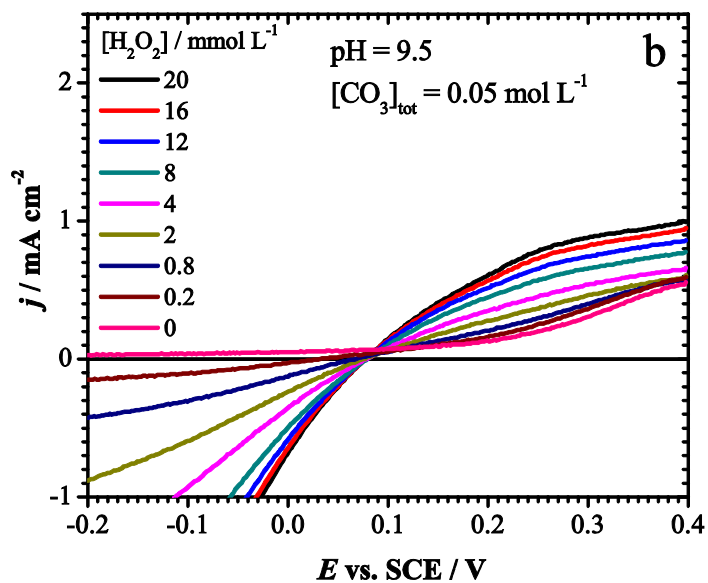


Fig. 6.1. CVs recorded on 1.5 at. % SIMFUEL in 0.1 mol L^{-1} NaCl (dashed line), and 0.1 mol L^{-1} NaCl + 0.1 mol L^{-1} $Na_2CO_3/NaHCO_3$ (solid line), both solutions at pH 9.7. Rotation rate = 16.7 Hz ; scan rate = 10 mV s^{-1} . Data from Ref [7].

A series of voltammetric measurements were performed in a HCO_3^-/CO_3^{2-} -free solution and a solution containing 0.05 mol L^{-1} HCO_3^-/CO_3^{2-} at various $[H_2O_2]$. Fig. 6.2 shows sections of the forward scans recorded at two pH values (9.5 and 11.0). At pH = 9.5, the cathodic reduction current readily increased with $[H_2O_2]$, while the increase in anodic

current was marginal compared to the background current recorded in the absence of H_2O_2 . In the presence of $\text{HCO}_3^-/\text{CO}_3^{2-}$, the cathodic current increased slightly probably due to the inhibition of the growth of the $\text{U}^{\text{IV}}_{1-2x}\text{U}^{\text{V}}_{2x}\text{O}_{2+x}$ layer. This effect has been studied in detail previously [7]. At pH = 9.5 in the presence of $\text{HCO}_3^-/\text{CO}_3^{2-}$ the anodic currents increased markedly and displayed a dependence on $[\text{H}_2\text{O}_2]$. At the more alkaline pH of 11.0, the current for H_2O_2 oxidation is increased in both the absence and presence $\text{HCO}_3^-/\text{CO}_3^{2-}$, but particularly so in the latter case.





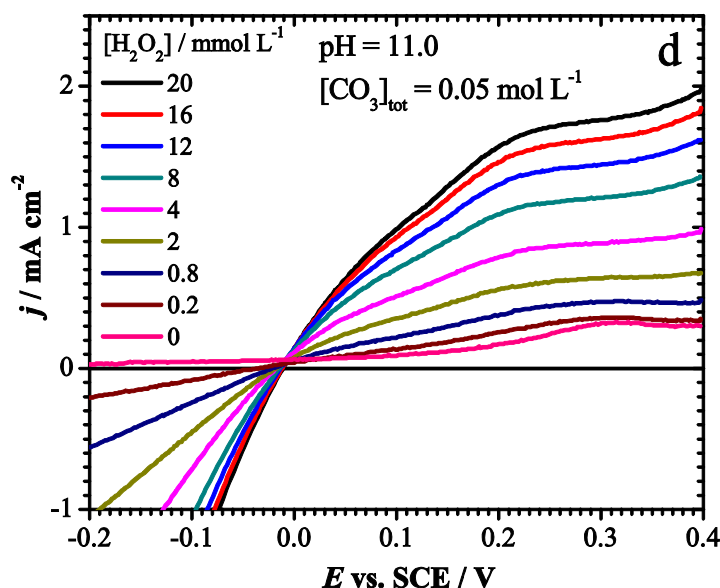


Fig. 6.2. Current densities recorded on 1.5 at.% SIMFUEL on the forward scan of CVs in 0.1 mol L^{-1} NaCl containing different $[\text{H}_2\text{O}_2]$ at pH 9.5 and 11.0; rotation rate = 25 Hz; scan rate = 15 mV s^{-1} ; (a) and (c): $[\text{CO}_3]_{\text{tot}} = 0$; (b) and (d): $[\text{CO}_3]_{\text{tot}} = 0.05 \text{ mol L}^{-1}$.

Fig. 6.3 shows the anodic currents at $E = 0.4 \text{ V}$, after correction for the background current ($[\text{H}_2\text{O}_2] = 0 \text{ mol L}^{-1}$), taken from Fig. 6.2 as a function of $[\text{H}_2\text{O}_2]$. When $\text{HCO}_3^-/\text{CO}_3^{2-}$ is present, the anodic currents became increasingly dependent on $[\text{H}_2\text{O}_2]$ compared to the values measured in $\text{HCO}_3^-/\text{CO}_3^{2-}$ -free solutions. At the higher pH (11.0), the anodic current was directly proportional to $[\text{H}_2\text{O}_2]$ at low $[\text{H}_2\text{O}_2]$ but suppressed at $[\text{H}_2\text{O}_2] > 5 \text{ mmol L}^{-1}$. The increase in anodic current with potential can be attributed to a combination of the anodic dissolution of UO_2 and the oxidation of H_2O_2 . When $\text{HCO}_3^-/\text{CO}_3^{2-}$ is present the insulating U^{VI} surface species are chemically dissolved (as $\text{U}^{\text{VI}}\text{O}_2(\text{CO}_3)_y^{(2-2y)+}$) which exposes the underlying conductive $\text{U}^{\text{IV}}_{1-2x}\text{U}^{\text{V}}_{2x}\text{O}_{2+x}$ surface allowing enhanced electron transfer to H_2O_2 . In the absence of $\text{HCO}_3^-/\text{CO}_3^{2-}$ the

dissolution rate of U^{VI} surface species (as $U^{VI}O_2(OH)_y^{(2-y)+}$) is considerably slower and both the anodic reactions are inhibited by the presence of a partially permeable U^{VI} surface oxide/hydroxide layer. This influence of pH has been discussed previously in Chapter 5. A possible explanation for the enhanced anodic current when HCO_3^-/CO_3^{2-} is present is that the oxide/hydroxide layer is either not present or considerably reduced in thickness.

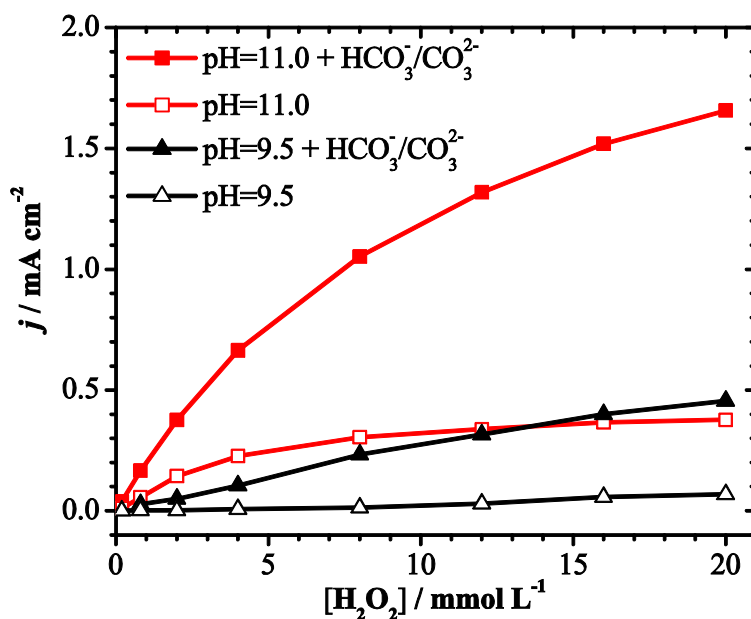


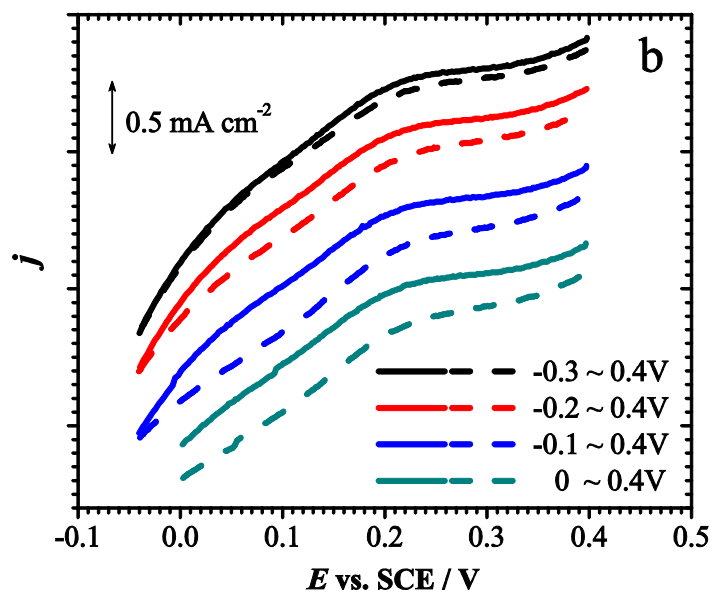
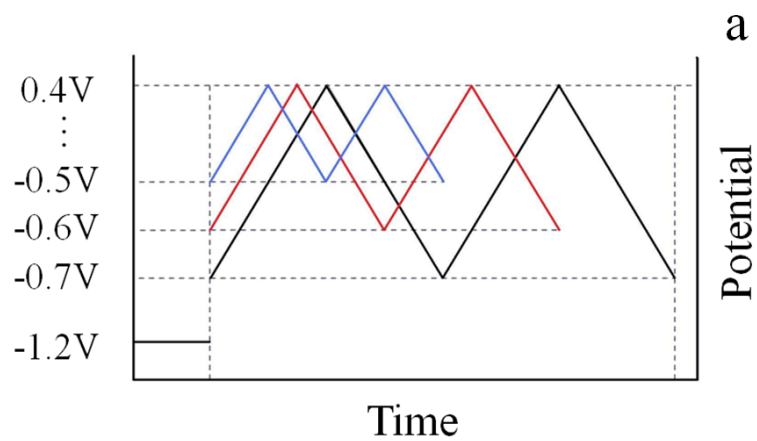
Fig. 6.3. Anodic current densities recorded on SIMFUEL as a function of $[H_2O_2]$ in HCO_3^-/CO_3^{2-} -free/-containing solution. Data points were taken at $E = 0.4$ V in the CV scans (Fig. 6.2) and are corrected for the background current recorded in a solution without H_2O_2 .

To examine this possibility, a dual scan experiment was performed. The potential was scanned from various negative limits to the same positive limit (+0.4 V) and back,

followed immediately by a second scan over the same potential range. An illustration of the scan procedure is provided in Fig. 6.4 (a). The relevant sections of the forward scans are plotted in Fig. 6.4 (b) and (c). A lower current on the second scan indicates that the anodic current was suppressed on the second forward scan due to the formation of an oxidized surface layer on the first scan. Providing the negative limiting potential is ≥ -0.3 V, a discrepancy exists between the anodic currents measured on the two scans confirming that the anodic reaction is inhibited by the presence of a surface film. However, this discrepancy became less significant as the cathodic limiting potential was made more negative, and was negligible once the potential was < -0.3 V. This potential dependence confirms that the anodic current up to potentials of $+0.4$ V is inhibited by the presence of a U^{VI} layer which can be removed by cathodic reduction over the potential range -0.2 V to -0.4 V. Previously, in experiments conducted in the absence of HCO_3^-/CO_3^{2-} , the anodically formed surface layer could not be removed unless the potential at the negative limit was ≤ -0.7 V [7]; i.e., the potential range of the reduction peak C_1 in Fig. 6.1.

These results show the electrode surface is more readily cathodically regenerated in HCO_3^-/CO_3^{2-} , which is consistent with the absence of the reduction peak (C_1) in the CV in Fig. 6.1, when HCO_3^-/CO_3^{2-} was present. In the absence of HCO_3^-/CO_3^{2-} anodic oxidation processes were shown to be inhibited by a $U^{IV}_{1-2x}U^V_{2x}O_{2+x}/U^{VI}$ oxide/hydroxide layer. Other studies [8] have shown the $U^{IV}_{1-2x}U^V_{2x}O_{2+x}$ layer formed anodically is considerably thinner when HCO_3^-/CO_3^{2-} is present and these results confirm that anodic oxidation processes are limited by the presence of a $U^{VI}CO_3$ surface layer which

chemically dissolves much more rapidly than the U^{VI} oxide/hydroxide present in the absence of HCO_3^-/CO_3^{2-} , and is much more readily cathodically reduced.



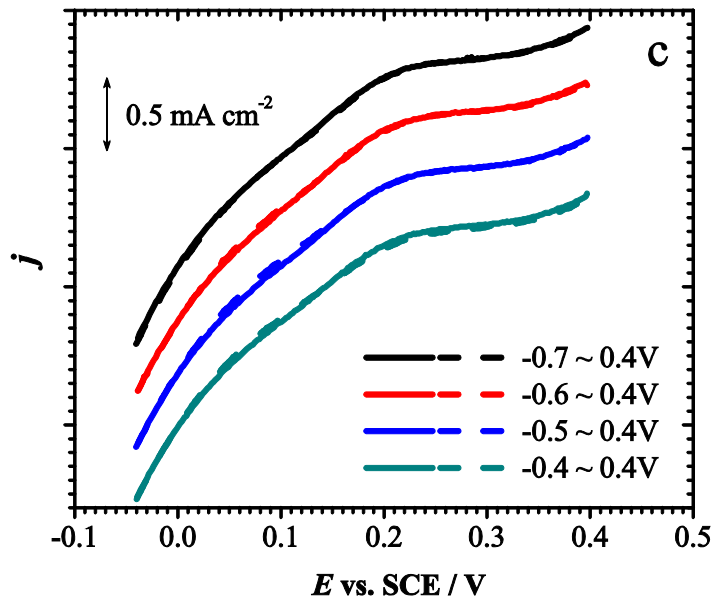


Fig. 6.4. Anodic currents recorded on 1.5 at.% SIMFUEL for various potential scan ranges as shown in the illustration of the scan procedure. Each color indicates two consecutive scans from a specific negative potential limit. Solid lines are the 1st forward scan and dashed lines are the 2nd forward scan. $[\text{NaCl}] = 0.1 \text{ mol L}^{-1}$; $[\text{CO}_3]_{\text{tot}} = 0.05 \text{ mol L}^{-1}$; $[\text{H}_2\text{O}_2] = 0.02 \text{ mol L}^{-1}$; $\text{pH} = 11.0$; rotation rate = 25 Hz; scan rate = 15 mV s^{-1} .

6.3.2 Dissolution experiments

To separate the contributions to the anodic current from the dissolution of UO_2 and the oxidation of H_2O_2 , the U^{VI} content of the solution was analyzed after anodic oxidation at 0.3 V for 4 h in solutions with and without $\text{HCO}_3^-/\text{CO}_3^{2-}$. At this positive potential the likelihood of H_2O_2 decomposition by the coupling of its oxidation and reduction is assumed to be negligible since the open circuit potential is $\leq 0.05 \text{ V}$, Fig. 6.2. Similarly the corrosion of UO_2 by H_2O_2 is also assumed to be negligible. The analyzed amount of

UO_2^{2+} was converted to the charge required for oxidative dissolution of UO_2 . Over this period of anodic oxidation the charge consumed in producing the $\text{U}^{\text{VI}}\text{CO}_3$ layer would be negligible. The total anodic charge was obtained by integration of the measured anodic current over the time interval recorded, and the difference between the two charges can be attributed to H_2O_2 oxidation. Table 6.1 compares the values obtained in a solution free of $\text{HCO}_3^-/\text{CO}_3^{2-}$ and in a solution containing $\text{HCO}_3^-/\text{CO}_3^{2-}$ with two different $[\text{H}_2\text{O}_2]$. In $\text{HCO}_3^-/\text{CO}_3^{2-}$ -free solution, a large fraction (71.5%) of the current went to H_2O_2 oxidation, and a similar fraction went to H_2O_2 oxidation in $\text{HCO}_3^-/\text{CO}_3^{2-}$ -containing solution with the same $[\text{H}_2\text{O}_2]$ (76.8%). This similarity suggests, but does not confirm, that $\text{HCO}_3^-/\text{CO}_3^{2-}$ promoted both H_2O_2 oxidation and UO_2 dissolution. In a solution with a lower $[\text{H}_2\text{O}_2]$ ($10^{-3} \text{ mol L}^{-1}$), only 27.3% of anodic charge went to H_2O_2 oxidation.

Inspection of the CVs in Fig. 6.2c shows that ($\text{pH} = 11$, $E = 0.3 \text{ V}$, $[\text{CO}_3]_{\text{tot}} = 0 \text{ mol L}^{-1}$ and $[\text{H}_2\text{O}_2] = 20 \text{ mmol L}^{-1}$) the ratio of the anodic currents in H_2O_2 -free and H_2O_2 -containing solutions is 0.3; i.e., 30% of the current at this potential should go to anodic oxidation/dissolution of UO_2 . Considering that 71.5% of the anodic current was consumed in H_2O_2 oxidation (Table 6.1) (i.e., 28.5% was consumed by UO_2 dissolution), the increase of current from H_2O_2 -free to H_2O_2 -containing solutions was mainly due in H_2O_2 oxidation; i.e., the addition of H_2O_2 did not significantly accelerate UO_2 dissolution. A similar comparison of currents for the $\text{HCO}_3^-/\text{CO}_3^{2-}$ solution (Table 6.1 and Fig. 6.2d) showed this current ratio to be ~20%. Based on the analytical results this percentage should be 23.2%. While these results suggest a slight catalysis of UO_2 dissolution by the combination of H_2O_2 and $\text{HCO}_3^-/\text{CO}_3^{2-}$ a more extensive analysis is required to justify this claim.

Table 6.1. Distribution of charge between UO₂ oxidative dissolution and H₂O₂ oxidation^a

	[CO ₃] _{tot} =0 mol L ⁻¹ , [H ₂ O ₂] = 0.02 mol L ⁻¹	[CO ₃] _{tot} =0.05 mol L ⁻¹ , [H ₂ O ₂] = 0.02 mol L ⁻¹	[CO ₃] _{tot} =0.05 mol L ⁻¹ , [H ₂ O ₂] = 0.001 mol L ⁻¹
Total anodic charge (C)	0.0978	0.812	0.170
Charge due to UO ₂ dissolution (C)	0.0279	0.188	0.124
Charge due to H ₂ O ₂ oxidation (C)	0.0699	0.624	0.0464
Fraction of H ₂ O ₂ oxidation	71.5%	76.8%	27.3%

^a SIMFUEL electrode potentiostatically oxidized at 0.3 V for 4 h in a solution containing [NaCl] = 0.1 mol L⁻¹, pH = 11.0. No rotation was applied.

6.3.3 Steady-state currents at various [CO₃]_{tot}

Steady-state anodic currents recorded potentiostatically at [H₂O₂] = 0.02 mol L⁻¹ are plotted in the Tafel form in Fig. 6.5. As expected, the anodic current increased with [CO₃]_{tot} over the range from 0 to 0.1 mol L⁻¹ although the increase became marginal for [CO₃]_{tot} > 0.05 mol L⁻¹. Also, the current was only weakly dependent on potential over the range 0.15 V to 0.30 V consistent with control of the current by the chemical dissolution of a U^{VI} surface layer (U^{VI}O_{3.y}H₂O in the absence and U^{VI}O₂CO₃ in the presence of HCO₃⁻/CO₃²⁻). The increase in current for E > 0.3 V appears to be due to the oxidation of H₂O₂ on ε-particles and is presented in Chapter 7.

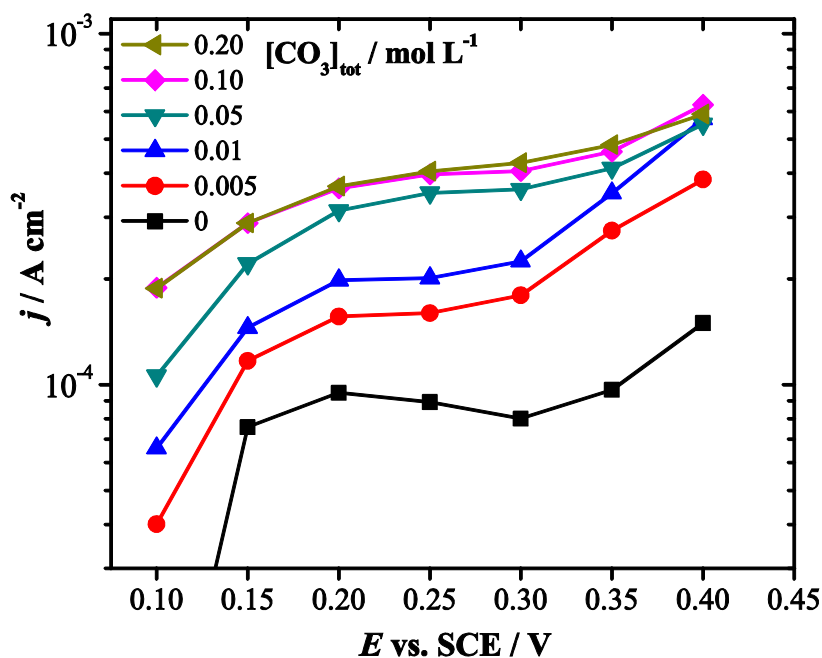
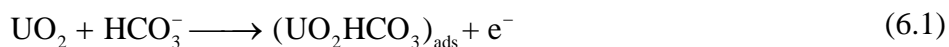
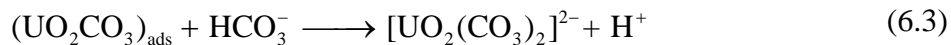


Fig. 6.5. Tafel plots recorded on 1.5 at.% SIMFUEL in solutions containing different $[\text{CO}_3]_{\text{tot}}$. $[\text{NaCl}] = 0.1 \text{ mol L}^{-1}$; $[\text{H}_2\text{O}_2] = 0.02 \text{ mol L}^{-1}$; $\text{pH} = 9.7$; rotation rate = 16.7 Hz.

Fig. 6.6 shows the anodic currents plotted against $[\text{CO}_3]_{\text{tot}}$. At the lowest potential, 0.10 V, the reaction order (equal to the slope of the corresponding line) is 0.42, but decreases to ~0.25 over the potential range 0.15 to 0.30 V, and to 0.09 at 0.40 V. The relatively high reaction order (~0.42) with respect to $[\text{CO}_3]_{\text{tot}}$ at low potentials suggests a very significant fraction of the total anodic current can be attributed to the anodic dissolution of UO_2 which in $\text{HCO}_3^-/\text{CO}_3^{2-}$ solution has been shown to proceed via the reaction sequence [8],





However, the decrease in reaction order at higher potentials suggests a change in dominant reaction from $\text{HCO}_3^-/\text{CO}_3^{2-}$ -induced UO_2 dissolution to H_2O_2 oxidation. Attempts to confirm this are underway. That H_2O_2 oxidation is the dominant reaction at high potentials is confirmed by the analyses in Table 6.1. The influence of potential on the balance between UO_2 dissolution and H_2O_2 remains to be determined.

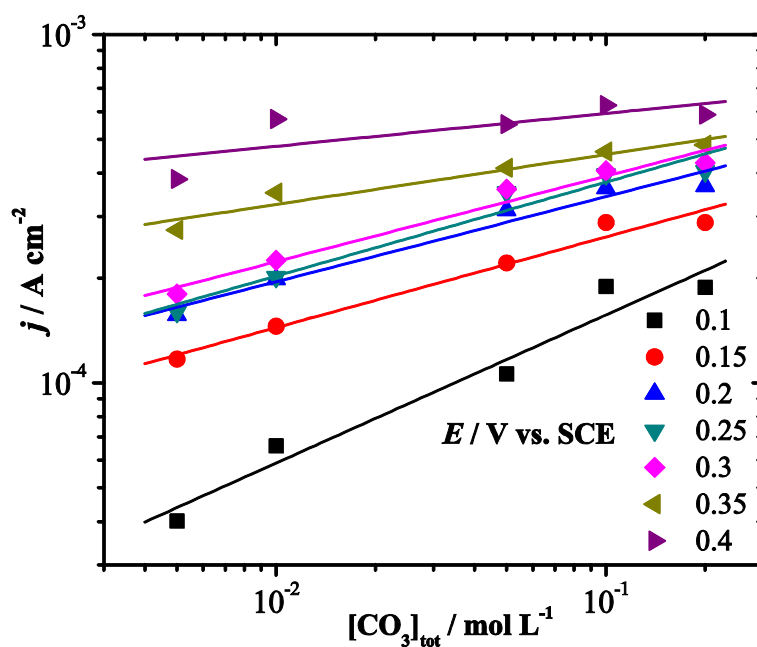


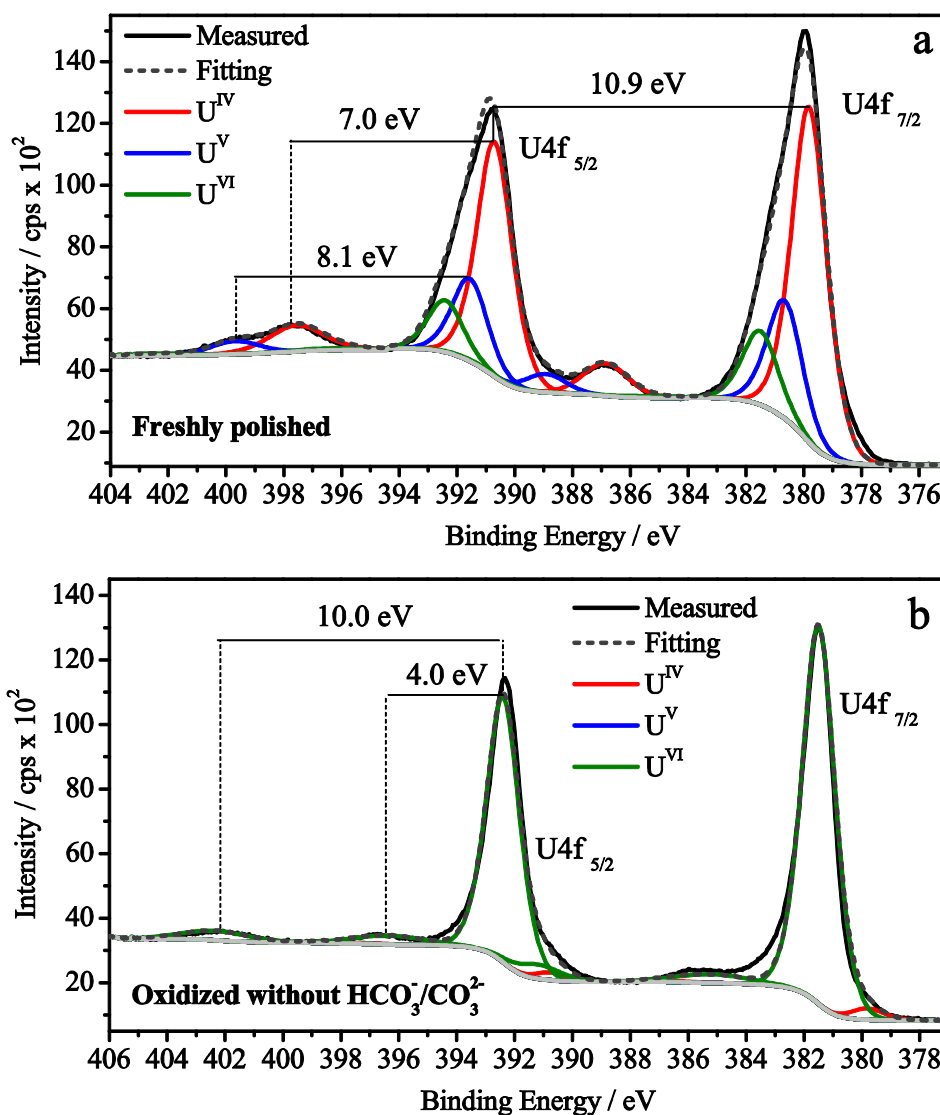
Fig. 6.6. Plots of the anodic current densities as a function of $[\text{CO}_3]_{\text{tot}}$ at various applied potentials. (■) +0.10 V, slope = 0.42; (●) +0.15 V, slope = 0.26; (▲) +0.20 V, slope = 0.24; (▼) +0.25 V, slope = 0.27; (◆) +0.30 V, slope = 0.25; (◄) +0.35 V, slope = 0.14; (►) +0.40 V, slope = 0.09.

6.3.4 XPS analysis

XPS analyses were performed to confirm that the anodic oxidation processes were partially controlled by the presence of surface films in the potential region 0.15 V to 0.3 V. A detailed description of the data analysis and the fitting procedures can be found in Section 2.2.2. Fig. 6.7 shows high resolution XPS spectra for the U 4f_{5/2} and U 4f_{7/2} regions and their associated satellites recorded on SIMFUEL specimens before and after oxidation at +0.3 V in a H₂O₂ containing solution with and without HCO₃⁻/CO₃²⁻. The deconvoluted U 4f_{7/2} peak recorded on the freshly polished electrode, Fig. 6.7(a), shows that U^{IV} and U^V are the dominant oxidation states (> 85%). This is supported by the location of the satellite peaks at binding energies of 7.0 eV and 8.1 eV higher than the U 4f_{5/2} peak. It is possible that the small amount of U^{VI} present on the surface can be attributed to slight air oxidation of the surface on transfer to the spectrometer. The surface of the electrode anodically oxidized at +0.3 V in HCO₃⁻/CO₃²⁻-free solution (Fig. 6.7(b)) was dominated by U^{VI} (97%). This conclusion is supported by the presence of the satellite peaks at binding energies of 4.0 eV and 10.0 eV above the U(4f_{5/2}) peak [9-11]. This analysis confirms the presence of a dominantly U^{VI} oxide/hydroxide surface layer when the anodic oxidation current is suppressed in the absence of HCO₃⁻/CO₃²⁻, Fig. 6.2(a).

This surface U^{VI} layer was considerably thinner in the presence of HCO₃⁻/CO₃²⁻, Fig. 6.7(c), a mixture of all three oxidation states being observed. Since the U^{VI} layer formed is rapidly dissolving at 0.3V it is likely that the measured U^{VI} content of the surface is not a true measure of the U^{VI} surface coverage when the potential was applied but reflects the difficulty in extracting the electrode from the cell without a partial loss of the U^{VI} surface layer. Table 6.2 shows the fractions of individual oxidation states determined after anodic

oxidation at two potentials, +0.2 V and +0.3 V. In both the presence and absence of $\text{HCO}_3^-/\text{CO}_3^{2-}$ the U^{VI} content of the surface is greater at the more positive potential consistent with the thickening of, or more extensive coverage by, a surface U^{VI} layer expected if the anodic current is to be independent of potential as observed, Fig. 6.5.



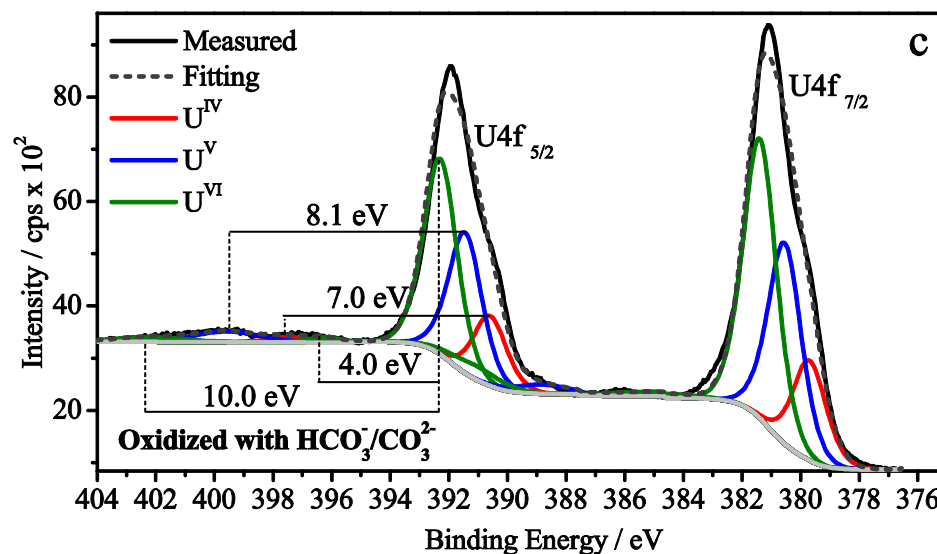


Fig. 6.7. Resolved U ($4f_{5/2}$)/U ($4f_{7/2}$) regions of XPS spectra recorded on a 1.5 at.% SIMFUEL surface before and after anodic oxidation at $E = 0.30$ V for 0.5 hour in 0.1 mol L^{-1} NaCl + 0.02 mol L^{-1} H_2O_2 at pH 11.0 with or without $\text{HCO}_3^-/\text{CO}_3^{2-}$. The horizontal lines indicate the separation between specific satellite peaks and the U $4f_{5/2}$ peak. (a) freshly polished specimen; (b) specimen after anodic oxidation in a $\text{HCO}_3^-/\text{CO}_3^{2-}$ -free solution; (c) specimen after anodic oxidation in a solution containing 0.05 mol L^{-1} $\text{Na}_2\text{CO}_3/\text{NaHCO}_3$.

Table 6.2. The fractions of U^{IV} , U^{V} , and U^{VI} in the surface of a SIMFUEL electrode before and after anodic oxidation in 0.1 mol L^{-1} NaCl + 0.02 mol L^{-1} H_2O_2 , pH = 11.0.

Oxidation states	Freshly polished surface	$[\text{CO}_3]_{\text{tot}} = 0 \text{ mol L}^{-1}$		$[\text{CO}_3]_{\text{tot}} = 0.05 \text{ mol L}^{-1}$	
		0.2 V	0.3 V	0.2 V	0.3 V
U^{IV}	64%	2%	3%	23%	17%
U^{V}	22%	17%	0%	40%	35%
U^{VI}	14%	81%	97%	37%	48%

To confirm these analyses the valence band spectra were also recorded, Fig. 6.8. The occupancy of the 5f level (~ 1 eV) is in accordance with the deconvoluted 4f spectra varying in intensity as the dominant oxidation state changes from U^{IV} to U^{VI} . These analyses confirm that the suppression of anodic oxidation in the absence of carbonate can be attributed to the presence of a U^{VI} surface layer thick enough to obscure the underlying $U^{IV}_{1-2x}U^V_{2x}O_{2+x}$ layer. In the presence of HCO_3^-/CO_3^{2-} the surface remains partially blocked consistent with the potential-independent currents measured in this potential region, Fig. 6.2(d) and Fig. 6.5.

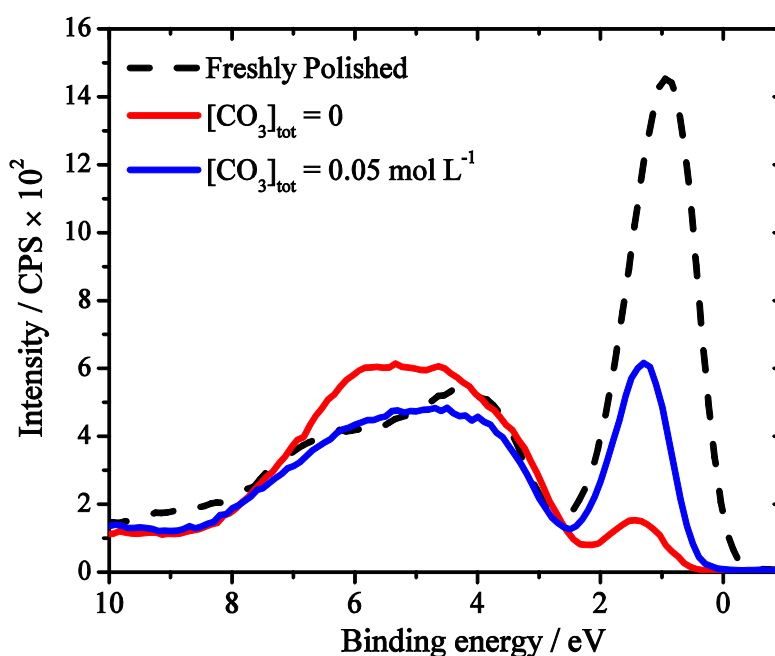
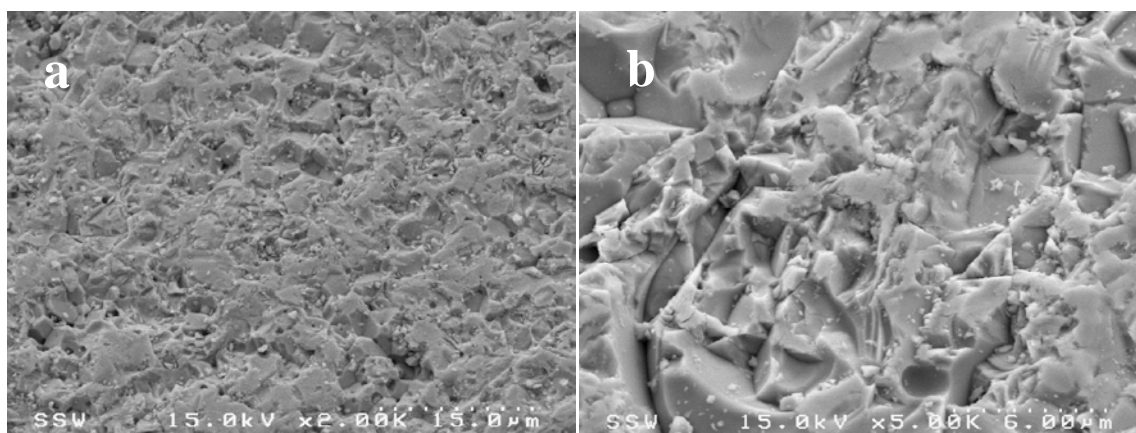


Fig. 6.8. The valence band region of the XPS spectra recorded on a 1.5 at.% SIMFUEL surface before and after anodic oxidation at $E = 0.30$ V for 0.5 hour in 0.1 mol L^{-1} NaCl + 0.02 mol L^{-1} H_2O_2 at pH 11.0 with or without HCO_3^-/CO_3^{2-} . Dashed line: freshly

polished specimen; red line: specimen after oxidation in $\text{HCO}_3^-/\text{CO}_3^{2-}$ -free solution; blue line: specimen after oxidation in solution containing $0.05 \text{ mol L}^{-1} \text{ Na}_2\text{CO}_3/\text{NaHCO}_3$.

6.3.5 SEM imaging

Fig. 6.9 (a) and (b) show micrographs of the freshly polished SIMFUEL specimen. Micrographs (c) and (d), recorded after anodic polarization at $E = 0.30 \text{ V}$ for 1.5 hours in $\text{HCO}_3^-/\text{CO}_3^{2-}$ -free solution, indicate little change in surface morphology had occurred, confirming the limited extent of oxidative dissolution. By contrast, after an equal period of anodic oxidation in the presence of $\text{HCO}_3^-/\text{CO}_3^{2-}$ the electrode surface had undergone significant dissolution with the development of many etch pits and pores, Fig. 6.9 (e) and (f), consistent with the data in Table 6.1 showing the consumption of a considerable dissolution charge.



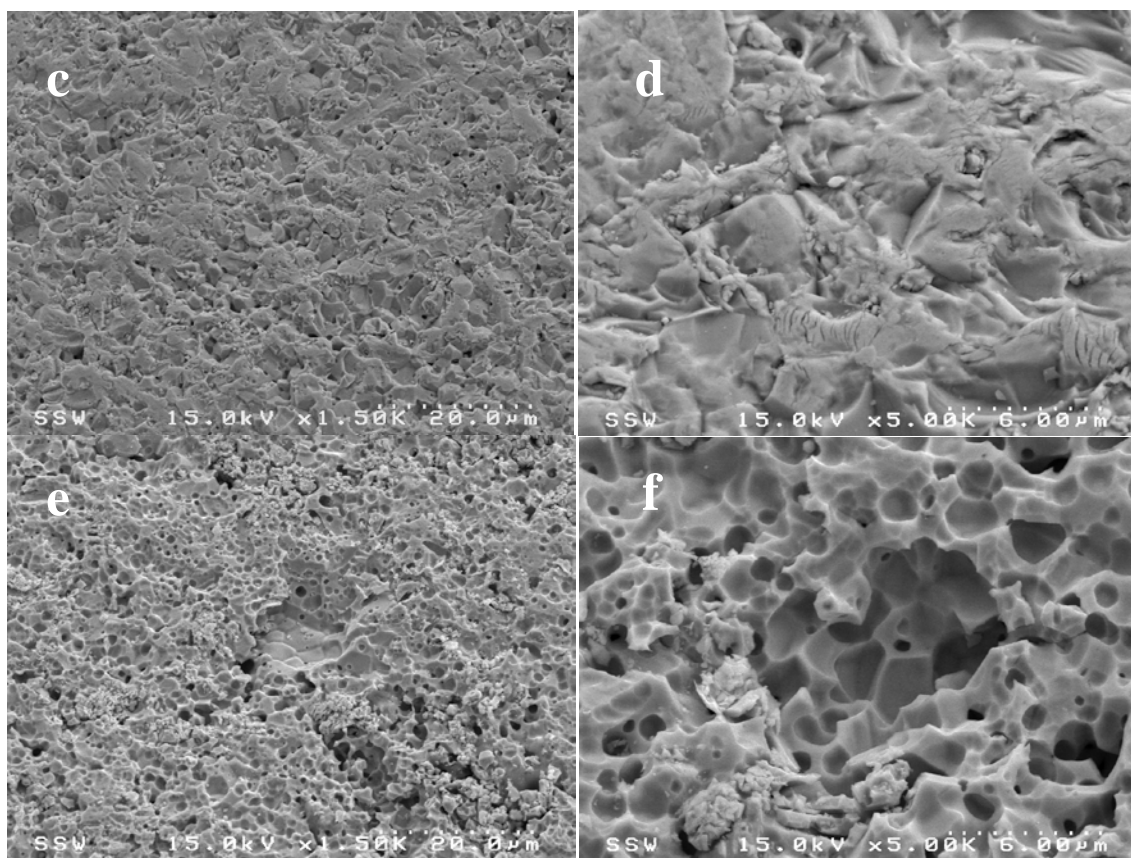


Fig. 6.9. SEM micrographs of SIMFUEL specimens before and after anodic oxidation at $E = 0.30$ V for 1.5 hours in $0.1 \text{ mol L}^{-1} \text{ NaCl} + 0.02 \text{ mol L}^{-1} \text{ H}_2\text{O}_2$ at pH 11.0 with or without 0.05 mol L^{-1} of $\text{HCO}_3^-/\text{CO}_3^{2-}$: (a) and (b) freshly polished specimen at 2k and 5k magnification; (c) and (d) surface after anodic oxidation in carbonate-free solution at 1.5k and 5k magnification; (e) and (f) surface after anodic oxidation in solution containing $0.05 \text{ mol L}^{-1} \text{ Na}_2\text{CO}_3/\text{NaHCO}_3$ at 1.5k and 5k magnification.

6.3.6 Open circuit behaviour

Fig. 6.10 shows values of E_{CORR} recorded as a function of $[\text{H}_2\text{O}_2]$ in solutions containing various $[\text{CO}_3]_{\text{tot}}$. For $[\text{CO}_3]_{\text{tot}} < 5 \times 10^{-3} \text{ mol L}^{-1}$, E_{CORR} values decrease with increasing $[\text{CO}_3]_{\text{tot}}$ and show a similar dependence on $[\text{H}_2\text{O}_2]$ to that observed in the absence of $\text{HCO}_3^-/\text{CO}_3^{2-}$ [12]; i.e., E_{CORR} is independent of $[\text{H}_2\text{O}_2]$ for $[\text{H}_2\text{O}_2] \leq 5 \times 10^{-3} \text{ mol L}^{-1}$

(region 1 in Fig. 6.10) but increases at higher $[\text{H}_2\text{O}_2]$ (region 2 in Fig. 6.10). As the $[\text{CO}_3]_{\text{tot}}$ is increased further, E_{CORR} values decrease substantially indicating a possible depolarization of the UO_2 corrosion rate. The E_{CORR} values maintain the differences between the two $[\text{H}_2\text{O}_2]$ ranges up to $5 \times 10^{-3} \text{ mol L}^{-1}$ $[\text{CO}_3]_{\text{tot}}$ but at higher $[\text{CO}_3]_{\text{tot}}$ employed ($10^{-1} \text{ mol L}^{-1}$) E_{CORR} varies only by $\sim 12 \text{ mV}$ over the whole $[\text{H}_2\text{O}_2]$ range.

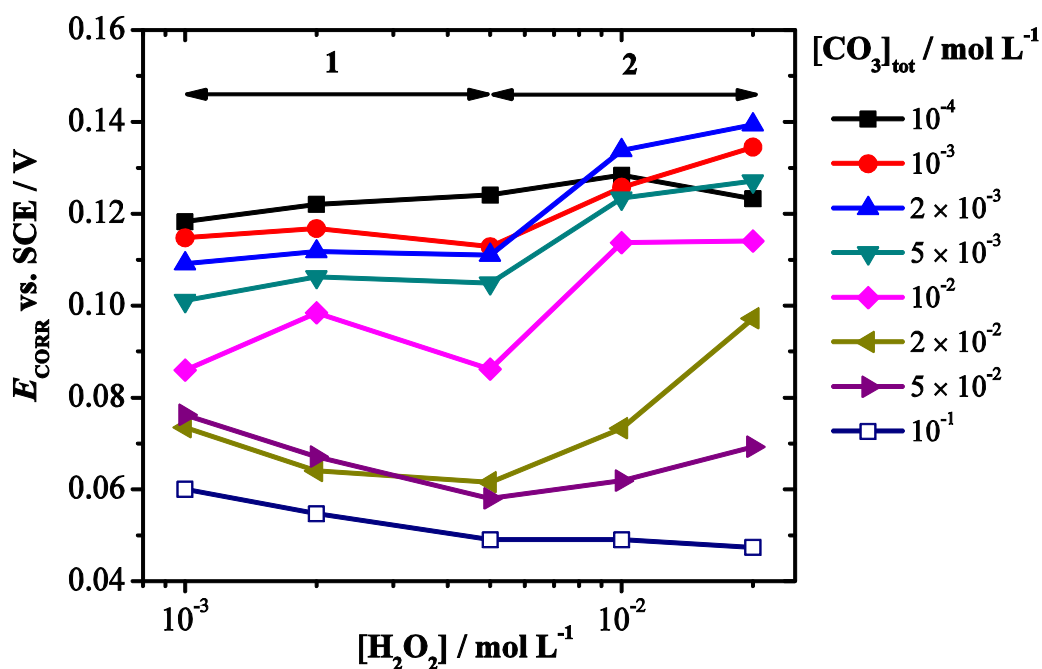


Fig. 6.10. E_{CORR} recorded on a 1.5 at.% SIMFUEL electrode as a function of $[\text{H}_2\text{O}_2]$ in 0.1 mol L^{-1} NaCl at $\text{pH} = 9.5$ with different $[\text{CO}_3]_{\text{tot}}$: (■) $10^{-4} \text{ mol L}^{-1}$; (●) $10^{-3} \text{ mol L}^{-1}$; (▲) $2 \times 10^{-3} \text{ mol L}^{-1}$; (▼) $5 \times 10^{-3} \text{ mol L}^{-1}$; (◆) $10^{-2} \text{ mol L}^{-1}$; (◄) $2 \times 10^{-2} \text{ mol L}^{-1}$; (►) $5 \times 10^{-2} \text{ mol L}^{-1}$; (□) $10^{-1} \text{ mol L}^{-1}$.

Fig. 6.11 and Fig. 6.12 show the fractions of individual oxidation states as a function of $[\text{H}_2\text{O}_2]$ recorded in a solution free of $\text{HCO}_3^-/\text{CO}_3^{2-}$, Fig. 6.11, and in a solution containing the maximum $[\text{CO}_3]_{\text{tot}}$ used in the separate series of E_{CORR} measurements (Fig. 6.10), Fig.

6.12. In the absence of $\text{HCO}_3^-/\text{CO}_3^{2-}$, Fig. 6.11, the fraction of U^{VI} on the electrode surface remained effectively independent of $[\text{H}_2\text{O}_2]$ over the potential region 1 (Fig. 6.10) when E_{CORR} does not change before increasing in potential region 2 (Fig. 6.10) as E_{CORR} increases. This behaviour confirms that observed previously [12], and would be consistent with dissolution controlled by slow U^{VI} release in potential region 1 evolving to localized dissolution at acidified locations in the surface asperities (Fig. 6.9c and d) on a more extensively covered U^{VI} surface at higher $[\text{H}_2\text{O}_2]$.

In the presence of $[\text{CO}_3]_{\text{tot}} = 0.1 \text{ mol L}^{-1}$, Fig. 6.12, the fractions of the individual oxidation states in the electrode surface did not change with $[\text{H}_2\text{O}_2]$ and the U^{VI} fraction was significantly lower than that observed in the absence of $\text{HCO}_3^-/\text{CO}_3^{2-}$, especially at the higher $[\text{H}_2\text{O}_2]$. This behaviour suggests that this $[\text{CO}_3]_{\text{tot}}$ (0.1 mol L^{-1}) prevents the accumulation of the U^{VI} surface layer leading to the blockage of the electrode surface observed in the anodic polarization scans in Fig. 6.2.

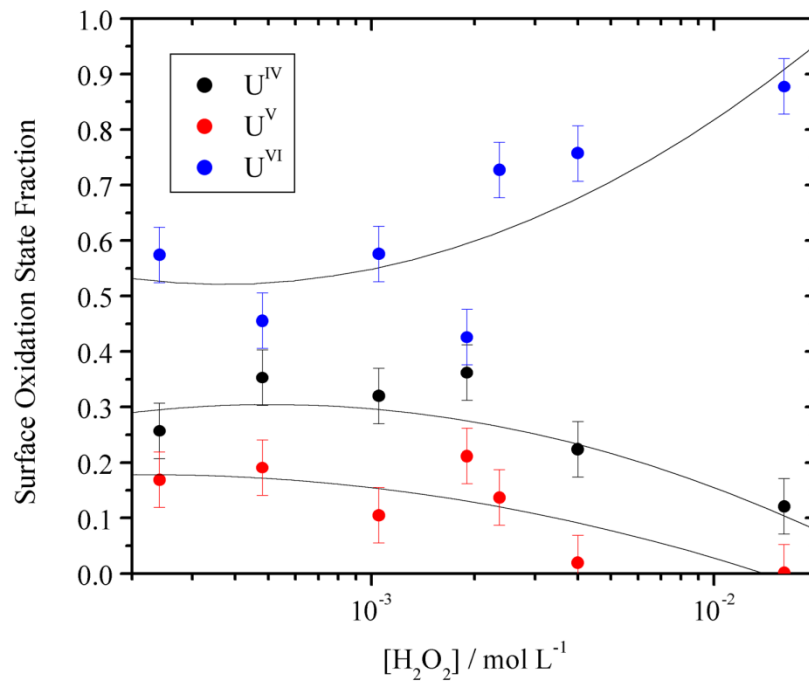


Fig. 6.11. The fraction of individual oxidation states present in the surface of a 1.5 at.% SIMFUEL electrode as a function of the H_2O_2 concentration in 0.1 mol L^{-1} NaCl at pH 9.7; (●) U(IV); (●) U(V); (●) U(VI).

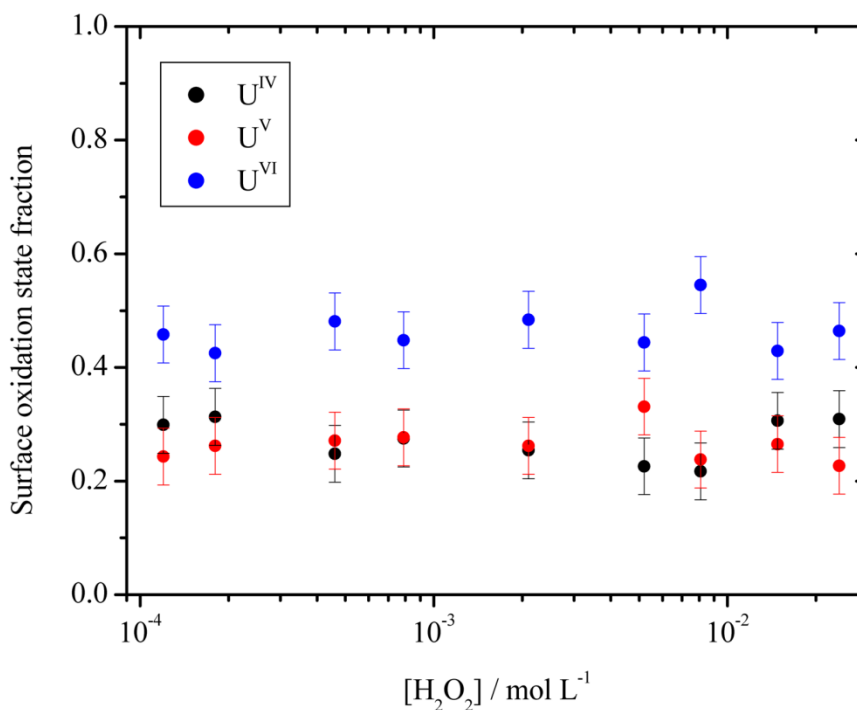


Fig. 6.12. The fraction of individual oxidation states present in the surface of a 1.5 at.% SIMFUEL electrode as a function of the [H₂O₂] in 0.1 mol L⁻¹ NaCl + 0.1 mol L⁻¹ Na₂CO₃/NaHCO₃ at pH 9.7; (●) U(IV); (●) U(V); (●) U(VI).

6.3.7 CSV measurements

To confirm the influence of HCO₃⁻/CO₃²⁻, CSV experiments were performed after the E_{CORR} measurements (plotted in Fig. 6.10). Fig. 6.13 shows the CSVs recorded after corrosion in 0.02 mol L⁻¹ H₂O₂ in solutions with different [CO₃]_{tot}. At the two low concentrations a significant reduction peak, indicating the presence of a substantial U^{VI} surface layer, is observed. As expected from the CV in Fig. 6.1 this peak is located in the potential range -0.65 V to -0.85 V and can be attributed to the cathodic reduction of a U^{IV}_{1-2x}U^V_{2x}O_{2+x}/U^{VI}O_{3.y}H₂O layer formed by corrosion in the H₂O₂ solution. As the

$[\text{CO}_3]_{\text{tot}}$ is increased the size of this peak decreases with only a very shallow peak being observed at the highest $[\text{CO}_3]_{\text{tot}}$. A reasonable estimate of the extent of formation of this U^{VI} surface layer can be obtained by integrating the CSVs between -0.6 V and -0.9 V to obtain the charge associated with the cathodic reduction of this film. The charges obtained in this manner are plotted for the whole series of corrosion experiments in Fig. 6.14.

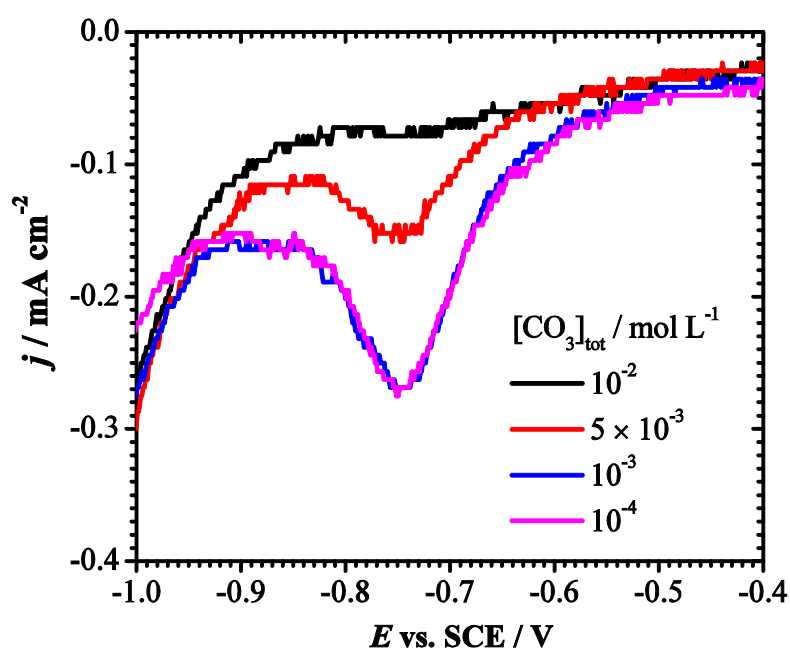


Fig. 6.13. CSVs recorded on a SIMFUEL electrode after 30 min of E_{CORR} measurement in $0.02 \text{ mol L}^{-1} \text{ H}_2\text{O}_2$ and various $[\text{CO}_3]_{\text{tot}}$ at $\text{pH} = 9.5$.

Fig. 6.14 shows the extent of surface oxidation (expressed as a surface charge) calculated from the integration of the stripping current from -0.9 V to -0.6 V as a function of $[\text{CO}_3]_{\text{tot}}$. In the solution with the lowest $[\text{CO}_3]_{\text{tot}}$ ($10^{-4} \text{ mol L}^{-1}$ as shown in the dashed box) the charge is almost independent of $[\text{H}_2\text{O}_2]$ up to 0.01 mol L^{-1} but increased significantly

for $[\text{H}_2\text{O}_2] = 0.02 \text{ mol L}^{-1}$. This trend is consistent with the XPS results which show U^{VI} becoming the dominant surface oxidation state at high $[\text{H}_2\text{O}_2]$ (Fig. 6.11). By contrast the surface charge at the highest $[\text{CO}_3]_{\text{tot}}$ (0.1 mol L^{-1}) (solid box in Fig. 6.14) is very low and independent of $[\text{H}_2\text{O}_2]$. This low charge together with the low U^{VI} content of the surface is consistent with the presence of a rapidly dissolving, and hence difficult to capture by *ex-situ* XPS analysis, thin layer of $\text{U}^{\text{VI}}\text{CO}_3$.

Over the intermediate $[\text{CO}_3]_{\text{tot}}$ range the surface charge decreases with increasing $[\text{CO}_3]_{\text{tot}}$. This range (10^{-3} to $\sim 2 \times 10^{-2} \text{ mol L}^{-1}$) is independent of $[\text{H}_2\text{O}_2]$. These data demonstrate that whether or not the surface accumulates a U^{VI} deposit depends on the relative rates of surface oxidation (R_{H} determined by $[\text{H}_2\text{O}_2]$) and chemical dissolution of U^{VI} states (R_{U} determined by $[\text{CO}_3]_{\text{tot}}$). For $[\text{CO}_3]_{\text{tot}} \leq 10^{-3} \text{ mol L}^{-1}$, $R_{\text{H}} > R_{\text{U}}$, while the opposite is the case at high $[\text{CO}_3]_{\text{tot}}$.

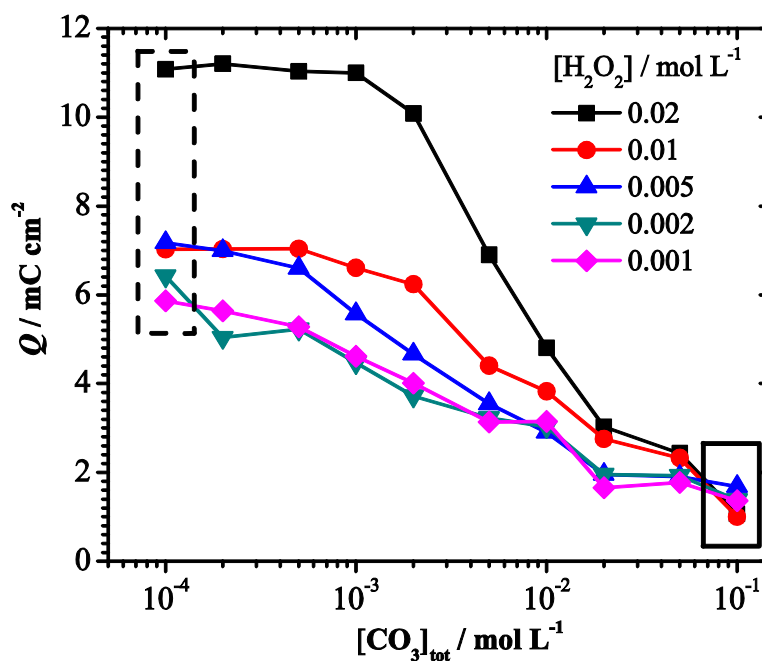


Fig. 6.14. The surface charge (proportional to the thickness of the corrosion product film) on a SIMFUEL surface as a function of $[\text{CO}_3]_{\text{tot}}$ in solutions containing different $[\text{H}_2\text{O}_2]$: (■) $2 \times 10^{-2} \text{ mol L}^{-1}$; (●) $10^{-2} \text{ mol L}^{-1}$; (▲) $5 \times 10^{-3} \text{ mol L}^{-1}$; (▼) $2 \times 10^{-3} \text{ mol L}^{-1}$; (◆) $10^{-3} \text{ mol L}^{-1}$.

6.3.8 Polarization resistance measurements

Using the plots in Fig. 6.2, it is possible to measure a polarization resistance (R_p) for charge transfer reactions occurring at E_{CORR} by measuring the slope of the current–potential plots over the range $E_{\text{CORR}} \pm 10 \text{ mV}$. Since two open circuit reactions are possible, UO_2 corrosion and H_2O_2 decomposition, any measured R_p value is a measure of the resistance to charge transfer of the sum of these two reactions. Values of R_p^{-1} measured as a function of $[\text{H}_2\text{O}_2]$ in solutions with and without $\text{HCO}_3^-/\text{CO}_3^{2-}$ at pH = 9.5 and 11.0 are plotted in Fig. 6.15.

Presently, the open circuit balance between these two reactions is unknown and may change with $[\text{H}_2\text{O}_2]$ as observed under anodic polarization conditions (Table 6.1). These results showed that the relative importance of the H_2O_2 decomposition reaction decreased as $[\text{H}_2\text{O}_2]$ decreased. At the relatively high $[\text{H}_2\text{O}_2]$ of 0.02 mol L^{-1} these analyses show that ~75% of the current goes to H_2O_2 decomposition under electrochemical conditions.

If a similar balance between dissolution and decomposition is assumed to prevail at E_{CORR} then the reciprocal of the polarization resistance, R_p^{-1} , can be taken as an approximate measure of the H_2O_2 decomposition rate, at least for higher $[\text{H}_2\text{O}_2]$ when Fig. 6.15 shows R_p^{-1} values to be effectively independent of $[\text{H}_2\text{O}_2]$. Irrespective of these difficulties it is clear that an increase in both pH and $[\text{CO}_3]_{\text{tot}}$ increases the rate of H_2O_2

decomposition. Previously in the absence of $\text{HCO}_3^-/\text{CO}_3^{2-}$ this was attributed to a combination of the increased rate of dissolution of the inhibiting U^{VI} surface layer (as $\text{U}^{\text{VI}}\text{O}_2(\text{OH})_y^{(2-y)+}$) and an increase in concentration of the electroactive form of peroxide, HO_2^- (by H_2O_2 dissociation) in Chapter 5. However, the data in Fig. 6.5 show that the rate of interfacial reaction (R_p^{-1}) can be increased by adding $\text{HCO}_3^-/\text{CO}_3^{2-}$ without changing the pH. This would suggest that the rate of chemical dissolution of U^{VI} species (as $\text{U}^{\text{VI}}\text{O}_2(\text{CO}_3)_x^{(2-2x)+}$) is the key feature controlling the surface reactivity. However, since a similar but smaller increase in R_p^{-1} is observed by changing the pH at the same $[\text{CO}_3]_{\text{tot}}$ the possibility remains that HO_2^- is more electroactive than H_2O_2 .

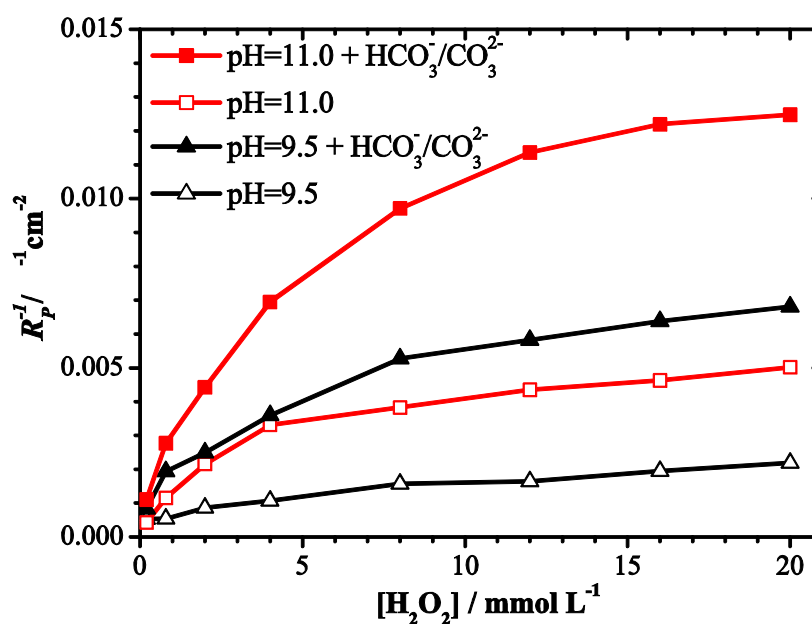


Fig. 6.15. Reciprocal of polarization resistance, R_p^{-1} , as a function of $[\text{H}_2\text{O}_2]$ at pH 9.5 and 11.0. $[\text{CO}_3]_{\text{tot}} = 0$ or 0.05 mol L^{-1} , rotation rate = 25 Hz.

6.4 Summary and conclusions

The anodic behaviour of SIMFUEL in solutions containing H_2O_2 and $\text{HCO}_3^-/\text{CO}_3^{2-}$ has been studied electrochemically and using surface/solution analytical techniques.

(i) Two anodic reactions are possible: the dissolution of UO_2 and the oxidation of H_2O_2 . In the absence of $\text{HCO}_3^-/\text{CO}_3^{2-}$, the dissolution rate of U^{VI} (as $\text{U}^{\text{VI}}\text{O}_2(\text{OH})_y^{(2-y)+}$) is slow and both anodic reactions are inhibited by the presence of a partially permeable U^{VI} surface oxide/hydroxide layer, as illustrated in Fig. 6.16. When $\text{HCO}_3^-/\text{CO}_3^{2-}$ is present the more rapid chemical dissolution of U^{VI} (as $\text{U}^{\text{VI}}\text{O}_2(\text{CO}_3)_x^{(2-2x)+}$) exposes the underlying conductive $\text{U}^{\text{IV}}_{1-2x}\text{U}^{\text{V}}_{2x}\text{O}_{2+x}$ surface which facilitates the anodic oxidation and decomposition of H_2O_2 .

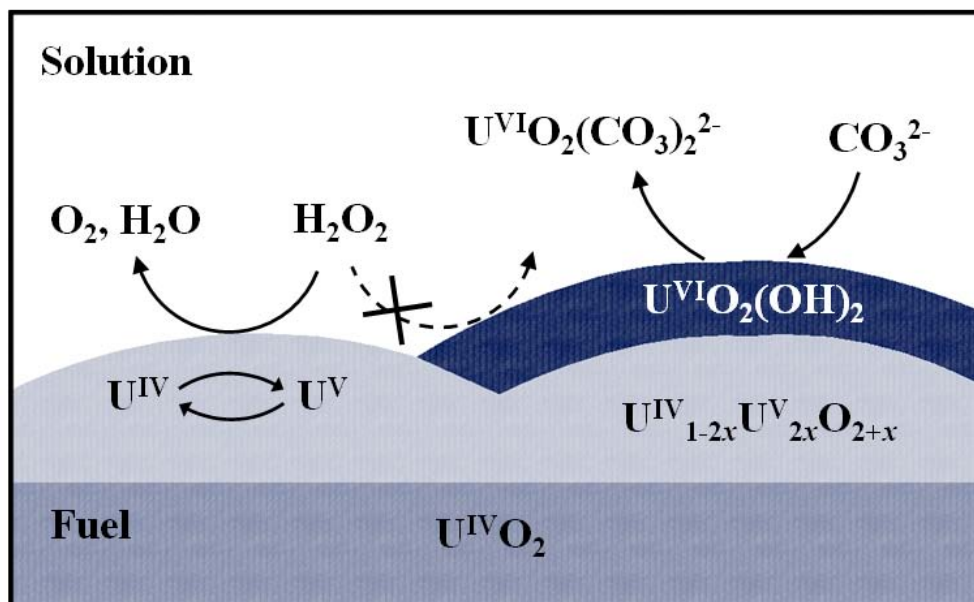


Fig. 6.16. Schematic illustration describing the H_2O_2 decomposition on UO_{2+x} surface and the effect of $\text{HCO}_3^-/\text{CO}_3^{2-}$.

(ii) The dependencies of the anodic current on $[\text{CO}_3]_{\text{tot}}$ and $[\text{H}_2\text{O}_2]$ in Fig. 6.5 and Fig. 6.6 indicate that the rate of anodic dissolution increases at potentials positive to the open circuit (corrosion) potential, but at higher potentials when the dissolution rate is limited by the chemical release of U^{VI} , the anodic oxidation of H_2O_2 is the dominant reaction. It is possible that both anodic reactions are dependent on $[\text{H}_2\text{O}_2]$ due to the formation of a uranyl peroxocarbonate complex ($\text{U}^{\text{VI}}\text{O}_2(\text{O}_2)_x(\text{CO}_3)_y^{2-2x-2y}$) although this remains to be conclusively demonstrated.

(iii) Under open circuit (corrosion) conditions both UO_2 corrosion and H_2O_2 decomposition are controlled by the rate of chemical release of U^{VI} surface species. Since the rate of release is accelerated in the presence of $\text{HCO}_3^-/\text{CO}_3^{2-}$ the rates of both reactions increase with $[\text{CO}_3]_{\text{tot}}$. This is clearly indicated in polarization resistance measurements. However, such measurements cannot distinguish between these two reactions and future studies to quantitatively separate them are required.

6.5 References

- [1] J. McMurry, Reference Water Compositions for a Deep Geological Repository in the Canadian Shield, Report 06819-REP-01200-10135-R01, Ontario Power Generation, Toronto, ON, 2004.
- [2] I. Grenthe, D. Ferri, F. Salvatore, and G. Riccio, *J.Chem.Soc.Dalton Trans.* 11 (1984) 2439.
- [3] I. Grenthe, J. Fuger, R.J. Konings, R.J. Lemire, A.B. Muller, C. Nguyen-Trung, and H. Wanner, *Chemical Thermodynamics of Uranium*, North Holland, Amsterdam, 1992.
- [4] D.W. Shoesmith, S. Sunder, and W.H. Hocking, *Electrochemistry of Novel Materials*, in ", edited by J. Lipkowski, and P.N. Ross, VCH publishers, New York, 1994.
- [5] M. Hossain, E. Ekeröth, and M. Jonsson, Effects of HCO_3^- on the kinetics of UO_2 oxidation by H_2O_2 , *J. Nucl. Mater.* 358 (2006) 202-208.

- [6] J. de Pablo, I. Casas, J. Gimenez, V. Marti, and M.E. Torrero, Solid surface evolution model to predict uranium release from unirradiated UO_2 and nuclear spent fuel dissolution under oxidizing conditions, *J. Nucl. Mater.* 232 (1996) 138-145.
- [7] J.S. Goldik, J.J. Noël, and D.W. Shoesmith, Surface electrochemistry of UO_2 in dilute alkaline hydrogen peroxide solutions: Part II. Effects of carbonate ions, *Electrochim. Acta* 51 (2006) 3278-3286.
- [8] P.G. Keech, J.S. Goldik, Z. Qin, and D.W. Shoesmith, The anodic dissolution of SIMFUEL (UO_2) in slightly alkaline sodium carbonate/bicarbonate solutions, *Electrochim. Acta* 56 (2011) 7923-7930.
- [9] Y.A. Teterin, V.M. Kulakov, A.S. Baev, N.B. Nevzorov, I.V. Melnikov, V.A. Streltsov, L.G. Mashirov, D.N. Suglobov, and A.G. Zelenkov, A Study of Synthetic and Natural Uranium Oxides by X-ray Photoelectron Spectroscopy, *Physics and Chemistry of Minerals* 7 (1981) 151-158.
- [10] S. Bera, S.K. Sali, S. Sampath, S.V. Narasimhan, and V. Venugopal, Oxidation state of uranium: an XPS study of alkali and alkaline earth uranates, *J. Nucl. Mater.* 255 (1998) 26-33.
- [11] S. Van den Berghe, J.-P. Laval, B. Gaudreau, H. Terryn, and M. Verwerft, XPS investigations on cesium uranates: mixed valency behaviour of uranium, *J. Nucl. Mater.* 277 (2000) 28-36.
- [12] S. Sunder, N.H. Miller, and D.W. Shoesmith, Corrosion of uranium dioxide in hydrogen peroxide solutions, *Corros. Sci.* 46 (2004) 1095-1111.

Chapter 7

THE ANODIC REACTIONS ON SIMULATED NUCLEAR FUEL (SIMFUEL) IN HYDROGEN PEROXIDE SOLUTIONS – EFFECT OF FISSION PRODUCTS

7.1 Introduction

In this chapter, the effect of noble metal (ϵ) fission products on H_2O_2 decomposition has been studied electrochemically and using surface/solution analytic techniques.

The decomposition of H_2O_2 can be catalyzed on various sites on the surface of spent fuel surface, in particular on the partially oxidized surface containing mixed oxidation states of U ($\text{U}^{\text{IV}}_{1-2x}\text{U}^{\text{V}}_{2x}\text{O}_{2+x}$) and on noble metal particles (ϵ -particles) produced by in-reactor fission, as illustrated in Fig. 7.1. Catalysis by a $\text{U}^{\text{IV}}/\text{U}^{\text{V}}$ surface would be expected since decomposition has been shown to occur on oxide surfaces especially those containing mixed oxidation states [1-4]. It is known that H_2O_2 decomposition can also be accelerated in the presence of metallic catalysts [5], the kinetics having been studied on noble metals, such as Pd and Ru, which has been reviewed in Section 1.5.2.3. Trummer et al. [6] observed that H_2O_2 consumption on doped UO_2 pellets increased with Pd content in a deaerated 2 mmol L^{-1} H_2O_2 solution. The observation that the amount of H_2O_2 consumed was not balanced by the amount of dissolved UO_2^{2+} suggested catalytic H_2O_2 decomposition. In recent studies [7-9], a significant difference in the ratio of dissolved U to consumed H_2O_2 was found on both pure UO_2 pellets and doped $\text{UO}_2/\text{SIMFUEL}$ pellets, and attributed to H_2O_2 decomposition.

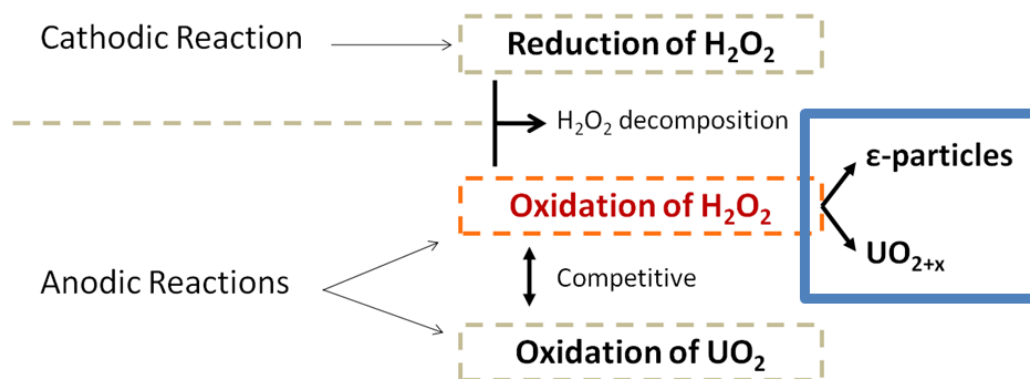


Fig. 7.1. An illustration of the possible coupling of the primary redox reactions involving H_2O_2 on fuel surface, with the emphasis on the H_2O_2 oxidation reaction being catalyzed by a UO_{2+x} surface or noble metal (ϵ) particles.

Chapters 5 and 6 have shown that the relative importance of the two anodic reactions, H_2O_2 oxidation and UO_2 dissolution, will determine the stability of UO_2 in H_2O_2 solutions. In the present chapter, a series of electrochemical experiments has been conducted on SIMFUEL electrodes containing different dopants with the primary purpose of determining the relative importance of the UO_2 and ϵ -particle surfaces in the balance between UO_2 oxidation/dissolution and H_2O_2 decomposition.

7.2 Experimental

The electrochemical equipment setup and the SIMFUEL electrode preparation were described in Section 2.1. As previously mentioned, the two key categories of dopants in SIMFUEL are (i) rare earth elements which dissolve in the UO_2 matrix, influence the structure of the UO_2 lattice [10, 11] and significantly increase its conductivity; and (ii) noble metal elements which segregate in to noble metal (ϵ) particles. The average

composition of these ϵ -particles in SIMFUEL is 42-Ru/33-Mo/21-Pd/3-Rh in atomic percent [12, 13]. The SIMFUELS used in this study were doped to simulate an in-reactor burnup of 3 at%. Two types of electrodes were used in experiments, one containing Nd, Ce, Zr, Sr, Ba, La and Y with the rare earths retained as dopants within the UO_2 lattice (designated **RE**) and a second containing these elements and Ru, Mo, Pd and Rh which segregate to form the noble metal particles (designated **RE + ϵ**).

Solutions were prepared with deionized water with a resistance of 18.2 M Ω cm purified using a Millipore Milli-Q Plus unit. All experiments were Ar-purged (ultra-high purity, Praxair) and conducted at room temperature. The base electrolyte was 0.1 mol L⁻¹ NaCl, and the solution pH was adjusted to 9.7 or 11.0 with NaOH (Caledon Chemical). For solutions containing carbonate, NaHCO₃ (Caledon Chemical) was added to a concentration in the range 0 to 0.2 mol L⁻¹ and the pH subsequently adjusted. Hydrogen peroxide (3% w/v, LabChem, Pittsburgh) was added immediately prior to experiments to obtain a concentration in the range 0 to 0.02 mol L⁻¹. In dissolution experiments, a small electrochemical cell (V = 140 mL) was used to facilitate analyses for dissolved U. The small cell was wrapped with Al foil and measurements performed in a dark box to minimize any effect of light exposure on H₂O₂ decomposition. The electrodes used in this small cell were not rotated.

The working electrode was cathodically cleaned at an applied potential of -1.2 V for 1 min prior to each experiment to remove any air-formed oxides. Cyclic voltammetric (CV) experiments were conducted at a scan rate of 10 mV s⁻¹. Anodic polarization experiments were conducted for 10 min to achieve a steady-state current at a sequence of applied potentials between +0.1 V and +0.4 V (with an increase between settings of 0.05 V).

Electrochemical impedance spectroscopy (EIS) measurements were performed by coupling the potentiostat with a Solartron model 1255B frequency response analyzer. A ± 10 mV (rms) sinusoidal potential waveform was applied, and data accumulated as a function of frequency from 10^5 to 10^{-2} Hz. That the system remained at steady-state was checked by recording a small number of data points on a reverse scan. In dissolution experiments, the working electrode was potentiostated at either 0.2 V or 0.35 V for 1 hour, and the solution subsequently analyzed for U by inductively coupled plasma atomic emission spectroscopy (ICP-AES). A detailed description of each experimental technique can be found in Chapter 2.

7.3 Results and discussion

7.3.1 Voltammetry

Fig. 7.2 shows CVs recorded on the two electrodes in a 0.1 mol L^{-1} NaCl solution (pH = 9.5). At potentials < -1.0 V, the RE + ϵ electrode exhibits higher currents due to the catalysis of H_2O reduction on ϵ -particles [14]. Otherwise the currents on the two electrodes are very similar.

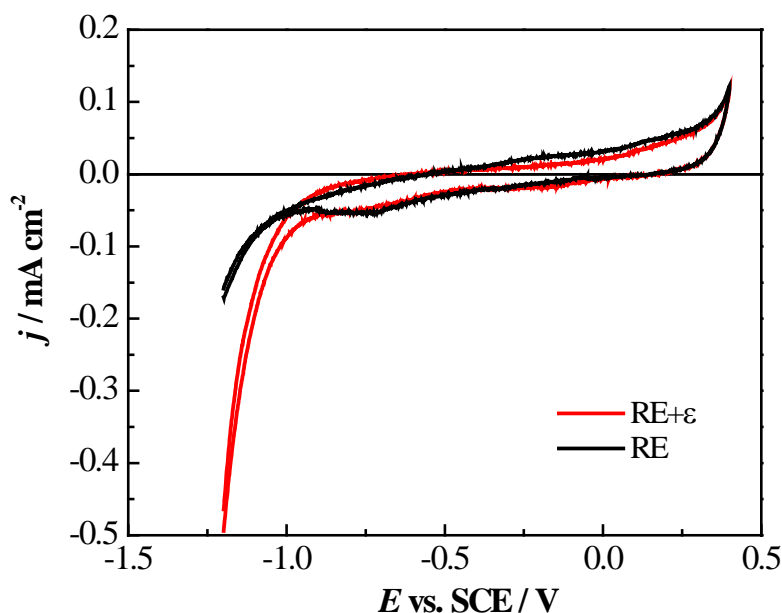


Fig. 7.2. CV recorded on the RE and RE + ϵ electrodes in an Ar-purged 0.1 mol/L NaCl solution at pH 9.5. Scan rate=5mV/s, and the rotation rate=0Hz. IR compensated.

7.3.2 Potentiostatic measurements

Fig. 7.3(a) shows the steady-state background currents recorded on the two electrodes (RE+ ϵ and RE) at anodic potentials in a 0.1 mol L⁻¹ NaCl + 0.01 mol L⁻¹ HCO₃⁻/CO₃²⁻ solution containing no H₂O₂. The currents were effectively identical on the two electrodes except at the most positive potentials (0.35 V and 0.4 V). The increase in current on SIMFUELS over this potential range in solutions containing HCO₃⁻/CO₃²⁻ has been studied [15] and shown to be attributable to the formation of a thin surface layer of U^{IV}_{1-2x}U^V_{2x}O_{2+x} followed by the more copious further oxidation to U^{VI}O₂²⁺ and dissolution as U^{VI}O₂(CO₃)^{(2-2x)+}. The potential independence of the current at high potentials was attributed to control of the overall oxidation dissolution process by the chemical

dissolution of a $U^{VI}CO_3$ surface layer. The slightly higher currents recorded on RE + ϵ than those on RE at $E \geq 0.35$ V can be attributed to H_2O oxidation catalyzed on the ϵ -particles.

When H_2O_2 was present the currents observed were significantly higher than the background current ($[H_2O_2] = 0$), and the currents measured on the RE + ϵ electrode were considerably higher than those on the RE electrode, Fig. 7.3(b). Whether these increased currents are attributable to enhanced UO_2 oxidation or H_2O_2 oxidation cannot be determined electrochemically.

For the RE electrode, the current reached a maximum at $E = 0.2$ V and then decreased with potential to the background current observed in the absence of H_2O_2 . As noted above, the current in this potential range is controlled by the chemical dissolution of a $U^{VI}CO_3$ layer [16]. By contrast, on the RE + ϵ electrode the current first achieved a plateau in the potential region 0.2 V to 0.3 V before subsequently increasing at more positive potentials.

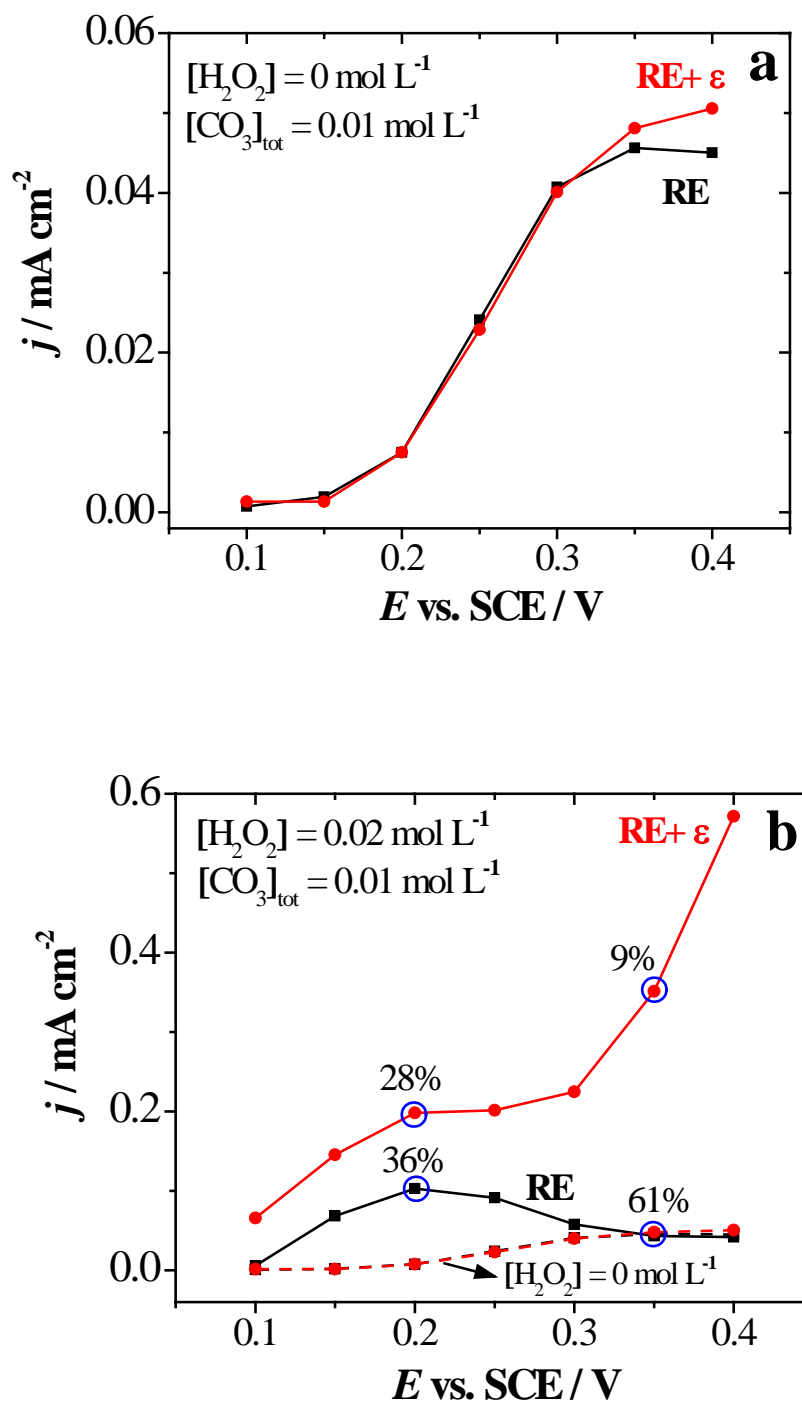


Fig. 7.3. Steady-state currents recorded as a function of potential on the RE + ϵ and RE electrodes in $0.1 \text{ mol L}^{-1} \text{ NaCl} + 0.01 \text{ mol L}^{-1} \text{ HCO}_3^-/\text{CO}_3^{2-}$ solution at pH 9.7, $\omega=16.7\text{Hz}$. (a) no H_2O_2 ; (b) $0.02 \text{ mol L}^{-1} \text{ H}_2\text{O}_2$. The dashed line in (b) shows the

background current measured in the absence of H_2O_2 (from (a)). The circled data points in (b) indicate the potential values chosen for potentiostatic dissolution experiments with the percentage noting the fraction of the current consumed by the UO_2 oxidative dissolution process over a period of 1 hour (Table 7.1).

7.3.3 Dissolution experiments

To achieve the separation of the two anodic reactions (UO_2 oxidation and H_2O_2 oxidation), a series of dissolution tests was performed at 0.2 V and 0.35 V, and the amount of dissolved U measured by ICP-AES and converted into the corresponding anodic charge, Table 7.1. A small fraction of the oxidized U (as $\text{U}^{\text{V}}/\text{U}^{\text{VI}}$) remains on the electrode surface, and cathodic-stripping voltammetric measurements in H_2O_2 -free solutions showed this surface charge was of the order of 1 mC. This is negligible compared to the charge consumed to produce dissolved U^{VI} (Table 7.1), and the analyzed amount of dissolved U can be taken as a measure of the charge consumed in the oxidation of UO_2 .

The values of the total anodic charge are in the same order as the steady-state currents plotted in Fig. 7.3(b), although the currents in the dissolution tests, in which no electrode rotation was employed, decreased with time due to transport limitations for H_2O_2 at the electrode surface. Table 7.1 shows the amounts of dissolved U are not too different for the two electrodes even at the higher potential of 0.35 V when the measured currents, Fig. 7.3(b), are distinctly different. SEM micrographs recorded on the two electrodes after 1 hour of potentiostatic dissolution at 0.35 V are shown in Fig. 7.4. Similar surface morphologies were observed before and after dissolution, despite the observation that the

total anodic charges consumed in these two experiments are very different. (0.078 for RE compared to 0.34 for RE + ϵ). Neither electrode exhibits the porosity and presence of etch pits observed after extensive anodic dissolution as observed previously in Chapter 6 (Fig. 6.9e and 6.9f) after anodic dissolution in concentrated $\text{HCO}_3^-/\text{CO}_3^{2-}$ solutions. These observations are consistent with the analyses showing that only a small fraction of the anodic charge (9%) goes to anodic dissolution at 0.35 V on the RE + ϵ electrode. It would be reasonable to conclude that the large majority of the charge was consumed by the anodic oxidation of H_2O_2 .

Table 7.1. The amount of the dissolved uranium in the anodic dissolution tests and the fraction of the total charge due to dissolution

E / V	Working Electrode	Dissolved [U] / 10^{-3} g L^{-1}	n_{U} convert to charge / C	Total anodic charge / C	Dissolved UO_2 charge / Total anodic charge
0.20	RE + ϵ	0.623	0.083	0.30	28%
0.20	RE	0.728	0.097	0.27	36%
0.35	RE + ϵ	0.225	0.030	0.34	9%
0.35	RE	0.351	0.048	0.078	61%

The eventual establishment (at $E = 0.35 \text{ V}$ in Fig. 7.3b) of a steady-state current on the RE electrode equal to that observed in the absence of H_2O_2 is consistent with control of anodic reactions by the chemical dissolution of a $\text{U}^{\text{VI}}\text{O}_2\text{CO}_3$ layer. The decrease in current

on this electrode when the potential is increased from 0.2 V to 0.35 V and the switch from dominantly H_2O_2 oxidation (64% at 0.2V) to dominantly UO_2 dissolution (only 39% of the charge going to H_2O_2 oxidation) at 0.35 V confirm that rapid anodic formation but slow chemical dissolution of this layer blocks access of H_2O_2 to the underlying catalytic $\text{U}^{\text{IV}}_{1-2x}\text{U}^{\text{V}}_{2x}\text{O}_{2+x}$ layer.

In the presence of both $\text{HCO}_3^-/\text{CO}_3^{2-}$ and H_2O_2 , U^{VI} can form a soluble peroxocarbonate complex, $(\text{U}^{\text{VI}}\text{O}_2(\text{O}_2)_x(\text{CO}_3)_y)^{2-2x-2y}$ [17, 18] which could accelerate the dissolution of U^{VI} species thereby facilitating the conversion of U^{IV} to U^{V} in the $\text{U}^{\text{IV}}_{1-2x}\text{U}^{\text{V}}_{2x}\text{O}_{2+x}$ sublayer.

Depending on the optimum $\text{U}^{\text{IV}}/\text{U}^{\text{V}}$ ratio required for the H_2O_2 oxidation reaction the rate of this latter reaction could also be influenced.

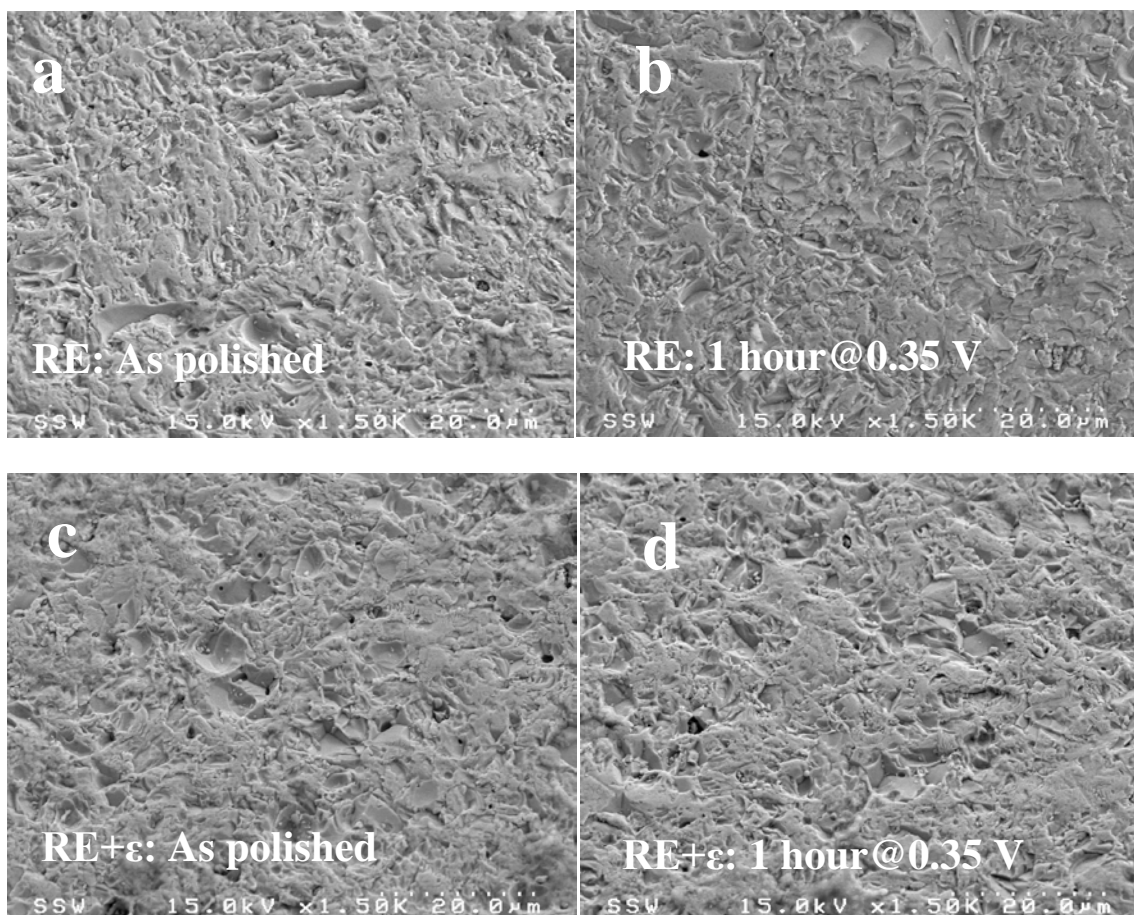
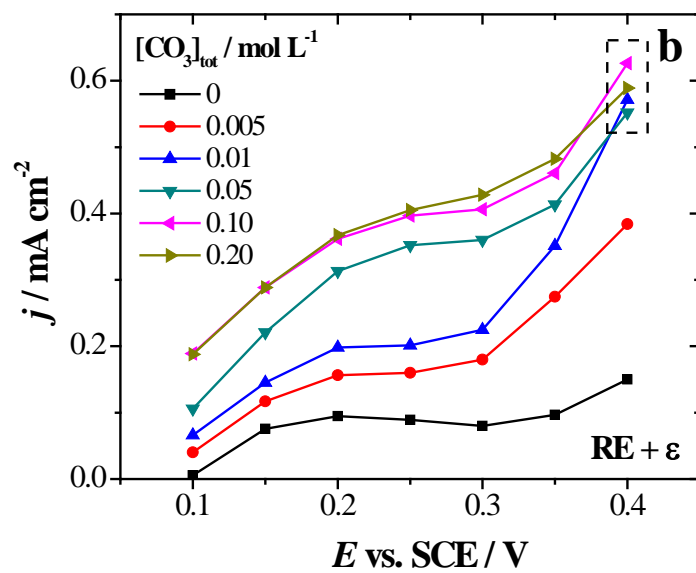
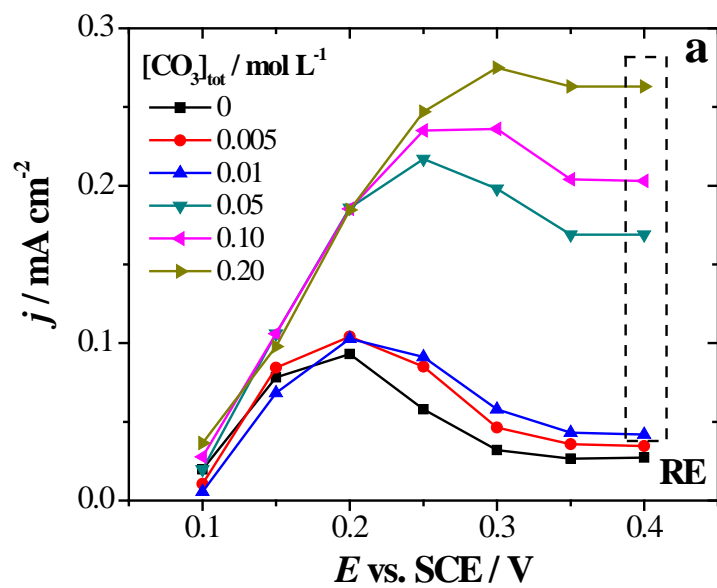


Fig. 7.4. SEM micrographs of SIMFUEL specimens before and after oxidation at $E = 0.35$ V for 1 hour in $0.1 \text{ mol L}^{-1} \text{ NaCl} + 0.01 \text{ mol L}^{-1} \text{ HCO}_3^-/\text{CO}_3^{2-} + 0.02 \text{ mol L}^{-1} \text{ H}_2\text{O}_2$ solutions at pH 9.7 (1.5k magnification).

7.3.4 Steady-state currents at various $[\text{CO}_3]_{\text{tot}}$

As stated above, the anodic current on the RE electrode included contributions from at least two simultaneous reactions: (i) oxidative dissolution of UO_2 and (ii) H_2O_2 oxidation on $\text{U}^{\text{IV}}/\text{U}^{\text{V}}$ surface species. For the RE + ϵ electrode, an additional reaction, (iii) H_2O_2 oxidation on ϵ -particles, is also possible. In the presence of carbonate and H_2O_2 , U^{VI} can form soluble peroxocarbonate complexes [17, 18] that will facilitate the dissolution/desorption of U^{VI} surface species and consequently increase the fraction of exposed surface $\text{U}^{\text{IV}}/\text{U}^{\text{V}}$ species. This process is likely to accelerate reaction (i), leading to a promotion of reaction (ii) due to the consequent exposure of the more reactive $\text{U}^{\text{IV}}/\text{U}^{\text{V}}$ sites, whereas reaction (iii) is expected to be unaffected. Thus, we conducted experiments with a range of carbonate concentrations with the other conditions remaining the same as in the experiments presented in Fig. 7.3. Fig. 7.5 (a and b) plots the steady-state anodic currents in various $[\text{CO}_3]_{\text{tot}}$ on the two electrodes RE and RE + ϵ . The differences between the two currents are plotted in Fig. Fig. 7.5(c).



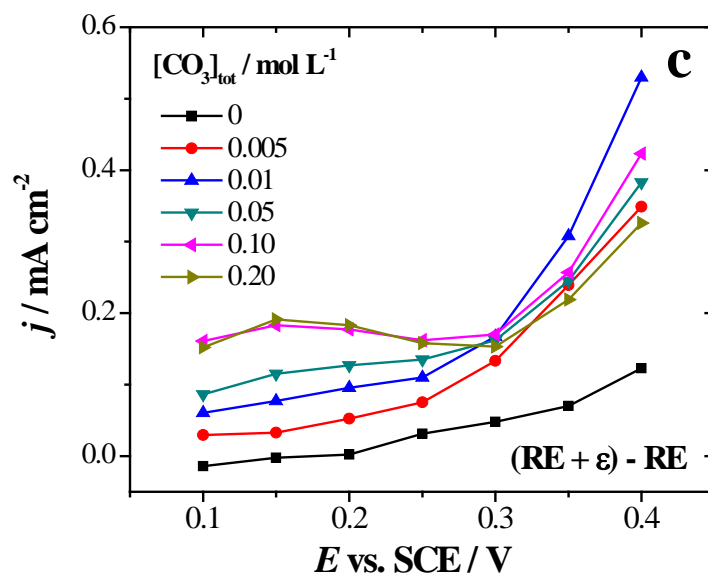


Fig. 7.5. Oxidation current densities as a function of potential on SIMFUEL doped with (a) RE and (b) RE + ϵ in $0.1 \text{ mol L}^{-1} \text{ NaCl} + 0.02 \text{ mol L}^{-1} \text{ H}_2\text{O}_2$ solutions, $[\text{CO}_3]_{\text{tot}}$ varies from 0 to 0.2 mol L^{-1} . (c) is the difference in oxidation current densities between SIMFUEL doped with RE + ϵ and RE. All solutions are Ar-purged, $\text{pH} = 9.7$, $\omega = 16.7\text{Hz}$.

In Fig. 7.5(a) for electrode RE, the anodic currents in various carbonate concentrations showed two distinct behaviours. When $[\text{CO}_3]_{\text{tot}}$ was $< 0.01 \text{ mol L}^{-1}$, the currents increased at first but became suppressed at $E \geq 0.25 \text{ V}$, which was attributed to blockage of the surface by U^{VI} species present as an oxide/hydroxide layer (Chapter 6). By contrast, when $[\text{CO}_3]_{\text{tot}} > 0.01 \text{ mol L}^{-1}$, the currents increased and reached a peak value before decreasing to a plateau. This increase indicated the increased availability of the underlying $\text{U}^{\text{IV}}/\text{U}^{\text{V}}$ sites and a higher reactivity towards both dissolution and H_2O_2 oxidation. A similar $[\text{CO}_3]_{\text{tot}}$ threshold for the acceleration of anodic reactions has been

observed in corrosion experiments (Fig. 6.10) and CSV measurements (Fig. 6.13 and 6.14) in Chapter 6 confirmed this could be attributed to the dissolution of a surface films.

Further inspection of Fig. 7.5(a) showed some more interesting features on the RE electrode. At $E \leq 0.25$ V and $[\text{CO}_3]_{\text{tot}} > 0.01$ mol L⁻¹, the currents were independent of $[\text{CO}_3]_{\text{tot}}$ and increased with potential, indicating that the anodic reaction (mainly H₂O₂ oxidation (Fig. 7.3b and Table 7.1) occurring on a U^{IV}_{1-2x}U^V_{2x}O_{2+x} layer) was activation-controlled and not limited by the availability of surface active sites (U^{IV}/U^V). However, as the potential increased to > 0.25 V, the dominant reaction switched to the oxidative dissolution of UO₂ (Fig. 7.3b and Table 7.1) At these potentials the chemical dissolution of U^{VI} surface species became the rate determining step, leading to a current independent of potential and dependent on $[\text{CO}_3]_{\text{tot}}$.

Given the possibility of an additional anodic reaction (H₂O₂ oxidation on ϵ -particles), the anodic currents on the RE + ϵ electrode, Fig. 7.5(b), are difficult to resolve. Since the only difference between the two electrodes is the presence of ϵ -particles in the RE + ϵ electrode it can be presumed that the difference in currents, Fig. 7.5 (c), can be attribute to the anodic reaction supported on these particles. At $E \leq 0.25$ V, the anodic current difference was not strongly dependent on potential but increased with $[\text{CO}_3]_{\text{tot}}$ up to 0.1 mol L⁻¹. A possible explanation is that the current was due to the carbonate-mediated oxidation of H₂O₂ on the ϵ -particles. The combination of H₂O₂ and HCO₃⁻/CO₃²⁻ to form a more reactive peroxide carbonate species (in the form of CO₄²⁻, HCO₄⁻ or C₂O₆²⁻) has been reported [19-21], more detailed descriptions in Section 1.5.2.2. The current for the anodic oxidation of such a species would be expected to increase with $[\text{CO}_3]_{\text{tot}}$ as observed. At the highest $[\text{CO}_3]_{\text{tot}}$ (0.20 mol L⁻¹) the current becomes independent of

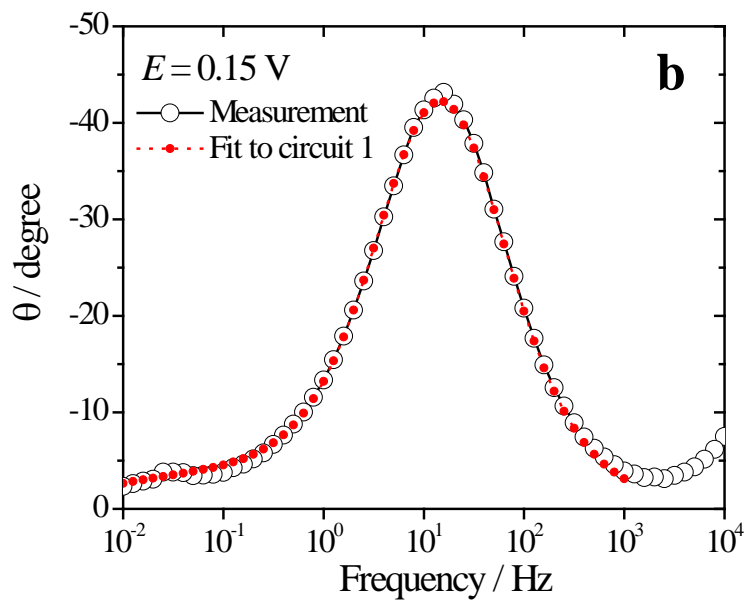
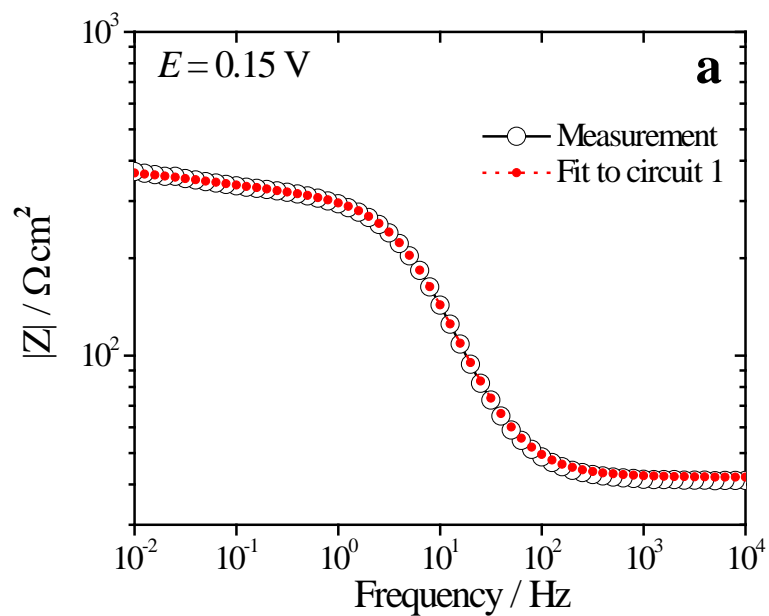
$[\text{CO}_3]_{\text{tot}}$ which most likely reflects a limited availability of ϵ -particle sites. The weak dependence of the current on potential indicates a rate-determining influence for a chemical reaction step, although this remains unresolved.

For $E > 0.25$ V, Fig. 7.5(c), distinctly different behaviour was observed: the currents rapidly increased with potential but appeared to become independent of $[\text{CO}_3]_{\text{tot}}$. This could be attributed to the direct anodic oxidation of uncomplexed H_2O_2 on the ϵ -particles. Johnston et al. [22] reported a substantial increase in H_2O_2 oxidation at a potential > 0.2 V on a 13Pd-87Au composite film electrode at pH 7.5, while virtually no anodic current was observed on a pure Au electrode until $E > 0.8$ V. Similar potential thresholds in the range of 0.1-0.3 V have been found in other electrochemical studies for Pd [23] and Pt [24-27]-catalyzed oxidation of H_2O_2 . Gorton [23] suggested that H_2O_2 oxidation was favored on an oxidized Pd surface since the reaction occurred in the potential region of $\text{Pd}(\text{OH})_2$ formation, according to the scheme proposed by Lingane and Lingane [28] for Pt. Johnston et al. [22] proposed, based on electrochemical experiments, that the H_2O_2 reduced the Pd(II) oxide film to Pd followed by the electrochemical regeneration of the active Pd(II) sites, and that a surface Pd(II)/ H_2O_2 complex was formed prior to the rate-determining reduction of Pd(II). A similar mechanism was used to successfully modelled H_2O_2 oxidation on a Pt RDE by Hall et al. [24].

7.3.5 EIS measurements

To determine whether this claim that two distinct H_2O_2 oxidation processes occur, depending on the potential range, on the ϵ -particle surface, impedance spectra were

recorded at 0.15 V and 0.35 V, Fig. 7.6; i.e., within the two regions of behaviour exhibited in Fig. 7.5(c).



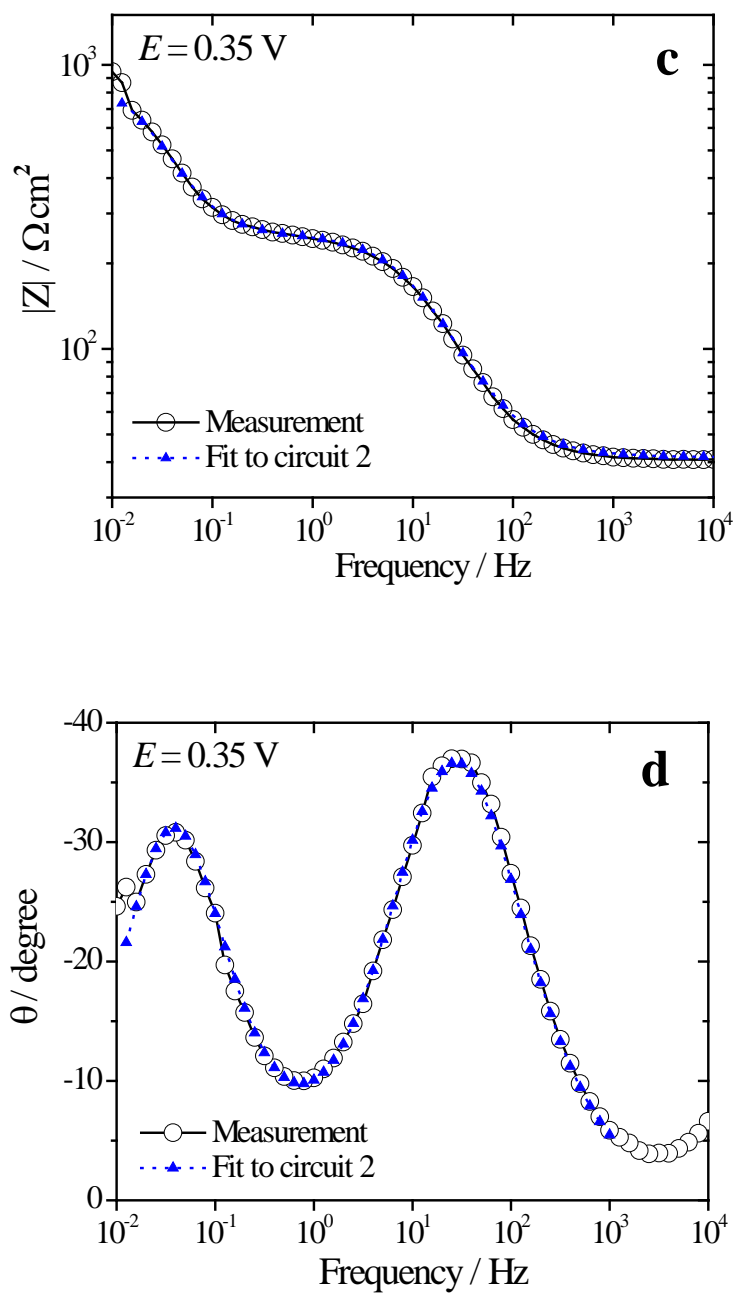


Fig. 7.6. Bode plots for SIMFUEL (RE + ϵ) at different potentials; $[\text{H}_2\text{O}_2] = 0.02 \text{ mol L}^{-1}$; $[\text{CO}_3]_{\text{tot}} = 0.05 \text{ mol L}^{-1}$; $[\text{NaCl}] = 0.1 \text{ mol L}^{-1}$. The plots in (a) and (b) were fitted using equivalent circuit 1 in Fig. 7.7; (c) and (d) were fitted using equivalent circuit 2 in Fig.

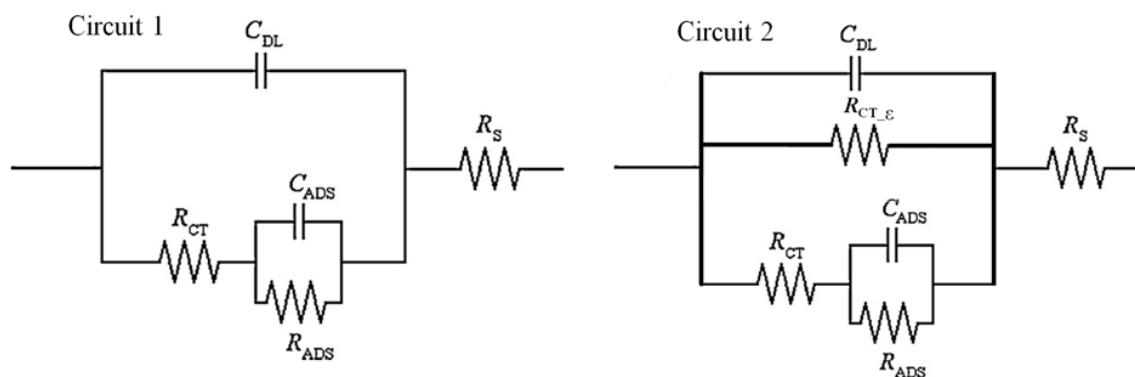


Fig. 7.7. Equivalent circuit used for fitting EIS data for $E < 0.25$ V (circuit 1) and $E \geq 0.25$ V (circuit 2).

At $E = 0.15$ V a single time constant response is observed with a peak in the phase angle (θ) plot at ~ 10 Hz. A second minor response is observed between 10^{-1} and 10^{-2} Hz. This spectrum can be fitted using the electrical equivalent circuit 1 shown in Fig. 7.7 providing the minor low frequency response is ignored. The impedance data recorded at $> \sim 10^4$ Hz is an artifact of the cell design and was not used in fitting either this or the following spectrum.

In equivalent circuit 1, C_{DL} represents the double layer capacitance, R_{CT} , the charge transfer resistance, and C_{ads}/R_{ads} the capacitance and resistance associated with adsorbed intermediates. Considering that three anodic reactions appear possible, the observation of a single time constant response indicates these reactions are not kinetically separable. For the two reactions occurring on the UO_2 surface, anodic dissolution and H_2O_2 oxidation a single response is not unexpected since it is feasible that these two reactions proceed via a common adsorbed uranyl peroxocarbonate intermediate. The absence of an additional response means this single spectrum cannot confirm the claim that these reactions on

UO₂ are accompanied by the simultaneous anodic oxidation of a peroxide-carbonate species on the ϵ -particles.

The spectrum in Fig. 7.6 (c and d) recorded at a potential of 0.35 V shows two very distinct responses; a high frequency response in the same frequency region as the minor response observed at 0.15 V in Fig. 7.6 (a and b) and a low frequency response in the range 10^{-1} to 10^{-2} Hz. The location on the frequency scale of this second response suggests it is the development of the small response at the lower potential. The high frequency response remains unchanged from that observed at the lower potential consistent with the potential-independent behaviour of the steady-state current that would be expected if the behaviour at low potentials persisted at the higher potential, Fig. 7.5 (b and c).

The spectrum recorded at 0.35 V cannot be adequately fitted by circuit 1, Fig. 7.7, but can be fitted by circuit 2, Fig. 7.7, which includes an additional charge transfer resistance ($R_{CT,\epsilon}$). The need for such an additional parallel circuit element is consistent with the claim that the additional impedance response, and increased anodic current in Fig. 7.5 (b and c), at this higher potential can be attributed to the direct anodic oxidation of H₂O₂ on ϵ -particles. This, and the lack of change in the higher frequency response when increasing the potential, indicate this reaction is occurring in addition to the anodic reactions isolated at the lower potential. The solution analyses for dissolved U (Table 7.1) show that > 90% of the current at 0.35 V goes to H₂O₂ oxidation. These impedance spectra suggest reactions on the UO₂ surface may be effectively blocked with the anodic oxidation of H₂O₂ occurring on the ϵ -particles irrespective of whether it is complexed by carbonate or not. An extended EIS study is presently underway on both electrodes in an attempt to

separate and elucidate the anodic reactions involved on both the UO_2 and ϵ -particle surfaces.

A possibility not considered in this study is that the doped UO_2 matrix in the RE and RE + ϵ electrodes may not be the same. The distribution and nature of the lattice dopants, in particular the Zr content, are known to change the overall reactivity of the oxide matrix [11, 29] making it possible that the differences in anodic reactivity observed on the two electrodes at potentials < 0.25 V, Fig. 7.3(b), may not be solely attributable to the presence of ϵ -particles. This possibility is also under investigation.

7.4 Summary and conclusions

The anodic behaviour of SIMFUELS containing UO_2 matrix dopants (RE) and matrix dopants plus segregated noble metal particles (RE + ϵ) has been studied in $\text{HCO}_3^-/\text{CO}_3^{2-}$ solutions containing H_2O_2 .

At potentials ≤ 0.25 V, both electrodes have been shown to support H_2O_2 oxidation as the dominant anodic reaction, with the dissolution of the UO_2 matrix occurring simultaneously. On the RE electrode, the currents at positive potentials $> \sim 0.25$ V are significantly suppressed and UO_2 dissolution becomes the dominant reaction. This is attributed to the formation of a U^{VI} oxide/hydroxide at low $\text{HCO}_3^-/\text{CO}_3^{2-}$ whose slow chemically-controlled dissolution controls the availability of the underlying $\text{U}^{\text{IV}}/\text{U}^{\text{V}}$ sites required to sustain both anodic reactions. An increase in $[\text{CO}_3]_{\text{tot}}$ accelerates this film dissolution and both anodic reactions increase in rate.

On the RE + ϵ electrode the anodic currents are increased at both low potentials (≤ 0.25 V) and higher potentials, especially at the latter. In the low potential region it is speculated that the increased current may be attributable to the anodic oxidation of a reactive peroxide-carbonate species on the ϵ -particle surfaces, although an impedance measurement could not elucidate whether this was the case.

At higher potentials on the RE + ϵ electrode, the direct anodic oxidation of H_2O_2 on ϵ -particles is observed, making H_2O_2 oxidation the dominant reaction, the UO_2 surface being partially blocked by the presence of U^{VI} surface species.

7.5 References

- [1] F. Haber, and J. Weiss, The catalytic decomposition of hydrogen peroxide by iron salts, Proc. R. Soc. London, Ser. A. 147 (1934) 332-351.
- [2] D.W. Shoesmith, and S. Sunder, An electrochemistry-based model for the dissolution of UO_2 , Report AECL-10488, Atomic Energy of Canada Ltd., Pinawa, Canada, 1991.
- [3] C.M. Lousada, A.J. Johansson, T. Brinck, and M. Jonsson, Mechanism of H_2O_2 Decomposition on Transition Metal Oxide Surfaces, J. Phys. Chem. C 116 (2012) 9533-9543.
- [4] A. Hiroki, and J.A. LaVerne, Decomposition of Hydrogen Peroxide at Water-Ceramic Oxide Interface, J. Phys. Chem. B 109 (2005) 3364-3370.
- [5] Gmelin Handbook of Inorganic Chemistry, Oxygen. Verlag Chemie, Weinheim. (1967) pp. 2353-2355
- [6] M. Trummer, S. Nilsson, and M. Jonsson, On the effects of fission product noble metal inclusions on the kinetics of radiation induced dissolution of spent nuclear fuel, J. Nucl. Mater. 378 (2008) 55-59.
- [7] S. Nilsson, and M. Jonsson, H_2O_2 and radiation induced dissolution of UO_2 and SIMFUEL pellets, J. Nucl. Mater. 410 (2011) 89-93.

- [8] C.M. Lousada, M. Trummer, and M. Jonsson, Reactivity of H_2O_2 towards different UO_2 -based materials: The relative impact of radiolysis products revisited, *J. Nucl. Mater.* 434 (2013) 434-439.
- [9] R. Pehrman, M. Trummer, C.M. Lousada, and M. Jonsson, On the redox reactivity of doped UO_2 pellets – Influence of dopants on the H_2O_2 decomposition mechanism, *J. Nucl. Mater.* 430 (2012) 6-11.
- [10] M. Razdan, Electrochemical and Surface Compositional Studies on UO_2 Corrosion Under Nuclear Waste Disposal Conditions, PhD Thesis, Western University, London, ON, 2013.
- [11] M. Razdan, and D.W. Shoesmith, Influence of Trivalent -Dopants on the Structural and Electrochemical Properties of Uranium Dioxide (UO_2), *J. Electrochem. Soc.* 161 (2014) H105-H113.
- [12] P.G. Lucuta, R.A. Verrall, H.-J. Matzke, and B.J.F. Palmer, Microstructural features of SIMFUEL - Simulated high-burnup UO_2 -based nuclear fuel, *J. Nucl. Mater.* 178 (1991) 48-60.
- [13] S. Sunder, N.H. Miller, W.H. Hocking, and P.G. Lucuta, X-ray photoelectron spectra of SIMFUEL, *J. Alloys Compd.* 213/214 (1994) 503-505.
- [14] M.E. Broczkowski, P.G. Keech, J.J. Noël, and D.W. Shoesmith, Corrosion of Uranium Dioxide Containing Simulated Fission Products in Dilute Hydrogen Peroxide and Dissolved Hydrogen, *J. Electrochem. Soc.* 157 (2010) C275-C281.
- [15] P.G. Keech, J.S. Goldik, Z. Qin, and D.W. Shoesmith, The anodic dissolution of SIMFUEL (UO_2) in slightly alkaline sodium carbonate/bicarbonate solutions, *Electrochim. Acta* 56 (2011) 7923-7930.
- [16] L. Wu, J.S. Goldik, and D.W. Shoesmith, The anodic reactions on simulated spent fuel (SIMFUEL) in H_2O_2 solutions - Effect of carbonate/bicarbonate, Submitted to *J. Electrochem. Soc.* (2014).
- [17] S.M. Peper, L.F. Brodnax, S.E. Field, R.A. Zehnder, S.N. Valdez, and W.H. Runde, Kinetic Study of the Oxidative Dissolution of UO_2 in Aqueous Carbonate Media, *Ind. Eng. Chem. Res.* 43 (2004) 8188-8193.
- [18] G.S. Goff, L.F. Brodnax, M.R. Cisneros, S.M. Peper, S.E. Field, B.L. Scott, and W.H. Runde, First Identification and Thermodynamic Characterization of the Ternary U(VI) Species, $\text{UO}_2(\text{O}_2)(\text{CO}_3)_2^{4-}$, in UO_2 - H_2O_2 - K_2CO_3 Solutions, *Inorg. Chem.* 47 (2008) 1984-1990.
- [19] D.E. Richardson, H. Yao, K.M. Frank, and D.A. Bennett, Equilibria, Kinetics, and Mechanism in the Bicarbonate Activation of Hydrogen Peroxide: Oxidation of Sulfides by Peroxymonocarbonate, *J. Am. Chem. Soc.* 122 (2000) 1729-1739.

- [20] T. Wu, and J.D. Englehardt, A New Method for Removal of Hydrogen Peroxide Interference in the Analysis of Chemical Oxygen Demand, *Environ. Sci. Technol.* 46 (2012) 2291-2298.
- [21] J. Zhang, and C.W. Oloman, Electro-oxidation of carbonate in aqueous solution on a platinum rotating ring disk electrode, *J. Applied Electrochem.* 35 (2005) 945-953.
- [22] D.A. Johnston, M.F. Cardosi, and D.H. Vaughan, The Electrochemistry of Hydrogen Peroxide on Evaporated Gold/Palladium Composite Electrodes. Manufacture and Electrochemical Characterization, *Electroanalysis* 7 (1995) 520-526.
- [23] L. Gorton, A carbon electrode sputtered with palladium and gold for the amperometric detection of hydrogen peroxide, *Analytica Chimica Acta* 178 (1985) 247-253.
- [24] S.B. Hall, H. Kheyrandish, and A.L. Hart, Electrochemical oxidation of hydrogen peroxide at platinum electrodes - Part II effect of potential, *Electrochim. Acta* 43 (1998) 2015-2024.
- [25] J. Wang, N. Naser, L. Angnes, H. Wu, and L. Chen, Metal-Dispersed Carbon Paste Electrodes, *Anal. Chem.* 64 (1992) 1285-1288.
- [26] Y. Zhang, and G.S. Wilson, Electrochemical oxidation of H₂O₂ on Pt and Pt + Ir electrodes in physiological buffer and its applicability to H₂O₂-based biosensors, *J. Electroanal. Chem.* 345 (1993) 253-271.
- [27] V.G. Prabhu, L.R. Zarpakar, and R.G. Dhaneshwar, Electrochemical studies of hydrogen peroxide at a platinum disc electrode, *Electrochim. Acta* 26 (1981) 725-729.
- [28] J.J. Lingane, and P.J. Lingane, Chronopotentiometry of hydrogen peroxide with a platinum wire electrode, *J. Electroanal. Chem* 5 (1963) 411-419.
- [29] H. He, P.G. Keech, M.E. Broczkowski, J.J. Noël, and D.W. Shoesmith, Characterization of the influence of fission product doping on the anodic reactivity of uranium dioxide, *Can. J. Chem.* 85 (2007) 702-713.

Chapter 8

SUMMARY AND FUTURE WORK

8.1 New contribution of this thesis

The overall research goal of this thesis was to investigate the corrosion of used nuclear fuel under permanent waste disposal conditions. Both modelling simulations and experimental approaches were presented in this thesis.

The model simulation in Chapters 3 and 4 was geared towards the Canadian nuclear waste disposal program. It incorporated most elementary reaction steps including radiolysis and corrosion reactions. It also took into account the geometric distribution and diffusion of all the species included in the model. To date, only one other similarly comprehensive model has been published for the Swedish program (Jonsson et al., *Environmental Sci. &Tech.* 41 (2007) 7087). A recent model endeavour (Trummer and Jonsson, *J. Nucl. Mater.* 396 (2010) 163) considered a closed system, as oppose to the open system (connected to groundwater) modelled in this thesis, and it did not include the effect of the container corrosion product, Fe^{2+} . Presently, as is the case with other models, our model is 1-dimensional and considers only the corrosion of a planar fuel surface. However, the capabilities of COMSOL Multiphysics allow the model to be expanded to 2-D and 3-D using customized geometry. As discussed in the introduction this will enable us to account for the influence of the fractured nature of spent fuel and the complex fuel bundle geometry on the local accumulation of radiolytic species and the ability of container corrosion products (Fe^{2+} and H_2) to influence the redox conditions at

geometrically awkward locations.

The experimental work in Chapters 5-7 mainly discussed the electrochemical oxidation of H_2O_2 on spent fuel surface. Although the cathodic reduction of H_2O_2 has been studied extensively, the anodic oxidation behaviour has received minimal attention. The anodic oxidation of H_2O_2 is important since it will determine the H_2O_2 decomposition rate and eventually the fuel corrosion rate. The influence of pH, carbonate/bicarbonate and noble metal fission products on this process has been investigated.

8.2 Project summary

An improved model for nuclear fuel corrosion inside a failed waste container has been developed (Chapters 3 and 4). The model takes into account the full α -radiolysis effect of water, the reaction of radiolytic H_2O_2 with UO_2 including the direct reaction of UO_2 with H_2O_2 and the galvanically-coupled oxidation by H_2O_2 reduction on noble metal particles, the reaction with H_2 via galvanic coupling, the Fenton reaction, the H_2O_2 decomposition and other related redox reactions involving H_2O_2 and H_2 . A full α -radiolysis reaction set has been incorporated and the analysis shows that a simplified calculation which only accounts for the radiolytic production of $\text{H}_2\text{O}_2/\text{H}_2$ would provide a reasonable and conservative approximation, only overestimating H_2O_2 production and UO_2 corrosion rate by ~20%.

Calculations have been performed in Chapter 4 to determine the influence of steel corrosion products (Fe^{2+} and H_2) on the α -radiolytic corrosion of spent fuel. The calculated fuel corrosion rate is very sensitive to $[\text{Fe}^{2+}]_{\text{bulk}}$ produced by corrosion of the steel vessel. When the $[\text{Fe}^{2+}]_{\text{bulk}}$ is greater than $4.2 \mu\text{mol L}^{-1}$ even the radiolytically

produced H_2 alone can suppress fuel corrosion without assistance from external H_2 for CANDU fuel with an age of 1000 years or larger. The ability of H_2 to suppress fuel corrosion is shown to be sensitive to fuel burnup (number/density of ϵ -particles) and a complete suppression of corrosion can be achieved at bulk H_2 concentrations in the order of $0.1 \mu\text{mol L}^{-1}$. The small difference between the calculation results and previous experimental/modelling data is likely due to the different fuel types used in different studies and the uncertainties associated with different disposal conditions.

The anodic oxidation and open circuit decomposition of H_2O_2 on SIMFUEL (doped with noble metal fission products) surfaces were investigated under various conditions: alkaline pH values and different bicarbonate/carbonate concentrations. The influence of the oxidized surface species (U^{VI}) on the electrochemical oxidation of H_2O_2 and eventually the dissolution rate of fuel were also studied under these conditions. A series of electrochemical and surface/solution analytical techniques were applied including X-ray photoelectron spectroscopy (XPS), scanning electron microscopy (SEM), and inductively coupled plasma atomic emission spectroscopy (ICP-AES). The results in Chapters 5-7 can be summarized as follows:

- In the absence of HCO_3^-/CO_3^{2-} , the dissolution rate of U^{VI} (as $U^{VI}O_2(OH)_y^{(2-y)+}$) is slow and H_2O_2 oxidation is inhibited by the presence of a partially permeable U^{VI} surface oxide/hydroxide layer. When HCO_3^-/CO_3^{2-} is present the more rapid chemical dissolution of U^{VI} (as $U^{VI}O_2(CO_3)_x^{(2-2x)+}$) exposes the underlying conductive $U^{IV}_{1-2x}U^V_{2x}O_{2+x}$ surface which facilitates the anodic oxidation of H_2O_2 .

- In non-complexing solutions, at pH = 9.5 the anodic oxidation is slow and appears to be blocked by the presence of an insulating U^{VI} surface layer. As the pH is increased to > 10.5 the anodic oxidation is accelerated but controlled partially by transport through a thin but chemically dissolving U^{VI} oxide/hydroxide surface layer. At open circuit the H_2O_2 decomposition reaction rate appears to be controlled by the cathodic half reaction. At low pH (≤ 10.5) it is blocked by the presence of U^{VI} surface states, but at higher pH appears to proceed rapidly on a $U^{IV}_{1-2x}U^V_{2x}O_{2+x}$ surface due to the increased solubility. The pH dependence of the rate suggests that HO_2^- is the electroactive form of peroxide.
- At positive electrode potentials, a significant fraction ($\sim 70\%$) of the anodic current goes to H_2O_2 oxidation and the remainder to UO_2 dissolution, as $U^{VI}O_2(OH)_x^{(2-x)+}$ or $U^{VI}O_2(CO_3)_x^{(2-2x)+}$ depending on the solution type, at relatively high $[H_2O_2]$ (0.02 mol L^{-1}). This fraction is similar in HCO_3^-/CO_3^{2-} -free or HCO_3^-/CO_3^{2-} -containing solutions, although the total anodic current is significantly higher in the presence of HCO_3^-/CO_3^{2-} .
- The dependencies of the anodic current on $[CO_3]_{tot}$ and $[H_2O_2]$ indicate that the rate of anodic dissolution increases at potentials positive to the open circuit (corrosion) potential, but at higher potentials when the dissolution rate is limited by the chemical release of U^{VI} , the anodic oxidation of H_2O_2 is the dominant reaction. It is possible that both anodic reactions are dependent on $[H_2O_2]$ due to the formation of a uranyl peroxocarbonate complex $(U^{VI}O_2(O_2)_x(CO_3)_y)^{2-2x-2y}$ although this remains to be conclusively demonstrated.

- The anodic behaviour of SIMFUELS containing UO_2 matrix dopants (RE) and matrix dopants plus segregated noble metal (RE + ϵ) particles has been studied in $\text{HCO}_3^-/\text{CO}_3^{2-}$ solutions containing H_2O_2 . At potentials ≤ 0.25 V, both electrodes have been shown to support H_2O_2 oxidation as the dominant anodic reaction, with the dissolution of the UO_2 matrix occurring simultaneously. On the RE electrode, the currents at more positive potentials (≥ 0.25 V) are significantly suppressed and UO_2 dissolution becomes the dominant reaction. This is attributed to the formation of a U^{VI} oxide/hydroxide at low $\text{HCO}_3^-/\text{CO}_3^{2-}$ whose slow chemically-controlled dissolution controls the availability of the underlying $\text{U}^{\text{IV}}/\text{U}^{\text{V}}$ sites required to sustain both anodic reactions. An increase in $[\text{CO}_3]_{\text{tot}}$ accelerates this film dissolution and both anodic reactions increase in rate. By contrast, on the RE + ϵ electrode the anodic currents are increased at both low potentials (≤ 0.25 V) and higher potentials, especially at the latter. In the low potential region one possibility is that the increased current may be attributable to the anodic oxidation of a reactive peroxide-carbonate species on the ϵ -particle surfaces. At higher potentials on the RE + ϵ electrode, the direct anodic oxidation of H_2O_2 on ϵ -particles is observed, making H_2O_2 oxidation the dominant reaction, the UO_2 surface being partially blocked by the presence of U^{VI} surface species.

8.3 Future work

- A primary goal of this model is to determine how the physical properties of the fuel and the geometry of the fuel cladding with respect to its failure influence the interaction of the two corrosion fronts. The present 1-D model is a precursor for

the eventual development of 2-D and 3-D models involving customized geometry to account for the fractured nature of the spent fuel and the complex fuel bundle geometry. Within such structures the local accumulation of radiolysis species is likely to occur and externally produced Fe^{2+} and H_2 may have limited access to reactive locations within fractures, porous grain boundaries and fuel bundles. Such geometric effects are expected to have a significant influence on the overall ability of container corrosion products to influence fuel corrosion and radionuclide release. This will require the extension of the model to include 2-D and 3-D processes and should be achievable using COMSOL procedures.

- One assumption in the current model is that the bulk concentrations of steel corrosion products will be constant. In reality, the supply of Fe^{2+} and H_2 will be determined by the corrosion performance of the steel vessel which will vary depending primarily on the available water. Consequently, the model could be improved by a more detailed analysis of the corrosion of the steel vessel.
- This model would need to couple the concentrations of H_2 and Fe^{2+} , and also to include the possibility that the rate of corrosion could be modified by the influence of the products of H_2O radiolysis and fuel dissolution (UO_2^{2+}).

Although the calculations presented in Chapters 3 and 4 appear to indicate that the Fenton reaction would rule out the transport of H_2O_2 to oxidize, and potentially passivate the steel surface, there is no similar restraint on the transport of the potential oxidant, UO_2^{2+} to the steel surface. While the evidence to determine whether the accumulation of U, either absorbed as U^{VI} or deposited as reduced U^{IV} , is presently unavailable, it is likely these processes will influence the overall

fuel corrosion rate. Similarly, the accumulation of Fe^{III} corrosion product deposits on the UO_2 surface could also influence the fuel corrosion rate.

- Further model development to account for the influence of groundwater species such as chloride and carbonate on aqueous radiolysis and UO_2 corrosion is also required.
- UV-vis spectrophotometric measurements can be performed to determine hydrogen peroxide concentration, and consequently, the rate of H_2O_2 consumption could be measured. And the results can be used to calculate the H_2O_2 decomposition rate combined with electrochemical and ICP-AES analysis.
- An extended EIS study is presently underway on both electrodes in an attempt to separate and elucidate the anodic reactions involved on both the UO_2 and ϵ -particle surfaces and to research the formation of anodic film in solution with/without carbonate.
- A series of extensive electrochemical and surface analysis experiments are required to elucidate the different behaviours between the electrodes with different dopants and the influence of the distribution and nature of the lattice dopants on the overall reactivity of the oxide matrix.

Linda (Michael) Wu**Education**

Ph.D. Candidate, Western University, London, ON. 2009-2014(expected)
B.Sc. in Chemistry, Nanjing University, Nanjing, China 2005-2009

Papers in Peer-Reviewed Journals

L. Wu, Y. Beauregard, Z. Qin, S. Rohani and D.W. Shoesmith, A model for the influence of steel corrosion products on nuclear fuel corrosion under permanent disposal conditions, *Corrosion Science* 61 (2012) 83-91.

L. Wu, Z. Qin, and D.W. Shoesmith, An improved model for the corrosion of used nuclear fuel inside a failed waste container under permanent disposal conditions, *Corrosion Science* 84 (2014) 85-95.

Papers in Peer-Reviewed Conference Proceedings

L. Wu and D.W. Shoesmith, Effect of carbonate on UO_2 corrosion in alkaline solution, 32nd Annual Conference of the Canadian Nuclear Society Conference and 35th Annual CNS/CNA Student Conference Proceedings, 2011.

Non-Refereed Industrial Reports

L. Wu, P. Keech and F. King, Internal Corrosion of Used Fuel Container, Technical Memorandum APM-03220-LOF, Nuclear Waste Management Organization, Toronto, ON, Dec 2013.

L. Wu, K. Liberda and P. Keech, Gamma Dose Rate Evolution in 4L-12 Used Fuel Container, Calculation APM-CALC-04300, Nuclear Waste Management Organization, Toronto, ON, Nov 2013.

Presentations and Posters

* indicates the presenter.

*L. Wu, Z. Qin, and D.W. Shoesmith, An improved model for nuclear fuel corrosion inside a failed container under permanent disposal conditions.

- 223rd Electrochemistry Society (ECS) Meeting, Toronto, ON. May 12-17, 2013. (Talk)
- 224th Electrochemistry Society (ECS) Meeting, San Francisco, CA, Oct 27-Nov 1, 2013. (Talk)

*L. Wu, Z. Qin, and D.W. Shoesmith, Electrochemical impedance spectroscopy study on SIMFUEL in hydrogen peroxide solution.

- 223rd Electrochemistry Society (ECS) Meeting, Toronto, ON. May 12-17, 2013. (Poster)

*L. Wu, and D.W. Shoesmith, The role of fission products on spent fuel corrosion in hydrogen peroxide solutions.

- Surface Canada 2013 Conference, London, ON. May 7-10, 2013. (Poster)
- 34nd Annual Conference of the Canadian Nuclear Society Conference and 37th Annual CNS/CNA Student Conference, Toronto, ON, Jun 9-12, 2013. (Poster)

*L. Wu, Z. Qin, and D.W. Shoesmith, A two-dimensional model for alpha radiolytic corrosion within the fuel fractures under permanent disposal conditions.

- PRiME Meeting and 222nd Electrochemistry Society (ECS) Meeting, Honolulu, HI. Oct 7-13, 2012. (Poster)
- Centre for Advanced Materials and Biomaterials Research (CAMBR) Conference, London, ON. Nov 13, 2012. (Poster)

*L. Wu, Z. Qin, and D.W. Shoesmith, Modelling study for influence of steel corrosion products on nuclear fuel corrosion inside a failed disposal container.

- 33rd Annual Conference of the Canadian Nuclear Society Conference and 36th Annual CNS/CNA Student Conference, Saskatoon, SK, June 10-13, 2012. (Poster)
- NACE student symposium, Toronto, ON. June 25, 2012. (Talk)
- Gordon Research Conference: Corrosion-Aqueous, New London, NH. July 8-13, 2012, & Gordon Research Seminar, July 7-8, 2012. (Poster)

*L. Wu and D.W. Shoesmith, Effect of pH on the electrochemical oxidation of H_2O_2 on uranium dioxide.

- 220th Electrochemistry Society (ECS) Meeting, Boston, MA, Oct 9-14, 2011. (Poster)

*L. Wu and D.W. Shoesmith, Effect of carbonate on SIMFUEL corrosion in alkaline H_2O_2 solutions.

- NACE Student Corrosion Research Symposium, Hamilton, ON, May 19, 2011. (Talk)
- 32nd Annual Conference of the Canadian Nuclear Society Conference and 35th Annual CNS/CNA Student Conference, Niagara Falls, ON, Jun 5-8, 2011. (Poster)
- NACE Northern Area Eastern Conference, Ottawa, ON, Aug 14-17, 2011. (1st place prize for posters)

*L. Wu and D.W. Shoesmith, The influence of pH and carbonate ions on H_2O_2 oxidation on UO_2 in neutral to alkaline solutions.

- Electrochemical Society Conference - Canadian Section, London, ON, Sep 18, 2010. (2nd place prize for posters)

Scholarships

Mitacs Accelerate Scholarship, Toronto, ON, 2013.

Western University Faculty WGRS and IGTS Scholarship, London, ON, Apr 2013.